THESIS

Development of a low frequency vibration isolation system for KAGRA, and study of the localization of coalescing binaries with a hierarchical network of gravitational wave detectors.

(KAGRA

)

29   1

Department of Astronomy
Graduate School of Science
The University of Tokyo
35-156128

Yoshinori Fujii

Abstract

This work describes the development of the seismic attenuation systems for the power recycling mirrors of the KAGRA interferometer. It also includes a study about source localization of a coalescing binaries by using a network of gravitational wave detectors with different sensitivities.

The KAGRA detector is the Japanese large-scale cryogenic gravitational wave telescope (LCGT) which is now being developed underground in the Kamioka mine. The core optics of the KAGRA detector will be suspended by the so-called seismic attenuation system (SAS). Their positions are actively controlled by using sensors and actuators implemented on SAS, in order to suppress the large displacements caused seismic noise driving the mechanical resonances of the suspension systems.

This work verified an existing simulation tool for the mechanical suspension system and active control systems by using one suspension system used in iKAGRA. The iKAGRA is a test run which was conducted in spring 2016 with Michelson configuration. This verification confirmed that the simulation tool worked properly for designing the active control system for the suspension system.

Active control systems for the suspension system which will suspend the power recycling mirrors are designed by using the simulation tool.

In the coming years, large-scale gravitational wave detectors will start coincident observations to achieve source localization. However, in the beginning, the sensitivities of those detectors can be different from each other, even if they are operated at the same time. Thus, one has to construct a method to effectively use the less sensitive detectors' information. This work investigated a hierarchical network search to deal with such a situation. In this search, the less sensitive detectors are included into the network with lower SNR threshold than the SNR of the higher sensitive detectors, only when a trigger is generated from the higher sensitive detector's coincidences search.

This study confirmed that this method can reduce the systematic error on a sky map probability by a factor of 0.7, by using 2 high sensitivity detectors and 1 or 2 low sensitivity ones. This is compared to a performance of a network search by the 2 high sensitivity detectors. The study supposed that the detection network composed by 3 (or 4) detectors whose detection ranges are 70 Mpc and 20 Mpc. It also confirmed that the hierarchical network search is useful for the observations involving gravitational wave detectors with different sensitivities.

Table of Contents

Theory and observation of gravitational waves

PartI

Introduction

Chapter 1

The theoretical background of gravitational waves is described in this chapter. The existence of gravitational waves was predicted by A. Einstein in 1916 according to his theory of general relativity [1]. 100 years after the prediction, gravitational waves were detected for the first time in 2015 by the Laser Interferometric Gravitational-wave Observatory (LIGO) in the U.S. [2].

The theory of gravitational waves is described in section 1.1. Section 1.2 introduces sources of gravitational waves that are targets for observation. The interferometric detection method, which is used for the current gravitational wave detectors, is summarized in section 1.3. Section 1.4 describes the motivations for expanding the sensitivity of the gravitational wave detectors to a lower frequency region, and for constructing a rapid localization method with different sensitivity gravitational wave detectors.

1.1   Gravitational waves in general relativity

In general relativity, the Einstein field equations, which describe the relationship between the metric of spacetime and the mass distribution, are

$$G_{\mu\nu} \equiv R_{\mu\nu} - \frac{1}{2}g_{\mu\nu}R = \frac{8\pi G}{c^4}T_{\mu\nu}. \tag{1.1}$$

Here:

- $g_{\mu\nu}$: Metric tensor, which characterizes the geometry of spacetime. Dimensionless quantity. It is defined as the inner product of basis vectors: $g_{\mu\nu} \equiv \boldsymbol{e}_\mu \cdot \boldsymbol{e}_\nu$.

- $T_{\mu\nu}$: Energy-momentum tensor, which characterizes mass distribution. The elements of $T_{\mu\nu}$ include the following quantities:
  T_{00}: Energy density, T_{i0}: ith element of momentum density,
  T_{0j}: jth element of energy flux,
  T_{ij}: Stress tensor in non-relativistic fluid dynamics ($i, j = 1, 2, 3$).

- $G_{\mu\nu}$: Einstein tensor

- $R_{\mu\nu} \equiv R^\alpha{}_{\mu\alpha\nu}$: Ricci tensor, which is defined by
  $R^\mu{}_{\alpha\beta\gamma} \equiv \frac{\partial \Gamma^\mu_{\alpha\beta}}{\partial x^\gamma} - \frac{\partial \Gamma^\mu_{\alpha\gamma}}{\partial x^\beta} + \Gamma^\mu_{\lambda\gamma}\Gamma^\lambda_{\alpha\beta} - \Gamma^\mu_{\lambda\beta}\Gamma^\lambda_{\alpha\gamma}$, where $\Gamma^\mu_{\alpha\beta} \equiv g^{\mu\nu}\left(\frac{\partial g_{\beta\nu}}{\partial x^\alpha} + \frac{\partial g_{\alpha\nu}}{\partial x^\beta} - \frac{\partial g_{\alpha\beta}}{\partial x^\nu}\right)$.

- $R \equiv g^{\mu\nu}R_{\mu\nu}$: Scalar curvature (or Ricci scalar).

- G : Gravitational constant.

- c : Speed of light.

In the equation (1.1), the line element ds between two points x^μ and $x^\mu + dx^\mu$, which are infinitesimally separated from each other, is $ds^2 = (dx^\mu \boldsymbol{e}_\mu) \cdot (dx^\nu \boldsymbol{e}_\nu) = g_{\mu\nu}dx^\mu dx^\nu$, where $\boldsymbol{e}_\mu, \boldsymbol{e}_\nu$ denote the basis vectors of the coordinates. In spacetime which is described by the metric $g_{\mu\nu}$ as defined above, the motion of a free particle is explained by its geodesic equation:

$$\frac{\mathrm{d}^2 x^\alpha}{\mathrm{d}\tau^2} = \Gamma^\alpha_{\mu\nu}\left(\frac{\mathrm{d}x^\mu}{\mathrm{d}\tau}\right)\left(\frac{\mathrm{d}x^\nu}{\mathrm{d}\tau}\right), \tag{1.2}$$

where τ is an arbitrary parameter. By using these equations, general relativity concludes that what we observe as gravity is a curvature of spacetime. The characteristics of gravity are described by the metric in general relativity.

1.1.1 Linearization of Einstein equation

In this section, we derive the equation which describes gravitational waves. A more detailed version of the following calculation is described in [3]. First, we derive the Einstein equation in a weak gravitational field. Since spacetime is flat if there is no gravity, we assume that the spacetime is mostly flat in the weak gravitational field, that is, the metric in the weak field $g_{\mu\nu}$ is explained by the superposition of a metric of flat spacetime(Minkowski metric) $\eta_{\mu\nu}$ and that of a small perturbation $h_{\mu\nu}$:

$$g_{\mu\nu} \;=\; \eta_{\mu\nu} \;+\; h_{\mu\nu} \;+\; \mathrm{O}(h^2) \qquad (\; |h_{\mu\nu}| \;\ll\; 1 \;) \tag{1.3}$$

In above equation, $h_{\mu\nu}$ describe actual spacetime as a perturbation from Minkowski spacetime. Here, some quantities are defined for following calculation:

$$h^{\mu}{}_{\nu} \equiv \eta^{\mu\lambda} h_{\lambda\nu} \;, \qquad h^{\mu\nu} \equiv \eta^{\mu\alpha}\eta^{\nu\beta} h_{\alpha\beta} \;, \qquad h \equiv \eta^{\mu\nu} h_{\mu\nu}. \tag{1.4}$$

Then, if one rearranges the Einstein equation by using a formula $g^{\mu\nu} = \eta^{\mu\nu} - h^{\mu\nu} + \mathrm{O}\left(h^2\right)$, following formula is obtained. Note that $g_{\mu\nu}$ denotes the inverse matrix of $g^{\mu\nu}$, and that terms in h^2 and higher are neglected in this calculation.

$$\begin{aligned} G_{\mu\nu} &= \frac{8\pi G}{c^4} T_{\mu\nu} \\ &\simeq R_{\mu\nu} \;-\; \frac{1}{2}\eta_{\mu\nu} R \\ &= \frac{1}{2}\left(-\Box h_{\mu\nu} + \partial_\nu \partial^\alpha h_{\mu\alpha} + \partial_\mu \partial^\alpha h_{\nu\alpha} - \partial_\mu \partial_\nu h - \eta_{\mu\nu} \partial^\alpha \partial^\beta h_{\alpha\beta} + \eta_{\mu\nu} \Box h \right), \end{aligned} \tag{1.5}$$

where, $\partial_\mu \equiv \frac{\partial}{\partial x^\mu}$, $\partial^\alpha = \eta^{\alpha\nu}\partial_\mu$ and $\Box \equiv \partial^\alpha \partial_\alpha = \eta^{\alpha\beta}\partial_\alpha \partial_\beta = -\frac{1}{c^2}\partial_t{}^2 + \nabla^2 = -\frac{1}{c^2}\frac{\partial^2}{\partial t^2} + \frac{\partial^2}{\partial x^2} + \frac{\partial^2}{\partial y^2} + \frac{\partial^2}{\partial z^2}$. Here, if one applies a gauge transformation which satisfies the following condition,

$$\partial^\alpha h_{\mu\alpha} \;-\; \frac{1}{2}\partial_\mu h \;=\; 0, \tag{1.6}$$

the equation below is obtained:

$$\Box \left(h_{\mu\nu} \;-\; \frac{1}{2}\eta_{\mu\nu} h \right) \;=\; -\frac{16\pi G}{c^4} T_{\mu\nu}. \tag{1.7}$$

This equation is called the linearized Einstein equation and is what is sought in this subsection. In most cases, eq (1.7) is expressed as follows by using another tensor $\bar{h}_{\mu\nu} \equiv h_{\mu\nu} \;-\; \frac{1}{2}\eta_{\mu\nu} h$:

$$\Box \bar{h}_{\mu\nu} \;=\; -\frac{16\pi G}{c^4} T_{\mu\nu}. \tag{1.8}$$

This $\bar{h}_{\mu\nu}$ is called trace-reversed tensor, and has the relationship below:

$$\bar{h} \equiv \bar{h}^\mu{}_\mu = -h^\mu{}_\mu = -h. \tag{1.9}$$

Note that under the condition of eq (1.6), $\bar{h}_{\mu\nu}$ satisfies $\partial_\mu \bar{h}^\mu{}_\nu = 0$.

Eq (1.8) denotes the wave equation of the $\bar{h}_{\mu\nu}$ which describes the small perturbation $h_{\mu\nu}$ from the Minkowski metric. Eq (1.8) also implies that $\bar{h}_{\mu\nu}$ propagates away from the source of the energy-momentum tensor $T_{\mu\nu}$ with the speed of light c. If one considers a vacuum condition $T_{\mu\nu} = 0 \,(= R_{\mu\nu} = R)$, i.e., a spacetime without masses, eq (1.8) becomes $\Box \bar{h}_{\mu\nu} = 0$. Consequently, one can obtain an expression similar to the wave equation for electromagnetic waves which propagate in vacuum. This ripple of the spacetime $\bar{h}_{\mu\nu}$, which propagates with speed of light c, denotes a gravitational wave which is described by eq (1.8).

1.1.2 Properties of gravitational wave

This subsection explores the properties of gravitational waves which propagate in vacuum by considering a monochromatic plane wave:

$$\bar{h}_{\mu\nu} \equiv a_{\mu\nu}e^{ik_\alpha x^\alpha} = a_{\mu\nu}\exp[i(\boldsymbol{k}\cdot\boldsymbol{r} - \omega t)], \tag{1.10}$$

where k^α denotes the wave vector $k^\alpha = (\omega/c, k^1, k^2, k^3)$, $a_{\mu\nu}$ describes its amplitude via a 4×4 matrix of constant numbers. Here, one can choose the following gauge conditions so that $a_{\mu\nu}$ (or $\bar{h}_{\mu\nu}$) holds only information about the gravitational waves:

$$\bar{h}_{0\nu} = 0, \tag{1.11}$$
$$\bar{h}^i{}_i = 0, \tag{1.12}$$
$$\partial_j \bar{h}^{ij} = 0. \tag{1.13}$$

The set of conditions chosen here (1.11) $\sim$ (1.13) is called the transverse traceless (TT) gauge. Gravitational waves are discussed under this gauge in most cases.

Under this gauge, one obtains the following properties of gravitational waves:

- Eq (1.11) says that gravitational waves have only space element.

- Eq (1.12) says that gravitational waves are traceless and thus the difference between $\bar{h}_{\mu\nu}$ and $h_{\mu\nu}$ vanishes due to this equation ($\bar{h}_{\mu\nu}^{\mathrm{TT}} = h_{\mu\nu}^{\mathrm{TT}}$).

- Eq (1.13) says that gravitational waves are transverse waves.

The argument about the eq (1.13) is obtained from following equation which is derived by inserting eq (1.10) into eq (1.13):

$$k^j a_{ij} = k^j \bar{h}_{ij} = 0. \tag{1.14}$$

This equation says that the wave vector is orthogonal with $\bar{h}_{ij}$. In addition, if one considers a plane gravitational wave which propagates along the z axis, the $a_{\mu\nu}$ below are obtained by using the equations $k^\mu = (k^0, k^1, k^2, k^3) = (\omega/c, 0, 0, \omega/c)$, $a_{12} = a_{21}$ and $a_{11} + a_{22} = 0$:

$$a_{\mu\nu}^{\mathrm{TT}} = \begin{pmatrix} 0 & 0 & 0 & 0 \\ 0 & a_+ & a_\times & 0 \\ 0 & a_\times & -a_+ & 0 \\ 0 & 0 & 0 & 0 \end{pmatrix}. \tag{1.15}$$

This expression implies that gravitational wave have two degrees of freedom.

Effect on free point mass

Here we consider how a gravitational wave affects free point masses. If one suppose that a free point mass is at rest at a coordinate and is then exposed to a gravitational wave in the TT gauge, the geodesic equation of the free point mass is expressed by

$$\frac{dU^\alpha}{d\tau} + \Gamma^\alpha{}_{\mu\nu}U^\mu U^\nu = 0, \tag{1.16}$$

where U^α denotes the coordinate velocity of the mass. Then due to $h_{\beta 0}^{TT} = 0$, the initial acceleration of the mass is

$$\left(\frac{dU^\alpha}{d\tau}\right)_{\mathrm{initial}} = -\Gamma^\alpha{}_{00} = \frac{1}{2}\eta^{\alpha\beta}(\partial_0 h_{\beta 0} + \partial_0 h_{0\beta} + \partial_\beta h_{00}) = 0, \tag{1.17}$$

which is always 0. Thus, if one chooses the TT gauge, the basis changes so that the each mass stays at the original coordinate position.

Here we examine the behavior of the proper distance between two free point masses. If one sets the masses at origin $(0,0,0)$ and $(L,0,0)$, the proper distance l is

$$
\begin{aligned}
l &= \int |ds^2|^{1/2} = \int |g_{\alpha\beta}dx^\alpha dx^\beta|^{1/2} \\
&= \int_0^L |g_{xx}|^{1/2}dx \simeq |g_{xx}(x=0)|^{1/2} \times L \\
&\simeq \{1 + \frac{1}{2}h_{xx}^{\mathrm{TT}}(x=0)\} \times L,
\end{aligned}
\tag{1.18}
$$

where $h_{xx}^{\mathrm{TT}}(x=0)$ is a non-zero term. Thus the eq(1.17) and eq(1.18) implies that neither of the two masses move but the proper distance l is changed if a gravitational wave is injected. Consequently, one can sense the gravitational waves by observing the proper distance(s) between two (or more) masses. In addition, according to eq(1.18), the length shift due to the gravitational wave injection ΔL is described by

$$
\frac{\Delta L}{L} = \frac{1}{2}h,
\tag{1.19}
$$

where h is the spatial distortion in the measurement direction.

Polarization

The remaining two degrees of freedom appear as polarizations. These two polarizations are called 'plus mode' and 'cross mode' according to the distortion shapes. Suppose that some free point masses are put in a circle around a point $(0,0,0)$ whose radius is given by L. First, the line element ds^2 between the origin and one of the masses is

$$
ds^2 = -(cdt)^2 + (1+h_+)dx^2 + 2h_\times dxdy + (1-h_+)dy^2 + dz^2.
\tag{1.20}
$$

Then, if a two dimensional plane is considered, ds^2 is deformed by

$$
dl^2 = (1+h_+)dx^2 + 2h_\times dxdy + (1-h_+)dy^2.
\tag{1.21}
$$

In this condition, if a gravitational wave is injected along the z axis, the infinitesimal distances between the origin and one of the masses, dx, dy vary as

$$
dl^2 \simeq dx'^2 + dy'^2
\tag{1.22}
$$

$$
\begin{pmatrix} dx' \\ dy' \end{pmatrix} = \begin{pmatrix} 1+\frac{1}{2}h_+ & \frac{1}{2}h_\times \\ \frac{1}{2}h_\times & 1-\frac{1}{2}h_+ \end{pmatrix} \begin{pmatrix} dx \\ dy \end{pmatrix}.
\tag{1.23}
$$

Finally, if one chooses $(dx, dy) \equiv (L\cos\theta, L\sin\theta)$, the proper distance l is

- if $h_+ \neq 0, h_\times = 0$; according to $dl^2 = (1+h_+)dx^2 + (1-h_+)dy^2 \simeq L^2(1+h_+\cos 2\theta)$,

$$
l = L \times \left(1 + \frac{1}{2}h_+\cos 2\theta\right) \qquad : \quad + \text{ mode},
\tag{1.24}
$$

- if $h_+ = 0, h_\times \neq 0$; according to $dl^2 = dx^2 + dy^2 + 2h_\times dxdy \simeq L^2(1+h_\times\sin 2\theta)$,

$$
l = L \times \left(1 + \frac{1}{2}h_\times\sin 2\theta\right) \qquad : \quad \times \text{ mode}.
\tag{1.25}
$$

Then, if one inserts $h_+ = a_+\exp[i(kz-\omega t)]$, or $h_\times = a_\times\exp[i(kz-\omega t)]$ into these equations, the location of the masses become as shown in figure 1.1.

Plus mode

Cross mode
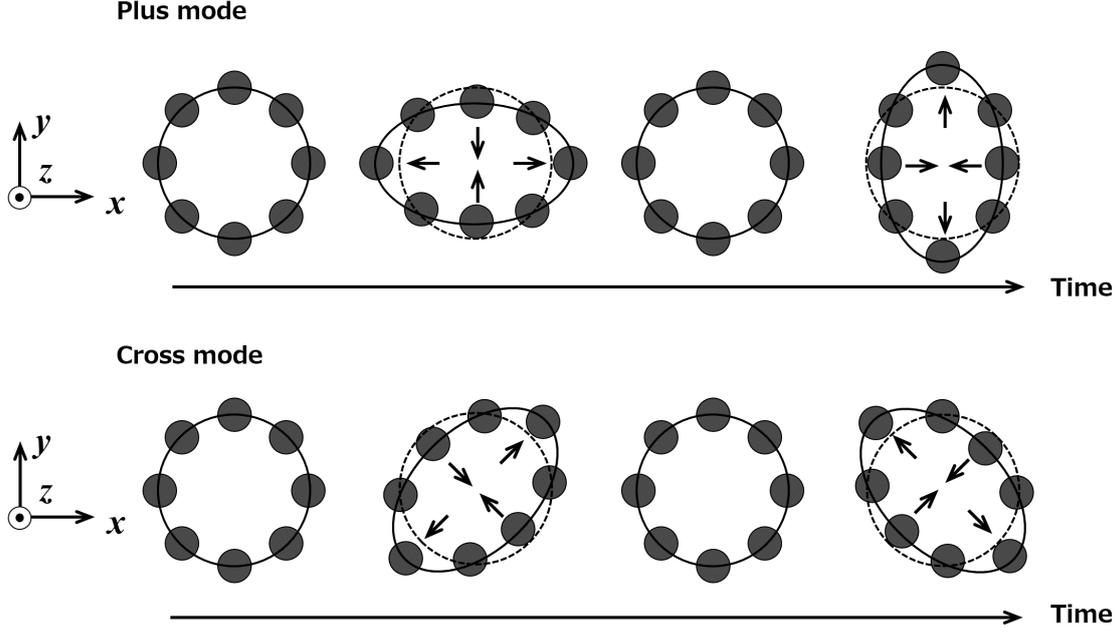
Figure 1.1: Polarizations of a gravitational wave. If a gravitational wave incidents into $+z$ axis, the positions of free particles arrayed in circle are changed as shown in this figure. Black points denote free particles.

1.1.3   Emission of gravitational wave

This subsection derives the gravitational wave emissions according to the linearized Einstein equation. First, transform eq(1.8) as follows by using a Green's function for the d'Alembert operator $G(x^\sigma - y^\sigma)$:

$$G(x^\sigma - y^\sigma) \quad = \quad -\frac{1}{4\pi|\boldsymbol{x} - \boldsymbol{y}|}\delta\left(|\boldsymbol{x} - \boldsymbol{y}| - (x^0 - y^0)\right)\theta(x^0 - y^0), \qquad (1.26)$$

$$\Box G(x^\sigma - y^\sigma) \quad = \quad \delta^{(4)}(x^\sigma - y^\sigma) \ = \ \delta(x^0 - y^0)\delta(x^1 - y^1)\delta(x^2 - y^2)\delta(x^3 - y^3), \qquad (1.27)$$

where $\sigma = 0, 1, 2, 3$, $\delta(x)$ denotes Dirac's δ function and $\theta(x)$ means a step function. Here, we assume that $\boldsymbol{x}$ and $\boldsymbol{y}$ are the observing location and the source position respectively, and thus the distance between $\boldsymbol{x}$ and $\boldsymbol{y}$ is $|\boldsymbol{x} - \boldsymbol{y}| = \{\delta_{ij}(x^i - y^i)(x^j - y^j)\}^{1/2}$. Note that $\theta(x^0 - y^0)$ is equal to 1 where $x^0 > y^0$ is satisfied, otherwise it equals 0. Then, $\bar{h}_{\mu\nu}$ can be expressed as below by using (1.8), (1.26) and (1.27), if one also assumes $r \equiv |\boldsymbol{x}| \gg |\boldsymbol{y}|$ (it assumes that the observation point is far enough away compared with the size of the source):

$$\bar{h}_{\mu\nu}(t, \boldsymbol{x}) \quad = \quad -\frac{16\pi G}{c^4}\int G(x^\sigma - y^\sigma)T_{\mu\nu}(y^\sigma)d^4y \ = \ \frac{4G}{c^4}\int\frac{T_{\mu\nu}(ct - |\boldsymbol{x} - \boldsymbol{y}|, \boldsymbol{y})}{|\boldsymbol{x} - \boldsymbol{y}|}d^3y,$$

$$\simeq \quad \frac{4G}{rc^4}\int T_{\mu\nu}(ct - r, \boldsymbol{y})d^3y. \qquad (1.28)$$

As a next step, modify this eq (1.28) using the integration below:

$$\int T^{ij}d^3y \ = \ \frac{1}{2}\frac{d^2}{dt^2}\int T^{00}y^iy^jd^3y \ = \ \frac{1}{2}\frac{d^2}{dt^2}\int \rho c^2 y^iy^jd^3y. \qquad (1.29)$$

This equation is obtained by using the relationship $\partial_\alpha \partial_\beta (T^{\alpha\beta} x^\mu x^\nu) = 2T^{\mu\nu}$, which is calculated by $\partial_\nu T^{\mu\nu} = 0$ (this denotes local energy-momentum conservation). Then if a quadrupole mass distribution I_{ij} is defined as

$$I_{ij} \equiv \int \rho c^2 y^i y^j d^3 y, \tag{1.30}$$

$\bar{h}_{ij}$ is

$$\bar{h}_{ij}(t, \boldsymbol{x}) = \frac{2G}{rc^4} \ddot{I}_{ij}(ct - r). \tag{1.31}$$

This denotes that the amplitude of a gravitational wave is proportional to the second derivative of the quadrupole with respect to time. Then, if one considers the TT gauge, eq (1.31) becomes

$$\bar{h}_{ij}^{\mathrm{TT}}(t, \boldsymbol{x}) = \frac{2G}{rc^4} \ddot{\mathcal{I}}_{ij}(ct - r), \tag{1.32}$$

$$\text{where } \mathcal{I}_{ij} \equiv \int \rho c^2 \left(x^i x^j - \frac{1}{3} \delta_{ij} r^2 \right) d^3 x, \quad \bar{h}_{ij}^{\mathrm{TT}} = \left(P_i^k P_j^l - \frac{1}{2} P_{ij} P^{kl} \right) \bar{h}_{kl},$$

and $P_j^i \equiv \delta_j^i - n^i n_j$, $n^i \equiv x^i / r$. Consequently, gravitational waves are generated only when the quadrupole moment changes with time according to eq (1.31) or when the source is not distributed spherically due to eq (1.32). Here, if one considers two 100-kg masses connected with a 2-m bar, which are rotating at 100 cycles per second, one obtains that the system emits 200-Hz gravitational wave with amplitude $h \sim 10^{-43}$ at a distance of 1,500 km from the source [4]. This implies that detectable gravitational waves come not from events on the earth but from violent celestial events.

Luminosity of gravitational waves

The scale of the luminosity of gravitational waves is briefly summarized here. The luminosity of a gravitational wave is given by [4]

$$\frac{dE_{\mathrm{GW}}}{dt} = \frac{G}{5c^5} \langle \dddot{\mathcal{I}}^{ij} \dddot{\mathcal{I}}_{ij} \rangle. \tag{1.33}$$

Here, we calculate the typical luminosity of gravitational waves. If the source is characterized by mass M, size R, emitting time duration T and the velocity $v = R/T$, eq (1.33) becomes

$$\frac{dE_{\mathrm{GW}}}{dt} \sim \frac{G}{c^5} \left(\frac{MR^2}{T^3} \right)^2 \sim \frac{c^5}{G} \left(\frac{GM}{Rc^2} \right)^2 \left(\frac{v}{c} \right)^6 \sim 3.6 \times 10^{59} [\mathrm{erg/s}] \left(\frac{GM}{Rc^2} \right)^2 \left(\frac{v}{c} \right)^6$$
$$\sim 1.0 \times 10^{26} \times L_\odot \left(\frac{r_s}{2R} \right)^2 \left(\frac{v}{c} \right)^6, \tag{1.34}$$

where r_s denotes the Schwarzschild radius $2GM/c^2$. Moreover, if one supposes a system where the virial theorem ($Mv^2 \sim GM^2/R$) is available, eq (1.34) becomes

$$\frac{dE_{\mathrm{GW}}}{dt} \sim 1.0 \times 10^{58} [\mathrm{erg/s}] \left(\frac{r_s}{R} \right)^5 \sim 2.6 \times 10^{25} \times L_\odot \left(\frac{r_s}{R} \right)^5. \tag{1.35}$$

Eq (1.35) implies that compact objects such as neutron stars and black holes are important candidate sources of gravitational waves.

For another example, consider two equal-mass objects which obey Kepler's law. Using a formula which is available in the system: $2GM \sim (2\pi/T)^2 R^3$, the luminosity can be expressed as

$$\frac{dE_{\mathrm{GW}}}{dt} \sim 1.2 \times 10^5 \times L_\odot \left(\frac{1\mathrm{s}}{T} \right)^{10/3} \left(\frac{M}{M_\odot} \right)^{10/3}. \tag{1.36}$$

Then, if one sets $T = 30$ s, $M = M_\odot$, the luminosity becomes about 1.5 $L_\odot$. Eq (1.36) implies that one easy method to catch a gravitational wave with luminosity $\sim L_\odot$, is to look for celestial phenomena with compact objects. Otherwise, one would not be able to detect the gravitational wave due to the smallness of the luminosity or energy.

1.2   Astrophysical gravitational wave sources

This subsection introduces gravitational wave sources which would be detectable by current gravitational wave detectors. As described in the above section, gravitational waves are emitted if the quadrupole moment of the mass distribution of the source changes with time. However due to the small energy/amplitude scale, to detect gravitational waves one has to observe motion of compact celestial objects. The following four events are thought to be promising sources: compact binary coalescence, spin of compact stars, supernovae and stochastic background. More details about the sources of gravitational waves are summarized in [5].

1.2.1   Compact binary coalescence

A binary system consisting of two compact objects, either neutron stars or black holes, is a thoroughly investigated gravitational-wave source. In particular, a neutron star binary coalescing system has the most promising electromagnetic counterpart. General relativity predicts that the two objects orbit each other while emitting gravitational waves, and the orbital radius and period decrease due to loss of the energy and the angular momentum. This lasts until they collide and form one body. The coalescing process is divided into three phases: the inspiral phase, the merger phase and the ring-down phase.

During the inspiral phase, the two objects orbit each other with increasing amplitude and frequency of the emitted gravitational waves. The waveforms in this period are known as chirp signals[6]. The amplitude and the frequency of the chirp signal are described by

$$f_{\rm GW}(\tau) \sim 135 \text{ [Hz]} \left(\frac{M_{\rm chirp}}{1.2M_\odot}\right)^{5/8} \left(\frac{1{\rm s}}{\tau}\right)^{-3/8} \tag{1.37}$$

$$h(\tau) \sim 2.1 \times 10^{-23} \left(\frac{M_{\rm chirp}}{1.2M_\odot}\right)^{5/3} \left(\frac{\tau}{1{\rm s}}\right)^{-1/4} \left(\frac{r}{200{\rm Mpc}}\right)^{-1}, \tag{1.38}$$

where τ denotes time to coalescence of the binary stars, r is the distance between the source and observation location and $M_{\rm chirp}$ describes the chirp mass, defined by $M_{\rm chirp} = (m_1 m_2)^{3/5}(m_1 + m_2)^{-1/5}$. Here m_1, m_2 are the masses of each object. For instance, if one considers a time 1 ms before the merger, the amplitude and frequency of a gravitational wave which is emitted by a two-equal-mass binary system with $30M_\odot$ at 200 Mpc away from the source are 70 Hz and 2×10^{-21} respectively. The inspiral phase can last millions of years and the emitted gravitational waves are not detectable during most of the time, because the frequency of the waves in the period is too low to be observed by current (terrestrial interferometric) gravitational wave detectors. Only just before the merger, does the chirp signals enter the detection bandwidth of the detectors due to the rapid increase of the frequency and the amplitude.

In the merger phase, which last only milliseconds, the two objects get close each other and the gravitational forces becomes so strong that the two bodies start to plunge towards each other, colliding and forming one object. During the ring-down phase, the newly formed object calms down to a steady state by radiating gravitational waves.

Nowadays, computation of the inspiral, merger and ring-down phase of the binary coalescences is actively being researched. The goal of this computation is to provide templates for matched filtering [9]. In this process, the numerical waveforms are compared to the output signals generated by gravitational wave detectors.

1.2.2 Spin of compact stars

A spinning compact star such as a radio pulsar is also a possible gravitational wave source. It is expected that this system would provide a long continuous wave at a single frequency, double the spin frequency of the pulsars, if the object has an asymmetry around its rotation axis. The amplitude of the wave from an asymmetric spinning compact star h is given by [6]

$$h \sim 1.06 \times 10^{-25} \left(\frac{\varepsilon}{10^{-6}} \right) \left(\frac{I}{10^{38} \text{kgm}^2} \right) \left(\frac{10 \text{kpc}}{r} \right) \left(\frac{f_{\text{GW}}}{1 \text{kHz}} \right), \quad (1.39)$$

where ε denotes the equatorial ellipticity, I is the moment of inertia about the spin axis and f_{GW} represents the frequency of the gravitational wave, which is twice the spin frequency. h is scaled by typical parameters of neutron stars.

1.2.3 Core-collapse supernovae

A core-collapse supernova is a candidate source which emits a large-amplitude gravitational wave. This is because it accelerates an huge amount of mass dramatically in a short period and asymmetrically. The prediction of the actual waveforms emitted from supernovae is challenging; however, progress in the field of numerical relativity allows the magnitude of the emitted gravitational waves to be estimated [7]. The amplitude from a supernova that happens in a nearby galaxy is of the order of $h \sim 10^{-22} - 10^{-21}$. According to the models for this calculation, the frequency of the gravitational waves emitted from the supernovae are spread widely around 1 kHz. Thus, supernovae in a nearby galaxy can be reasonable target sources for current gravitational wave detectors.

1.2.4 Stochastic background

A stochastic background of gravitational waves is expected from numerous unresolved astrophysical sources such as white dwarf binaries, cosmological origins such as inflation, phase transition in the early universe and cosmic strings [8]. The amplitude and the frequency of the gravitational waves with cosmological origins depends on the theory considered. Detection of stochastic backgrounds is generally conducted by investigating cross-correlation between observations by several detectors. Previous analyses by using terrestrial interferometric gravitational wave detectors provided some restrictions and upper limits to several theories on cosmological gravitational wave sources [10].

1.3   Interferometric detection

Nowadays, gravitational wave detectors are developed based on laser-interferometric techniques. The interferometric detection schemes and the characteristics of detectors are described in this subsection.

1.3.1   Basic principle

In order to detect gravitational waves, one needs to monitor the differential displacements of two masses in orthogonal directions, according to the polarization. Thence, the simplest interferometric gravitational wave detector is a Michelson interferometer built with suspended mirrors. Figure 1.2 illustrates its optical configuration. A laser beam is split into two by the beam splitter. The two beams are reflected at the end mirrors and then recombined at the beam splitter. As the result of interference, a fraction of the beam goes to the photodiode and the remainder goes back to the laser source. The beam intensity P_{output} output to the photodiode is given by

$$P_{\mathrm{output}} = \frac{1}{2} P_{\mathrm{L}} \left(1 - \cos \delta\phi \right), \tag{1.40}$$

where P_{L} denotes the laser power and $\delta\phi = 2\pi(l_1 - l_2)/\lambda$ represents the phase difference between the two optical paths. Here λ denotes the wavelength of the laser beam. The beam power at the photodiode is converted to current signals. One can obtain information about the phase shift by monitoring the beam intensity on the photodiode.
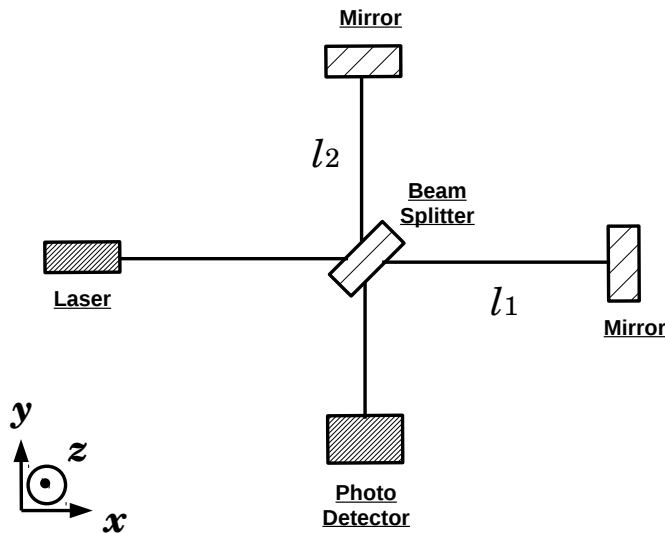

Figure 1.2: Optical configuration of a Michelson interferometer. Here l_1, l_2 denote the arm length.

Here, suppose that a gravitational wave, which has plus polarization and amplitude $h(t)$, is injected along the $+z$ direction. The response of the laser beam to the injected gravitational wave is calculated as follows. If one considers one of the photons comprised by the laser beam in the x direction, from

eq (1.20) and this configuration, the line element ds^2 of the photon is given by

$$\frac{dx}{dt} = \frac{c}{\sqrt{1 + h_+(t)}}, \tag{1.41}$$

by using $dy = dz = ds^2 = 0$. The round trip time Δt_1 of a photon between the beam splitter and the end mirror is

$$\int_t^{t+\Delta t_1} \frac{dt'}{\sqrt{1 + h_+(t')}} = \frac{2l_1}{c}. \tag{1.42}$$

Then, by assuming $|h_+| \ll 1$, namely $(1 + h)^{-1/2} \sim (1 - h/2)$, the above equation becomes

$$\Delta t_1 = \frac{2l_1}{c} + \frac{1}{2} \int_t^{t+\Delta t_1} h_+(t')\, dt'. \tag{1.43}$$

Here, we assume that the first term is large compared to the second term due to $|h_+| \ll 1$ on the right hand side and set the integral upper limit at $t + 2l_1/c$. Consequently, the phase shift ϕ_1 due to Δt_1 can be written

$$\phi_1 = \frac{2\pi c}{\lambda} \left(\frac{2l_1}{c} + \frac{1}{2} \int_t^{t+2l_1/c} h_+(t')\, dt' \right), \tag{1.44}$$

where λ is the wavelength of the laser. In the same way, one can describe the phase shift ϕ_2 for the other axis as

$$\phi_2 = \frac{2\pi c}{\lambda} \left(\frac{2l_2}{c} - \frac{1}{2} \int_t^{t+2l_2/c} h_+(t')\, dt' \right). \tag{1.45}$$

By using ϕ_1 and ϕ_2, the phase difference $\Delta\phi = \phi_1 - \phi_2$ of the two optical paths is

$$\Delta\phi = \frac{4\pi}{\lambda}(l_1 - l_2) + \frac{2\pi c}{\lambda} \left(\frac{1}{2} \int_t^{t+2l_1/c} h_+(t')\, dt' + \frac{1}{2} \int_t^{t+2l_1/c} h_+(t')\, dt' \right). \tag{1.46}$$

The first term is the phase shift due to the arm length shift, while the second term is the shift due to the gravitational wave transient. Here, if one supposes that $l_1 \sim l_2 = l$ for simplicity, the phase shift due to the gravitational wave (the second term) $\delta\phi_{\mathrm{GW}}$ is written by

$$\delta\phi_{\mathrm{GW}}(t) = \frac{2\pi c}{\lambda} \left(\int_t^{t+2l/c} h_+(t')\, dt' \right). \tag{1.47}$$

If the change of $h_+(t)$ is slow enough, $\delta\phi_{\mathrm{GW}}(t) = 4\pi h_+ l/\lambda$. Thence, one method to largen a phase shift caused by gravitational wave transient is to construct a Michelson interferometer with large arm.

Here consider the frequency response $H_{\mathrm{MI}}(\omega)$ of the Michelson interferometer to gravitational waves is given by following equation by using the Fourier transform

$$H_{\mathrm{MI}}(\omega) = \frac{\tilde{\phi}_{\mathrm{GW}}(\omega)}{\tilde{h}_{\mathrm{GW}}(\omega)} = \frac{4\pi c}{\lambda} \exp\left(-i\omega l/c\right) \frac{\sin(\omega l/c)}{\omega l/c}. \tag{1.48}$$

where ω is an angular frequency of a gravitational wave. This equation implies that the response $|H_{\mathrm{MI}}|$ is maximized at

$$l = \frac{\pi c}{2\omega} = \frac{c}{4f_{\mathrm{GW}}}. \tag{1.49}$$

Thus, for a gravitational wave of 250 Hz, the optimal arm length is 300 km. Since one cannot construct such a large interferometer on the Earth, some techniques to expand effective arm lengths are necessary for improvement of the sensitivities.

Delay-line and Fabry-Perot cavity

One method to expand the effective optical path lengths is to use delay lines in the interferometer arms, whereby the light is multiply reflected at different points on the mirror surface. Another method is to use Fabry-Perot cavities, in which the light is reflected multiple times while keeping the optical paths aligned.

Optical configurations of these types are illustrated in figure 1.3. Since a delay-line expands the effective arm length by a factor of $N/2$ when the beam is reflected on the mirror surfaces $N-1$ times, the frequency response of a delay-line Michelson interferometer (DLMI) to gravitational waves is given by

$$H_{\text{DLMI}}(\omega) = \frac{2\pi N l}{\lambda} \exp\left(-i\omega N l/2c\right) \frac{\sin(\omega N l/2c)}{\omega N l/2c}. \tag{1.50}$$

By contrast, a Fabry-Perot cavity uses multiple interference of the laser beam. The light incident into the cavity is reflected many times between the mirrors and a fraction of the stored light inside the cavity is allowed to leak out, back to the incident direction. The frequency response of a Fabry-Perot Michelson interferometer (FPMI) to gravitational waves is given by

$$H_{\text{FPMI}}(\omega) = \frac{4\pi l\alpha}{\lambda} \frac{\exp\left(-i\omega l/c\right)}{1 - r_F r_E \exp(-2i\omega l/c)} \frac{\sin(\omega l/c)}{\omega l/c}, \tag{1.51}$$

when the two Fabry-Perot cavities are in resonance condition [13]. Here α is given by

$$\alpha = \frac{t_F^2 r_E}{1 - r_F r_E}, \tag{1.52}$$

where r_F and r_E denote the amplitude reflectivity of the front and end mirrors, and t_F represents the transmissivity of the front mirror. The bounce number N_{FP} in a Fabry-Perot cavity is given by

$$N_{\text{FP}} = \frac{2\sqrt{r_F r_E}}{1 - r_F r_E} = \frac{2\mathcal{F}}{\pi}. \tag{1.53}$$

Here $\mathcal{F}$ denotes the sharpness of the resonance of the Fabry-Perot cavity and is called the finesse.
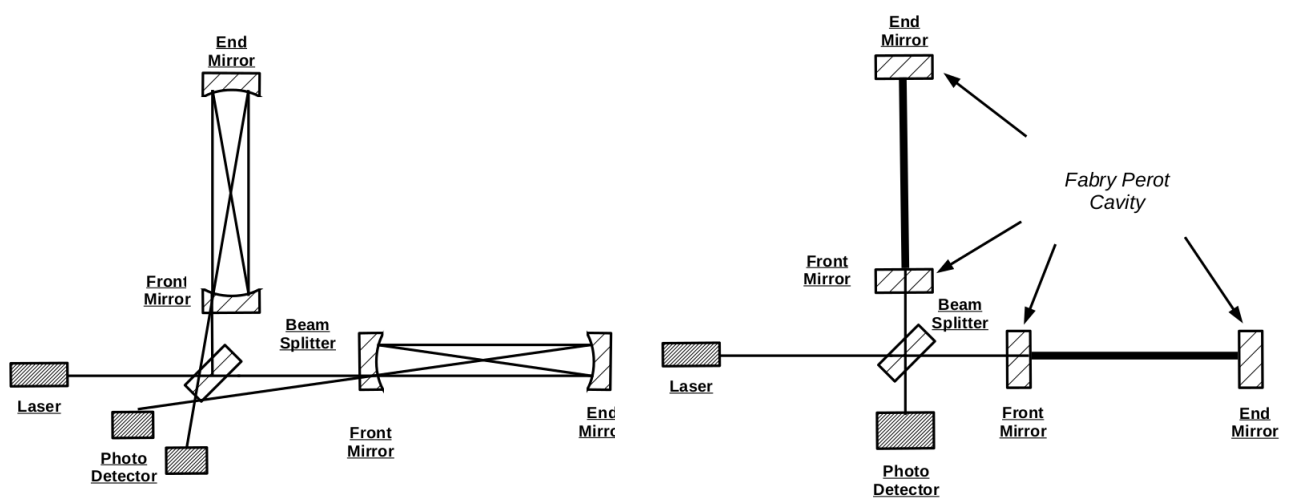
Figure 1.3: Optical configuration of a delay-line Michelson interferometer (*left*) and a Fabry-Perot Michelson interferometer (*right*).

Figure 1.4 shows amplitudes of the frequency responses H_{MI}, H_{DLMI} and H_{FPMI}. The arm lengths are set to 3 km in all cases and the responses of the delay-line Michelson and Fabry-Perot Michelson interferometers are optimized for a gravitational wave below around 100 Hz. Nowadays, newly constructed large-scale gravitational wave detectors use Fabry-Perot cavities due to the smooth frequency response.
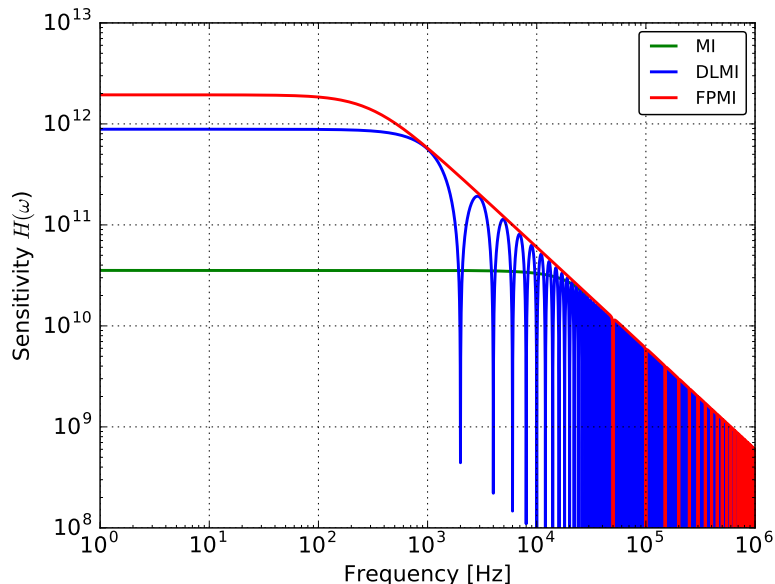

Figure 1.4: Amplitudes of the frequency responses H_{MI}, H_{DLMI} and H_{FPMI} with 3 km arm length. The value of N for Delay-line Michelson interferometer (DLMI) is set at 50. The finesse $\mathcal{F}$ is set at 80 for Fabry-Perot Michelson interferometer (FPMI). Here the wavelength of the laser is $\lambda = 1064$ nm. MI denotes Michelson interferometer.

1.3.2 Recycling cavities

In addition to the cavities for expansion of the effective arm lengths, interferometric gravitational wave detectors use other cavities, called recycling cavities, for further improvement of the sensitivities. In this scheme, one creates optical cavities with interference, by implementing additional partial-reflection mirrors before and/or after the Michelson interferometer. These are called the power recycling mirror and the signal recycling mirror respectively. The optical configuration of a Michelson interferometer with power recycling and signal recycling mirrors is illustrated in figure 1.5. More detail of the detection scheme and resulting sensitivities is given in references [14], [15].
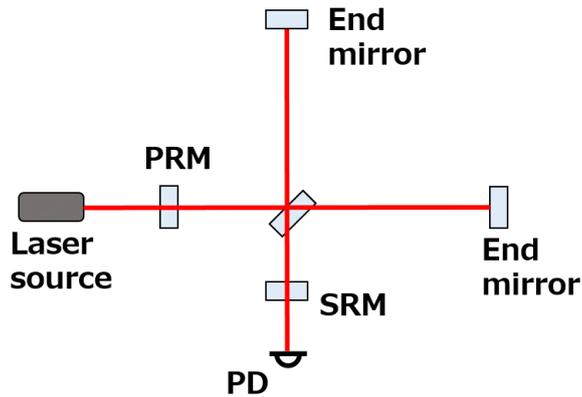
Figure 1.5: Optical configuration of a dual-recycling Michelson interferometer. PRM and SRM denote the power recycling mirror and signal recycling mirror respectively.

1.3.3 Noise sources in interferometer

This subsection introduces some noise sources which fundamentally or possibly limit the sensitivity of a interferometric gravitational detector.

Seismic noise

The sensitivity of a terrestrial detector in the low frequency region depends critically on vibrations of the optics due to seismic vibration, which are called seismic noise. Seismic noise is attenuated by isolating the optics from the seismic motion using vibration isolation systems based on pendulum systems and springs. The details are provided in the following chapter.

Thermal noise

Since the mirror and the suspension system stay in thermal baths and receive energy from their surroundings, a random energy flow to and from the thermal baths can occur, and this causes a fluctuation of the optical paths of the interferometer. This noise is called thermal noise. In the field of gravitational wave detection, thermal noise induced in mirror substrates is called mirror thermal noise, while the noise caused in the suspension systems is called suspension thermal noise. In order to mitigate the impact from the thermal noise, fused silica is typically used for room-temperature mirror substrates [16], while sapphire is a good candidate for cryogenic detectors [17],[18].

Shot noise

Shot noise is a fundamental noise in optical power sensing, associated with the quantum nature of light. A photodetector counts the number of photons and converts it to photocurrent. In the process, the number of photons counted, or the electrons composing the photocurrent, has a probability distribution, which results in fluctuations of the measured rate. The noise induced by this fluctuation is called shot noise.

The noise in length sensing caused by the probability distribution is proportional to $\sqrt{P_{\mathrm{in}}}$, where P_{in} is the incident power on the mirrors. While the signal amplitude of the gravitational wave is proportional to P_{in}, the signal to noise ratio is proportional to $1/\sqrt{P_{\mathrm{in}}}$. The shot noise can be reduced by increasing the power of the laser.

laser noise

Noise of a laser, such as frequency and intensity fluctuation, degrades the detector sensitivity, since interferometric gravitational wave detector monitors the length between the mirrors using the wavelength of the laser as a reference. In order to minimize the impact of the intensity fluctuation, the interferometer is operated at a dark fringe. At a dark fringe, the photodetector receives no light in the absence of gravitational wave signals.

Newtonian noise

The Newtonian noise is the direct coupling between the moving ground and the optics due to Newtonian gravitational attraction. Since the vibration isolation system attenuates mainly mechanical motion, this noise cannot be reduced by the isolation system. One method to reduce this noise is to place the interferometer underground, where the optics are less affected by the gravity gradient field of surrounding rocks. Another method is to subtract the noise by calculating the gravity gradient from measurements of the ground motion surrounding the optics [11].

Residual gas noise

Random motions of molecules can cause fluctuation of the refraction index in the optical paths of an interferometer and this causes fluctuations of the effective arm lengths. This noise is called the residual gas noise. In order to mitigate the impact of the residual gas noise, recent interferometric gravitational wave detectors are operated in an ultrahigh vacuum condition, of order $10^{-7} \sim 10^{-6}$ Pa.

control noise

During interferometer operation, the optical components are controlled to keep the Fabry-Perot and recycling cavities in resonance conditions and the detection port at a dark fringe. Several auxiliary beam monitoring signals are used for these feedback loops. The detection and digitization noise of these auxiliary detectors, as well as the noise of the electric circuits for the control, may degrade the sensitivity of the interferometer. Also the noise in the active controls of the suspension systems can degrade the detector sensitivity.

The noises in local sensors and actuators can introduce vibration to the suspension system components through active controls. This can cause fluctuation of mirror displacements. The strategies of the active suspension controls will be discussed in following section.

1.3.4   Large-scale interferometric detectors

Large-scale interferometric gravitational wave detectors, so-called second-generation detectors, have started operation or are being constructed. Within a few years, these detectors will start coincident observation in order to improve detection reliability and accuracy of GW source localization in the sky. This subsection describes world-wide network of the second-generation gravitational wave observatories.

Detector projects

Projects for gravitational wave detection using large-scale interferometers are summarized in table 1.3.4. Two Advanced LIGO detectors conducted the first scientific operation in 2015 and started a second run from 2016. Advanced Virgo should start operation in 2017 and a Japanese detector KAGRA will come on line in 2018. The inspiral range of these second generation detectors are designed to be around 200 Mpc for 1.4-1.4 $M_\odot$ neutron star binaries.

Project	Baseline	Place
Adv. LIGO	4 km	Livingston/Hanford, USA
Adv. Virgo	3 km	Pisa, Italy
KAGRA	3 km	Kamioka, Japan

Table 1.1: The second generation gravitational wave detector projects.

Optical configuration

In second generation detectors, a dual-recycling Fabry-Perot interferometer is adopted. A typical optical configuration (that of KAGRA) is shown in figure 1.6. A seed laser beam from a Nd:YAG non-planar ring oscillator (NPRO) is passed through amplifiers, and is increased in power up to $\sim$200 W. The laser beam is sent to a prestabilization system and phase/amplitude modulation is applied for interferometer sensing and controls. After this process, the laser enters the input mode cleaner (IMC), which filters the spatial modes and polarization of the laser beam with a triangular optical cavity composed of suspended mirrors. The filtered beam is input to the main part of the interferometer, which is a dual-recycled Fabry-Perot interferometer with km-scale arm lengths. In order to improve the spatial mode stability of the recycling cavities, the beam between recycling mirrors and the beam splitter is folded into a Z-shape. The transmited beam from the signal recycling mirror is filtered by an output mode cleaner (OMC), which aims to remove unwanted higher-order spatial modes from the beam. The detailed optical design of the KAGRA interferometer are described in reference [40].
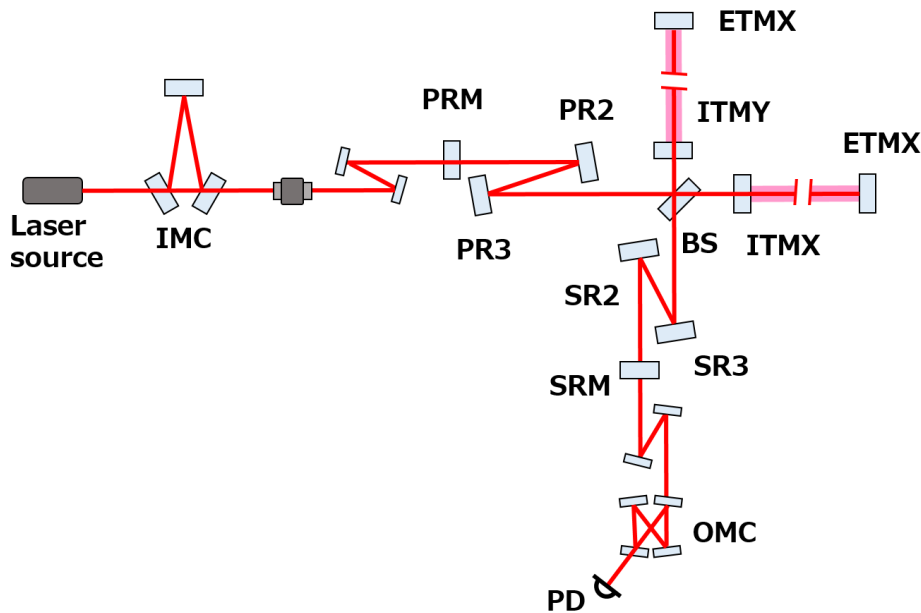

Figure 1.6: Optical configuration of the second generation detector, in the case of KAGRA interferometer. The power recycling mirrors are located at PRM, PR2 and PR3. SRM, SR2 and SR3 are the positions of the signal recycling mirrors. Test masses are located at ITMX, ITMY, ETMX and ETMY (Input/End Test Mass X/Y). IMC and OMC denote input mode cleaner and output mode cleaner respectively. PD represents photo diode.

1.4 Targets and Outline

The work described in this thesis has independent two parts:

- Development of a low frequency vibration isolation system for the KAGRA detector.

- Study of the localization of coalescing binaries with a hierarchical network of gravitational wave detectors.

The first part describes the development of a low frequency vibration isolation system for the KAGRA detector. In particular, this part focuses on the system for power recycling mirrors of the KAGRA detector. As described in the previous section, vibration of the core optics of a gravitational wave detector will be reduced by the vibration isolation system and their positions are actively controlled by using sensors and actuators implemented on the system. This aims to suppress the large displacements caused seismic noise driving the mechanical resonances of the suspension systems, as explained in the next part. The targets in the first part are to confirm an existing simulation tool works properly for designing the active control system for the suspension system, and to design the active control systems for the suspension system which will suspend the power recycling mirrors of the KAGRA detector by using the simulation tool.

The second part describes a study of source localization by a network of gravitational wave detectors. In the coming years, gravitational wave detectors will start coincident observations to achieve source localization. However, in the beginning, the sensitivities of those detectors can be different from each other, even if they are operated at the same time. Then, one has to construct a method to effectively use the less sensitive detectors' information. A hierarchical network search to deal with such a situation is investigated in this part. The main target is to estimate the benefit of this detection network with 3 or 4 gravitational wave detectors.

The outline of this thesis is as follows. Part II presents the topic of the development of the seismic attenuation system of the KAGRA detector. Chapter 2 describes working principle of the vibration isolation system. Chapter 3 explains the low frequency vibration isolation system, so-called seismic attenuation system (SAS), adopted in the KAGRA detector. Chapter 4 introduces the requirements on the active control system of the SAS. Chapter 5 describes the verification of the simulation tool by using a SAS called iKAGRA-PR3 SAS, which was conducted at KAGRA site in the Kamioka underground. Chapter 6 focuses on designing the active control system for the SAS which will suspend power recycling mirrors.

In part III, the study of the localization performance with a hierarchical network search is described. Chapter 7 briefly introduces background knowledge on data analysis of the gravitational wave detection. Chapter 8 explains the elements of a pipeline, in which the hierarchical network is assumed to be implemented. This pipeline is the one developed for the gravitational wave and electromagnetic wave (GW-EM) follow- up observations. Chapter 9 explains the localization quantities and the set up for this work. Then, in chapters 10 and 11, the optimization of the SNR threshold for the low sensitivity detectors in the hierarchical search with three or four detectors is described. Chapter 12 summarizes the expected fast localization performance with the hierarchical network search.

Part IV summarizes the development of the KAGRA-SAS and the study of the localization performance.

Development of a low frequency vibration isolation system for KAGRA PartII

Low frequency vibration isolation
Chapter 2

2.1   Vibration isolation

Seismic vibration is a fundamental and unavoidable noise source in terrestrial gravitational wave detectors. Seismic motion limits the detector sensitivity at low frequency by introducing vibration into the mirrors. This section describes the characteristics of seismic noise and of basic mechanisms to reduce its contribution to the detector sensitivity limit.

2.1.1   Seismic vibration

The ground vibrates continuously and randomly due to oceanic, atmospheric and human activities. The amplitude of the seismic vibration changes by a few orders of magnitude depending on the site and time, as well as surrounding environment influences such as weather, industrial activities.

The worldwide seismic background noise, was investigated by J. Peterson [19]. He estimated typical seismic vibration based on data from a worldwide network of seismometers and constructed the New High/Low Noise Model (NHNM/NLNM), according to the upper and lower bounds of the measured power spectral densities. Figure 2.1 shows power spectrum densities of the seismic noise measured in his research. This figure also shows power spectrum densities from 1.5 years (from September 2009 to February 2011) of seismic noise data from a Güralp CMG-3T seismometer underground at Kamioka, where the Japanese second generation detector, KAGRA, is located, measured at the site of the Cryogenic Laser Interferometer Observatory (CLIO), over a long period as a joint research project of the Disaster Prevention Research Institute and the CLIO [44]. The seismic motion of Kamioka mine was modeled, according to the investigation [45]. Key features of the spectrum are:

- At low frequencies below 1 mHz, the amplitude increases due to the tidal deformation of the ground caused by the gravitational attraction from the sun and moon. At these low frequencies, the seismic vibration moves the optics of gravitational wave detectors coherently.

- The peak measured at $0.1 \sim 0.5$ Hz is known as the microseismic peak and is mainly caused by oceanic wave activities. Thus the peak has a large magnitude along the coast while it is smaller in the middle of the continents [20]. In large-scale gravitational wave detectors, the seismic vibration at these frequencies has an impact on stable interferometer operation by inducing optic vibration which is not coherent among the optics. To attenuate this impact due to the microseismic peak is one of the main purposes of the vibration isolation system gravitational wave detectors.

- The seismic vibration at frequencies above 1 Hz has been investigated in the field of gravitational wave detection. The typical displacement amplitude spectra of the seismic motions at frequencies higher than ~ 1 Hz is given by

$$\tilde{x}_{\text{seismic}}(f) \;=\; A \times \left(\frac{f}{1\ \text{Hz}} \right)^{-2} \ \text{m}/\sqrt{\text{Hz}}, \tag{2.1}$$

The factor A is a constant which depends on sites and is typically about $10^{-9} \sim 10^{-6}$.

- At frequencies higher than ~ 10 Hz, the typical amplitude of the seismic vibration is larger than about 10^{-12} m$/\sqrt{\mathrm{Hz}}$. On the other hand, the required arm-length fluctuation of the gravitational wave detectors is on the order of 10^{-20} m$/\sqrt{\mathrm{Hz}}$. This implies that the displacement of the mirror caused by seismic vibration has to be attenuated by a factor of $10^{-10} \sim 10^{-8}$, for detection of gravitational waves.

It is known that, in the underground environment, the seismic vibration is reduced compared with that on the surface of the ground. This is because, underground, the surrounding rocks tend to isolate the vibration from atmospheric and human activities on the surface [21]. This vibration mitigation due to the underground environment is effective above 1 Hz, where the atmospheric and human activities dominate. However the microseismic peak is not reduced much, since the origin of the microseismic peak is the motion which propagates through the continents.
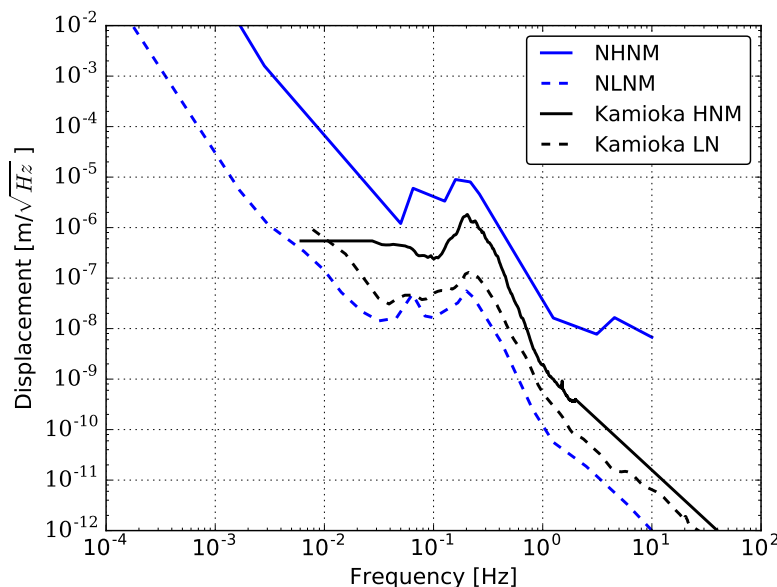

Figure 2.1: The worldwide seismic noise from J. Peterson's study (blue) and seismic motion measured at Kamioka underground (black). The blue and dashed-blue line show the new high-noise model (NHNM) and the new low-noise model (NLNM) respectively. The black and dashed-black lines denote the seismic motion in the environment underground at Kamioka mine. The Kamioka HNM (high noise model) shows modeled spectra based on measurement of high-noise seismic motion, and Kamioka LN (low noise) shows a measurement when the seismic noise was low.

2.1.2   Vibration isolation system

Core optics of an interferometric gravitational wave detector are suspended by pendulum systems so that, in the detection band, the optic moves almost as a free particle in the sensitive plane of the interferometer. Such suspensions also work as mechanical isolators from ground vibration. As shown in the previous section, the seismic vibration is one of the fundamental noise sources for a terrestrial gravitational wave detector. In order to detect a gravitational wave, the vibration of the optics due to the seismic noise should be attenuated by on the order of $10^{-8} \sim 10^{-10}$ at 10 Hz. In a terrestrial gravitational wave detector, this attenuation performance is achieved by using suspension systems

composed of mechanical filters and active control systems mounted on the suspension system. This section summarizes the principle of the vibration isolation performance of these mechanical filters.

Harmonic oscillator

Isolating optics from seismic motion is realized by using mechanical filters composed of elastic components such as springs and suspension wires. This subsection derives the vibration isolation performance of a mechanical filter using a one-dimensional harmonic oscillator. If one considers a single-pendulum system consisting of a payload with mass m, which is suspended by massless wire from a ceiling (mechanical ground) as illustrated in figure 2.2, its equation of motion is:

$$m\ddot{x} = -\frac{mg}{l}\,(x - X),\tag{2.2}$$

where g denotes local gravitational acceleration, l is the length of the wire and x, X are the displacements of the payload and the suspension point respectively. Taking the Fourier transformation, this equation becomes:

$$H(\omega) \equiv \frac{\tilde{x}}{\tilde{X}} = \frac{\omega_0{}^2}{\omega_0{}^2 - \omega^2},\tag{2.3}$$

where $\omega_0 = 2\pi f_0 = \sqrt{g/l}$ represents the resonant angular frequency of the suspension system. $H(\omega)$ is the transfer function from the vibration of the suspension point to the payload vibration. The amplitude and the phase of the transfer function of this system are shown in figure 2.2 as well. The plot illustrates the following:

- At low frequencies where $f \ll f_0$,
  Since the amplitude and the phase of the transfer function are close to 1 and 0 respectively, the payload follows the motion of the suspension point.

- Near the resonant frequency, where $f \simeq f_0$,
  the amplitude of the transfer function increases substantially and goes to infinity at the resonant frequency.

- At higher frequencies where $f \gg f_0$,
  The amplitude of the transfer function decreases in proportional to f^{-2}. Thence, the payload is isolated from the vibration at the suspension point and the vibration isolation ratio is described by $(f/f_0)^2$ at higher frequencies than the resonant frequency of the system. If the resonant frequency of the oscillator is set at lower frequencies, one can realize the more isolated payload from the suspension point.

In a realistic system, the transfer function has finite amplitude at the resonant frequency due to dissipation from such as residual gas damping, thermoelastic damping. The dissipation due to anelasticity in the elastic components is called structural damping. This is described by adding an imaginary part to the spring constant $k(1 + i\phi)$, where $k = m\omega_0^2$ and ϕ is the loss angle, which is defined as the phase angle by which displacement response would lag behind a sinusoidal driving force exerted on the payload. The typical value of ϕ is much less than 1. The loss angle is related to the quality factor of the oscillator by $Q = 1/\phi$. According to eq (2.3), the peak amplitude of the transfer function is expressed by $1/\phi$ at the resonant frequency.
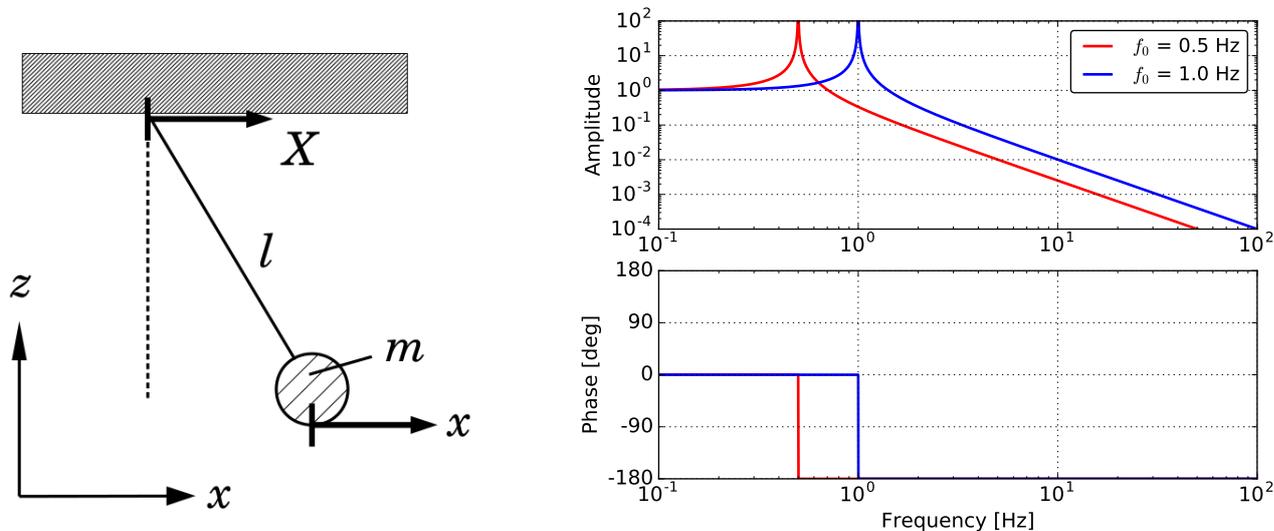
Figure 2.2: A pendulum system considered as a mechanical oscillator ($left$) and its transfer function $x/X(right)$ for various resonant frequencies ($f_0 = 0.5$ Hz, $f_0 = 1.0$ Hz). If one can lower the resonant frequency of the system, the attenuation performance at high frequencies is improved.

Multi-stage suspension

In an N-stage pendulum system, the ground vibration induces the payload vibration with an attenuation factor which is proportional to f^{-2N}, at a frequency higher than the resonant frequencies of the system. The vibration isolation performance of a suspension with various numbers of stages is shown in figure 2.3. One can obtain strong attenuation of seismic vibration in these high frequency region by implementing a sufficient number of isolation stages.

Since the resonant frequencies of an actual suspension system realized by a pendulum with a length of a few tens of cm are around 1 Hz, the attenuation ratio of a single-suspension is on the order of 10^{-3} at 10 Hz, which is not enough for an interferometric gravitational wave detector. Thus, in such a detector, a multi-stage suspension system is used to achieve the required attenuation.

Couplings from vertical and rotational vibration

In an actual system, not only the horizontal ground vibration but also the vertical ground vibration can contribute to the changes in the optical path length of the interferometer. This vertical-to-horizontal coupling can be caused by mechanical imperfections in each attenuation stage and also by the non-parallelism of the verticality at locations kilometers apart in the detector. Due to the curvature of the ground, the front and end mirrors of the Fabry-Perot cavities make an angle of $\alpha = L/2R_\oplus$ with the vertical direction for the interferometer, as shown in figure 2.4 $left$. Here L denotes the cavity length and $R_\oplus$ is the radius of the earth. If the optic shifts vertically by δz, it couples to a variation $\alpha \delta z$ of the cavity length. Thus if one considers a 3-km interferometer, the minimum coupling caused by earth curvature is $\alpha \sim 2 \times 10^{-4}$.

The rotational motions of the optic can also change the optical path length, as shown in figure 2.4 $right$. If the laser beam locates at the center of the optic, the rotational motion of a mirror does not couple to the motion in the beam direction. However, the beam spot can be off-centere to some extent in reality, and an angular displacement causes a change of the optical path length. If the beam spot

29
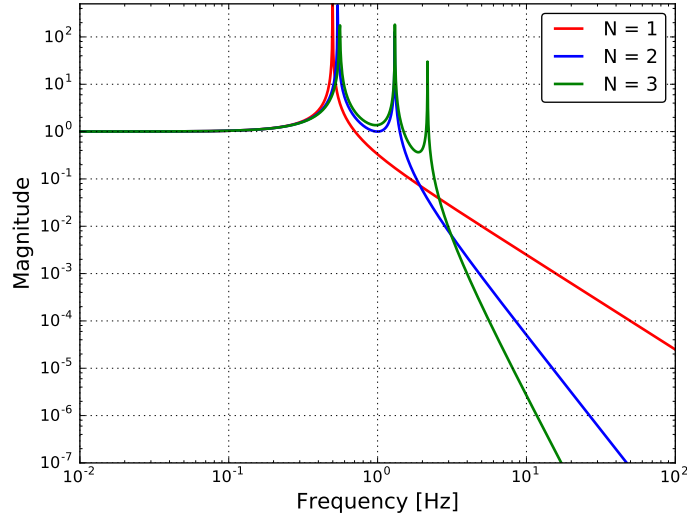
Figure 2.3: The amplitudes of the transfer functions from the suspension point displacement to an N-th stage mass displacement with $N = 1 \sim 3$. The total length of the suspension is set at 1 m in all cases.

is off-center by a distance d, the rotation angle of the optic $\delta\theta$ couples to the length variation along the beam axis by $d\delta\theta$. Here it is assumed that angle of the other test mass does not shift.
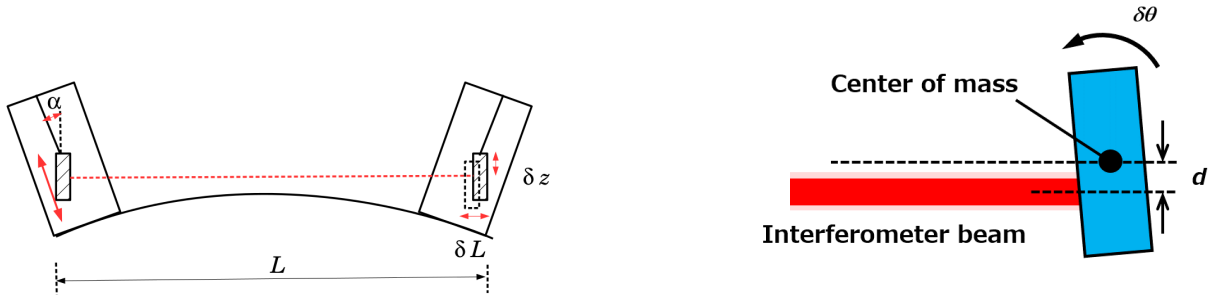

Figure 2.4: Couplings from vertical vibration due to the Earth curvature ($left$) and that from rotational motion due to beam shit ($right$).

Note that the coordinate system used in this thesis is defined in figure 2.5. The longitudinal direction is taken to be the beam axis of the interferometer. The names for the rotational degrees of freedom are taken from aircraft terminology.
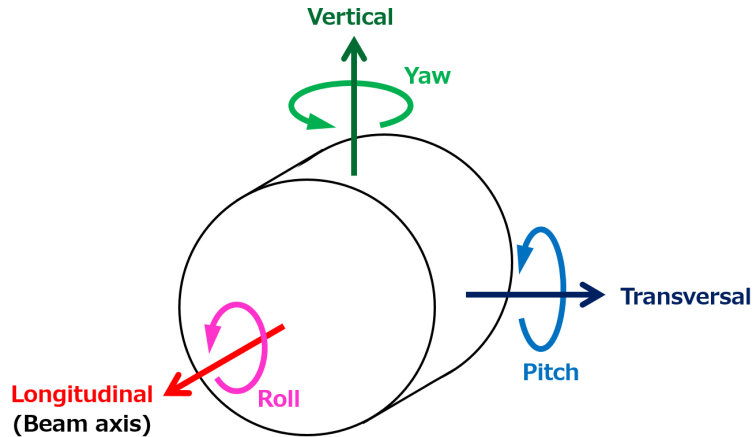
Figure 2.5: Definition of the coordinate system in this thesis.

Active vibration isolation system

The previous subsection explained that a multi-stage suspension system can attenuate the seismic noise down to the required level for gravitational wave detectors. However, by using only passive systems, it is difficult to reduce low-frequency vibration, such as vibration caused by microseismic motion at around 0.2-0.5 Hz. Since a mechanical oscillator can attenuate a vibration only above its natural resonant frequency, one cannot have sufficient vibration isolation performance if the natural resonant frequency is not low enough. In an actual system, to realize such low-frequency oscillators is difficult.

To complement the passive damping system and passive vibration isolation performance, active control systems are implemented. One can suppress the motion of the suspended mass in all DoFs individually, if one sets sensors and actuators in sufficient numbers and proper configuration. Active isolation systems isolate the target objects from seismic vibration with active feedback and feedforward controls. Active controls can reduce the targets' vibration in any frequency band in principle, if the vibration sensors used have sufficient sensitivities and low noise levels.

2.1.3   Damping system

For operation of an interferometer or cavity, one has to reduce the RMS (Root Mean Square) amplitude of the mirror displacement and velocity, in order to keep in the resonant condition. The previous subsection explains that a mechanical filter isolates the ground motion at frequencies higher than the resonant frequencies. However, a seismic isolation system can induce large fluctuation of the optic through mechanical resonances at low frequencies. Thus the resonances of the seismic attenuation chains have to be damped strongly. These motions are suppressed by using passive damping system and also by active control systems. Here I introduce the principle of the passive damping system.

One benefit to introducing passive damping mechanism is to enhance robustness to unwanted disturbances such as earthquakes and actuation noise. These disturbances can excite the mechanical resonances and the oscillation at the resonant frequencies persists for a long period unless they are appropriately damped. Since one cannot operate an interferometer if the optics are swinging with large amplitudes, the time for observation is reduced if the vibration isolation systems do not have such damping system. It is required to suppress the decay time of mechanical resonances which may

be excited by external disturbances and affect the interferometer operation.

Passive damping system

This subsection considers a damped-pendulum system as shown in figure 2.6. The passive damping system can be modeled by adding a viscous damper which makes a braking force proportional to the relative velocity between the damper and the object to be damped. The equation of motion of such system is:

$$m\ddot{x} = -k\,(x - X) - \gamma(\dot{x} - \dot{X}),\tag{2.4}$$

where k denotes the spring constant, γ is the damping coefficient of the damper, and X represents the ground motion. Taking the Fourier transform gives the transfer function from the ground motion to the suspended payload:

$$H(\omega) = \frac{\tilde{x}}{\tilde{X}} = \frac{\omega_0{}^2 + 2i\eta\omega\omega_0}{\omega_0{}^2 + 2i\eta\omega\omega_0 - \omega^2} = \frac{\omega_0{}^2 + i\omega\omega_0/Q}{\omega_0{}^2 + i\omega\omega_0/Q - \omega^2},\tag{2.5}$$

where the damping ratio $\eta = \gamma/2m\omega_0$ and Q is the quality factor of the resonance.
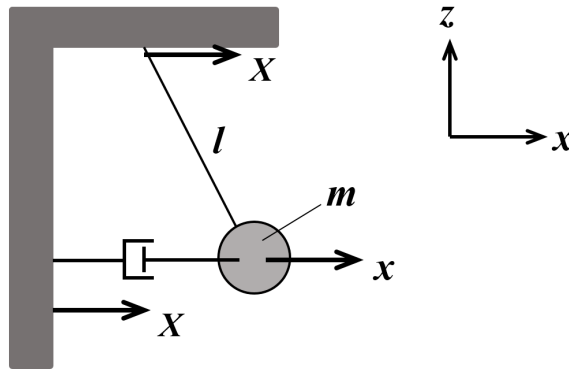

Figure 2.6: An example of a passively damped suspension system.

The amplitude and the phase of $H(\omega)$ with various quality factors are plotted in figure 2.7 *left*. The figure illustrates that:

- The amplitude of the peak at the resonant frequency gets smaller when the damping gets stronger. The quality factor Q corresponds roughly to the height of the peak.

- The amplitude of the transfer function is proportional to f^{-1} instead of f^{-2}, where f is well above the frequency Qf_0, if a damper is mechanically grounded.

Thus, the performance of the mechanical filter is degraded at high frequencies in a viscously damped system such as one shown in figure 2.6. Here, this subsection demonstrates an impulse response to a driving force on the suspended mass to test the robustness for the unwanted acceleration disturbance. Figure 2.7 *right* shows the impulse response of a viscously damped mechanical oscillator with some Q factors. When the system has small dissipation, the suspended mass moves a sinusoidal oscillation with decaying amplitude. The oscillation amplitude decays faster if the damping factor is increased. The decay time τ, in which the oscillation amplitude decreases by a factor of $1/e$, described by $\tau = 1/\eta f_0 = Q/\pi f_0$. In the critical damping condition where the damping factor $\eta = 1$ ($Q = 0.5$), the displacement of the suspended decays with decay time $\tau = 1/\omega_0$, without oscillation. In the

over-damped condition where $\eta > 1$, the excited displacement amplitude is decreased but the decay time gets longer than that of the critically damped oscillator. This is because the damper resists the suspended mass returning to its original condition.

The degradation of vibration isolation performance due to a damper can be avoided by isolating the damper from the ground vibration. Passive damping system in a gravitational wave detector is basically suspended.
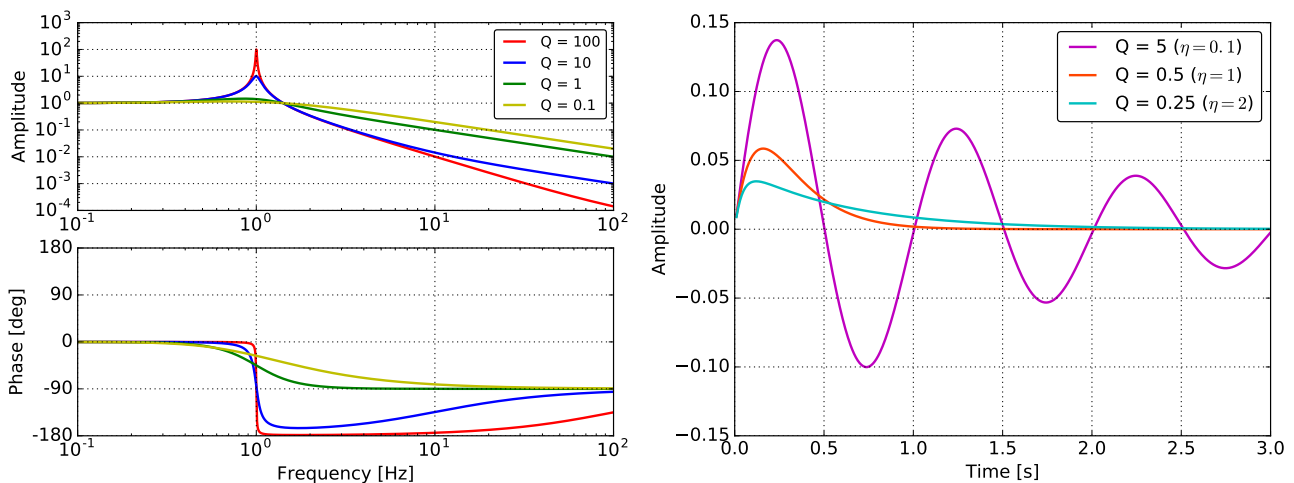

Figure 2.7: The amplitude and the phase of $H(\omega)$ (*left*) and the response of a damped mechanical oscillator to an impulsive force injected to the suspended mass (*right*), with various Q factors (viscous damping factors) .

Viscous dampers in suspensions

An eddy-current damper [22] is a viscous damping system often used in the vibration isolation system of a gravitational wave detector. An eddy-current damping system is composed of permanent magnets on one component acting on conductive objects placed on the oscillator to be damped. The working principle is as follows: When a conductive material faces on a time-varying magnetic field, eddy currents are generated in the conductor. These currents induce a magnetic field with opposite polarity of the applied field and a delay due to the induced field decay, causes a resistive force. Figure 2.8 shows the working mechanism of an eddy current damper. The damping coefficient if an eddy current damper is

$$\gamma_x = A\sigma B \frac{\partial B}{\partial x}, \tag{2.6}$$

where B is the magnetic field from the permanent magnet, σ denotes the electrical conductivity of the conductor and A represents a factor determined from the geometry of the conductor. Generally, a large damping strength is obtained by using a permanent magnet with strong magnetic field and a conductive object with large electric conductivity.

Suspension thermal noise

According to the above subsection, the RMS displacement or velocity of the suspended optics can be well suppressed if one implements a viscous damper such as the eddy-current damping system.
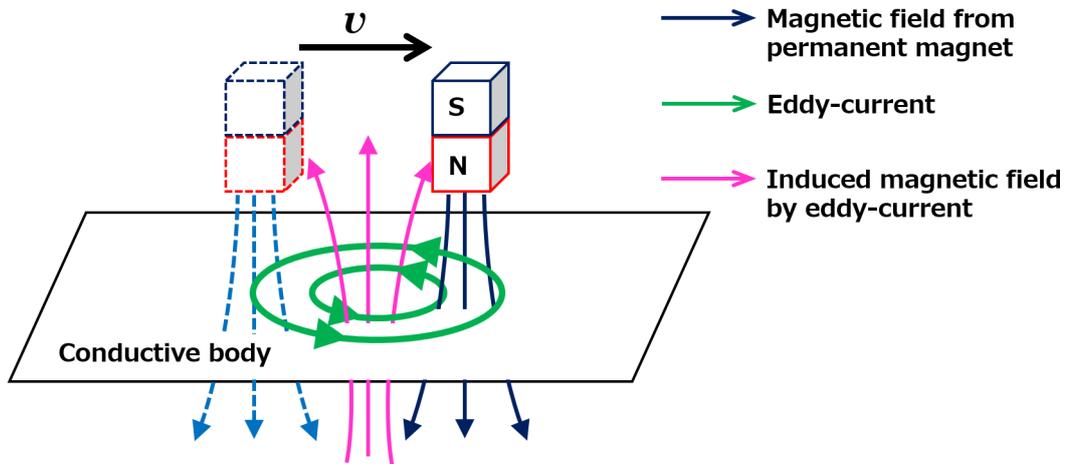
Figure 2.8: Working mechanism of an eddy-current damping system.

However, this damping system can degrade the detector sensitivity by inducing thermal fluctuation of the suspended optics in the detection band. The fluctuation dissipation theorem provides a general relation between the frequency response of systems in equilibrium to external perturbation forces ($H_{\mathrm{force}}(\omega)$) and the power spectral density of their spontaneous fluctuations $S_{\mathrm{thermal}}(\omega)$:

$$S_{\mathrm{thermal}}(\omega) \;=\; -\frac{4k_B T}{\omega} Im[H_{\mathrm{force}}(\omega)], \tag{2.7}$$

where k_b denotes the Boltzmann constant and T is the temperature. In particular, the power spectrum density of a harmonic oscillator's thermal fluctuations in a viscously damped system is described by

$$S_{\mathrm{thermal}}(\omega) \;=\; \frac{4k_B T}{m} \frac{2\eta\omega_0}{(\omega_0^2 - \omega^2)^2 + 4\eta^2\omega_0^2\omega^2}. \tag{2.8}$$

Thus, in a multi-stage suspension, the passive dampers should be implemented well apart from the optics so that thermal fluctuations due to their dissipation can be filtered out by mechanical filters and do not affect the detector sensitivity.

Active damping system

One can damp the mechanical resonances using passive dampers as described above. However, it is difficult to design the passive dampers so that all the resonant motions of the suspended mass in the translational and rotational direction are damped sufficiently. In addition, suspension systems with eddy current dampers induces suspension thermal noise at high frequencies, and thus one has to avoid using them near the optics. In active damping systems, the vibration of the suspended mass is suppressed by feedback controls with sensors and actuators. One can tune the active damping strength more flexibly compared to passive damping system.

2.1.4   Summary

Consequently, the vibration isolation for an interferometric gravitational wave detector is achieved as follows:

- Implement multi-stage suspension systems, which include low-resonant-frequency components, so that the optic vibration induced by the seismic vibration is efficiently attenuated in detection band for the detector.

- Using passive/active damping system, suppress the large amplitude disturbances due to the mechanical resonances of the seismic attenuation systems, which can disturb the interferometer operation.

2.2   Mechanical seismic attenuation systems for GW detectors

This subsection briefly describes the mechanical seismic attenuation systems, which are implemented in the low frequency vibration isolation system called the Seismic Attenuation System(SAS). More detailed information is found in [42],[26].

Since a mechanical oscillator can attenuate the vibration at frequencies higher than its natural resonant frequency, one method to improve the attenuation performance is reducing the natural frequency of the mechanical filter. In order to realize a system with low natural frequencies, the SAS makes use of anti-spring technologies. SAS has two key mechanical components called the inverted pendulum (IP) and the geometric anti-spring (GAS) filter, which provide horizontal and vertical vibration isolation respectively. The resonant frequency of the IP can be lowered to about 30 mHz and it can passively attenuate the ground vibration at the microseismic peak (0.2-0.5 Hz), which contributes significantly to the RMS amplitude of the optic displacement and velocity. The resonant frequency of the GAS filter can be lowered to $\sim$ 200 mHz, and thus by using the GAS filter, one can obtain vertical vibration isolation performance comparable to the horizontal. Since these lowest resonant frequencies are limited by hysteretic behaviors of elastic components, they can be more lowered if better elastic materials are found.

2.2.1   Inverted pendulum

Working principle

An inverted pendulum (IP) is a horizontal mechanical oscillator. Its resonant frequency is tunable lower than 0.1 Hz, and thus the IP attenuates the microseismic motion at around 0.2-0.5 Hz by one order of magnitude. An analytic model of the IP is shown in $left$ of figure 2.9. The IP is composed of a flexure fixed to the ground, a rigid cylindrical leg connected onto it and a mass on the top of the leg. If one consider that the mass displaces horizontally from the vertical point. a restoring force acts on it, with an effective spring constant of

$$k_{\text{eff}} = \frac{k_\theta}{L^2} - \frac{Mg}{L},\tag{2.9}$$

where k_θ denotes the bending spring constant of the flexure, M is the mass of the payload, and L represents the length of the IP leg. It is assumed that the mass of the leg m is negligibly small ($m \ll M$), and thus the term k_θ/L^2 corresponds to the elastic restoring force of the flexure. The second term denotes a repulsive force due to gravitational anti-spring effect. According to eq (2.9), k_{eff} decreases as the mass of the payload increases and it goes to 0 when the mass reaches $M = M_c = k_\theta/gL$. This mass M_c is called the critical mass. The resonant frequency of the IP which is loaded with a mass lighter than M_c is given by

$$f_{\text{IP}} = \frac{1}{2\pi}\sqrt{\frac{g}{L}\left(\frac{M_c - M}{M}\right)}.\tag{2.10}$$

Attenuation performance

Here, it is assumed that the IP leg has a uniform mass distribution between the flexure and the payload with total mass of m and moment of inertia of I. The transfer function H_{IP} from the ground displacement to the payload displacement on the IP is given by [23]

$$H_{\text{IP}} = \frac{A + B\omega^2}{A - \omega^2},\tag{2.11}$$

$$\text{where} \quad A = \frac{k_{\text{eff}}}{M + \frac{m}{4} + \frac{I}{L^2}}, \quad B = \frac{\frac{m}{4} - \frac{I}{L^2}}{M + \frac{m}{4} + \frac{I}{L^2}}.\tag{2.12}$$
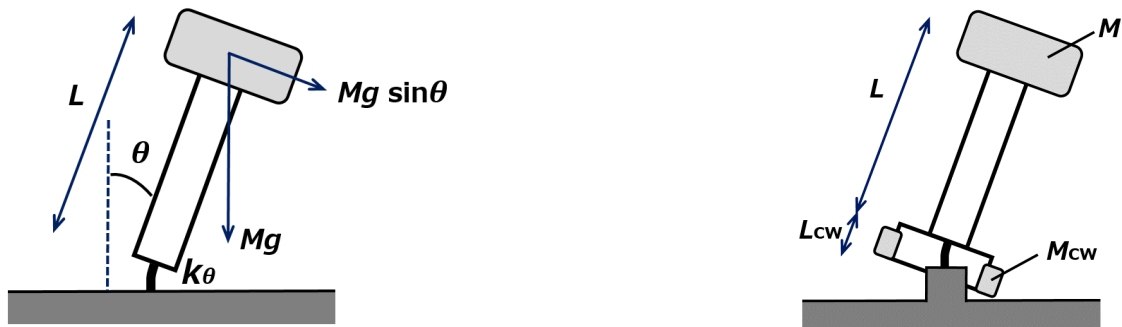
Figure 2.9: Working principle of the IP (*left*) and IP with counter weight mounted at the bottom of the leg (*right*).

According to eq (2.12), the amplitude of H_{IP} saturates at high frequencies due to the coefficient B. This saturation is known as the Center of Percussion (CoP) effect [24],[23]. In order to minimize the CoP effect and to improve the isolation performance at high frequencies, the IP legs should be made as light as possible. In the KAGRA detector, for further compensation of the CoP effect the mass distribution of the leg is optimized by introducing a counter weight at the bottom of the leg, as shown in figure 2.9. In the actual SAS for gravitational wave detectors, three IPs are implemented into the primary isolation stage [42].

2.2.2   Geometric Anti-Spring filter

Geometric Anti-Spring (GAS) technique allows increases of attenuation performance and simplicity of the mechanics, with low resonant frequencies [25]. A GAS filter is a vertical isolator using the GAS technique. This subsection briefly describes the working principle and expected mechanical properties of the GAS filter.

Working principle

The GAS filter has a set of radially arranged cantilever blades clamped on the base frame and to the central small disk called the keystone. The blades are bent when they are installed. The typical behavior of the GAS filter is described by a simple analytical model which is shown in figure 2.10. A more mathematically detailed description is given in [25]. In this model, a cantilever spring is represented as a combination of vertical and horizontal linear springs.

Here, the height where the forces of the horizontal springs cancel each other is called the working point z_{eq}. It is assumed that the force of the vertical spring balances the gravitational force on the suspended mass. In this situation, the working point is given by $z_{eq} = m_0 g / k_z + l_{0z}$, where g denotes the gravity acceleration, m_0 is the mass of the payload, k_z and l_{0z} are the stiffness and the natural length of the vertical spring respectively. Then, consider a situation where the suspended payload, whose mass is m, shifts vertically by z, as shown in figure 2.10 (*right*). The equation of motion of the payload is described by

$$m\ddot{z} = -k_z(z - z_{eq} - l_{0z}) - 2k_x(l - l_{0x})\sin\theta - mg, \tag{2.13}$$

where k_x, l_{0x} are the stiffness and the natural length of the horizontal spring respectively, θ represents the angle between the horizontal axis and the horizontal spring at the clamp point, and l is the length of the horizontal spring when the payload shifts vertically by z. Here x_0 is the horizontal distance
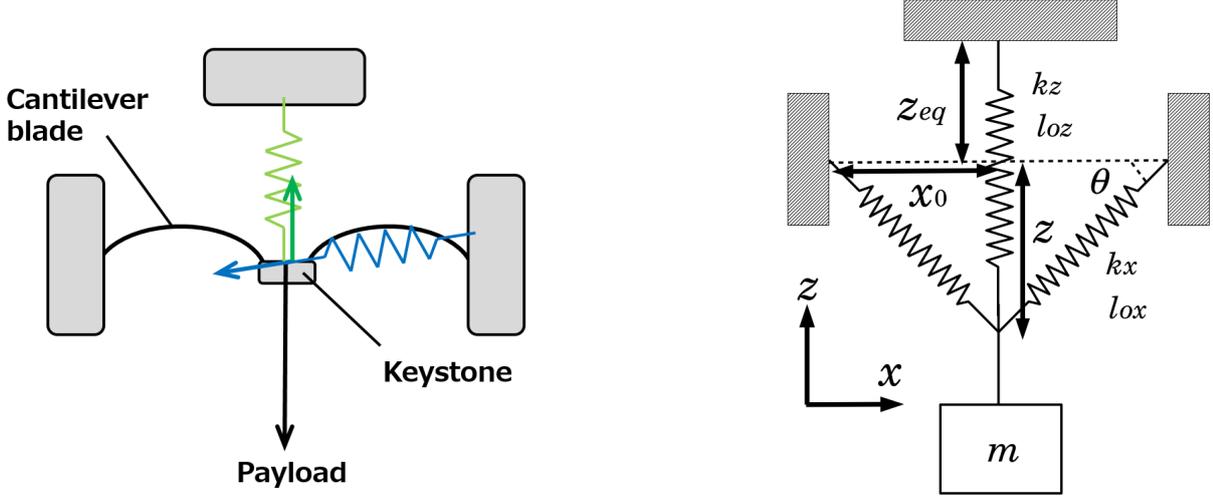
Figure 2.10: A simple analytical model of the GAS filter (*left*) and schematic working principle of a GAS filter (*right*).

between keystone and the clamping point of the spring. If one inserts $l = \sqrt{x_0{}^2 + z^2}$, z_{eq} and define $k_x{}' \equiv 2k_x$, the eq (2.13) becomes

$$m\ddot{z} = -k_z(z - \frac{m_0 g}{k_z}) - k_x{}'\left(1 - \frac{l_{0x}}{\sqrt{x_0{}^2 + z^2}}\right)z - mg \tag{2.14}$$

$$= -(k_z + k_x{}')z + k_x{}'l_{0x}\frac{z}{\sqrt{x_0{}^2 + z^2}} - (m - m_0)g. \tag{2.15}$$

Then, one can obtain the effective stiffness k_{eff} of the modeled GAS filter as

$$k_{\text{eff}} = -\frac{\partial f}{\partial z} = (k_z + k_x{}') - \frac{k_x{}'l_{0x}x_0{}^2}{(x_0{}^2 + z^2)^{\frac{3}{2}}}, \tag{2.16}$$

$$\sim \left[k_z - \left(\frac{l_{0x}}{x_0} - 1\right)k_x{}'\right], \quad (\text{if } x_0 \gg z). \tag{2.17}$$

The k_{eff} obtained implies that when the horizontal spring is compressed ($x_0 < l_{0x}$), it makes a repulsive force in the vertical direction and thus k_{eff} is reduced from that of the vertical spring ($k_{\text{eff}} < k_z$). This is the anti-spring effect. The effective stiffness and the resonant frequency can be reduced by increasing the compression of the blades by decreasing x_0.

Effect of blade compression

In an actual system, the compression of the GAS blades has to be tuned carefully so that the keystone balances the suspended payload at the working point. According to eq (2.17), k_{eff} can have a negative value depending on the compression, in which case the system becomes unstable and the GAS filter does not work properly. This situation is explained graphically in figure 2.11 through eq (2.17) and the following equation:

$$m - m_0 = -\frac{(k_z + k_x{}')z}{g} + \frac{k_x{}'l_{0x}}{g}\frac{z}{\sqrt{x_0{}^2 + z^2}}, \tag{2.18}$$

38

which is obtained supposing that the keystone is in its equilibrium position ($\ddot{z} = 0$) in eq (2.15). Figure 2.11 shows the suspended mass dependence of the working point and resonant frequency with some compression $C = (l_{0x} - x_0)/l_{0x}$, through a simple analytic model. The parameters used are summarized in table 2.1. For the GAS filters used in KAGRA, their compression is tuned so that the effective stiffness of the GAS filter has a positive minimum value. Typically, the compression is tuned so that the GAS behaves like the case of 9% compression in figure 2.1.

Property	k_z	$k_x{'}$	l_{0x}	x_0
Value	1.0×10^5 N/m	1.0×10^6 N/m	0.3 m	0.3 m

Table 2.1: Parameters used for the figure 2.11 without blade compression. If one fixes the value of l_{0x}, corresponding x_0 with compression $C = 9$ %, 9.08 % and 9.15 % are 273 mm, 272.76 mm, 272.55 mm respectively, in this model.
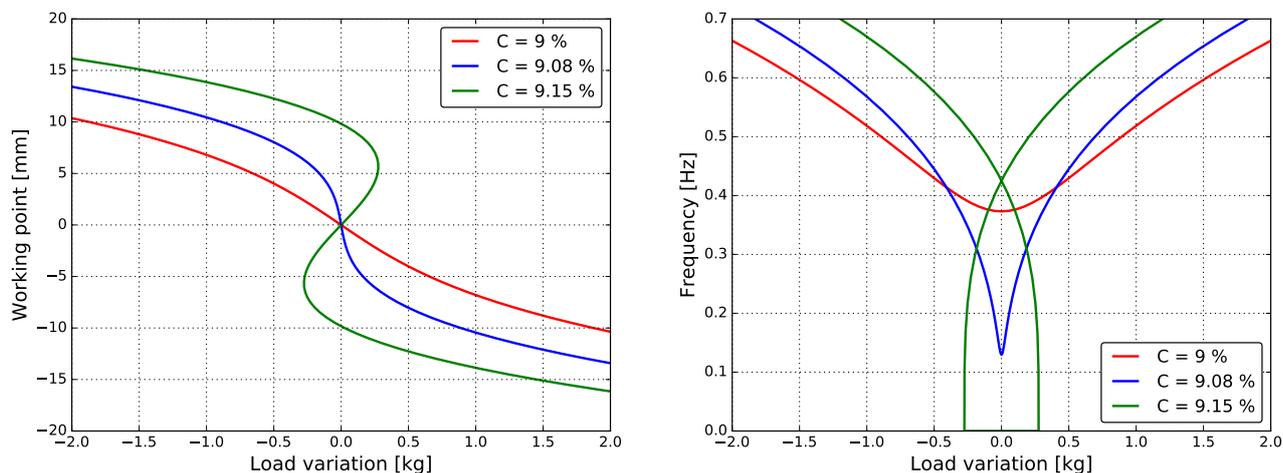

Figure 2.11: Behavior of the working point of the keystone (*left*) and its resonant frequency (*right*) with various compression of the GAS blade, as a function of tip load of the suspended payload, and which are obtained through the model. In the *right* plot, it is assumed $m_0 = 200$ kg.

Attenuation performance

The transfer function of the GAS filter from the vertical displacement of the frame to that of the keystone is given in the same form as that of the IP, which is described in eq (2.11) Thus, the attenuation performance saturates at high frequencies is typically limited to $\sim 10^{-3}$, due to the CoP effect, as shown in figure 2.12. This saturation can be compensated by implementing a wand with a counter-weight in parallel with the blades, which is called magic wand [27].
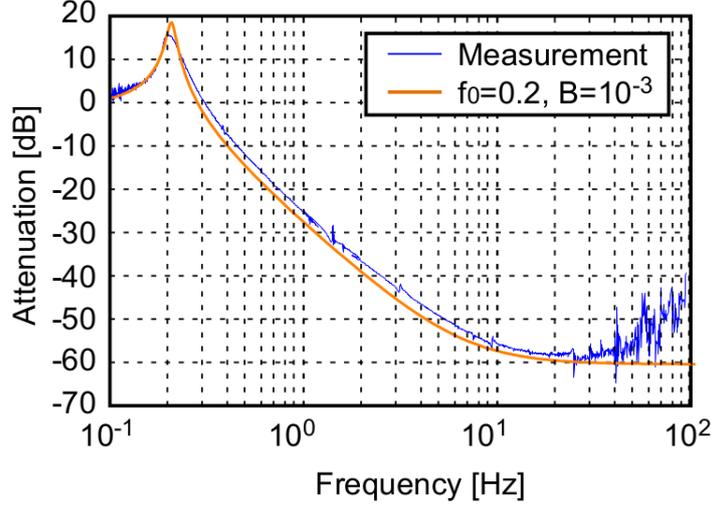
Figure 2.12: Attenuation performance of the GAS filter without the magic wand [27].

Thermal drift

In the GAS system, the vertical position of the keystone can be changed easily due to the softness, by a slight variation of the payload mass and the physical properties of the blade splings. The thermal drift of the keystone due to the temperature dependence of the Young's modulus of the blade spring material is a big problem in operating the GAS filter. Here estimate the temperature dependence of the position of the keystone. If the GAS filter balances at the working point with a payload mass of m, the optimal load to keep the keystone at the working point is changed with the temperature shift ΔT by:

$$\frac{\Delta m}{m} \sim \frac{1}{E} \frac{\partial E}{\partial T} \Delta T, \tag{2.19}$$

where E is the Young's modulus of the blade spring material. If one supposes a small perturbation and the this shift is equivalent to an an additional force applied to the keystone ($\Delta F = \Delta mg$), displacement due to thermal shift can be described by

$$\Delta z = \frac{\Delta F}{k_{\text{eff}}} = \frac{g}{\omega_0^2 E} \frac{\partial E}{\partial T} \Delta T. \tag{2.20}$$

Here $k_{\text{eff}} = m\omega_0^2$ is the effective stiffness of the GAS filter and $\Delta F = k_{\text{eff}} \Delta z$ is used. Thence, the temperature dependence with typical parameters [28],[29] is

$$\frac{\Delta z}{\Delta T} = 0.69 \,[\text{mm/K}] \left(\frac{0.33 \text{ Hz}}{\omega_0/2\pi} \right)^2 \left(\frac{\frac{1}{E} \frac{\partial E}{\partial T}}{3.0 \times 10^{-4} \,[1/\text{K}]} \right). \tag{2.21}$$

This implies that the position shift of the keystone gets more sensitive to the temperature if the resonant frequency is reduced the anti-spring effect. Note that it was confirmed this estimation of the temperature dependence was consistent with a measurement at 0.33 Hz [42].

Seismic attenuation system in KAGRA detector

Chapter 3

KAGRA uses SAS technologies for vibration isolation of its core optics, in order to expand the detection band toward lower frequency, ~ 10 Hz. This chapter introduces the SAS developed for KAGRA (KAGRA-SAS), which is the Japanese second-generation detector. The previously introduced mechanical filters are integrated into the KAGRA-SAS. The conceptual design of KAGRA-SAS, some detailed design of mechanical components and simulations for verifying the isolation performance are briefly explained.

3.1   Basic requirement

General things basically required to the seismic attenuation systems for KAGRA detector are summarized here:

- Passive attenuation of the seismic noise level should be below the target sensitivity level or other noise levels, in the detection band.

- RMS velocity and displacement of the suspended optics should be suppressed enough, for rapid lock acquisition and stable interferometer operation.

- Low-frequency mechanical resonances of the SAS should be damped actively or passively, for rapid recovery from unwanted excitation states.

- Actuators for the suspended optics should have enough range to allow lock acquisition, alignment and beam-spot optimization of the interferometer.

- Active control systems should not induce vibration noise of the optics in the detection band.

- The mechanics and the active control systems should be stable to allow long-term observation of gravitational waves.

- The mechanics should be set in Ultra-High Vacuum (UHV) condition to avoid degrading the detector sensitivity through the residual gas noise or contamination on the mirror surfaces.

The seismic isolation systems for KAGRA have been developed to meet these considerations. More detailed requirements for KAGRA-SAS, especially in the detection band ($\gtrsim 10$ Hz), are described in this subsection.

Displacement noise requirement

In the KAGRA detector, dual-recycled Fabry-Perot Michelson interferometer will be used in order to enhance and to optimize the detector sensitivities. In the gravitational wave detectors, differential length variation of the arm cavities, which is called DARM signal, is the most important DoF, since it contains information of gravitational waves. Since the displacement noise of the optics, which composes the arm cavities, directly affects to the DARM signal, these optics have the strictest requirement on their displacement noise. Here the optics which composes the arm cavities are conventionally called test masses. Displacement noise of auxiliary optics also couples to the detector sensitivity due to the couplings in the length sensing and control schemes of the interferometer [30]. Thus, displacement

noise of those auxiliary optics also should be suppressed, even though the requirements for these optics are less strict than the test masses.

The purpose of the vibration isolation system is to reduce the seismic noise level well below compared to other noise levels, such as the thermal noise or quantum noise, in the detection band of gravitational waves. The requirement for the seismic noise level is to be lower by a factor of 10 in spectrum densities than other noise levels above 10 Hz. The required displacement noise level of the core optics of the KAGRA detector is shown in figure 3.1 [31]. The figure shows two optional detection modes called BRSE (Broadband Resonant Sideband Extraction) and DRSE (Detuned Resonant Sideband Extraction) [32]. These two modes can be switched by changing the resonant condition of the signal recycling cavity.

Table 3.1 summarizes the maximum permitted displacement noise level at 10 Hz. lower values of the displacement noise required in the two detection modes are selected in the table. The positions of the optics in table 3.1 are illustrated in figure 3.2. The auxiliary optics can have larger displacement noise than test masses, by a factor of 10^2 for the beam splitter and signal recycling mirrors, and by a factor of 10^4 for the power recycling mirrors. Here the folding mirrors, PR2 and PR3, have more strict displacement noise requirements than PRM. This is because PR2 and PR3 mirrors can change the optical path of the power recycling cavity by twice, compared to the optical-path change due to PRM. The requirements on SR2 and SR3 are also more strict by a factor of 2 with the same reason.

Note that, in the following discussion, it assumes that 1 % of vertical motion transferred to the longitudinal direction. This is because 0.1-1 % of the mechanically vertical-longitudinal couplings to can happens, as described in subsection 2.1.2 (figure 2.4). In the KAGRA detector, except for the mechanical couplings, the vertical motion is coupled to the longitudinal direction at least by 0.3% at least. This coupling is caused by the fact that the KAGRA detector is not constructed in the horizontal plane for one practical reason. Since the Kamioka mine, where the site of the KAGRA detector, has a lot of groundwater sources in it, the interferometer arm tunnels have been bored with a tilt of 1/300 for drainage.
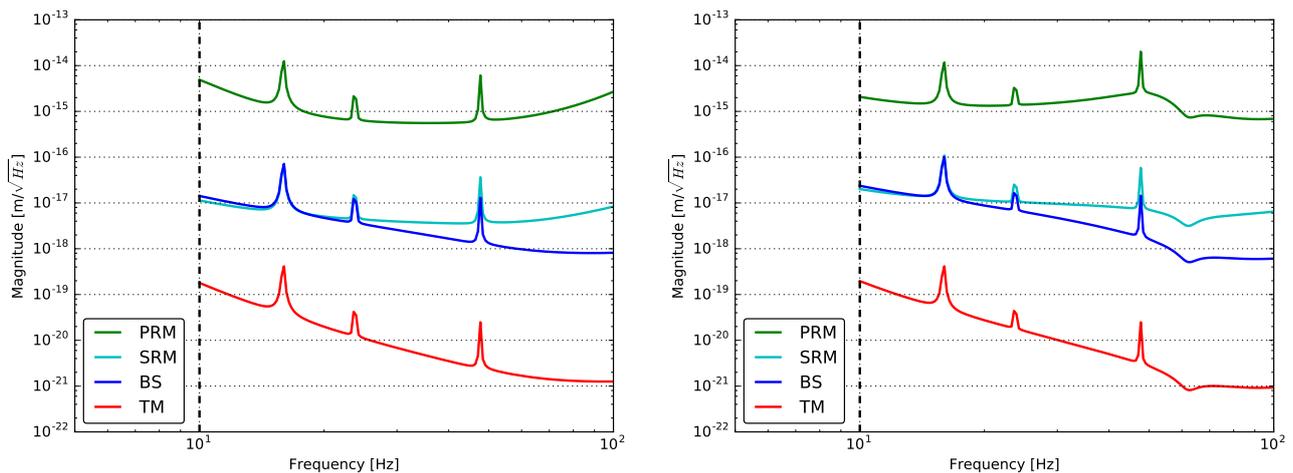

Figure 3.1: Displacement requirement in BRSE detection mode (*left*) and DRSE detection mode (*right*). PRM, SRM, BS, and TM denote power recycling mirror, signal recycling mirror, beam splitter, and test mass respectively.

Optic	Spectrum density at 10 Hz
TM	1×10^{-19} m/$\sqrt{\text{Hz}}$
BS	1×10^{-17} m/$\sqrt{\text{Hz}}$
PRM	2×10^{-15} m/$\sqrt{\text{Hz}}$
PR2,3	1×10^{-15} m/$\sqrt{\text{Hz}}$
SRM	1×10^{-17} m/$\sqrt{\text{Hz}}$
SR2,3	5×10^{-18} m/$\sqrt{\text{Hz}}$

Table 3.1: Requirements on longitudinal displacement noise of the core optics for the KAGRA interferometer.
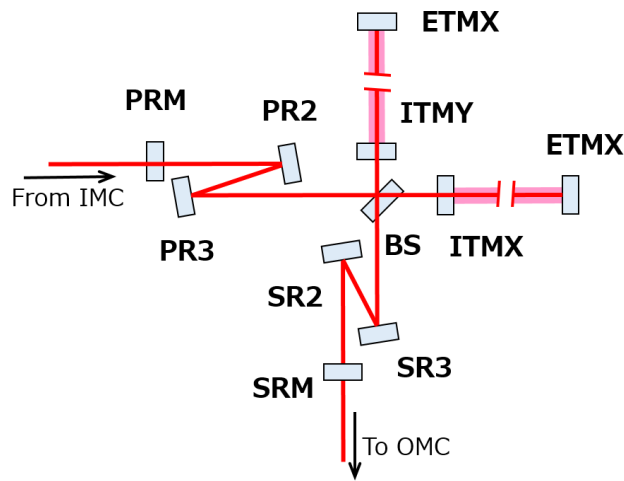
Figure 3.2: Positions of the core optics of the KAGRA interferometer. PRM, PR2 and PR3 are the positions of the power recycling mirrors. SRM, SR2 and SR3 are the positions of the signal recycling mirrors. Test masses are located at ITMX, ITMY, ETMX and ETMY (Input/End Test Mass X/Y). IMC and OMC denote input mode cleaner and output mode cleaner respectively.

3.2   System overview

This subsection introduces the three types of the KAGRA suspension systems for the core optics and their design concepts. They are implemented depending on the required seismic attenuation levels. The conceptual designs of the three types of KAGRA-SAS and their location are shown in figure 3.3 and figure 3.4 respectively. Table 3.2 describes their basic specification.

	Type-A	Type-B	Type-Bp
Suspended optics	TM	BS, SRM, SR2, SR3	PRM, PR2, PR3
Number of horizontal stages	9 (included IP)	5 (included IP)	3
Number of vertical stages	6	3	2
Payload temperature	cryogenic (~ 20 K)	room-temperature	room-temperature

Table 3.2: Basic specification of three types of the KAGRA-SAS
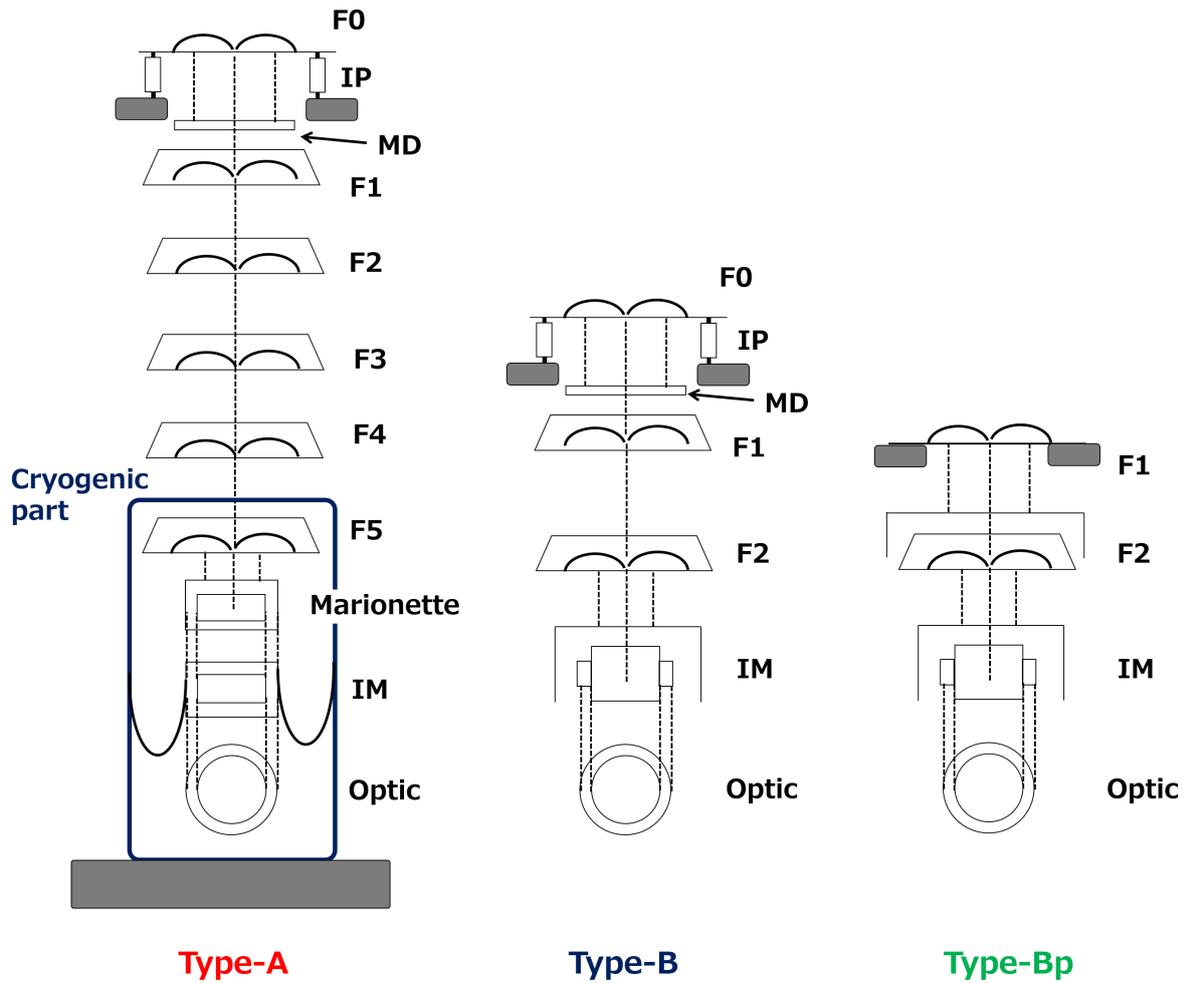
Figure 3.3: Conceptual designs of SAS for the KAGRA detector. F0 $\sim$ F5 represent the GAS filters for vertical seismic attenuation. MD is the magnetic damper, which is placed just above F1 in the type-A and type-Bp system and aims to damp the torsion modes of the attenuation chain. IM denotes the intermediate mass. The optic is suspended from the IM by suspension wires. All the systems are set inside vacuum chambers and are set in vacuum condition. The gray colored retangulars denote the mechanical ground positions.
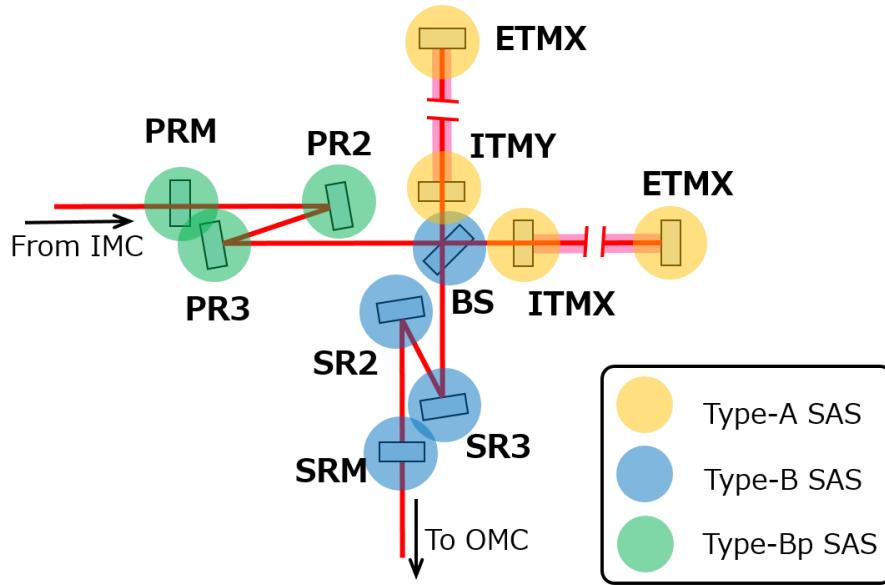
Figure 3.4: Location of SAS in the KAGRA main interferometer. PRM, PR2 and PR3 are the positions of the power recycling mirrors. SRM, SR2 and SR3 are the positions of the signal recycling mirrors. Test masses are located at ITMX, ITMY, ETMX and ETMY (Input/End Test Mass X/Y). IMC and OMC denote input mode cleaner and output mode cleaner respectively.

The largest suspension system, which is called type-A SAS, is used for the attenuation system of the test masses. It includes 9 stages of horizontal isolation and 6 stages of vertical isolation. The IP stage at the top of the chain aims to perform pre-isolation and static control of the whole suspension system. One passive damper, which aims to damp the torsion modes of the chain by using the eddy-current damping, is suspended from the beneath of the IP stage. This damper is called magnetic damper. The lower four stages are cooled down to cryogenic temperature in order to reduce thermal noise. The cryogenic part is covered with aluminum boxes to shield black-body radiation from room temperature components.

The type-B SAS are used for seismic isolation of the BS and signal recycling mirrors. It includes 5 stages of horizontal isolation and 3 stages of vertical isolation. The payload of this SAS is operated in a room temperature. The IP stage for pre-isolation and static control of the suspension chain, and magnetic damper are implemented in the type-B SAS, as for the type-A SAS.

The type-Bp SAS are the system for the power recycling mirrors, and has 3 stages for horizontal isolation and 2 stages for vertical isolation. This system does not include the IP stage. For the horizontal static position alignment of the suspended optic, a motorized stage called the traverser is implemented on the top of the suspension chain. In order to compensate the large RMS displacement and velocity, caused by absence of the IP stage, one damping system is implemented at the F2 stage. In the damping system, a recoil mass for the F2 is suspended from beneath of the F1 stage and the relative motion between the F2 and its recoil mass is sensed and actuated.

The design concepts are briefly summarized here. The implemented isolation systems can be categorized into following three parts:

- The pre-isolation and static-control stage at the top of the chain (top part).

- The chain of GAS filters to achieve the required seismic attenuation (middle part).

- The mirror suspension for providing control system for lock acquisition and alignment (bottom part).

The main role of the top part is to attenuate seismic motion above ~ 0.1 Hz, and to control the static position of the whole suspension system and yaw orientation of the chain. In order to attenuate the microseismic motion transfer and reduce the RMS amplitude of the suspended mirror displacement, the resonant frequencies of IP are tuned at lower than 0.1 Hz.

The middle part is in charge of achieving the required seismic attenuation both in horizontal and vertical directions. Each GAS filter is suspended by a single wire, and its suspension points are located nearby to its center of mass. This configuration helps to avoid large couplings between the motion of the upper filter and that of the suspended filters in every translational and rotational direction.

The role of the bottom part is to align the mirror position and orientation and conduct additional seismic attenuation. The mirror is suspended from the penultimate stage, which is called the intermediate mass, by four wires. The intermediate mass is suspended from the bottom GAS filter by a single wire. Due to this configuration, one can align the mirror orientation by rotating the intermediate mass like a marionette. The mirror and the intermediate mass are surrounded by their recoil masses which are also suspended from upper stage. The control force and torque are exerted onto the mirror and the intermediate mass from the coil-magnet actuators on their recoil masses. The main technical advantages of using a recoil mass are as following:

- One can isolate the actuator from seismic disturbances. This suppresses the fluctuation of the actuation efficiency due to the relative position change between the mass and the recoil mass, caused by the seismic vibration.

- The actuation of the mirror is isolated from the upper stages, since the reaction from the mass and its recoil mass compensates each other and hardly to transfer to the upper stage. This simplifies the servo system for active controls.

3.3   Detailed mechanical design

This subsection focuses on detailed mechanical designs of the suspension components of type-Bp SAS. The type-Bp SAS has two GAS filters: standard and bottom GAS filters. Below them, the suspension system has the mirror suspension system called payload, including a damping system at the F2 stage. Note that, in this thesis, the name of F2 is used when one considers the vertical motion of the bottom GAS filter. On the other hand, it is called BF when the relative motion between bottom GAS filter and its recoil mass is considered.

3.3.1   GAS filter chain

Figure 3.5 shows the detailed mechanical overview of the standard GAS filter. The cantilever blades and the suspension wires are made of maraging steel [28], in order to avoid creep under highly stressed conditions. The cantilever blades are clamped to the base plate at an inclination of $45°$ and their the other ends are attached to the keystone with an incidence angle of $-33°$.

The width and number of the cantilever blades are optimized so that the optimal load of the GAS filter coincides with the weight of the payload. The detailed design of the shape of a cantilever blade for the GAS filter is found in [26] The optimal load of a GAS blade is estimated by

$$F_{\text{optimal}} \;=\; G\frac{Et^3 w}{12L^2}, \tag{3.1}$$
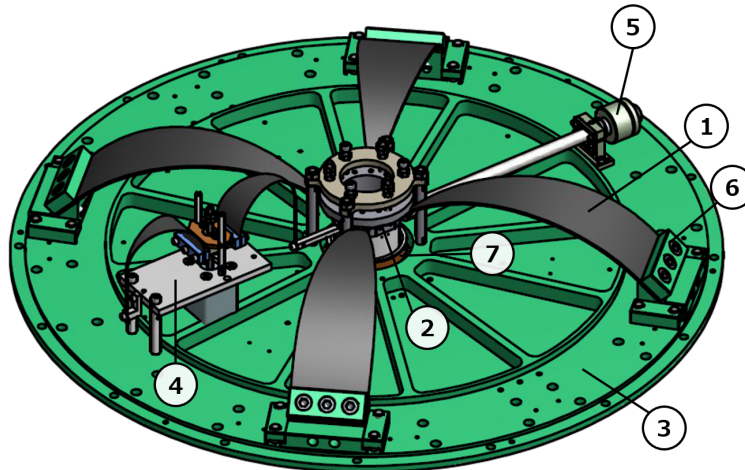
Figure 3.5: Overview of the standard GAS filter. 1) The cantilever blade, 2) the keystone, 3) the baseplate, 4) the motorized spring for initial positioning of the keystone, 5) the magic-wand for compensating CoP effect, 6) the base clamp, 7) the LVDT to monitor the displacement of the keystone.

where t, L and w denote the thickness, length and base width of the cantilever blade. E is the Young's modulus of the blade material. G represents the geometry factor depending on the blade shape, which is 1.71 in the standard blade.

The vertically relative motion of the keystone and the outer frame is controlled by using an Linear Variable Differential Transformer (LVDT) and a coil-magnet actuator. The LVDT is a relative position sensor making use of coil inductance and modulating magnetic fields [46]. The static position is to be tuned by a motorized spring with a thin cantilever blade.

3.3.2   Suspension wire

The designed suspension wires have large thickness in the middle and have small thickness at the ends, as shown in figure 3.6 [42]. This aims to effectively increase the torsion stiffness of the suspension wires without degrading the horizontal attenuation performance of the suspension system caused by the bending elasticity [34].
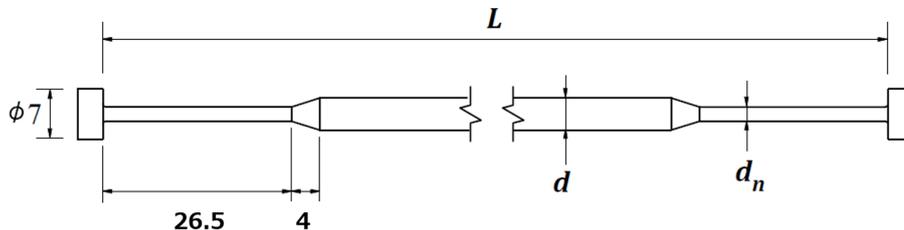

Figure 3.6: Designed suspension wire.

The suspension wire is hooked to the suspension components by the nail-head shapes machined into both ends of the wire.

3.3.3   Bottom filter damping system

In the type-Bp and type-A system, a recoil mass for the bottom GAS filter will be implemented in order to damp some resonant motion related to the swinging motion of the whole chain pendulum. In the type-Bp SAS, the recoil mass for the bottom GAS filter is suspended from beneath of the standard GAS filter by three maraging wires. The overview of the damping system is illustrated in figure 3.7.

The recoil mass is equipped with actuators and position sensors. The relative motions between the bottom GAS filter and its recoil mass are controlled by LVDT and a coil-magnet actuator units, which were originally developed for Advanced Virgo [36]. Since this LVDT unit has different system from that implemented at the keystone of the GAS filter, the LVDT unit for the bottom GAS filter damping is called BF-LVDT unit, in this thesis. BF-LVDT units are arrayed so that they can control the relative motion in every translational and rotational DoFs.
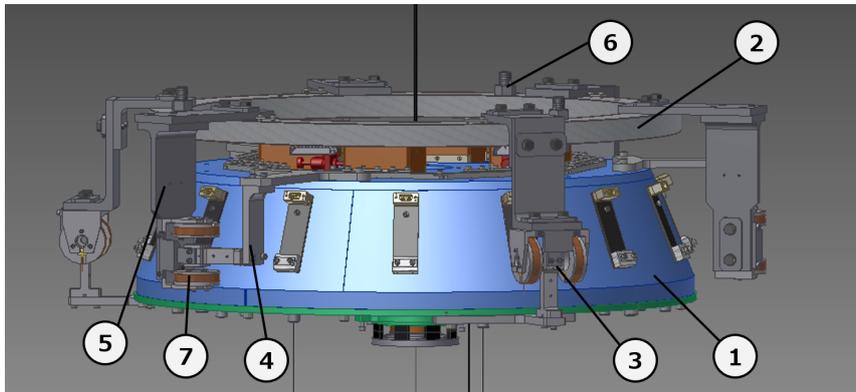

Figure 3.7: Overview of the bottom filter damping system. 1) The body of the bottom GAS filter, 2) the recoil mass for the bottom GAS filter, 3) the BF-LVDT and coil-magnet actuator unit, 4) the magnet holder of BF-LDVT unit, 5) the coil holder of BF-LDVT unit, 6) the hook for the suspension wire connects to beneath of the standard GAS filter, 7) the BF-LVDT coil.

3.3.4   Mirror suspension

A described above, the optic and its recoil mass are suspended from the intermediate mass by four wires, and the intermediate mass is suspended from the bottom GAS filter by a single wire. The recoil mass for the intermediate mass is suspended from beneath of the bottom GAS filter by three maraging wires. The overview of the payload is shown in figure 3.8.

The recoil mass for the intermediate mass is equipped with actuators and position sensors. This aims to control the motion of the intermediate mass. In the type-Bp system, Optical Sensor and Electro-Magnetic actuator (OSEM) [35], similar to developed for Advanced LIGO, is used for the position sensing and the actuating.
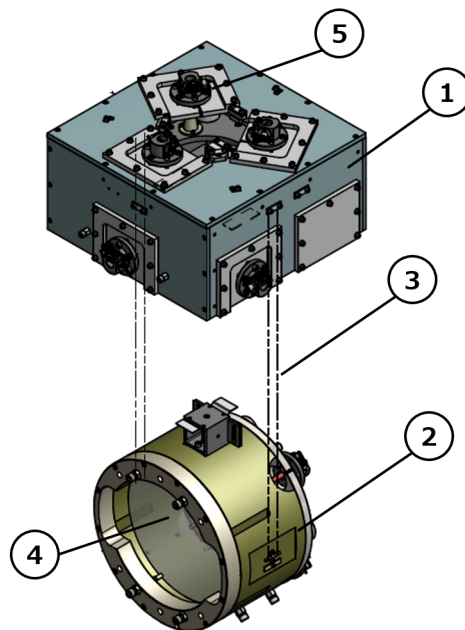
Figure 3.8: Overview of the payload of the type-Bp SAS. 1) The body of the intermediate recoil mass, 2) the recoil mass for the test mass, 3) the wires to suspend the recoil mass of the test mass, 4) the test mass, 5) the OSEM unit. The intermediate mass is covered by the intermediate recoil mass in this figure.

3.3.5   Expected isolation performance

The seismic isolation performance of the type-Bp SAS was calculated by mechanical simulation with rigid-body models [33]. This rigid-body modeling regards the suspension system as a combination of rigid-bodies and elastic elements connecting with them. It was confirmed that this modeling is valid at lower frequencies than ~ 50 Hz in KAGRA-SAS [42]. Figure 3.9 shows The predicted displacement noise level of the suspended optics with the type-Bp SAS in comparison with the requirement. It assumes the high noise model of the Kamioka site, which is described in subsection 2.1.1 (figure 2.1), as the seismic vibration. In the plot, the displacement noise spectra of the seismic vibration, horizontal vibration of the suspended optics, contribution from the vertical vibration of the optics assuming 1% vertical-longitudinal couplings, and the requirements described in section 3.1. According to the model, the suspension system satisfies the seismic isolation requirement in the frequency region above 10 Hz, with a safety margin of about 2 orders of magnitudes.
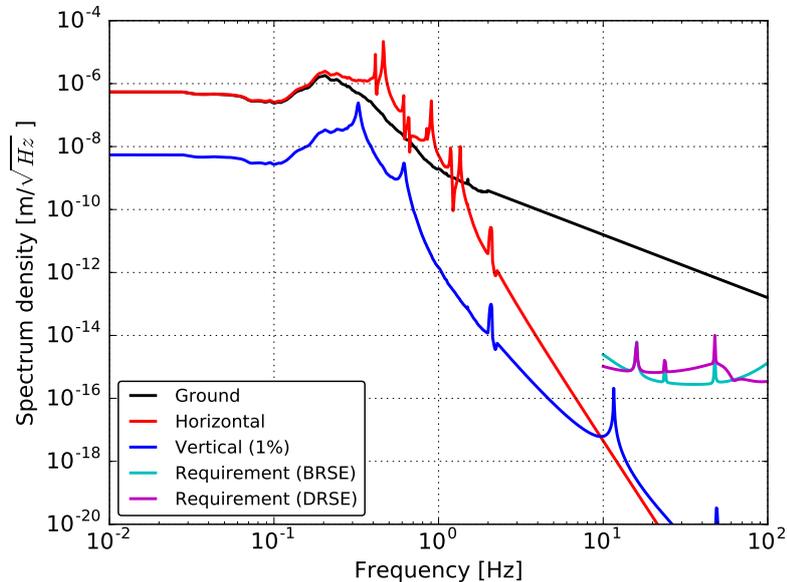

Figure 3.9: Predicted seismic isolation performance of the type-Bp SAS compared with the requirements and the seismic vibration. It assumes 1 % vertical-horizontal coupling.

Active suspension controls
Chapter 4

This chapter describes the active control systems for the suspension systems. These control systems are aimed at suppressing the low frequency fluctuation of the suspension masses and are required for stable operation of the interferometer. The control system described in this section focus on only local suspension controls.

4.1   Motivation for active controls

The mechanics of the passive suspension systems are designed to obtain enough vibration isolation performance in the frequency band of gravitational wave observation. However, in the absence of damping mechanisms, mirror vibration is expected to be enhanced at low frequencies by mechanical resonances which typically have high quality factors. Thence, for smooth and stable operation of the interferometer, the suspension systems have to suppress the low frequency mirror vibration. The low frequency oscillators of SAS such as IP and GAS filters are often affected by thermal drifts or creep, which bring the suspended mirrors away from the operation point of the interferometer.

To suppress the fluctuation at low frequency due to these mechanical characteristics, active control systems are implemented by using vibration sensors, actuators and servo systems. The damping for some mechanical resonances can be achieved by passive dampers such as eddy-current dampers, which have advantages in stability and ease of maintenance. Active control systems are more delicate than the passive dampers, and one has to design and tune the control servo carefully for stable operation. However, active systems are more flexible and can be switched on and off easily after installation into the suspension systems. This flexibility is a big motivation to use active control systems, even though the active systems tend to be more complex.

One point which one has to take care using the active control systems is the control noise. Electronics of sensors, actuators and digital servo systems introduce control noise. One has to check that the control noise does not affect the interferometer sensitivity beyond the acceptable level.

4.2   Requirement for active controls

4.2.1   Interferometer operation phases and requirements

For the KAGRA-SAS, there are different requirements on the active control systems depending on the operation phase of the interferometer. The operation status is categorized into following three phases:

- the calm-down phase

- the lock-acquisition phase

- the observation phase.

The operation phases of the interferometer summarized in figure 4.1.

In the calm-down phase, the active controls take care of vibration of suspension components with large amplitudes caused by large disturbances. In order to prevent the saturation of some delicate sensors and weak actuators due to the large vibration, sensors and actuators which has sufficient range have to be used in this phase. The controls in this phase is aimed at calming the suspension system

down and restore the position and the orientation of the suspension masses to the optimal position. Thence, the active controls in this phase require robustness, and mainly have to damp mechanical resonances of the suspension system. The requirement has been set that the $1/e$ decay time of the mechanical resonances, which disturb the interferometer operation, has to be less than 1 minute.

In the lock-acquisition phase, the optics which compose the interferometer are set at their operation points to start observation of the gravitational waves. In order to acquire the lock of the interferometer, the velocities of the optics have to be reduced so that control forces can suppress the vibration and trap them into the linear range of the interferometer signals. Thus the active controls in this phase are required to reduce the velocities of the optics sufficiently. Typically these RMS velocities of the suspended optics have to be suppressed less than 1 μm/s for the smooth lock of the interferometer. The mirror vibration in pitch and yaw direction should be also reduced, because these rotational motion induce fluctuations of the beam spot and mitigate the length control signals of the interferometer. These angular motions should typically stay below 1 μrad.

The controls on the observation phase are turned on after the interferometer is locked. The gravitational wave observation is conducted in this phase. In this phase, low-noise controls should be used so that the control noises do not contaminate the detector sensitivity in the detection band. Thence, active control loops which induce noises a lot needs to be opened or those control gains should be reduced. The mirror displacements and orientations also have to be kept in a certain range to keep good sensitivity to gravitational waves. The more detailed requirements for the lock-acquisition and observation are described in following sections.
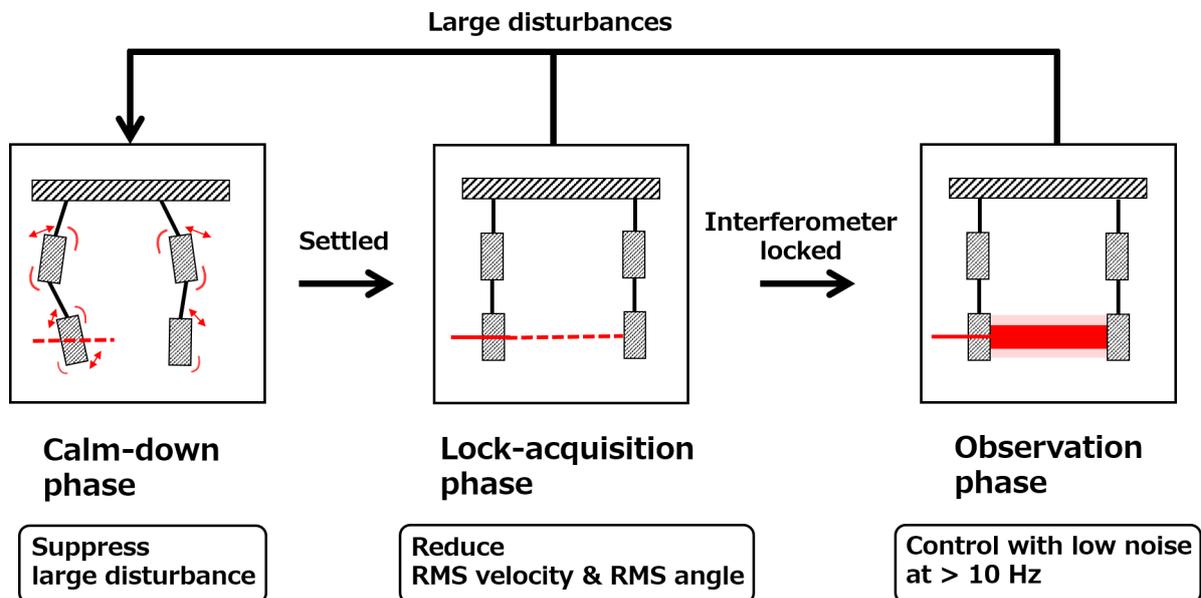

Figure 4.1: Operation phases of the interferometer and the main purposes of the active suspension controls.

4.2.2 Mirror velocity requirement

Lock-acquisition of interferometer

For the length sensing and controls of the interferometer, the frontal modulation techniques [37] is used. In this method, the laser phase is modulated at radio frequencies before being injected into the interferometer. By demodulating the detected laser power with the proper phase, an error signal proportional to the length displacement around the operation point is obtained. The width of the linear range ΔL_{lin} is obtained from the finesse of the cavity $\mathcal{F}$, wave length of the laser λ as

$$\Delta L_{lin} = \frac{\lambda}{2\mathcal{F}}. \tag{4.1}$$

The finesses are set at 38 for the signal recycling cavity, 57 for the power recycling cavity and 1550 for the arm cavities for the KAGRA detector. The wavelength of the laser is 1064 nm. The KAGRA detector uses the green-lock scheme [38] for guiding the lock-acquisition of the arm cavities. This method introduces an auxiliary green laser with half wavelength of the main laser. The auxiliary laser has resonance in the arm cavities with lower finesse of about 50.

The velocity of cavity length variation should be nulled by feedback forces applied to suspended optics while the optics pass through the linear range, to obtain the lock of an optical cavity. The momentum which is applicable to the suspended optic by feedback force is limited by the time that the optics spend in the linear range τ_s and the maximum actuation force.

Actuation force limit

In order to acquire the lock of optical cavities, the velocity of cavity length variation should be nulled within the liner regime ΔL_{lin}. Here, it suppose that the incident velocity of the cavity length variation is obtained by v_0 and also one mirror is resting. In this situation, the equation of motion of the other mirror is described as

$$m\frac{d^2 x}{dt^2} = F_{\text{act}}(t), \tag{4.2}$$

where m denoted the mass of the mirror, $F_{\text{act}}(t)$ gives the actuation force. Then, if the mechanical actuators applies the actuation power within the linear regime ΔL_{lin}, the equation of motion can be deformed to

$$\frac{1}{2}m\left(v^2 - v_{\text{in}}^2\right) = \int_{-\Delta L_{lin}/2}^{\Delta L_{lin}/2} dx \; F_{\text{act}}(t). \tag{4.3}$$

If the actuators always produce the maximum actuation forces F_{max}, the requirement on v_0 to achieve $v = 0$ is described as

$$v_{\text{in}} \lesssim \sqrt{a_{\text{max}}\Delta L_{lin}} = \sqrt{\left(\frac{F_{\text{max}}}{m}\right)\Delta L_{lin}} = \sqrt{\left(\frac{F_{\text{max}}}{m}\right)\frac{\lambda}{2\mathcal{F}}}. \tag{4.4}$$

The actuator designs for PR and SR test mass are summarized in table 4.1. The maximum forces are obtained from 10 V by gathering 4 coil forces. The masses of the PR and SR mirrors are set at 10.7 kg. For actuation of the PR mirrors, a coil driver which performs 13.6 mA/V will be used. While, for actuation of the SR mirrors, a coil driver which exerts 0.128 mA/V will be implemented.

For the lock-acquisition of the arm cavities, since the cavity length signals are fed back to voltage controlled oscillators (VCOs), which modulate the frequencies of the auxiliary (green) laser, the phase of the auxiliary laser is locked to the arm cavity length variation. The frequency of the auxiliary laser is to be compared to that of the main laser by observing the frequency of their heterodyne beat.

Optics	Coil-magnet coupling [N/A]	Current [mA]	$F_{\max}$ [N]	$a_{\max}$ [m/s^2]
PR mirrors	0.129	136	7.1×10^{-2}	6.6×10^{-3}
SR mirrors	0.0225	1.28	1.2×10^{-4}	1.1×10^{-5}

Table 4.1: Actuator design for PR and SR test masses.

According to the beat frequency, it is obtained that how far the main laser is from resonating in the arm cavity. Then, the feedback controls derived from these signals are sent to the coil-magnet actuators on the optics. This method expands the linear regime of the cavity length measurement and gives looser requirement on the velocity of the optic. Consequently, the velocity limit due to maximum actuation power is not defined for the arm cavities, since the VCOs for locking these cavities have large actuation range enough.

The requirements on the velocity of each cavity length variation calculated from equations (4.4) is summarized in table 4.2.

Cavity	Requirement [μm/s]
Arm cavity	$-$
Power recycling cavity	7.8
Signal recycling cavity	0.6

Table 4.2: Requirements on the velocity of the cavity length variation.

RMS velocity requirement

Since the optics of the optical cavities vibrates randomly, the incident velocity changes each time when the optics pass by the linear range. If it assumes that the velocity of the optics has Gaussian distribution, the probability distribution of the incident velocity of the optical cavity length variation $f(v)$ would be described as following [39]:

$$f(v) \equiv \frac{v}{v_{\mathrm{rms}}^2} \exp\left(-\frac{v^2}{2v_{\mathrm{rms}}^2}\right), \tag{4.5}$$

where v_{rms} means the RMS velocity of the cavity length variation. To obtain the lock-acquisition with higher than 50% probability in this model, the RMS velocity v_{rms} has to be reduced lower than 0.84 v_{req}, where v_{req} denotes the maximum permitted velocity to lock the cavity.

Based on these considerations, requirements on the RMS velocity of the suspended optics with the KAGRA-SAS is set to 0.5 μm/s for the type-A and type-B SAS, and 6.5 μm/s for the type-Bp system. This is because the type-A, the type-B and the type-Bp SAS will suspend arm cavity mirrors, SR mirrors and PR mirrors, respectively. Even though the requirement on the velocity for the arm cavity mirrors is set more looser, the two input test masses are also part of the power and signal recycling cavities. The vibration of these input test masses affect the length variation of these cavities. Thus, the requirement of the type-A SAS has to be as strict as that of the type-B SAS.

4.2.3   Angular vibration requirement

The angular vibration of the optic induces the fluctuation of the beam spot and spatial mode mismatch of the interferometer. For stable operation of the interferometer and preventing degradation of the sensitivity of the detector due to the mode mismatch, the optic RMS angles needs to be

suppressed so that they produce beam spot fluctuation on the optics smaller than 1 mm in RMS [40]. Table 4.3 shows the maximum permitted optic rotation angles according to the above requirement [41]. Thus, the requirement on the RMS angles of the optics suspended by the KAGRA-SAS is set to 0.2 μrad for the type-A, 1 μrad for the type-B, and 2 μrad for the type-Bp system. This requirement is kept both in the lock-acquisition and observation phase.

Optic	Requirement [μrad]
TM	0.2
BS	4
PRM	45
PR2	20
PR3	3
SRM	25
SR2	10
SR3	1

Table 4.3: Requirements on the RMS angles of the optics

4.2.4 Longitudinal displacement requirement

The longitudinal position of the optic has to be kept by the interferometer control signals and coil-magnet actuators in the observation phase. For keeping the lock of the interferometer, the amplitude of the control forces has to be kept within the maximum forces of the coil-magnet actuators.

The maximum force applied on the optic is described as $F_{\max} = ma_{\max}$, where m represents the mass of the optic and $a_{\max}$ denotes the maximum acceleration of the optic. Although the maximum acceleration $a_{\max}$ is defined from actuator designs in table 4.1, the maximum acceleration applicable from the mechanical actuators $a_{\max}$ is also limited by control noise requirement in practice. If the actuators generate stronger forces, the more noise is introduced from the electronics of the actuators. The typical noise level of the voltage exerted on the coil-magnet actuators is $\tilde{V}_{\mathrm{n}} = 10^{-8}$ V$/\sqrt{\mathrm{Hz}}$ above 10 Hz. The maximum applicable voltage is $V_{\max} = 10$ V. Then, the maximum acceleration that would be exerted on the optic is

$$a_{\max} = \frac{V_{\max}}{\tilde{V}_{\mathrm{n}}}\tilde{x}_{\mathrm{req}}\omega_{\mathrm{obs}}^2, \tag{4.6}$$

where $\tilde{x}_{\mathrm{req}}$ is the requirement on the longitudinal displacement in m$/\sqrt{\mathrm{Hz}}$ and ω_{obs} is the angular frequency at which the noise requirement should be met. For KAGRA detector, the frequency is set at $\omega_{\mathrm{obs}}/2\pi = 10$ Hz.

Since the optic RMS displacement largely depends on the low frequency resonances (< 0.5 Hz), the control force applied on the optic F_c can be described by using the optic displacement induced by seismic motion x_s, approximately,

$$F_c \simeq k_{\mathrm{sus}}x_s = m\omega_{\mathrm{sus}}^2 x_{\mathrm{m}}, \tag{4.7}$$

where k_{sus} represents the spring constant of the optic vibration in the longitudinal direction and ω_{sus} means the resonant frequency. The resonant frequency of the suspension, which contributes to the RMS displacement, is about 1 Hz for the type-A SAS and 0.6 Hz for the type-B and type-Bp SAS. Then, the maximum permitted optic displacement, before suppressed by the interferometer control, to keep the lock of the interferometer with the optic actuators is calculated as

$$x_{\max} = \frac{F_{\max}}{k_{\mathrm{sus}}} \simeq \frac{V_{\max}}{\tilde{V}_{\mathrm{n}}}\frac{\omega_{\mathrm{obs}}^2}{\omega_{\mathrm{sus}}^2}\tilde{x}_{\mathrm{req}}, \tag{4.8}$$

assuming $x_s/x_\mathrm{m} \sim 1$. Table 4.4 shows the maximum applicable force on the optic and the maximum permitted optic displacement obtained from the equation (4.8). The RMS displacement should be suppressed lower than the values in the table, to avoid saturation in actuators. Here the requirement on displacement RMS is set 1/4 of the maximum permitted ones. Consequently, the displacement requirements are 2 nm for the type-A SAS, 0.4 μm for the type-B SAS and 70 μm for the type-Bp system. The requirement on the long-term drift in the longitudinal direction is also set to the value. These requirements should be kept more than a few days so that these drifts do not break the lock of the optical cavities often.

These requirements are set by assuming that the lock of the interferometer is achieved only by the actuators implemented on the optics.

Optic	F_max [N]	x_max [μm]
TM	9×10^{-6}	0.01
BS	7×10^{-4}	3.3
PRM	9×10^{-2}	3.3
PR2,3	4×10^{-2}	1.6
SRM	4×10^{-4}	560
SR2,3	2×10^{-4}	280

Table 4.4: The maximum force which can be exerted on the optic and the maximum permitted optic displacement to keep the lock of the interferometer with the optic actuators.

4.2.5 Requirement of type-Bp SAS

The requirement set on the active controls for the type-Bp SAS is summarized in table 4.5. In the calm-down phase, the decay time of the mechanical resonances should be less than 1 minute. The residual translational displacement and angle of the optic should be suppressed lower than ~ 50 μm and ~ 50 μrad. These requirement are set for the smooth switching of the active controls in the the lock-acquisition phase.

In the lock-acquisition phase, the optic RMS velocity and RMS angle have to be suppressed to acquire the lock of the interferometer. Here, the RMS value is defined as integration of the spectrum density down to 0.01 Hz. The corresponding time scale (~ 100 sec.) is sufficiently long to cover the lock-acquisition process, and also the integration cover the frequency band of micro-seismic peak around $0.2 \sim 0.5$ Hz, which has large contribution to the RMS velocity or angle of the optic.

In the observation phase, the longitudinal displacement has to be suppressed, in order to avoid saturation of actuation forces by the interferometer control. The optic transversal and vertical displacement and its angle should be suppressed at the same time to keep the beam spot in the center. In addition, both of the RMS displacement, RMS angle in a short time (lower than 1 min), and long-term (longer than 1 min) drift of the optic displacement and angle are to be suppressed for the long-term observation. While the control noise, which couples to the optic longitudinal displacement in the detection band (> 10Hz), is to be suppressed lower than the required vibration level of the type-Bp SAS.

Items	Requirements	ref.
The calm-down phase		
$1/e$ decay time	< 1 min.	§ 4.2
RMS displacement (longitudinal)	< 50 μm	§ 4.2.5
RMS displacement (transversal, vertical)	< 1 mm	§ 4.2.3
RMS angle (pitch, yaw)	< 50 μrad	§ 4.2.5
The lock acquisition phase		
RMS velocity (longitudinal)	< 6.5 μm/sec.	§ 4.2.2
RMS displacement (transversal, vertical)	< 1 mm	§ 4.2.3
RMS angle (pitch, yaw)	< 2 μrad	§ 4.2.3
The observation phase		
Control noise at 10 Hz (longitudinal)	< 1×10^{-15} m/$\sqrt{\mathrm{Hz}}$	§ 3.3.5
RMS displacement (longitudinal)	< 70 μm	§ 4.2.4
RMS displacement (transversal, vertical)	< 1 mm	§ 4.2.3
RMS angle (pitch, yaw)	< 2 μrad	§ 4.2.3
Displacement by long-term drift (longitudinal)	< 70 μm/ a few days	§ 4.2.4
Displacement by long-term drift(transversal, vertical)	< 1 mm/ a few days	§ 4.2.3
Angular displacement by long-term drift (pitch, yaw)	< 2 μrad/ a few days	§ 4.2.3

Table 4.5: Requirements on the active controls for the type-Bp SAS in each active control phase. This requirements are for the controls of the local type-Bp SAS. The column labeled as ref. describes the section which explains the reason of the requirements. The RMS values are calculated by integrating the power spectrum density down to 0.01 Hz. The long-term drift is defined as the time scale longer than about 1 minute.

4.3   Active controls for type-Bp SAS

The detailed active control systems for the KAGRA-SAS, especially for the type-A and type-B SAS are described in [42]. This section focuses on concept of the active control systems for the type-Bp SAS, which are investigated in following section. The main role of the active control system for the KAGRA-SAS is to damp the mechanical resonances and to compensate the drift of low-frequency oscillators. It has three main control loops for the type-Bp SAS: the BF control, the GAS filter control, and the payload control. The BF control performs damping of the main pendulum resonance vibration, which has large contribution to the optic displacement and its angle fluctuation. The GAS filter control is aimed at compensating of the thermal drift of the GAS filters. The payload control deals with damping of the mechanical resonances of the suspension system, and also alignment control of the suspended optics. The concept of the design of the servo filters are discussed in the following subsection. The detailed design performances of the active control systems for the type-Bp SAS are described in chapter 6.

4.3.1   General concept

Control system

The control scheme for KAGRA-SAS is single input single output (SISO). Figure 4.2 shows the basic idea. In the figure, the system to be controlled is represented by $G(s)$. The properties of the $G(s)$, such as displacement or velocity, are monitored by sensors with response α. These sensors provide the input for the controller $H(s)$. This input is called an error signal. The controller is a suitable filter which gives the proper control signal that has to be exerted to the system to be controlled, for the wanted state. The correction signal is sent to actuators of strength β.
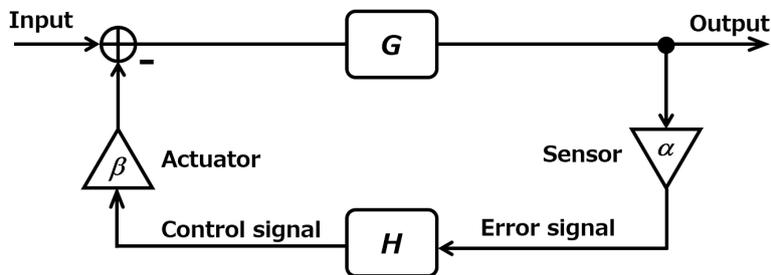
Figure 4.2: Single input single output (SISO) control scheme.

In the Laplace domain, the closed loop transfer function $\mathrm{TF}_{\mathrm{CL}}$ of the controlled system is described by

$$\mathrm{TF}_{\mathrm{CL}} \;=\; \frac{G(s)}{1 + \alpha\beta G(s)H(s)}. \tag{4.9}$$

Then, the motion of the system to be controlled is reduced with a factor $(1 + \alpha\beta G(s)H(s))^{-1}$. Here $\mathrm{TF}_{\mathrm{OL}} \equiv \alpha\beta G(s)H(s)$ is called an open loop transfer function. Note that one can obtain the impulse response of the system, from the inverse Laplace transform of the closed-loop transfer function. If the closed loop system is stable, the Nyquist diagram of the $\mathrm{TF}_{\mathrm{OL}}(s)$ does not surround the point $(-1, i0)$.

Control stability test

One simple test to verify a closed loop system is stable or not is to check the Bode plot of the $\mathrm{TF_{OL}}(s)$. If the Nyquist locus passes the point $(-1, i0)$ on the Nyquist diagram, the amplitude of the $\mathrm{TF_{OL}}$ passes 1 when its phase reaches $-180°$. By using a Bode plot, one can estimate how far the system from becoming unstable. Figure 4.3 shows a graphical representation of this stability test. The frequency where the gain of the $|\mathrm{TF_{OL}}| = 1$ is called unity gain frequency f_{UGF}, or control bandwidth. The phase margin of the system is described by $180° + \phi_{\mathrm{UGF}}$, where ϕ_{UGF} denotes the phase of $\mathrm{TF_{OL}}$ at f_{UGF}. The gain margin is defined as $1/G_{-180°}$, where $1/G_{-180°}$ describes the gain when the phase of the $\mathrm{TF_{OL}}$ reaches to $-180°$.
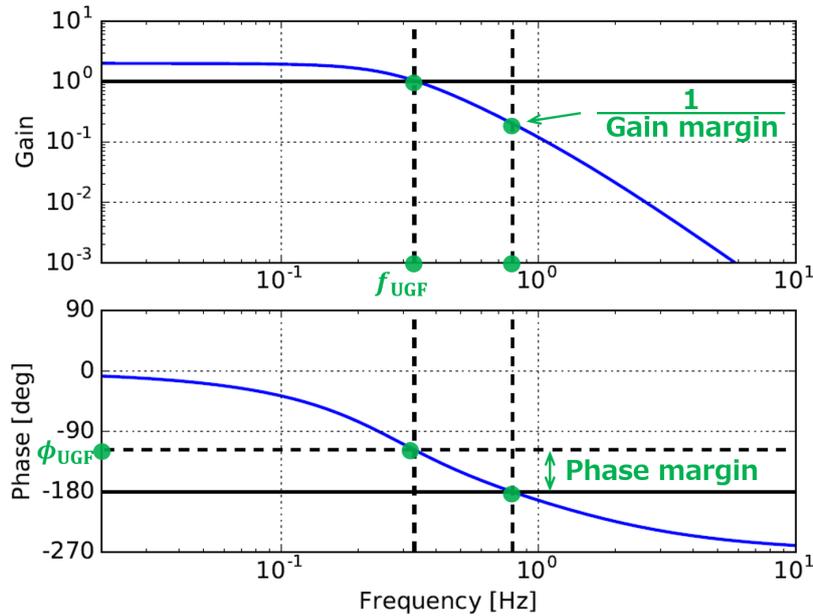
Figure 4.3: A graphical representation of control stability test.

4.3.2   GAS filter control

The main role of the GAS filter control is to compensate the static thermal drift of the GAS filter due to temperature change. Each GAS filter has a set of LVDT position sensors and coil-magnet actuators. The control loop is closed with each LVDT-actuator pair to lock the position of the keystone in each GAS filter. The bandwidth is set around 20 mHz, which is sufficiently below the resonant frequencies of the GAS filters at around 0.4 Hz. For the upper most GAS filter (standard GAS filter), not only DC control but also damping control is implemented to suppress the vertical GAS vibration due to their resonances.

The control loops of the GAS filter is to be closed constantly in each operation phase. Thence, one has to consider about the control noise due to the GAS filter control in the observation phase. Vertical motion induced to the lower-stage GAS filter is transmitted to the optic with small attenuation, and the noise from the control affects the detector sensitivity in the detection band. It assumes that typically 1 % of vertical vibration couples to the longitudinal motion in the KAGRA-SAS.

4.3.3   BF control

The BF control is aimed at damping the mechanical resonances of the main pendulum motion at 0.45 Hz, which cannot be suppressed by the payload control. The motion of the BF in 6 DoFs is measured by using displacement sensors which observe the relative displacement of the BF recoil mass and the BF. The implemented positioning sensor and coil-magnet actuator unit is called BF-LVDT.

4.3.4   Payload control

Damping control

The vibration of the payload is monitored by the displacement sensors which observe the relative vibration of the intermediate mass and mirror with respect to their recoil masses. The mechanical resonances of the payload which cannot be damped by the BF control is to be damped by using them. Particularly, rotational vibration of the optic can be monitored only in this part. As the intermediate mass is suspended by a single wire, the rotational vibrations are separated from the tilt of upper stages. In the type-B and type-Bp SAS, optical sensor and electro-magnetic actuators (OSEMs) [35] are used as the position sensing and for the control. The OSEMs are arranged so that they control the intermediate mass vibration in six DoFs. For the optic, the OSEM units are installed to control the optic motion in three DoFs (longitudinal, pitch and yaw), only in the test run (iKAGRA). In the bKAGRA, only the OSEM actuators are attached into the optic so that they can actuate the optic motion in the three DoFs. The vibration of the optic in the 3 DoFs are to be monitored by the optical lever and the optical length sensor. Note that the optical lever and optical length sensor are devices which is comprised by a light source illuminating the optic and a quadrant photo-diode (QPD) to monitor the beam spot position of the reflected light.

The control system has individual control loops among each DoF, because sensor signal of one DoF is fed back to the actuator in the corresponding DoF. For instance, the longitudinal control signal is sent to actuators for the longitudinal actuation.

Alignment control

For the payload controls, damping control by using position sensors are used for the controls in calm-down phase. On the other hand, controls to align the optic position and its orientation to the interferometer beam should be used for the in the lock-acquisition and the observation phase. For this purpose, the RMS pitch and yaw angular displacements should be suppressed. In the lock-acquisition phase, the pitch and yaw vibration of the optic are observed by the optical lever.

After acquiring the lock of the interferometer, the sensor signals from the optical lever are to be replaced by the signals from the wave front sensors (WFS) [40], which has better sensitivity. The WFS uses the interferometer beam as a reference. The control signals are sent to the actuators on the intermediate mass, because the mechanical resonances of the intermediate mass have a lot of contribution to the RMS angles of the optic.

Performance test of iKAGRA-PR3 SAS

Chapter 5

The iKAGRA-PR3 SAS was the first large vibration isolation system which was assembled and installed at the KAGRA site in the Kamioka underground. The role of the suspension system was to suspend the PR3 mirror which was a steering mirror of the Michelson interferometer during the test run (iKAGRA). The position of the iKAGRA-PR3 SAS is shown in the figure 5.1. This construction of this suspension system was aimed at establishing a safe assembly and installation procedure. The performance of the constructed suspension system was tested at KAGRA site to obtain more detailed information about the preciseness of the current predictions. In the investigation, following suspension responses were compared to the simulated results: frequency response, decay time of each mechanical resonances, and vibration spectra of the test mass. The frequency responses were investigated by monitoring forced transfer functions from implemented actuators to sensors attached in the suspension system. The decay time with and without active controls were measured to test the damping performance of the control system. Also prediction of the angular vibration spectra of the test mass was tested.

In this test, the seismic vibration at the KAGRA site was also observed. Since the used sensors were able to monitor at around $0.1 \sim 10$ Hz, the behavior around the resonant peak was investigated.

The requirements for the iKAGRA-PR3 SAS were to damp all the resonances at below 20 Hz, and to keep the angular fluctuation of the mirror within around 0.3 μrad so that the beam position at the end test mass is kept its position within 1 mm fluctuation. No other requirements are set for the iKAGRA-PR3 SAS.
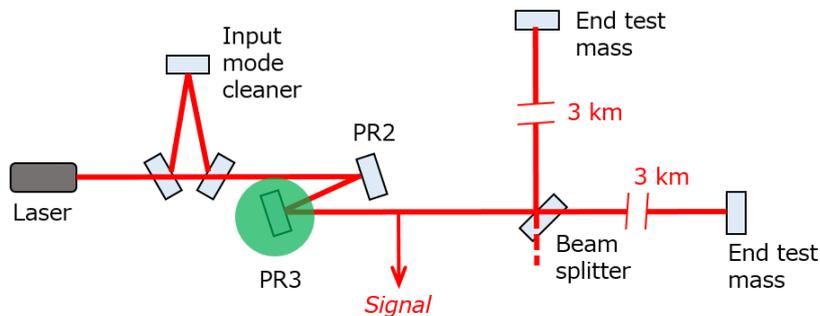
Figure 5.1: Optical configuration of the iKAGRA interferometer. The iKAGRA-PR3 SAS was installed at green circled area, which is situated on the central room of the KAGRA tunnel.

This chapter describes the detailed mechanics of the iKAGRA-PR3 SAS, its experimental performance test. An upgrading plan considered for bKAGRA PR mirror suspension system is also described. The reason is following. At first, another suspension system was planned to use as the suspension system for SAS of the PR3 mirror. However, it was found that the original system might not damp all the resonance motion which disturb the operation of the Michelson interferometer. Another damping system or low frequency mechanical oscillator was wanted for the original system to damp

these resonance motion. Also due to time constraint, one simplified suspension system which was able to damp all its resonance modes, was decided for the suspension. This simplified suspension system was the iKAGRA-PR3 SAS. Therefore, for the observation of bKAGRA, the suspension system for the PR mirrors are to be upgraded from the iKAGRA-PR3 SAS.

Section 6.2 explains the mechanics of the iKAGRA-PR3 SAS. Detailed information about the implemented sensors and actuators for initial alignment and the active controls is described in section 6.3. Section 5.4 summarizes the performance test of the suspension system with comparing the simulated results. In section 5.5, passive responses of the KAGRA-SAS are investigated. The current prediction of passive system such as mechanical quality factors is not so precise. For more precise predicting, one has to collect the information of the mechanical responses of the KAGRA-SAS more. Section 5.6 describes the concepts of the modification of the suspension system. The investigation is concluded in section 12.1.

5.1 Overview

A schematic view of the experimental setup is shown in figure 5.2. The iKAGRA-PR3 SAS is integrated in the central area at the KAGRA site. The system suspended the actual PR3 mirror made of silica glass and contained sensors and actuators for initial alignment and active controls. The signals from the sensors and that toward actuators were integrated into digital system which was set next to the iKAGRA-PR3 SAS. The digital system applied active controls, and stored data of input and output signals. The suspension system was assembled in the air, and was installed inside the vacuum chamber. The chamber was evacuated for reduction of acoustic and air-current noise.
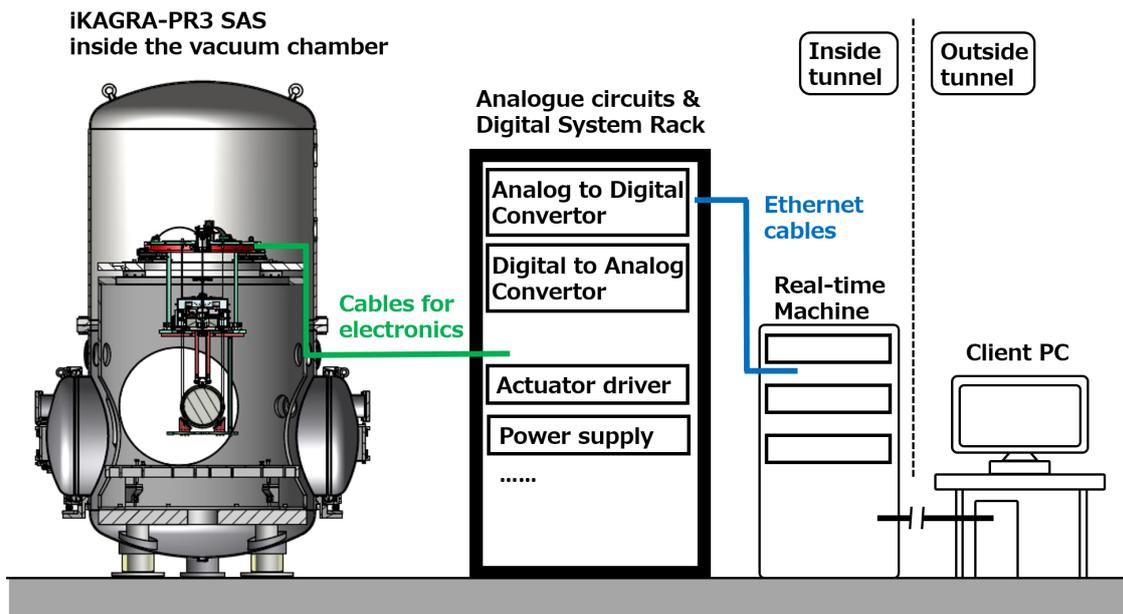
Figure 5.2: Overview of the experimental setup for the iKAGRA-PR3 SAS performance test.

5.2   Mechanics

This section describes the mechanics of the suspension system and its related structures. The iKAGRA-PR3 SAS and the surrounding mechanical components are illustrated in figure 5.3. The suspension system is located inside the vacuum chamber, and is surrounded by a metal frame structure called the security frame. The security frame is constructed in order to secure the suspension system in case mechanical failure occurs in suspension views. The base of the suspension system is supported by a metal frame, which is called inner frame, from inside the vacuum chamber. The inner frame stands on the ground with three legs. Following subsections give these detailed information.

5.2.1   Suspension system

The assembled iKAGRA-PR3 SAS is shown in figure 5.3. The bottom filter (BF) suspends the payload, which includes the test mass (TM), the recoil mass (RM), the intermediate mass (IM), and the intermediate recoil mass (IR), by single wire. The suspension wires connecting the components above the IM are made of maraging steel. The maraging steel is known for possessing superior strength and a particularly good creep characteristic [43]. They have nail-head ends, and are hooked into the masses. The wires are manufactured from rods and turned down on a lathe to the nail-head shape. The wires are heat treated after machining to increase the tensile strength. The BF is supported by an initial position alignment system called traverser. the traverser stands on the top surface of the inner frame.
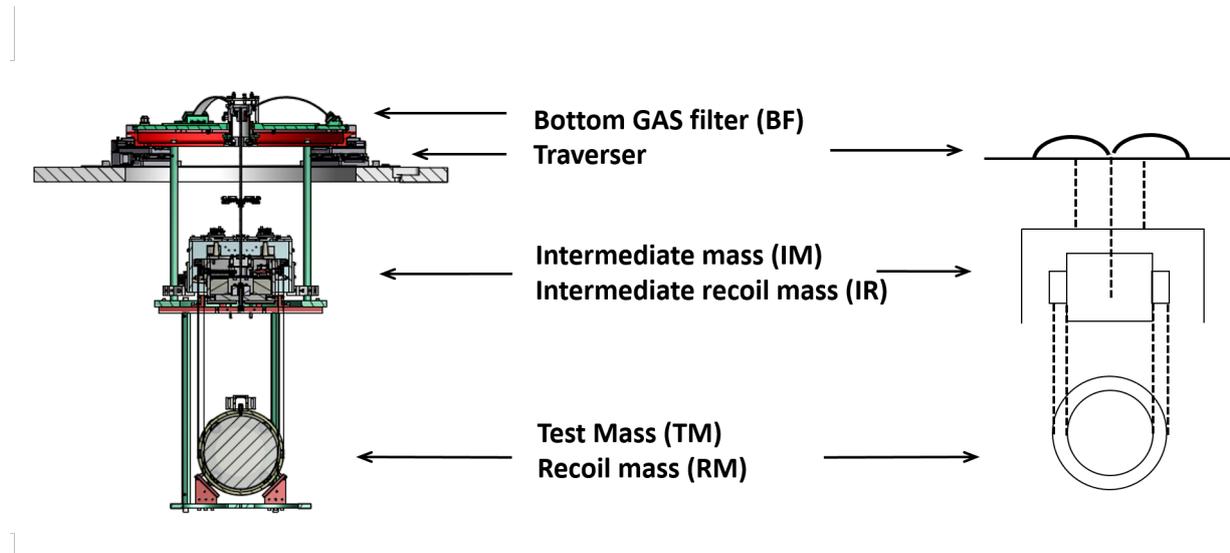
Figure 5.3: Cross section of the iKAGRA-PR3 SAS components.

Bottom GAS filter

In the iKAGRA-PR3 SAS, one GAS filter(BF) is implemented. The BF has 3 cantilever blades, and the number of the blades is designed so that their optimal loads fit with the weight of the payload. The table 5.1 shows the parameters of the cantilever blades and measured properties of the BF. The resonant frequency of the BF is tuned at around 0.4 Hz in advance by changing the radial compression of the cantilever blades. The resonant frequency is selected so that the filter gives enough isolation performance but does not suffer from hysteretic behavior. The magic wand (see subsection 2.2.2) was

not implemented in the iKAGRA-PR3 SAS, since there was no strict requirement on the GAS filter fluctuation.
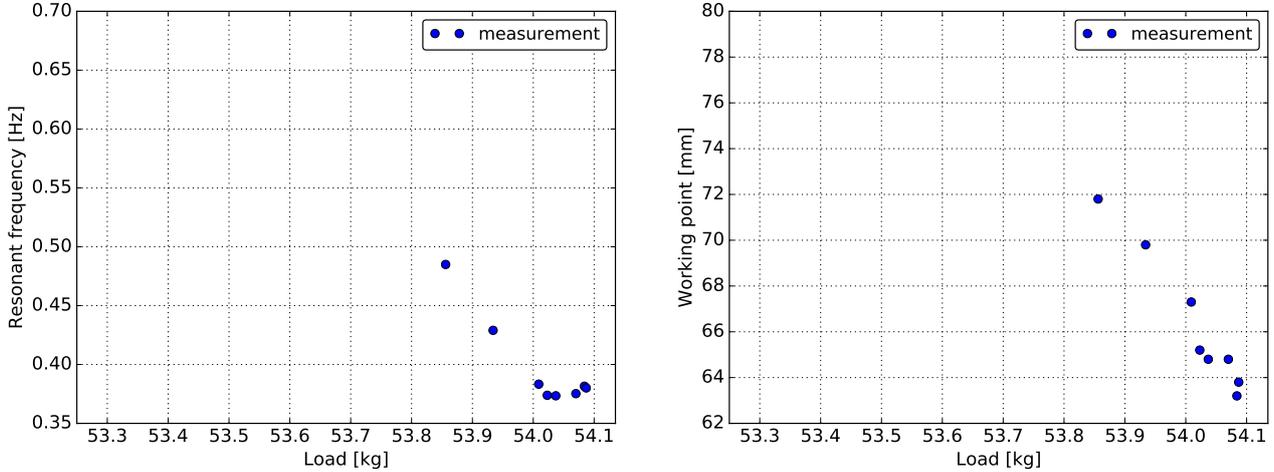

Figure 5.4: Measured bottom GAS filter response. *Left* plot shows the load dependence of the resonant frequency and *right* plot shows the load dependence of the working point.

Thickness	2.4 mm
Base width	35.3 mm
Length	274 mm
Number of blades	3
Optimal load	54.05 kg
Resonant frequency	0.37 Hz

Table 5.1: Parameters of the BF used for the iKAGRA-PR3 SAS. Upper four rows gives the parameters of the cantilever blades and lower two rows gives measured properties of assembled BF.

Payload

The payload consists of a mirror which is conventionally called test mass (TM), RM, IM, IR, as described above. The TM and the RM are suspended separately by two loops of metal wires. The wires for TM are 0.2 mm in diameter, and are made of high-carbon steel (piano-wire). The wires for RM are 0.65 mm in diameter, and made of tungsten. The length of the wires is about 587 mm. The two loops of wires are separated by a distance of 10 mm in the TM suspension and 20 mm in the RM suspension. The suspension wires are clamped on the surface of IM body at the same height of the nominal center of mass of IM. The IM is suspended from the BF with a single maraging steel wire to allow softness in controlling the three rotational DoFs. Its suspension wire is hooked into a piece whose lower section is screwed into bottom of the IM. This system allows to adjust the height of the suspension point and to change the stiffness in the pitch and roll motions. The height of the suspension point is adjusted so that the resonant frequency of the IM pitch mode becomes at around 0.4 Hz. The IM includes mechanisms for tuning the IM tilt in pitch and roll DoFs. The mechanism is composed of a stainless steel body of about 1 kg mass that moves back and forth under the action of a pico-motor, and a spring compressing the body against the pico-motor. The mechanism for aligning

the roll angle is illustrated in figure 5.9. The tuning masses were attached on the top of the IM, to used for adjusting the total weight of IM, RM and TM to its optimal load of the GAS filter (about 50 kg). The IR is suspended from the base plate of the BF by three maraging steel wires.
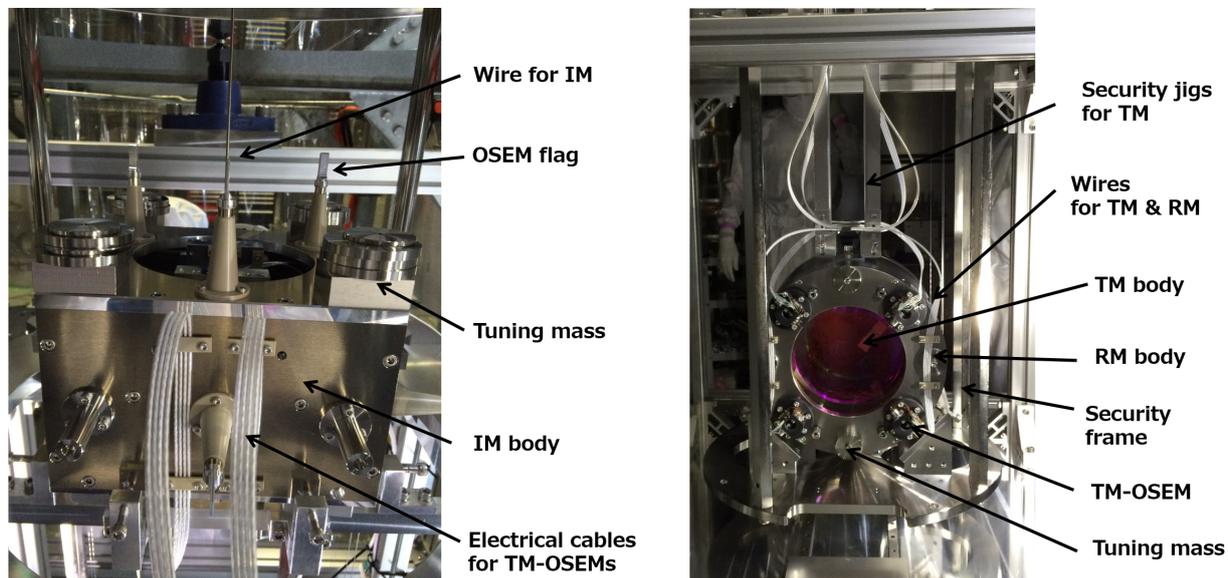

Figure 5.5: Overview of the assembled payload. *Left* figure shows the assembled IM, while the *right* depicts the assembled TM and RM.

Mass distribution

GAS filters work only when appropriate loads are applied, and thus the mass of each stage in the suspension system has to be adjusted to about 100 g precision. Detailed tuning of the weight distribution is achieved by attaching small metal plates on the suspension components. The plates are also used to balance the tilt of each stage. The mass distribution of the iKAGRA-PR3 SAS is shown in table 5.2.

	Mass [kg]	Note
TM	10.5	
RM	12.1	
IM	25.8	
Tuning mass	4.9	Load on BF: 53.3 kg
IR	8.4	

Table 5.2: The mass distribution of the iKAGRA-PR3 SAS. The mass of each stage is tuned so that the loads on BF is optimized.

5.2.2   Security frame

A metallic frame surrounds the suspension system as well as the iKAGRA-PR3 SAS and is called security frame. The purpose of the security frame is to avoid that the suspension system gets damaged when a mechanical failure is happened. It is connected to the underneath of the standard GAS filter. The frame was designed so that its structural resonant frequencies are higher than those of the suspension system.

5.2.3   Inner frame

The type-Bp SAS is supported by a metallic frame called inner frame, inside the vacuum chamber. Figure 5.6 shows the mechanics overview. The lower mechanical resonant frequencies of the inner frame were measured at 15.5 Hz, 17.5 Hz, 25 Hz, 38.5 Hz and 45 Hz, when the inner frame was supporting the iKAGRA-PR3 SAS.
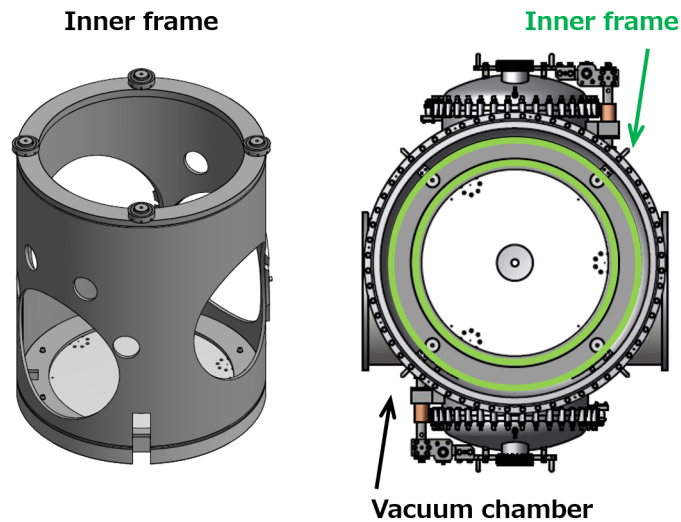
Figure 5.6: Overview of the inner frame (*left*) and its top view (*right*).

5.3   Sensors and actuators

The actuators for initial alignment, and the sensors and actuators for the active controls are described in this section. The motors which was used for the initial alignment of the suspension system was turned off during the observation, to avoid introducing external electromagnetic noises. The implemented sensors and actuators are summarized in table 5.3 and table 5.4.

5.3.1   For initialization

The actuators for the initialization was used for DC positioning and aligning the suspension system. In the iKAGRA-PR3 SAS, following 4 systems are implemented. Table 5.3 summarizes the initialization actuators and their equipped position.

Traverser

Initialization of the horizontal location of whole suspension system is exerted by a motorized aligning system called traverser. The traverser is implemented only into the type-Bp SAS, instead of the motorized spring system which is set at the pre-isolation stage for the type-A, type-B SAS. The standard GAS filter is set on the traverser. The traverser tunes the SAS position along with 3 DoFs, longitudinal, transversal, and yaw direction. The detailed structure is shown in figure 5.7. The compensation range is ± 5 mm in longitudinal and transversal direction, $\pm 5°$ in yaw direction.
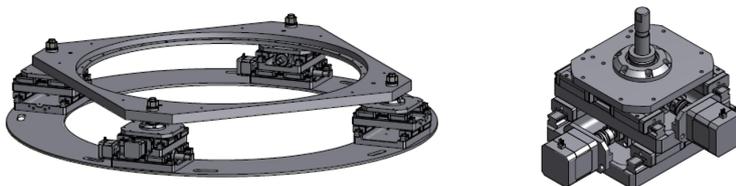
Figure 5.7: Overview view of the traverser. Traverser unit is shown in $left$ figure. Traverser is composed of the motor units shown in $right$ figure.

Vertical position aligning system

Each GAS filter has a motorized spring which aligns vertical position of the keystone of the GAS filter. The aligning system at the standard GAS filter adjusts the vertical position of the payload and also relative position between the bottom GAS filter and its recoil mass. The motorized spring at the bottom filter aligns the height of the payload. The adjustable range is about a few mm which compensates mass variation of a few hundred grams.

Tilt aligning system

The tilt of the payload is aligned by other 2 picomotors which are set inside the intermediate mass. The picomotors are set in the longitudinal and transversal direction and adjust the tilt by pulling or pushing a mass which is connected to the picomotor with a spring.
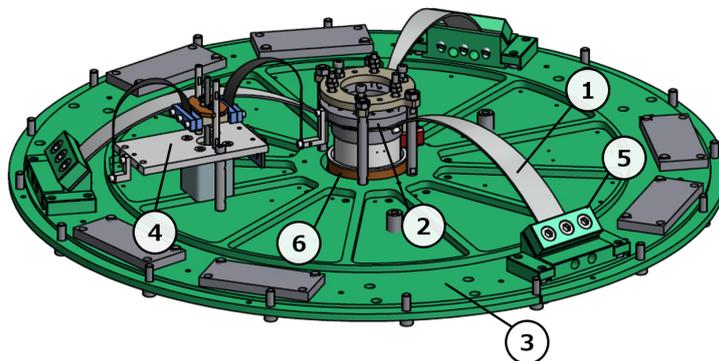
Figure 5.8: Overview of the bottom GAS filter and its vertical motorized aligning system. 1) The cantilever blade, 2) the keystone, 3) the baseplate, 4) the motorized spring for initial positioning of the keystone, 5) the base clamp, 6) the LVDT to monitor the displacement of the keystone.

Rotational position aligning system

In the suspension system for the PR mirrors, the bottom GAS filter has rotational position aligning system. This system aligns the rotational position of the mirror, its recoil mass and intermediate mass with respect to the bottom GAS filter.

Position	Name	Actuated DoF	Main purpose
Inner frame	Traverser	LF2, TF2, YF2	Horizontal positioning of TM
F2	Motorized spring	VIM	Relative positioning of IM and IR
	Rotation mechanism	YIM	Relative alignment of IM and IR
IM	Moving mass	RIM, PIM	Alignment of TM in pitch and roll

Table 5.3: Actuators for initial positioning and alignment of the iKAGRA-PR3 SAS.
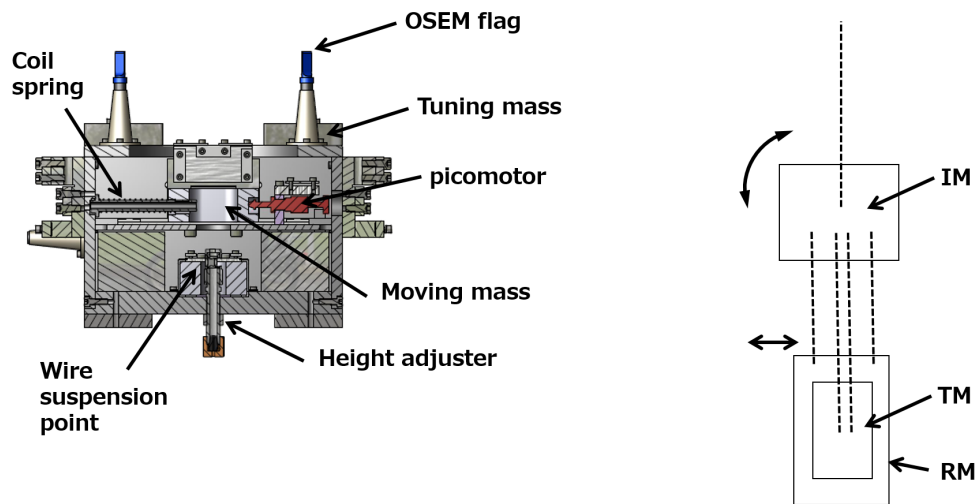
Figure 5.9: Cross section of the intermediate mass (IM) and the tilt aligning system at IM.

5.3.2   For active controls

Sensors and actuators for active controls are listed in table 5.4. The GAS-LVDT and coil-magnet actuator are mounted on the keystone of the GAS filter in vertical direction in order to compensate the thermal drift of the GAS filter. The OSEM units are implemented on the IM and TM for damping of mechanical resonances of the payload by active controls. An optical lever is set to monitor the alignment of the TM in yaw and pitch DoF.

GAS-LVDT

Figure 5.10 and figure 5.11 show the overview and the working principle of the LVDT. The GAS-LVDT consisted by three coils located at the center of the GAS filter. A sinusoidal excitation signal of 10 kHz is sent to the central emitter coil, which produces oscillating magnetic field around. Two other receiver coils coaxially mounted to the emitter coil sense the magnetic field then provide oscillating voltages. The induced voltage is canceled if the emitter coil is at the center of the two coils, since the two receiver coils are identical and counter-wound. When the emitter coil shifts from the center, the mutual inductance is also changed and that makes a difference in the induced voltages. The induced differential voltage is sent to a mixer which demodulates the oscillation signals and produce DC signals proportional to the oscillation amplitude. The driving circuit of the LVDT used in the experiment is the one developed for advanced Virgo, and the details are described in [47]. The linear range of the LVDT is ± 5 mm from the center position.
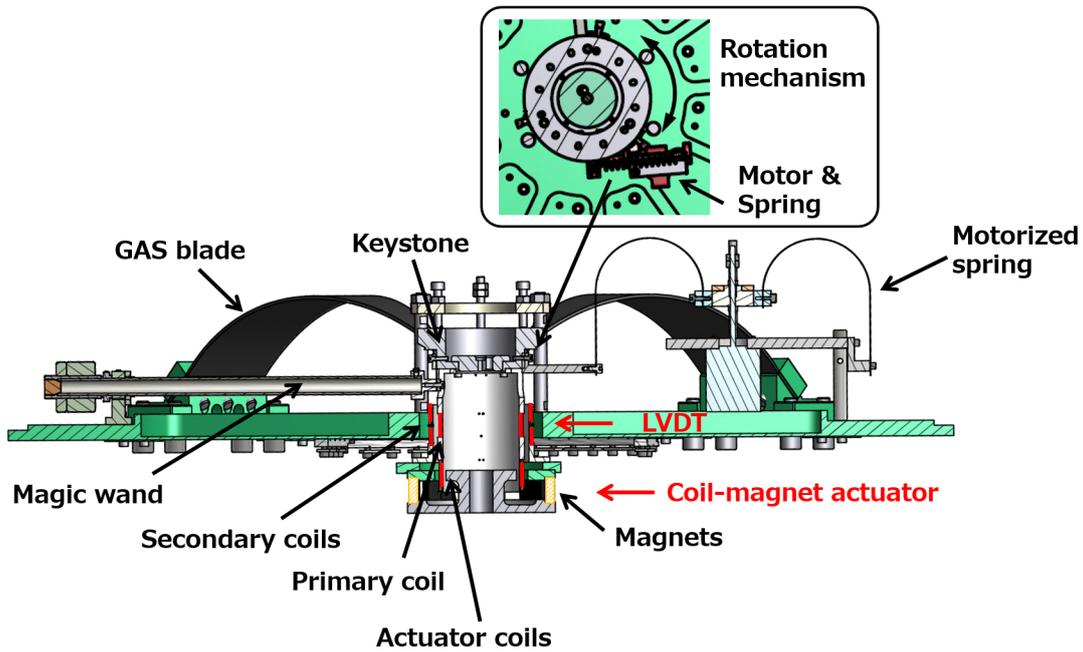
Figure 5.10: Overview of GAS-LVDT and its coil-magnet actuator unit.

OSEM

The OSEMs are implemented into the intermediate mass and test mass stages in the iKAGRA-PR3 SAS. The gaps between the LED and the PD was designed at 5.1 mm. The linear range for longitudinal direction is about ± 0.5 mm. The flags do not touch to the body of the OSEM unless the intermediate mass turns about ± 10 mrad in pitch and yaw direction comparing to its recoil mass. The overview of
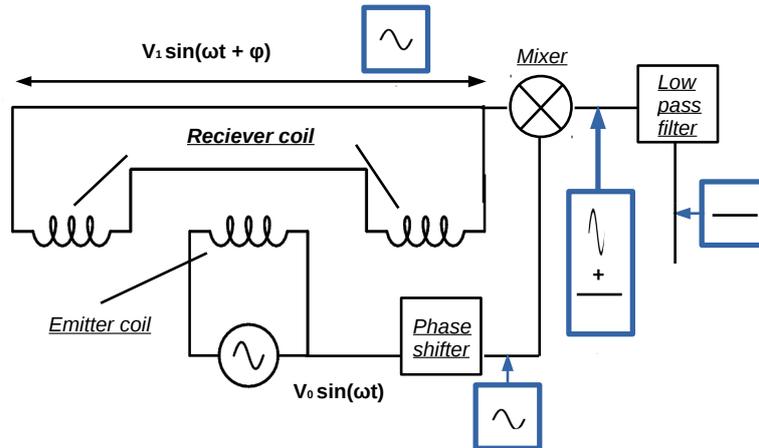
Figure 5.11: Working principle of the LVDT.

one OSEM is illustrated in figure 5.12, while the implemented location is shown in figure 5.13. Figure 5.14 shows the conceptual control loops by IM-OSEMs. In this performance test, one OSEM, which is labeled H4 in the figure, was not working. Also the control system by the TM-OSEMs was not implemented in the test. The details about this issue is explained in following section.
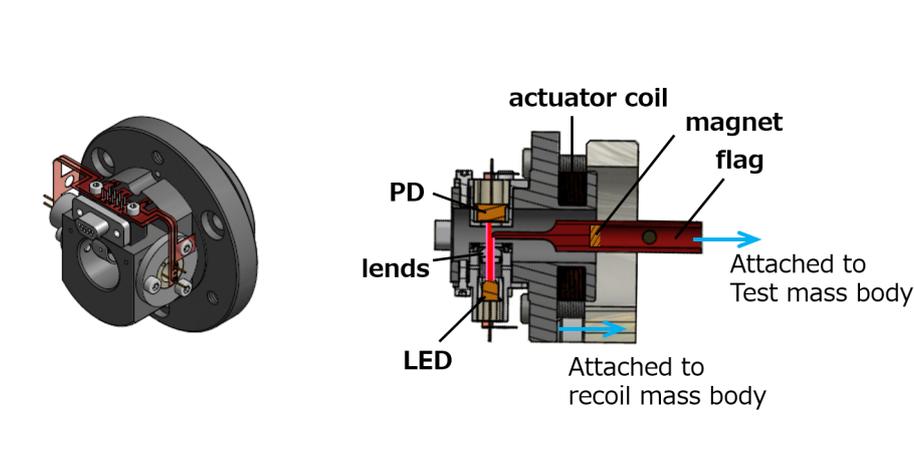

Figure 5.12: Overview view of OSEM unit used in iKAGRA (*left*) and its cross section (*right*). Gap between its PD and the LED was 5 mm.

Optical lever

A schematic view of the setup of the optical lever is shown in figures 5.15. A fiber-collimated light beam from a Super Luminescent Diode (SLD) was sent to the TM (PR3 mirror), and the reflected light reached a Quadrant Photo-Diode (QPD) fixed on an X-Z stage. The fiber head and the QPD are placed as close as possible to the viewports, in order to reduce air-current noise. The optics outside the chamber were covered by a plastic windshield for the same purpose. The optics are horizontally arranged on optical tables at the level of TM. The optical tables are supported by cylindrical supports

TM-OSEM   **IM-OSEM**
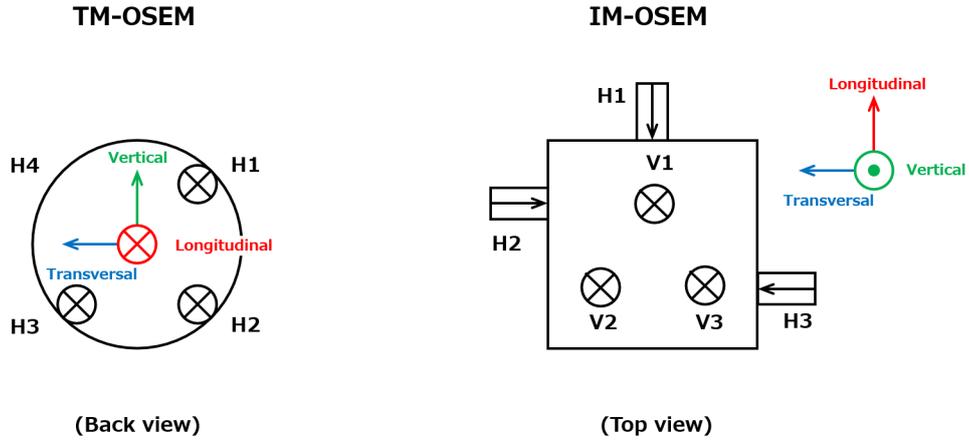
Figure 5.13: Positions of the OSEMs implemented into the payload in iKAGRA-PR3 SAS.
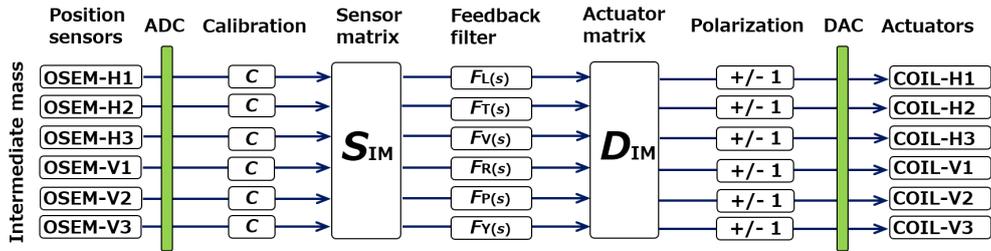
Figure 5.14: Conceptual control loops by the IM-OSEMs.

which were made of aluminum to have good thermal conductivity and reduce the tilts of the optical tables due to thermal inhomogeneity in the supports. The lowest mechanical resonant frequency of a support is about 40 Hz, which is much higher than the bandwidth of the optical lever controls ($\sim$1 Hz).

Position	Name	Sensed/actuated DoF
F2	GAS-LVDT+Act	VIM-VGND
IM	OSEM	LIM-LIR, TIM-TIR, VIM-VIR
		RIM-RIR, PIM-PIR, YIM-YIR
TM	OSEM	LTM-LRM, PTM-PRM, YTM-YRM
TM	Optical lever	PTM, YTM

Table 5.4: Sensors and actuators for active controls of the iKAGRA-PR3 SAS.
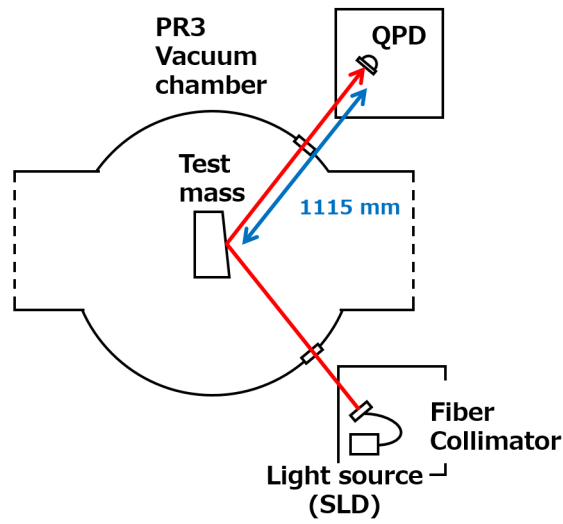
Figure 5.15: Overview of setting of the optical lever.

5.4 Performance test in Kamioka mine

This section describes the experimental performance test of the iKAGRA-PR3 SAS at the KAGRA site in the Kamioka underground. The main targets of this test were to characterize the KAGRA-SAS performance and to investigate the preciseness of the predictions.

First, the measurement of the seismic vibration at KAGRA site is described in section 5.4.1. The vibration is compared with seismic motions which were measured at other sites of Japanese gravitational wave detectors, for the characterization. The suspension responses are described in section 6.4.1 and section 5.4.3 by comparing the measurements and the predictions. In section 6.4.1, the mechanical response of the suspension system was checked with implemented sensors and actuators, before enabling active controls. Measured frequency responses were compared with simulated results using a three dimensional rigid-body model. The results were fed-back to the servo design of the active controls. In section 5.4.3, damping performance by the active controls was tested with the active control systems is described. This test focused on the control systems in the calm-down phase.

5.4.1 Seismic vibration at KAGRA site

KAGRA aims to make effective use of an underground environment with low seismic vibration. This section describes that the seismic vibration at KAGRA site which was firstly measured in this test.

The measured seismic vibration at the KAGRA site is shown in figure 5.16 including measured seismic vibration at the TAMA site and the modeled CLIO site (see subsection 2.1.1). TAMA is located in Mitaka campus of National Astronomical Observatory of Japan (NAOJ) in Tokyo. The vibration of TAMA site was measured by a L-4C seismometer, while the vibration at the KAGRA site was measured by a Trillium seismometer. Since both of the vibration at TAMA site and the KAGRA site were measured in a short period with a few minutes, the shown vibrations are not statistical ones. The shown micro seismic peaks of them have large uncertainties about 1 or 2 order of magnitudes, depending on the weather condition. Since there is no longterm data of the seismic vibration at the KAGRA site which is measured up to $\sim$ 10 Hz, here characterize the seismic motion at the KAGRA site according to the plots in figure 5.16. In the vibration of the KAGRA site, noise of the seismometer at the frequency below at 70 mHz and above at 10 Hz. At below around 70 mHz, since the noise of the sensors are dominant, the raw data is cut and flatted. Thence, the measurements are compared in the range between 0.1 to 10 Hz.

Figure 5.17 shows the differences. In all the frequency band, the seismic vibration at KAGRA site is lower than that of TAMA site. On the other hand, if one compares the vibration between the CLIO site and the KAGRA site, the vibration of KAGRA site was slightly different from the seismic noise measured at the CLIO site at 0.1 $\sim$ 10 Hz. The found differences between the vibration at the KAGRA site and CLIO site are described in below.

- At 0.1 Hz to 0.5 Hz, the amplitudes are different from each other. This is caused by the time depended uncertainty of the micro-seismic peak.

- At around 2 Hz, it was found that the vibration at KAGRA site had shallow peak. The amplitudes of the measured peak were larger than the model of CLIO site by about one order of magnitude. This peak introduced to larger seismic vibration at 1.5 Hz to 6 Hz. According to this measurement, the amplitude of the vibration at KAGRA site can be larger than that of CLIO high noise model by a factor of 2 or 3 at 4 to 10 Hz. However

- At above 10 Hz, the vibrations at KAGRA site are not measured due to the noise of the seismometer. It is expected that the spectrum of KAGRA site are proportional to f^{-2} with larger amplitudes by a factor of around 2 compared to that of CLIO site.

76

Consequently, it was experimentally confirmed that the seismic vibration at KAGRA site was consistent with the previously measured vibration at CLIO site except for some slight differences. It is found that the vibration at KAGRA site might be larger than the model of CLIO site at 1 to 10 Hz.

Note that the vibrations at KAGRA site were measured in a daytime, and there were working people at the KAGRA site. Thence the discrepancy at 1 to 10 Hz might come from human activities, and the behavior at the frequencies might get close to the model of CLIO site. For deeper understanding, the statistical seismic vibration at the KAGRA site is to be investigated with more long period data.
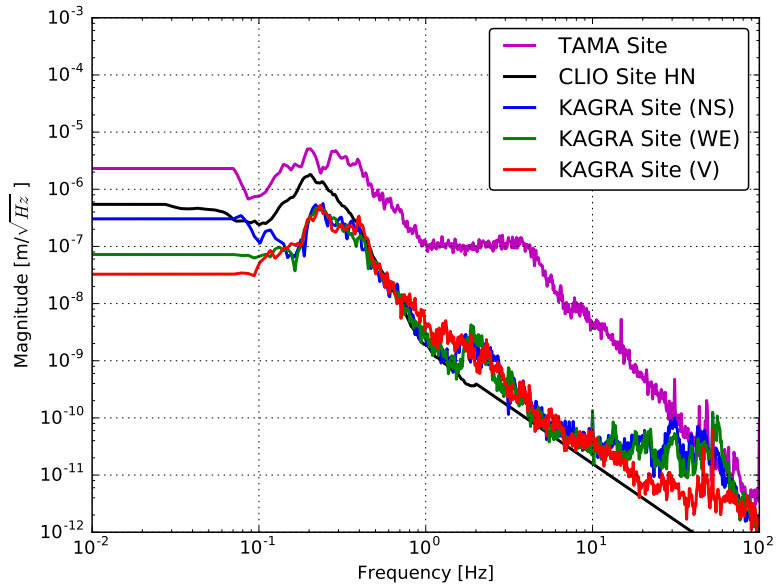
Figure 5.16: Measured seismic vibration at three sites of the Japanese gravitational wave detectors. The vibration of CLIO site is the high noise model obtained from a long period data (black), while the vibration of TAMA site (magenta) and KAGRA site (blue, green, red) are the measurements on October 2015 and May 2016, respectively.
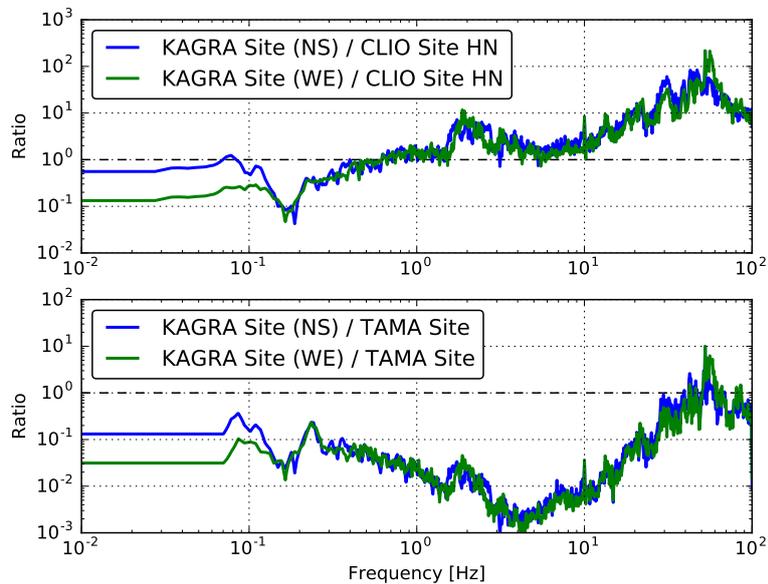
Figure 5.17: Horizontal seismic vibration at KAGRA site compared to high noise model of CLIO site (upper) and to the vibration TAMA site (lower).

5.4.2   Suspension mechanical response

The expected and measured mechanical suspension responses are described in this subsection. Table 5.5 summarizes all the eigenmodes of the iKAGRA-PR3 SAS predicted by 3 dimensional rigid-body model. Figure 5.18 shows their shapes of the eigenmodes. The eigenmodes whose resonant frequencies below at 20 Hz were taken care by active controls, and thus the mode #1 to #19 were actively controlled in this investigation. The measured responses are compared with the simulated results and the results were used for making the servo filter designs.

Here the variable names of L, T, V, R, P, Y are used for expressing the DoFs of the vibration in this subsection. They are the first letter of the direction of the vibration (longitudinal, transversal, vertical, roll, pitch, yaw). The following two letters describes the name of the rigid bodies in the suspension system.

#Mode No.	Frequency [Hz]	Mode shape	Note
#1	0.156	YIM, YRM, YTM	wire torsion
#2	0.430	RIM, RRM, RTM	IM roll
#3	0.470	PIM, PRM, PTM	IM pitch
#4	0.520	-RIM, TRM, -RRM, TTM, -RTM	main pendulum
#5	0.527	PIM, PRM, PTM	main pendulum
#6	0.659	-PIM, -LRM, -PRM, LTM, -PTM	TM-RM pendulum
#7	0.660	-RIM, TRM, -RRM, -TTM, -RTM	TM-RM pendulum
#8	0.680	VIM, VRM, VTM	GAS filter
#9	0.844	-PIM, -PRM, PTM	TM pitch
#10	1.029	YIR	IR yaw
#11	1.036	-YRM, YTM	TM yaw
#12	1.099	LIR	IR longitudinal
#13	1.099	TIR	IR transversal
#14	1.185	TIM, -TRM, TTM	main pendulum
#15	1.185	-LIM, PIM, LRM, PRM, LTM	main pendulum
#16	1.391	YIM, -YRM, YTM	TM yaw
#17	5.494	YIM, -YTM	RM pitch
#18	11.370	VIM, VRM, -VTM	TM vertical
#19	15.583	-RRM, RTM	TM roll
#20	53.309	VIM, -VRM	RM vertical
#21	73.134	RIM, -RRM	IM roll
#22	98.138	RIR	IR roll
#23	101.476	PIR	IR pitch
#24	124.871	VIR	IR vertical

Table 5.5: Simulated eigen mode list of the iKAGRA-PR3 SAS. In the column of each mode shape, main vibrations, whose amplitude are larger than others, are described.
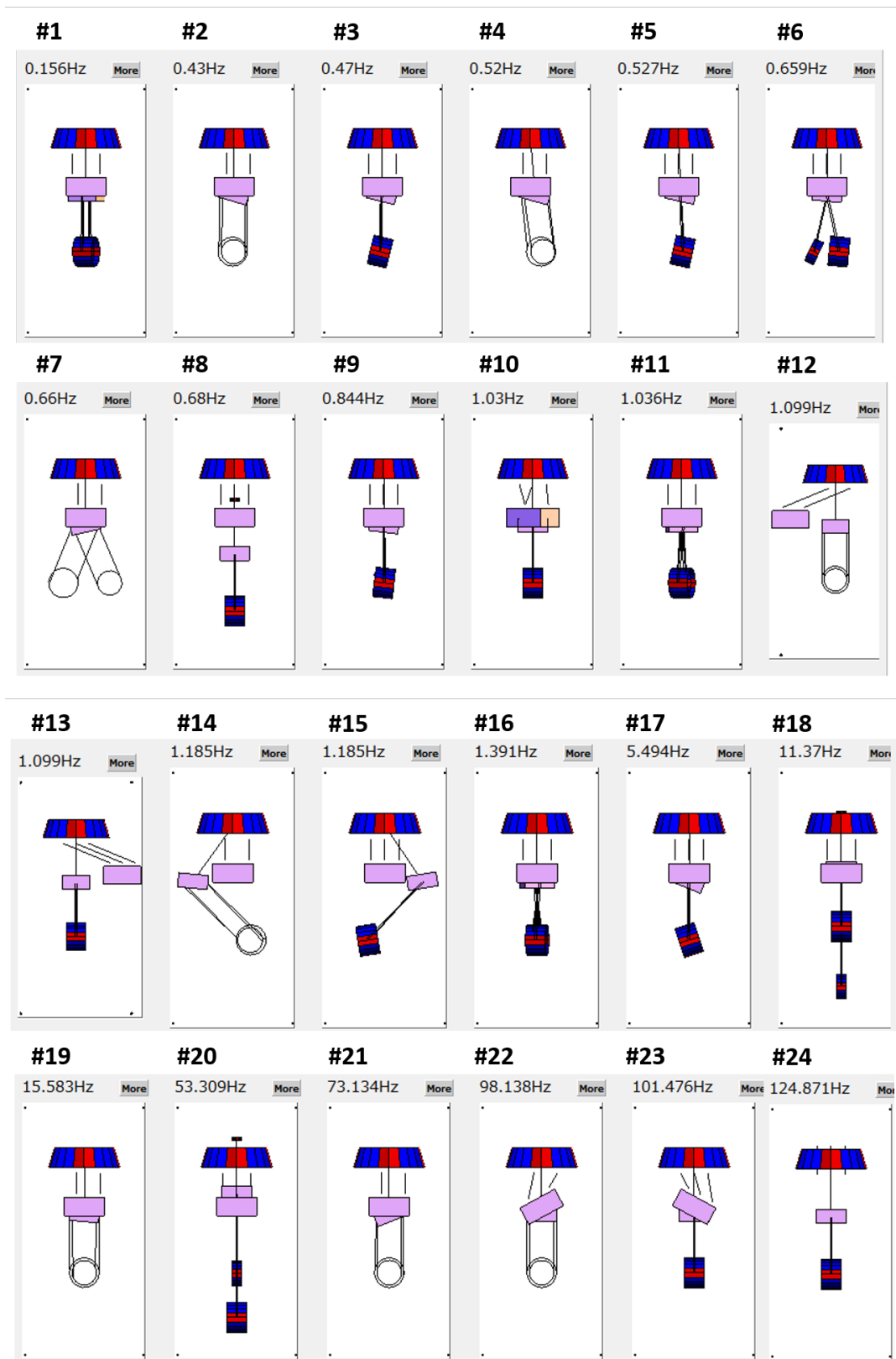
Figure 5.18: Eigen mode shapes of iKAGRA-PR3 SAS predicted by 3 dimensional rigid-body model.

Measurement setup

The iKAGRA-PR3 SAS was assembled at the center room of the KAGRA site in air and was installed inside the vacuum chamber.

The measurement was done after pumping down. The suspension had 2 unoptimized systems due to some constraints. First, 3 OSEMs were implemented into the TM level instead of 4 OSEMs. This is because one OSEM flag came off from the TM surface in final period of the assembling and there was no mechanics to fix the problem. Also this was because it was possible to control 3 DoFs (longitudinal, pitch and yaw) of the TM by using the 3 OSEMs in principle. Secondly, an aluminum sheet was installed at one of the suspension points of the TM, because one part which touched directly to the piano-wire did not have proper groove on it. Then, the sheet was attached to make enough friction at the suspension point.

The frequency responses of the iKAGRA-PR3 suspension system were explained by rigid-body vibrations of the suspension bodies in a Cartesian coordinate system. Virtual sensors and actuators were constructed in the digital system with linear combination of the actual sensors and actuators. They measure and excite the rigid-body vibration in certain DoFs. The measurement was conducted by injecting broadband Gaussian noise from a virtual actuator in a certain DoF and taking the excited displacements measured by virtual sensors. The virtual actuators were geometrically diagonalized beforehand. The amplitude and the excitation signal were adjusted so that enough signal to noise ratio was obtained in the whole frequency band but do not excite the mechanical resonances so much, so as to keep the sensors in the linear regimes. The measurements at the TM and IM level were conducted by using OSEMs. The vertical transfer function of the GAS filter was measured by using the LVDTs and the coil-magnet actuators.

Diagonal transfer functions

The measured frequency responses are described in this section by forced transfer functions of the suspension system, from the implemented actuators to the sensors, in diagonal DoFs (for instance, from longitudinal virtual actuator to longitudinal virtual sensor). Figure 5.19 to 5.28 shows the Bode plots of the measured transfer functions. Other measured transfer functions, including non-diagonal ones, are shown in [48]. The red curves show the predictions by 3 dimensional rigid-body model, while the blue curves and dots denote the measured ones. The measured curves fit well with the prediction in most case, except for following discrepancies:

- The measured transfer functions by IM-OSEMs for LIM and YIM had discrepancies above around 20 Hz. The transfer function measured at for the LVDT was also has different from the prediction above around 4 Hz. The discrepancies are caused by electromagnetic coupling between the actuation signals and sensing signals. The measurement of the LVDT had large couplings because the sensor coils were located coaxially with the actuation coil, and the signals can couple directly though the magnetic fields.

- Higher resonant frequencies measured in the transfer functions of the IM roll, vertical, and pitch DoFs deviate from the simulation. According to the simulation the resonant frequency is 5.5 Hz in the pitch transfer function, while, the observed resonant frequency was 4.6 Hz. Also the predicted resonances at 53 Hz in vertical, 73 Hz in roll transfer functions were higher than the measured results. The resonances of these modes correspond to the bounce modes of the RM in the pitch, roll, and vertical DoFs. One reason of the discrepancy might be that hanging of the RM was uneven. For simpleness, if one of 4 wires suspending RM was not loaded, the unloaded wire contributes to the vibration of the RM in pitch, vertical, roll DoFs. Then the

spring constant for the resonances would be reduced. This can be confirmed by measuring the resonances of the violin modes of the each wire for the TM and RM.

- The hight of the resonant peak (mechanical Q factor) at 0.15 Hz in the IM transfer function in yaw direction was much lower than the prediction. This implies that some of the IM-OSEM flags might be touched slightly during this measurement due to injected large actuation signals. However, it was confirmed that the mechanical Q factor of this resonance fitted with the prediction when the smaller amplitude signal was injected, according to following measurement. Thus, it was not because of failure of assembly nor failure of the prediction.

- In the measurement of the TM transfer functions, there were several peaks which were not predicted. This was caused by unoptimized diagonalization of the virtual actuators consisted by the 3 OSEMs in the iKAGRA-PR3 suspension system. Since all the coupled resonances are identified, this issue is not from the failure of the prediction.

- Several resonances which are not predicted by the simulation were measured at high frequencies. The resonances measured at 60 Hz are caused by hum in the electronics. Resonances at around 70 to 80 Hz in the roll and pitch transfer functions are due to violin modes of the wires suspending the RM.

Consequently, the measurement confirmed that simulation predicts precise resonant frequencies except for the bounce modes of the TM and RM, also except for the violin modes. The implemented sensors are not able to monitor the vibration at higher frequencies than about 20 Hz. This issue is not problematic, since the signals at these high frequencies basically are not used for the control systems.
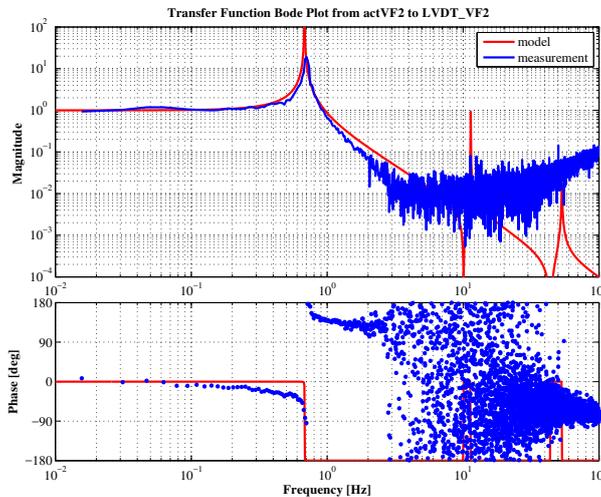

Figure 5.19: Diagonal transfer functions actuated and measured by LVDT + actuator unit at bottom GAS filter.
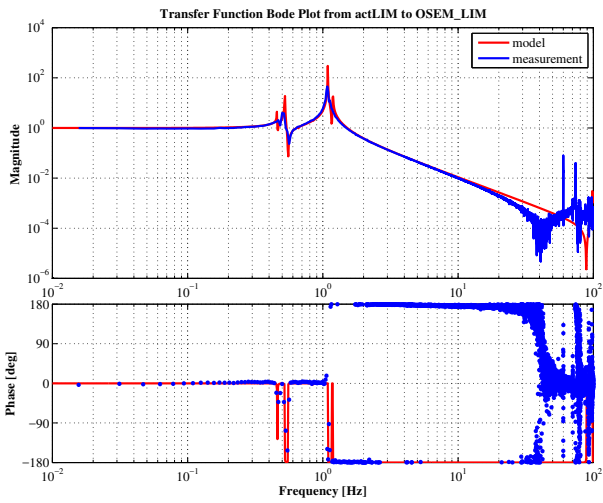
Figure 5.20: IM-OSEM (Longitudinal)
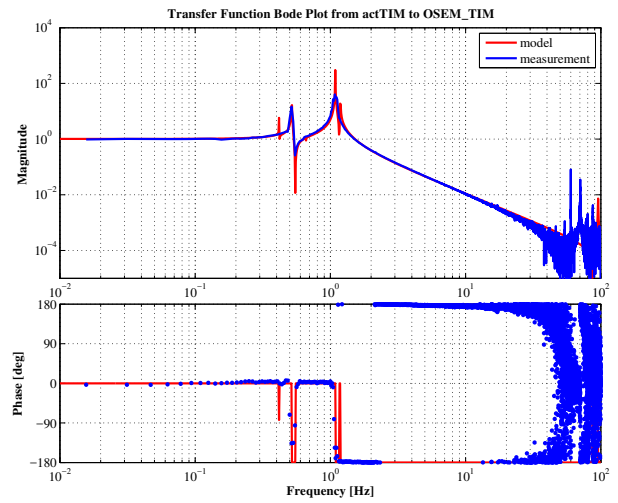
Figure 5.21: IM-OSEM (Transversal)
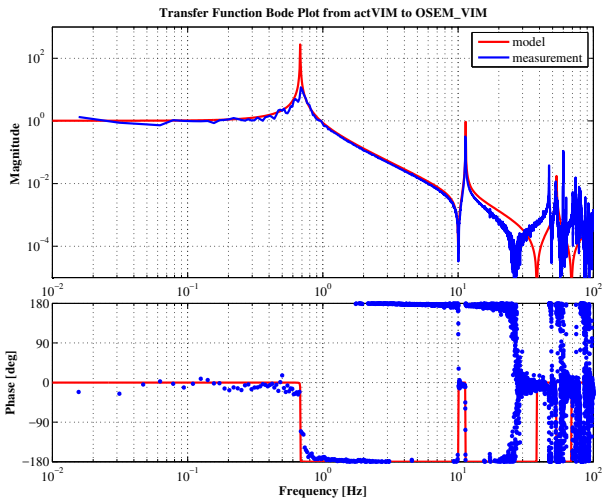
Figure 5.22: IM-OSEM (Vertical)
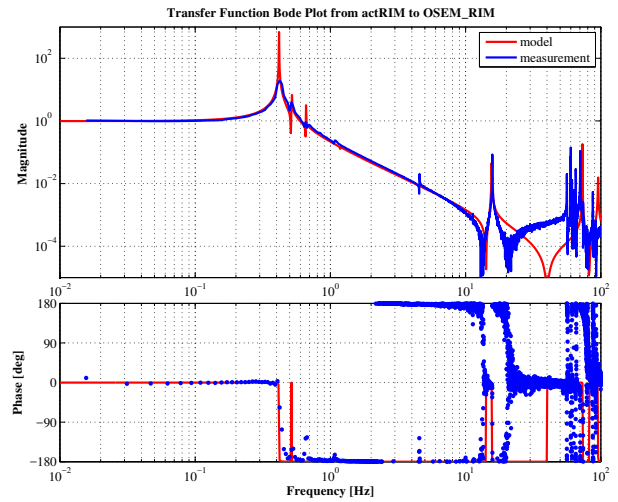
Figure 5.23: IM-OSEM (Roll)
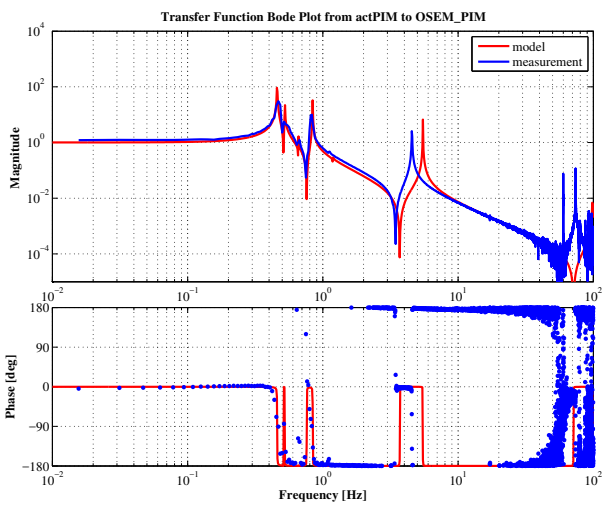
Figure 5.24: IM-OSEM (Pitch)
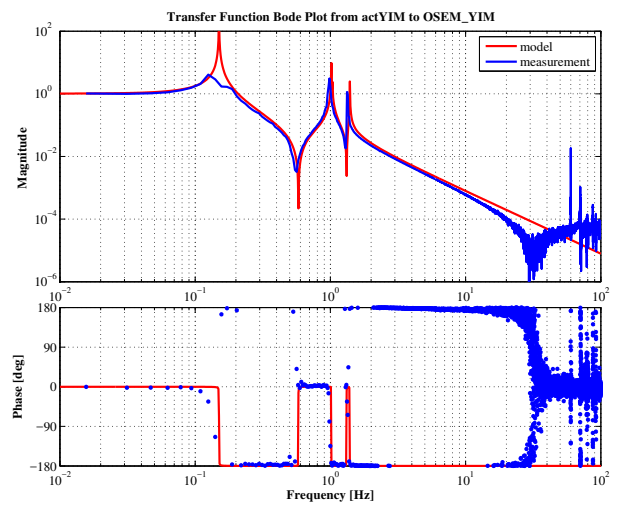


Figure 5.25: IM-OSEM (Yaw)
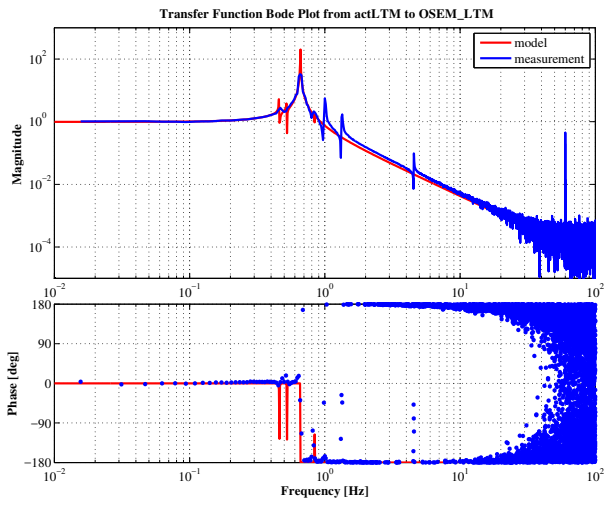
Figure 5.26: TM-OSEM (Longitudinal)
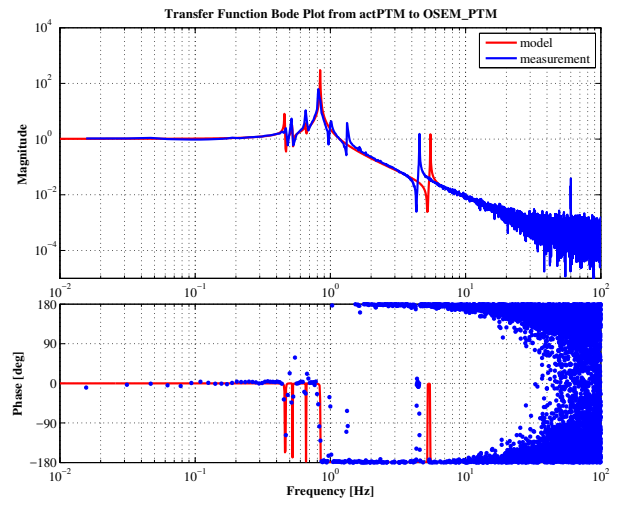

Figure 5.27: TM-OSEM (Pitch)
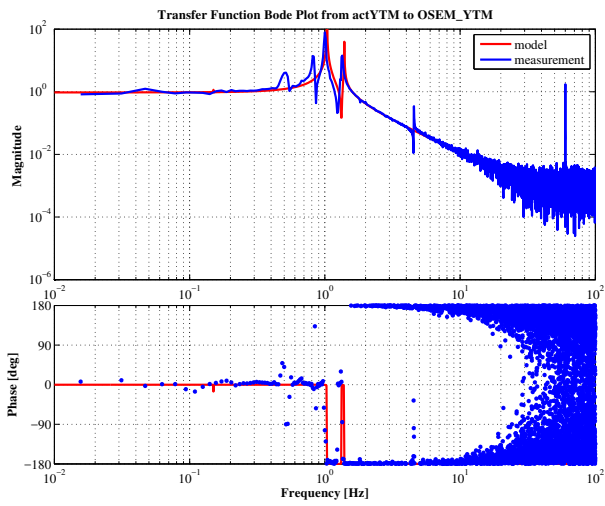
Figure 5.28: TM-OSEM (Yaw)

Couplings with other DoFs

This section notes the couplings between other DoFs seen in IM the transfer function measurements. The table 5.6 and table 5.7 shows the magnitudes of the coupling coefficients, obtained from amplitudes of the transfer functions, at a low frequency (30 mHz) and a high frequency (7 Hz).

	Sensor L	Sensor T	Sensor V	Sensor R	Sensor P	Sensor Y
Actuator L	1	0.009	0.003	0.019	0.007	0.006
Actuator T	0.025	1	0.031	0.009	0.016	0.016
Actuator V	0.036	0.032	1	0.121	0.059	0.003
Actuator R	0.053	0.102	0.037	1	0.066	0.004
Actuator P	0.046	0.080	0.050	0.119	1	0.035
Actuator Y	0.011	0.060	0.013	0.010	0.029	1

Table 5.6: Coupling coefficient in IM level at 30 mHz.

	Sensor L	Sensor T	Sensor V	Sensor R	Sensor P	Sensor Y
Actuator L	1	0.013	0.007	0.022	0.012	0.003
Actuator T	0.040	1	0.023	0.022	0.017	0.015
Actuator V	0.120	0.017	1	0.167	0.131	0.029
Actuator R	0.364	0.096	0.077	1	0.203	0.035
Actuator P	0.019	0.116	0.068	0.145	1	0.057
Actuator Y	0.013	0.090	0.030	0.053	0.028	1

Table 5.7: Coupling coefficient in IM level at 7 Hz.

Although the amplitudes of the non-diagonal transfer functions were lower than that of the diagonalized ones, some large couplings were measured especially in the couplings from the rotational (R, P, and Y) DoFs to other DoFs due to the uncompleted actuator diagonalization. The couplings to the longitudinal vibration could be a problem because they can cause the control noise coupling to the interferometer signals in the observation phase. Thus actuator diagonalization is needed for the bKAGRA operation.

5.4.3   Controls in the calm-down phase

This section focus on the implemented active control system in the calm-down phase. The servo filters were designed from the frequency responses from the implemented actuators and the sensors shown in above section. The servo filters were made only for the calm-down phase, since there was no need to take care about the control noise in the observation band (> 10 Hz). The requirements for the iKAGRA-PR3 SAS were to damp all the resonances, which disturb the operation of the Michelson interferometer, and to keep the angular fluctuation of the mirror with in 0.3 μrad in RMS.

Figure 5.29 shows the schematic control diagram in the calm-down phase. The damping controls are implemented at the IM level using OSEMs, while DC control was implemented on the BF vertical control with LVDT and coil-magnet actuator units. The resonances below 10 Hz were taken care in this control, since it was found that the resonances at 11 Hz and 15 Hz met the requirement of the decay time without active control. Also it was aimed at avoiding control instabilities due to those resonance peaks.
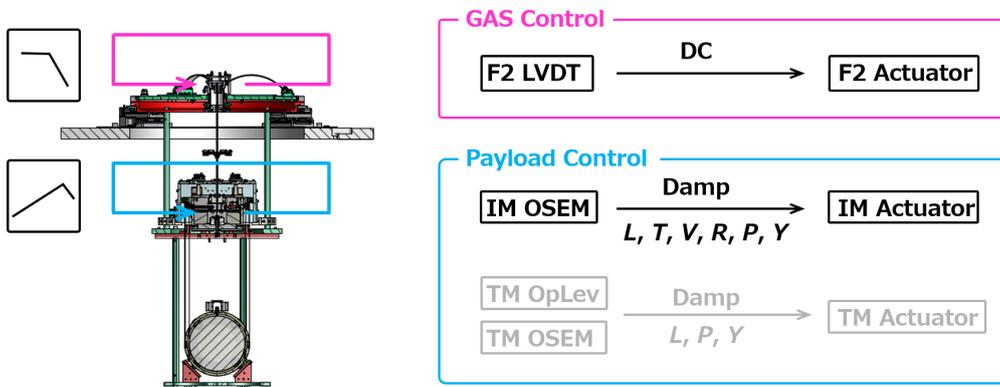

Figure 5.29: Control loops of the iKAGRA-PR3 SAS in the calm-down phase.

Servo filter design

Figure 5.30 to figure 5.31 show the implemented damping servo filters. The displacement signals monitored by virtual OSEM sensors and GAS-LVDT are converted into the velocities by using differential filters to obtain viscous damping force. Thence the servo gains were proportional to frequency f at $0.1 \sim 1$ Hz to suppress target mechanical resonances. The servo gains were cut off at around 10 Hz in order to suppress the peaks at around $0.1 \sim 2$ Hz. The converted signals were sent to the implemented actuators.
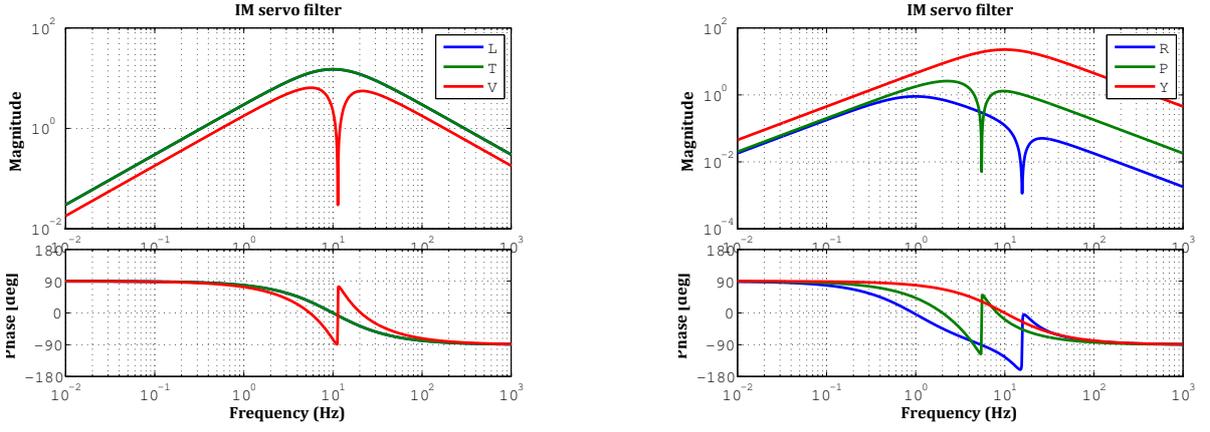
Figure 5.30: Servo filters for IM translational DoFs (*Left*) and for rotational (*Right*).
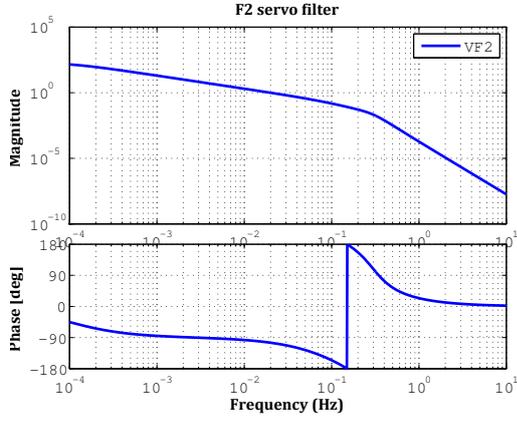
Figure 5.31: Servo filters for GAS filter.

Decay time measurement

Here, the damping performance of the control system in terms of $1/e$ decay time of the mechanical resonances. The requirement for the decay time is set at less than 1 minute in bKAGRA. The purpose of this measurement was to estimate the preciseness of the simulation.

The decay time measurement was conducted by following method. First, one target resonant motion was excited by using an appropriate virtual actuator with sinusoidal wave signal at the resonant frequency. Then, after the resonance was excited enough, the actuation was turned off and the decay signal was measured by built-in sensors. The measured decay signal was fitted by an exponential-decay sine wave function:

$$f(t) = A \exp\left(-\frac{t}{\tau_e}\right) \sin\left(2\pi f_0 t\right) + x_0, \tag{5.1}$$

where τ_e is the $1/e$ decay time. When it was difficult to excite only one resonant mode and beating signal was measured, the signals was fitted by two decay sine wave function:

$$f(t) = A_1 \exp\left(-\frac{t}{\tau_{e,1}}\right) \sin\left(2\pi f_1 t\right) + A_2 \exp\left(-\frac{t}{\tau_{e,2}}\right) \sin\left(2\pi f_2 t\right) + x_0 \tag{5.2}$$

87

These situation happened when some mechanical resonances exist with close resonant frequencies.

An example of measured decay signals is shown in figure 5.32 which were obtained from pendulum modes of IM. The *left* plot shows the decay signal without damping control, which is a superposition of mode #3 (0.47 Hz) and #5 (0.53 Hz). Fitting of the *left* curve was done with longer data than shown one, which was over the time between 0 and 120 sec. The *right* shows the decay signal mode #3 with damping control. The oscillation decayed faster when the damping control performed by a factor of more than 10 for the mode #3.
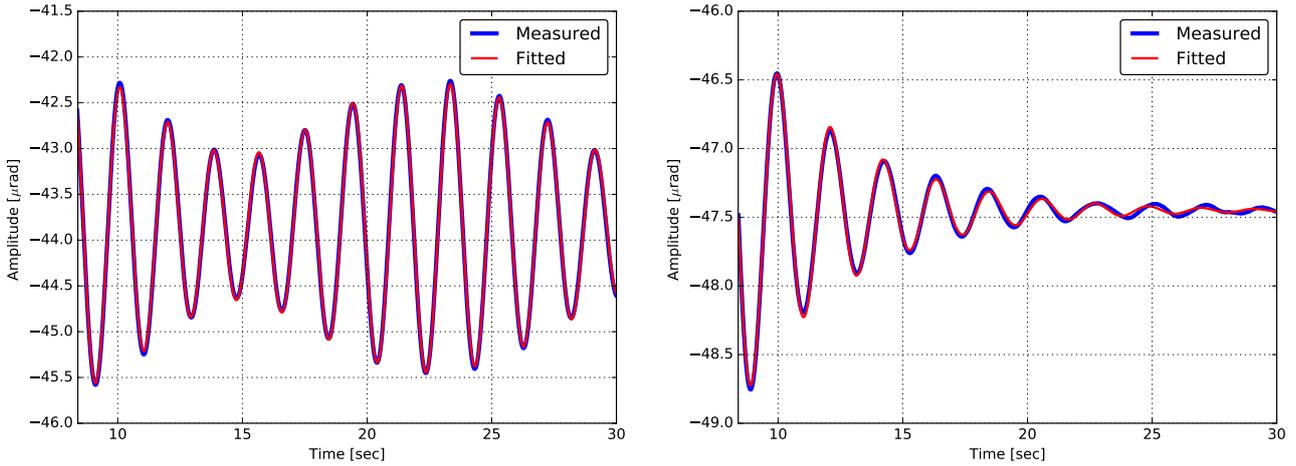
Figure 5.32: A example of measured decay signals. *Left* shows the signal from passive system of mode #3 and #5. *Right* describes the signal of mode #3 with active control. These signals are measured by the virtual pitch sensor at IM-OSEM. The measured frequencies and decay time without control were 0.46 Hz, 70 sec for mode #3 and 0.52 Hz, 91 sec for mode #5. Those with control were 0.47 Hz, 4 sec.

Table 5.8 and table 5.9 summarize the decay time for each resonances without and with active control respectively. It includes the resonance modes whose resonant frequencies are below 20 Hz. The decay time constants for each resonant frequency are plotted in figure 5.33. The *left* shows the measured result and the *right* denotes the simulated one.

According to the passive responses (blue) in these plots, the longest decay time of the passive system was in the order of 10^3 sec, while that of simulation was about 10^5 sec. The measured decay time at 11 Hz and 15 Hz were also shorter than the predictions by about one order of magnitude. Then, the current simulation for the passive mechanical response has large uncertainties for some resonances. One never know the actual passive Q factors, before they are measured, at this stage. Thence, the modeled passive mechanical Q factors of the passive suspension system have to be updated after measurement. This is because those passive Q factors are calculated from only information of each materials of the suspension system. On the other hand, the actual passive mechanical Q factors also depend on a friction at the suspension point and the effect of the cables. For more preciseness, one has to take into account such hanging condition into the simulation.

Concerning the decay time with the active controls, the measurement was consistent with the prediction. The resonance modes below 4 Hz which had long decay time were damped with the active control within 1 minute, except for 2 modes. According to the simulation, three resonances violate the requirement of the calm-down phase control for bKAGRA. About the three resonances above 4 Hz (at 4.6 Hz, 11 Hz, and 15 Hz), they were not actively controlled in this test, because

their decay time were already close to the requirement for the bKAGRA without control. This was also for avoiding instability of the control system. Thus those decay time were mostly same as the values without control. The resonances violating the requirement were the modes related with relative motion between the TM and RM, in longitudinal and yaw direction. Since monitoring the TM motion is needed to damp the two TM resonances and no sensors and actuators at TM level was used for this control, they were not damped enough. About the mode #7, which is the relative motion between TM and RM in transversal DoF, it was found that its damping time did not exceed 1 minute. This result differed from the simulation and expected to violate the requirement. Originally, this mode does not disturb the lock of the interferometer unless the amplitude gets larger than 1 mm and thus there is no problem if the decay time of this mode exceed the requirement of 1 minute. This reduction of the decay time might be caused by the aluminum sheet, which was inserted between the TM wire and TM. The sheet increased the friction at the suspension point and then might lead the shorter decay time.

Consequently, it was confirmed that if the local sensor for TM is available, it is expected that all the resonances which disturb the interferometer operation are suppressed within the requirement. The current prediction without active control should be fed back with measurement. On the other hand, that with control system gives prediction which is consistent with actual responses.

| #Mode Number | Frequency [Hz] | | Difference [%] | decay time [sec] | Q factor | exc. point |
	Simulated	Fitted				
#1	0.155	0.143	7.7	645	289	YIM
#2	0.430	0.427	0.7	43	58	RIM
#3	0.470	0.464	1.3	71	103	LIM
#4	0.520	0.517	0.6	222	361	TIM
#5	0.527	0.526	0.2	91	150	LIM
#6	0.659	0.661	0.3	268	557	LTM
#7	0.660	0.661	0.2	214	445	RIM
#8	0.680	0.681	0.1	16	35	VBF
#9	0.844	0.825	2.3	121	313	PIM
#10	1.029	0.980	4.8	698	2150	YIM
#11	1.036	1.000	3.5	398	1251	YIM
#12	1.099	1.069	2.8	219	735	TIM
#13	1.099	1.077	2.0	199	673	LIM
#14	1.185	1.110	6.3	366	1275	TIM
#15	1.185	1.110	6.3	357	1245	LIM
#16	1.391	1.342	3.5	1104	4655	YIM
#17	5.494	4.556	17	73	1051	PIM
#18	11.37	11.32	0.4	37	1324	VIM
#19	15.58	15.77	1.2	57	2826	RIM

Table 5.8: Measured resonant frequencies and decay time without damping control. The Q factors are converted from decay time τ_e by $Q = \pi f_0 T_e$.

#Mode Number	Frequency [Hz] undamped	damped	difference [%]	decay time [sec]	Q factor	exc. point
#1	0.143	0.140	2.0	5	2.1	YIM
#2	0.427	0.447	4.6	1.1	1.5	RIM
#3	0.464	0.470	1.5	4	6.4	PIM
#4	0.517	0.538	4.0	12	20.5	TIM
#5	0.525	0.510	2.9	12	19.4	LIM
#6	0.661	0.661	0	129	268	LTM
#7	0.661	0.655	0.9	24	50.1	RIM
#8	0.681	0.705	3.5	2.6	5.8	VBF
#9	0.825	0.831	0.7	9.8	25.6	PIM
#10	0.980	0.994	1.4	2	6.2	YIM
#11	1.000	0.998	0.2	174	546	YIM
#12	1.069	1.057	1.1	1	2.5	TIM
#13	1.077	1.053	2.2	1.0	3.46	LIM
#14	1.110	1.115	0.5	1	3.7	TIM
#15	1.110	1.190	7.2	0.8	2.96	LIM
#16	1.342	1.341	0.01	9.2	38.9	YIM
#17	4.556	4.562	0.13	24	350	PIM
#18	11.32	11.33	0.04	53	1889	VIM
#19	15.77	15.76	0.01	37	1846	RIM

Table 5.9: Measured resonant frequencies and decay time with controls.
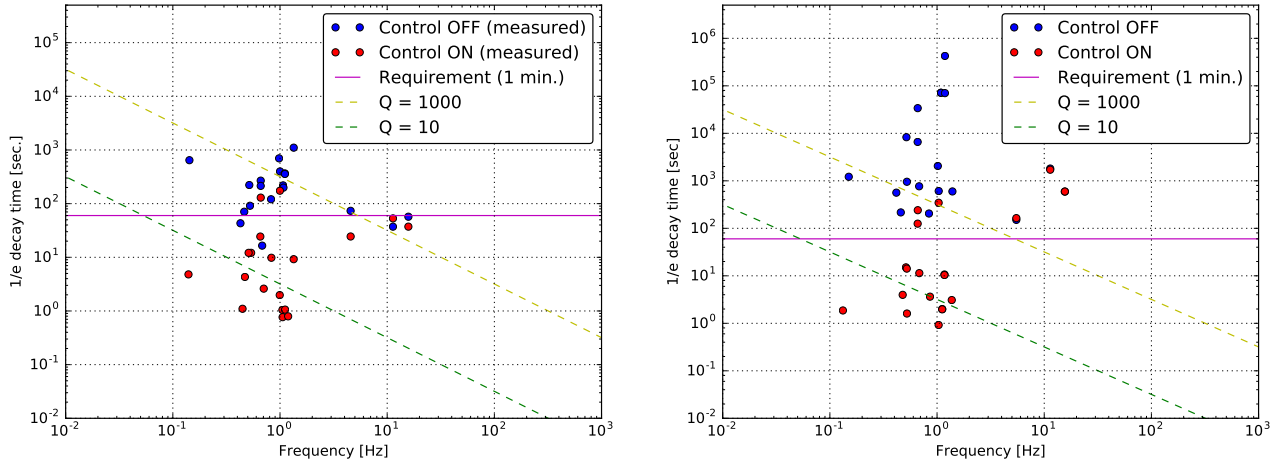
Figure 5.33: $1/e$ decay time for each mechanical resonances of the iKAGRA-PR3 SAS with and without active control at below 20 Hz. *Left* shows the measured result. *Right* expected result according to simulation.

Residual vibration spectra

The angular vibrations of the test mass measured by the optical lever are shown in figure 5.34. The *left* shows its pitch motion and the *right* shows the yaw motion, when the suspension system is calmed down in vacuum. It was confirmed that the angular vibration met the RMS requirement of the iKAGRA. The vibration signals were buried into the noise of the optical lever, except for the peaks. Table 5.10 describes RMS angular vibration after the suspension system calms down.
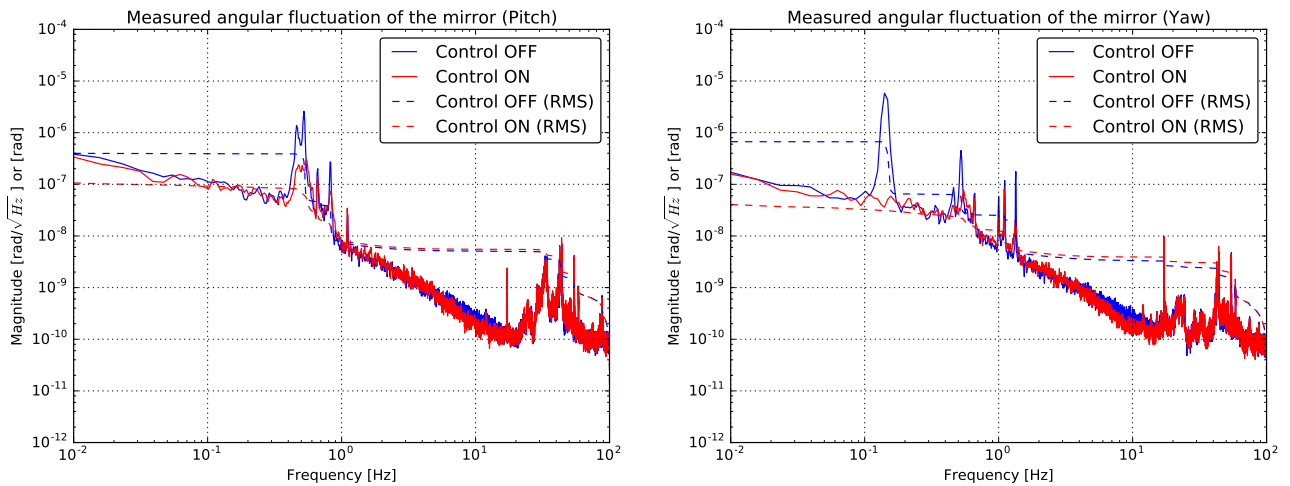
Figure 5.34: Measured spectra of TM angular motion in pitch (*left*) and yaw (*right*) DoFs.

DoF	Requirement [μrad]	Measurement [μrad]
(Residual) pitch	−	0.37
(Residual) yaw	−	0.63
(Controlled) pitch	0.3	0.10
(Controlled) yaw	0.3	0.04

Table 5.10: RMS angular vibration after the suspension system calms down. The pitch and yaw motion of the requirement of iKAGRA and the measurement are described in each column.

Comparison with prediction

Figure 5.35 compares the measurement and prediction of the vibration spectra in pitch direction. It includes the predicted and measured pitch vibration of the test mass with and without the active control. For this simulation, measured seismic vibration shown in figure 5.16 (KAGRA site NS) was supposed. Since noise from the optical lever is dominant except for the region of $0.4 \sim 1.5$ Hz, the comparison focuses on those frequencies. The measured resonant frequencies are well fit with the prediction, while, the measurement had different spectra from the prediction, especially below at 0.6 Hz. The plot implies following:

- The seismic vibration when the angular vibration was measured, might be smaller than the measurement shown in figure 5.16 at $0.2 \sim 0.6$ Hz. This is because the date of the seismic vibration measurement and the angular motion measurement, was different from that of the seismic measurement. Since the seismic vibration contributes to the spectra at around 0.2 Hz, one has to input the specific seismic vibration on the measurement date, for more precise prediction.

- Contribution of the asymmetry in the mechanical suspension system also might be taken account into the simulation for further preciseness. This simulation supposed that the suspension components are suspended optimally. However, shift of suspension points from the optimal positions should be happened in the actual system and this also contributes the difference by inducing coupling vibrations from other DoF motions. Thence, effect of the position between the center of mass position and the suspension position might be considered for more precise prediction.

- In order to obtain more realistic RMS values from the simulation, one has to fed back the experimental results into the model after the assembly. Table 5.35 notes that simulated and measured RMS angular vibration of the test mass in pitch direction.

DoF	Simulation [μrad]	Measurement [μrad]
(Residual) pitch	4.4	0.37
(Controlled) pitch	0.7	0.10

Table 5.11: Expected RMS values in the calm-down phase. The longitudinal, vertical, pitch displacement, and longitudinal velocity of the mirror are described in each column.

Consequently, the simulation predicts the actual resonant frequencies but tend to fail telling the precise RMS and detailed spectra except for the peaks. To acquire the more realistic prediction for them, one has to use specific seismic vibration and has to consider asymmetries caused by the assembly. However, for designing the active control systems, the calculation not only supposes high noise level

seismic vibration, which has larger micro-seismic peak but also tends to assume higher mechanical Q factors than actual ones. Then, if the prediction with these worst-case assumptions meets the RMS requirements for the active control systems, the actual systems should meet the RMS requirement with larger margin, in most case.
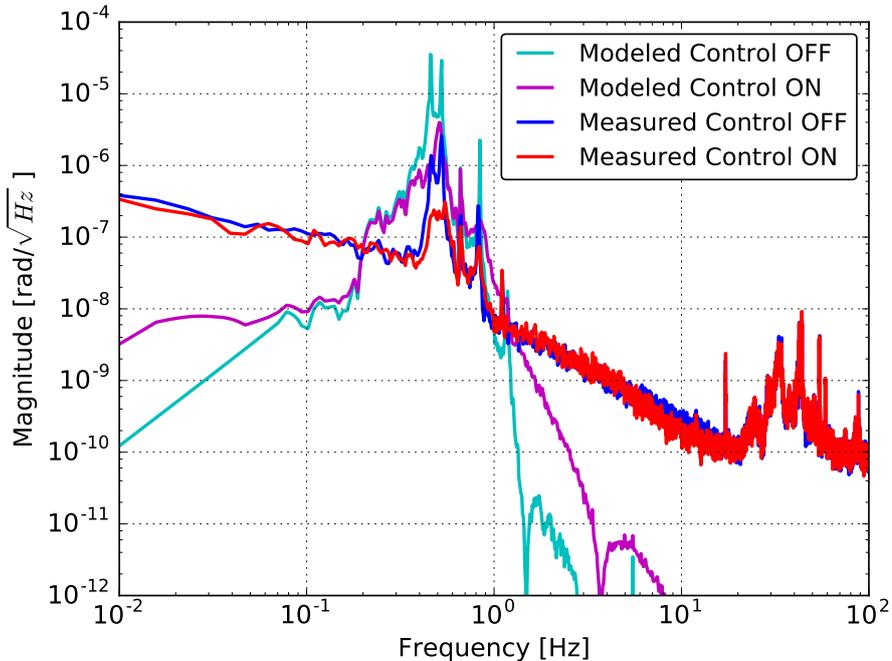

Figure 5.35: Comparison between the measurement and prediction of pitch vibration of the test mass.

5.5   Mechanical response of KAGRA-SAS

Passive mechanical frequency responses are described in terms of residual vibration of the test mass, mechanical Q factors of each suspension system.

So far two KAGRA-SAS has been assembled including this iKAGRA-PR3 SAS. First one was the type-B prototype SAS which was assembled and tested in the TAMA site [42]. The two SASs had mostly same mechanics for their payload and thus the frequency responses of the payload was expected to be same.

Residual angular vibration

The angular residual vibrations after the system calms down are described in this section. The comparison of the angular motion between the iKAGRA-PR3 SAS and tyep-B1 prototype SAS are shown in figure 5.36. According to the results, it was confirmed that the measured vibration of the iKAGRA-PR3 SAS at the KAGRA site were lower than those of the type-B prototype SAS by around one order of magnitude in all the frequencies. The RMS angles of the typeBpp SAS were also smaller than those of the type-B prototype as shown in table 5.12.

The reduction in the type-Bp SAS at around 0.2 Hz might come from the difference of the seismic vibration between the TAMA site in Tokyo and the KAGRA site in Kamioka. This is because the vibration at KAGRA site is smaller than that of the TAMA site in these frequency region by factor

of one or two order of magnitudes. Also the discrepancies between the suspension position and the center of the mass position might lead the reduction. The discrepancies at higher frequencies above at 1 Hz might be caused by the difference of the used power supply, since it depends on the noise of the optical lever.

Note that the shift of the 2 peaks at around 0.5 Hz in the pitch motion shown in the iKAGRA-PR3 SAS is caused by the difference of the height of the suspension point of the intermediate mass. Those resonant frequencies largely depend on the moment of inertia of the intermediate mass.

Concerning the yaw motion, coupling coefficients between amplitudes of the horizontal seismic vibration and test mass yaw motion were measured as follows: 15 rad/m for the type-B prototype SAS at the TAMA site, 4 rad/m for the iKAGRA-PR3 SAS at the KAGRA site in RMS. These values are calculated by using the plots shown in figure 5.16 and figure 5.36. Even though one has to collect more information about this coupling from horizontal to yaw motion, it is expected that the horizontal seismic vibration might couple to the test mass yaw motion with around 10 rad/m in RMS without active controls in the KAGRA-SAS. If one is able to damp the resonant peak of yaw motion at 0.15 Hz, the coupling is expected to be reduced by about one order of magnitude: ~ 1 rad/m in RMS.
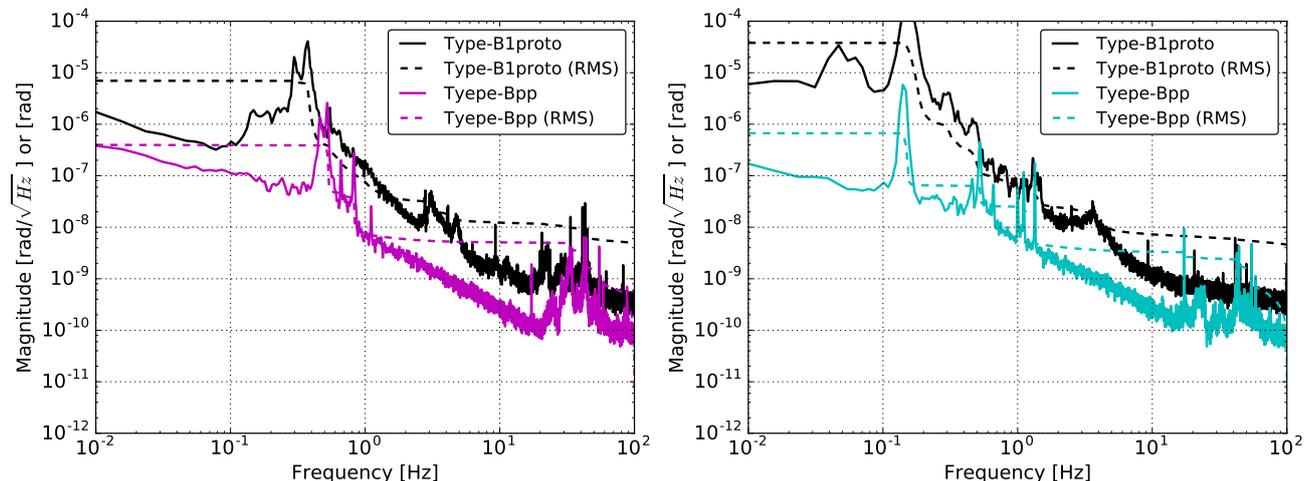
Figure 5.36: Residual pitch (*left*) and yaw (*right*) motion of the measured by optical lever at TM level. These plots show the TM motion suspended by the type-B prototype SAS (black), and that suspended by the typeBpp SAS (magenta and cyan). The signals of the type-B prototype were measured at TAMA site, while those of iKAGRA-PR3 SAS were observed at KAGRA site.

	pitch [μrad]	yaw [μrad]
Type-B proto	7.0	37
iKAGRA-PR3	0.4	0.6

Table 5.12: measured residual angular motion.

Mechanical Q factors of KAGRA SAS

Figure 5.37 shows the decay time of the mechanical resonance of the type-B prototype SAS and the iKAGRA-PR3 SAS without active controls. The *left* plot shows the measured response and the *right* denotes the simulated one. According to the plots below 20 Hz, the lower limit of the measured

mechanical Q factors is around 1 and is mostly same as that of the prediction. On the other hand, the measured upper limit is much lower than simulated one by about 2 orders of the magnitude. Based on the results, the mechanical Q factors of the KAGRA-SAS below at 20 Hz might be suppressed at 5×10^3. Thence, it might be helpful to set the maximum value at $Q \sim 10^4$.

Note that in order to set the upper limit on the mechanical Q factor more in detail, one has to gather more information of the assembled KAGRA-SAS. The upper limit of the Q factor largely depends on the resonances related to the test mass motion. However, the test mass of the iKAGRA-PR3 SAS had an aluminum sheet at the suspension point and it might affect reducing the mechanical Q factors, compared to the designed system. Thence, it might not be reliable that setting the upper limit of the mechanical Q factors of the KAGRA-SAS based only on these results. In order to feedback the information into the simulation model, one needs to collect more information about the mechanical Q factors of the KAGRA-SAS.
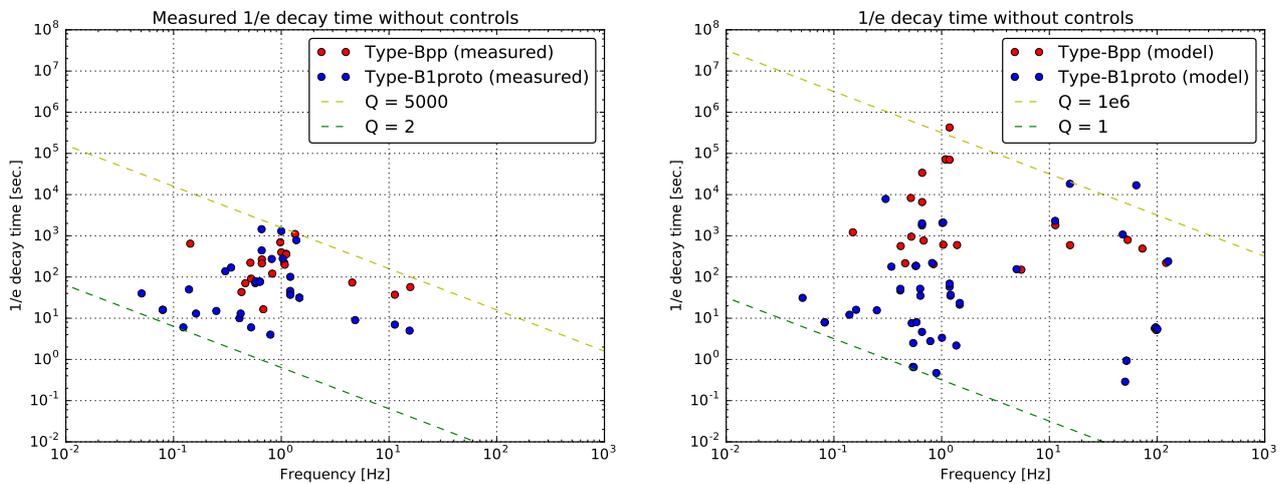
Figure 5.37: Decay time constants of the mechanical resonances without the active control. *Left* plot shows the measured results and *right* plot shows the simulated ones.

5.6   Modification for bKAGRA

Above sections describe characterization of the iKAGRA-PR3 SAS in iKAGRA. For the bKA-GRA, however, one more GAS filter needs to be added into the iKAGRA-PR3 SAS, to achieve the requirement for the displacement vibration of the PR mirror. Figure 5.38 shows the expected vibration isolation performances of the iKAGRA-PR3 SAS, type-Bp SAS and the requirement for the PR mirror in bKAGRA.

However, it was also found that the type-Bp SAS did not have a system to damp the main pendulum motion, which contributes to the RMS velocity a lot, in the original design. The type-Bp system failed to avoid the violation the requirement for velocity of the TM to lock the interferometer, as it was. The expected spectra of the test mass velocity in the longitudinal direction is shown in the *left* plot of figure 5.38. The *right* figure draws the resonant mode shape whose resonant frequency is at 0.45 Hz. These simulated results implied that a damping system for the resonance motion to should be equipped. The considered options are following two ones:

- Implement new damping system at BF level. It is aimed at damping the horizontal motion at around 0.45 Hz of the BF.

- Implement inverted pendulum system at top stage. It is aimed at damping the resonant modes at 0.45 Hz by adding an oscillator whose resonant frequency is lower than 0.45 Hz. By using the inverted pendulum system, one can also damp the resonances by monitoring the top stage on the inverted pendulums.

According to the simulation, it was conformed that both the option met the requirements about the damping control system and the control in the observation phase. Consequently, the option of the new damping system for the BF is adopted for the bKAGRA PR-SAS. This is because the option of the inverted pendulum system needs a lot of costs, compared to the new damping system. The details about the upgraded suspension performance for the power recycling KAGRA-SAS is summarized in chapter 6.
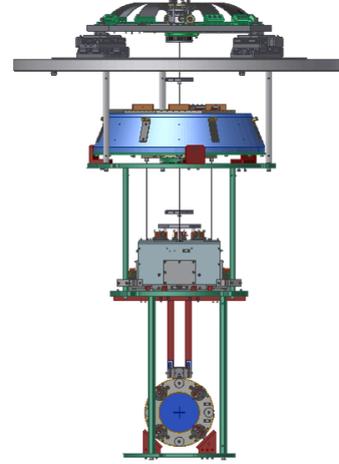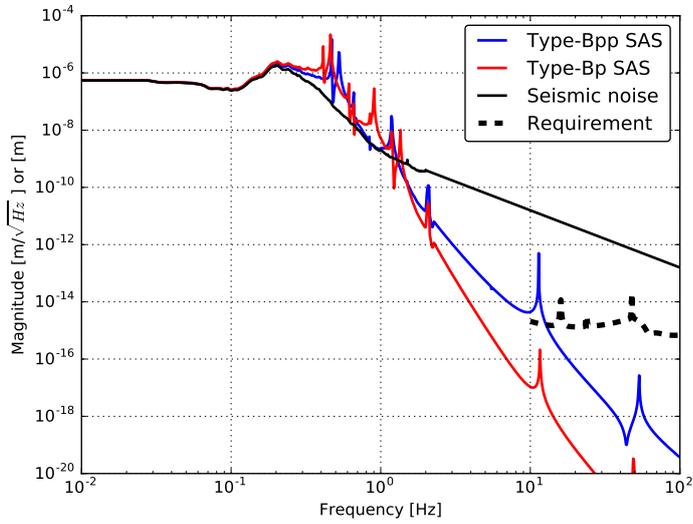
Figure 5.38: The simulated vibration isolation performances of the iKAGRA-PR3 SAS (blue), and that of the type-Bp SAS (red) without active controls. The ground displacement (black) and the requirement (dashed-black) are also shown in this plot. By adding one more GAS filter into the iKAGRA-PR3 SAS, the system is able to meet its requirement.
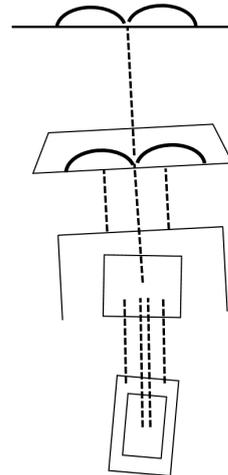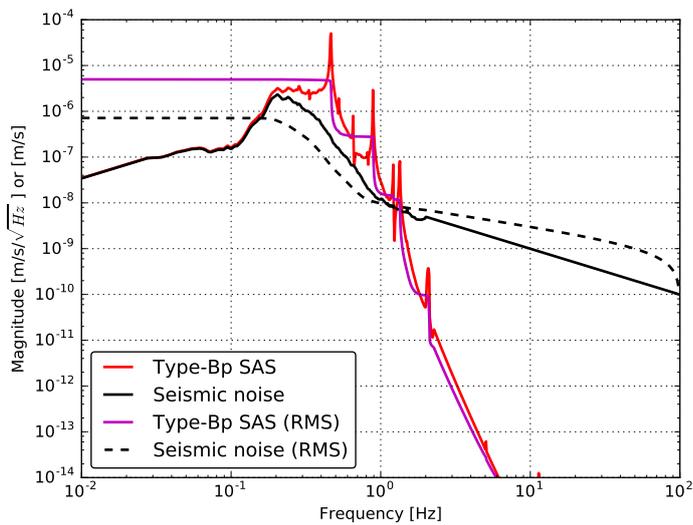

Figure 5.39: Expected mirror velocity of the type-Bp SAS without active controls. The right figure shows one resonant mode of the original type-Bp SAS which contributes to the RMS velocity. The original type-Bp SAS had no damping system for the resonance.

5.7   Conclusion

The first assembly and performance test of KAGRA SAS were conducted at the KAGRA site in the Kamioka underground.

It is found that the seismic motion of KAGRA site is slightly different from that of CLIO site. The seismic motion of KAGRA site might have a shallow peak at around 2 or 3 Hz, which is not measured at the CLIO site. Since, the data of the KAGRA site was measured with short-time data, the details should be investigated by using long-term data.

The test of the prediction of the mechanical suspension system and the active control system is summarized as follows:

- About the frequency response of the mechanical suspension system, simulation predicts actual resonant frequencies below at ~ 20 Hz. It tends to fail to predict the precise resonant frequencies of bounce modes and violin modes.

- About the passive response, the predicted mechanical Q factors tends to fail to fit with the actual ones. In order to acquire more actual values from the simulation, one has to feedback the experimental information to the model. According to this measurement, the upper limit of the mechanical Q factors of the KAGRA-SAS might be suppressed at $Q \sim 10^4$. The details of the passive Q factors are to be investigated by investigating KAGRA-SAS which are to be assembled in the near future.

- About the active control system, the predicted responses with the active controls are consistent with actual responses, according to the Q factors of the mechanical resonances. The predicted RMS values with controls tend to be larger than the actual system by one order of magnitude. For more precise predictions, one has to measure seismic vibration during the measurement period. One also might consider mechanical asymmetry of the suspension system, which induce vibrations from other DoFs.

Consequently, it is confirmed that the simulation works for the designing the active control systems for the suspension system. It tends to give larger RMS values than the actual ones. To get more precise predictions, one might have to take care of the uncertainties due to mechanical assembly. Note that in order to test the predictions at higher frequencies than 1 Hz, one needs more sensitive sensors. This test is to be conducted in the bKAGRA period by using the interferometer signals.

Local control system for type-Bp SAS in bKAGRA

Chapter 6

As described in the previous section, the suspension system for the PR mirrors are upgraded toward bKAGRA from that was used in the iKAGRA period. This new system is called type-Bp SAS, and three of them are to be installed at the site. This chapter describes the type-Bp SAS system, its controllability, and the expected performance.

6.1   Overview

The mechanical overview of the iKAGRA-PR3 SAS and the type-Bp SAS are shown in figure 6.1. The type-Bp SAS has two GAS filters to reduce coupling level from vertical to longitudinal vibration at higher frequency than 10 Hz. One recoil mass is also added at BF level with some sensor and actuator units called BF-LVDTs. It is suspended from beneath of the SF. This BF recoil mass (BR) system is aimed at damping main pendulum resonant modes by monitoring relative motion between the BF and the BR.

iKAGRA-PR3 SAS   **Type-Bp SAS**
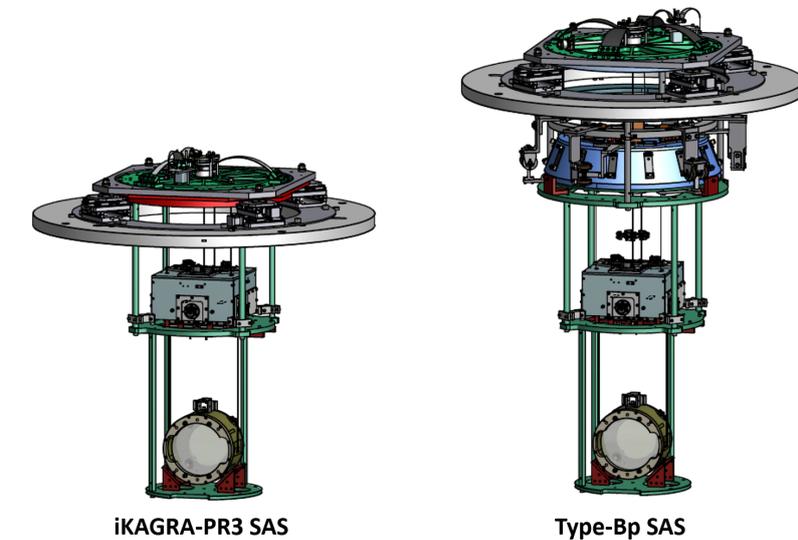
Figure 6.1: Mechanical overview of the iKAGRA-PR3 SAS (*left*) and the type-Bp SAS (*right*). In the type-Bp SAS, one GAS filter and a recoil mass for the bottom GAS filter are added into the iKAGRA-PR3 SAS.

In addition, OSEM units are modified for risk reduction. For the IM-OSEM units, gap between LED and photo diode in IM-OSEMs are widened. While for the TM-OSEM units, the implemented sensors are removed from the type-Bp SAS and their long flags are replaced into shorter ones. Thence the type-Bp SAS has only optical length sensor and optical lever as the test mass sensing system. Actuation system at test mass level by TM-OSEMs remains.

This chapter focus on detailed mechanics of the type-Bp SAS and its active control system in each phase. Chapter 6.2 describes the detailed mechanical design of the type-Bp SAS. The newly added sensor and actuator units are explained in chapter 6.3. Chapter 6.4 presents the expected vibration isolation performance of the type-Bp SAS with active control system, and the control noise couping into the test mass.

6.2   Mechanics

This section explains the mechanics of the suspension system and the related structures. Most of the environment is same as that of the iKAGRA-PR3 SAS. Thence, this section especially focuses on the newly modified points. The suspension system is inside the vacuum chamber, and is surrounded by the extended security frame. The base of the suspension system is located on the inner frame inside the vacuum chamber. The inner frame stands on the ground.

6.2.1   Suspension system

The detailed type-Bp suspension system is shown in figure 6.2. The suspension system of the payload is same as that of iKAGRA-PR3 SAS. The payload includes the test mass (TM), the recoil mass (RM), the intermediate mass (IM), and the intermediate recoil mass (IR). The BF and the payload are suspended from above system by single wire. The BF recoil mass (BR) is suspended from base of the standard GAS filter(SF) by three maraging rods. The suspension wire connecting the components above the IM are made of maraging steel. In the type-Bp SAS, the SF is supported by the traverser which conducts initial position alignment. the traverser stands on the top surface of the inner frame.
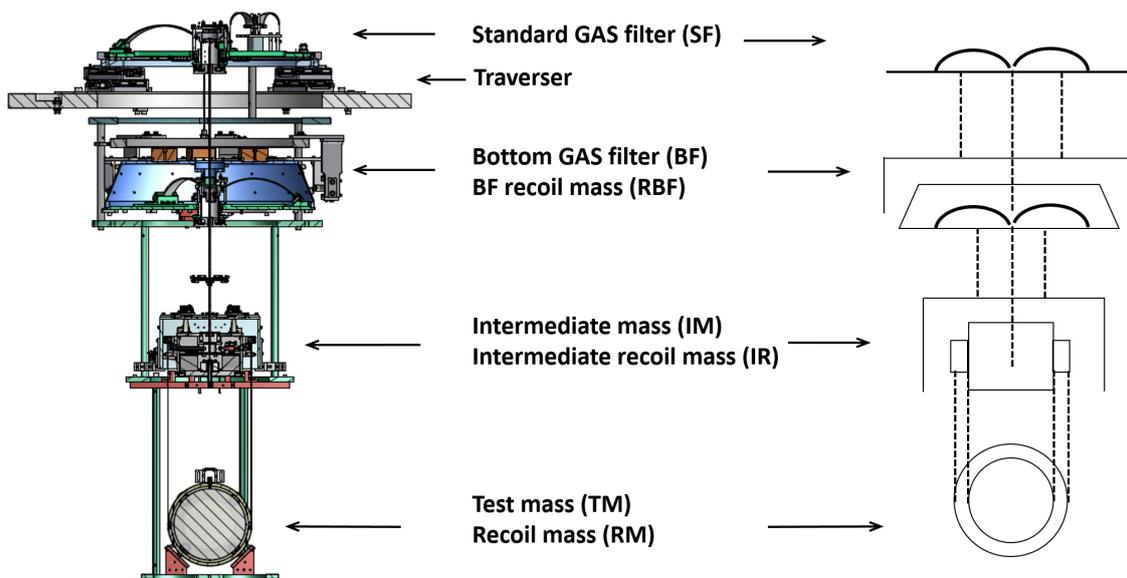
Figure 6.2: Overview of the type-Bp SAS.

6.2.2   Security frame

A metallic frame surrounds the suspension system as well as the iKAGRA-PR3 SAS and is called security frame. The purpose of the security frame is to avoid that the suspension system gets damaged during transportation. The security frame for the type-Bp SAS is extended from the ones which was used for the iKAGRA-PR3 SAS. It is suspended from the underneath of the standard GAS filter. The frame was designed so that its structural resonant frequencies are higher than those of the suspension system.

6.3   Sensors and actuators

The actuators for initial alignment, and the sensors and actuators for the active controls are explained in this subsection. The motors which are used for the initial alignment of the suspension system is turned off during the observation, to avoid introducing external electromagnetic noises as well as the case of the iKAGRA-PR3 SAS. The implemented sensors and actuators are summarized in table 6.1 and table 6.2.

6.3.1   For initialization

Initial alignment systems implemented below IM are same as those which were used in the iKAGRA-PR3 SAS. Above the BF, one tilt aligning system is added on the BF cap.

Tilt aligning system

The bottom GAS filter has moving masses and picomotors which are connected each other by a coil spring. They are set on the surface of the BF cap. This system adjust relative position between the intermediate mass and the its recoil mass by changing the tilt of the bottom filter as shown in figure 6.3.
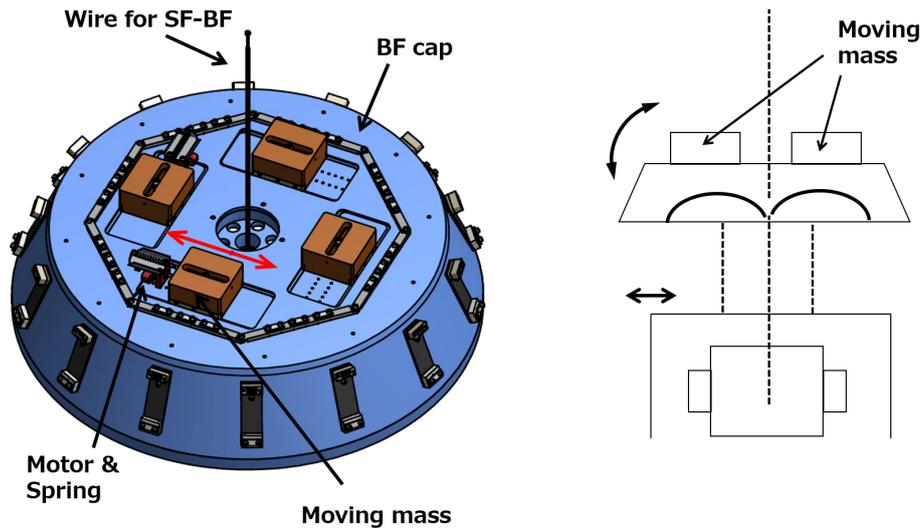
Figure 6.3: Overview of tilt aligning system at BF (*left*). *Right* figure shows the behavior of the BF, IR, and IM. Moving mass on the BF cap adjusts the gap between the IR and IM.

Position	Name	Actuated DoFe	Main purpose
Inner frame	Traverser	LF1, TF1, YF1	Horizontal positioning of TM
F1	Motorized spring	VF2	Relative positioning of BF and BR
F2	Motorized spring	VIM	Relative positioning of IM and IR
	Moving mass	RIM, PIM	Relative alignment of IM and IR
	Rotation mechanism	YIM	Relative alignment of IM and IR
IM	Moving mass	RIM, PIM	Alignment of TM in pitch and roll

Table 6.1: Actuators for initial positioning and alignment of the type-Bp SAS.

6.3.2   For active controls

Sensors and actuators for active controls in the type-Bp SAS are described in table 6.2. The GAS-LVDTs and coil-magnet actuators are implemented on the keystone of the GAS filters in vertical direction in order to compensate the thermal drift of the GAS filters. The BF-LVDTs and coil-magnet actuators are implemented on the bottom GAS filter stage in order to damp the main pendulum motion, which cannot be damped by the payload damping actuation. The OSEM units are implemented on the IM and TM for damping of mechanical resonances of the payload by active controls. An optical lever and a wave front sensor is to be set to monitor the alignment of the TM in yaw and pitch DoF. The sensor noises shown in this subsection (figure 6.9) are used for the following calculation.

Concerning the BF-LVDTs and OSEMs, the sensed signals are converted to a certain DoF digitally by linear combination and then they are sent to the virtual actuators. The conceptual procedure is summarized in figure 6.10.

Position	Name	Sensed/actuated DoF
F1	GAS-LVDT+Act	VF2-VGND
F2	GAS-LVDT+Act	VIM-VF2
	BF-LVDT+Act	LBF-LBR, TBF-TBR, VBF-VBR
		RBF-RBR, PBF-PBR, YBF-YBR
IM	wide cavity OSEM	LIM-LIR, TIM-TIR, VIM-VIR
		RIM-RIR, PIM-PIR, YIM-YIR
TM	Optical sensor	LTM, PTM, YTM

Table 6.2: Sensors and actuators for active controls of the type-Bp SAS.

GAS-LVDT

Sensing and actuating system for the keystones on the GAS filters are same as the ones explained in previous section. In the type-Bp SAS, two of GAS-LDVT and coil-magnet actuator units are implemented at SF and BF.

BF-LVDT

Newly designed LVDT and coil-magnet actuator units are implemented into the bottom GAS filter stage. Figure 6.4 shows the mechanical overview of the prototype unit and the designed implementation in the suspension system. The units are aligned in the pin-wheel configuration so that the units can sens and actuate in 6 DoFs, as illustrated in figure 6.4.

The measured sensor noise level of BF-LVDT prototype was about $10^{-8}\mathrm{m}/\sqrt{\mathrm{Hz}}$ at 10 Hz. It was confirmed that the BF-LVDT can meet the requirement of the active controls with low control noise coupling in the observation phase, according to the measurement. Its linear range of the sensor was measured 15 mm in its axial direction. The more details are discussed in [51].

Wide cavity OSEM

The OSEMs are implemented only into the intermediate mass stage in the type-Bp SAS. The gaps between the LED and the PD is also widen by 10 mm compared with the OSEMs of the iKAGRA-PR3 SAS. The gap of the wide cavity OSEM is 15.1 mm. The difference of the gap compared with the original OSEM is illustrated in figure 6.6. This is aimed at reducing the risk to damage the optics. The linear range of the sensor in longitudinal direction is about $\pm$ 0.5 mm. It was confirmed that the sensor
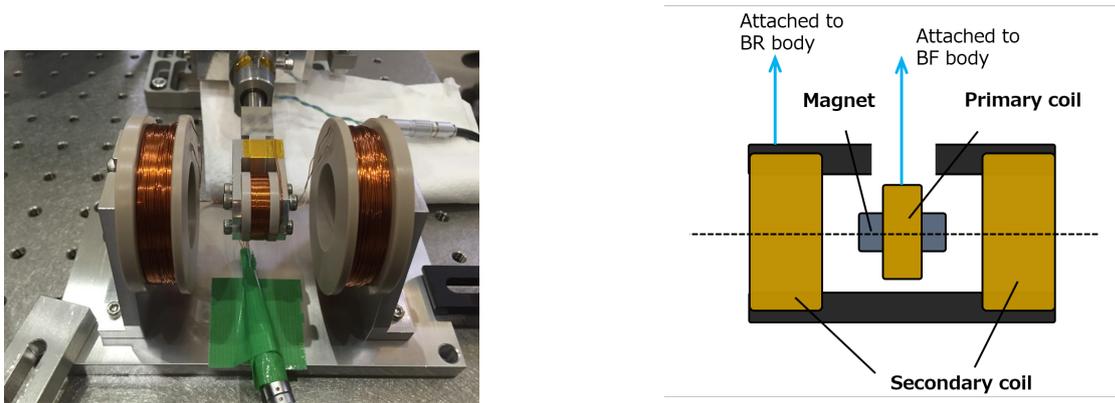
Figure 6.4: Overview of BF-LVDT system. *Left* picture shows the setup of the prototype measurement of the BF-LVDT unit. *Right* figure illustrates the schematic view of the system. The BF and the BR denote the bottom GAS filter and the Bottom GAS filter recoil mass respectively.
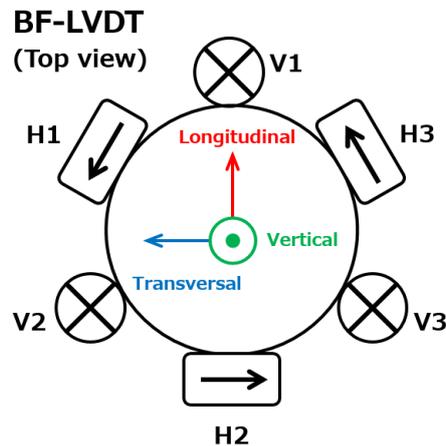

Figure 6.5: Location of the BF-LVDT in the suspension system.

linear range was able to be set as same as that of original OSEM if the output voltage was changeable, according to a prototype measurement. In the wide cavity OSEM system, the flags do not touch to the body of the wide cavity OSEMs unless the intermediate mass turns about ± 20 mrad in pitch and yaw direction comparing to its recoil mass. It was also confirmed that the couplings from other DoFs into longitudinal sensing is negligible around the optimal position in a previous measurement [49]. The positions of the IM-OSEM units are shown in figure 6.7. Figure 6.10 shows the conceptual control loops by the BF-LVDTs and IM-OSEMs.

TM OSEM actuator

In the type-Bp SAS, sensing system in the TM-OSEM is removed by replacing the OSEM flag to shorter one, which is called stab OSEM flag. This is also aimed at reducing the risk to damage the optics. The difference of the TM stage system is illustrated in figure 6.8. In the type-Bp suspension system, the OSEMs are aimed at only actuating the mirror motion compared with its recoil mass. The location of the TM-OSEM actuators are shown in figure 6.7.

**narrow cavity OSEM**   **Wide cavity OSEM**
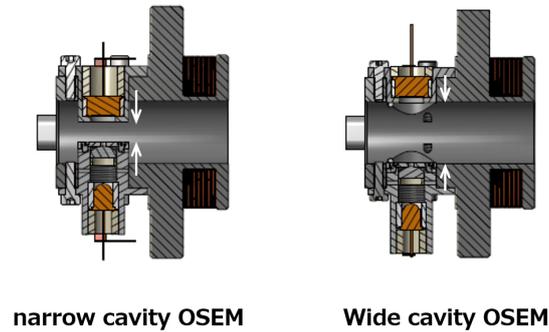
Figure 6.6: Overview of the OSEM in iKAGRA-PR3 SAS (*left*, 'narrow cavity OSEM') and that in the type-Bp SAS(*right*, 'wide cavity OSEM'). The gap is widen by 10 mm and the gap of the new system is 15 mm.

Optical sensors

An optical lever and a optical length sensor are to be installed to monitor tTM alignment in longitudinal, pitch and yaw direction. The optical lever is the same system as that was used in the iKAGRA-PR3 SAS. The details of the optical length sensor is summarized in [50]. It supposes that the sensor noise of the optical lever and the optical length sensor have flat noise of 10^{-7} rad/$\sqrt{\text{Hz}}$, 10^{-7} m/$\sqrt{\text{Hz}}$ in frequency domain.

Wave front sensor

The wave front sensor (WFS) is a low noise sensor which references the interferometer beam. The sensitivity of the WFS would be limited by only shot noise. It supposes that the sensor noise of the wave front sensor has flat noise of 10^{-12} rad/$\sqrt{\text{Hz}}$ rad in frequency domain.

105
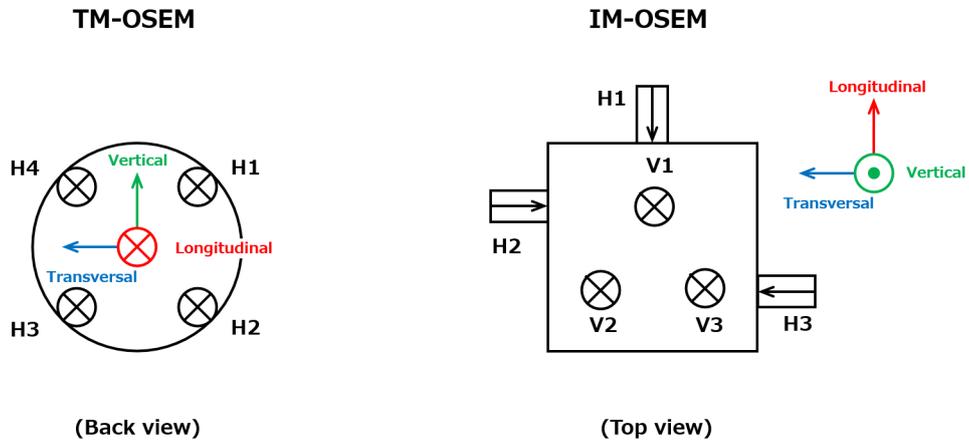
Figure 6.7: Positions of the OSEMs implemented into the payload. For the test mass, only the actuators are attached at the marked positions. For the intermediate mass, both of the sensors and actuators are equipped.
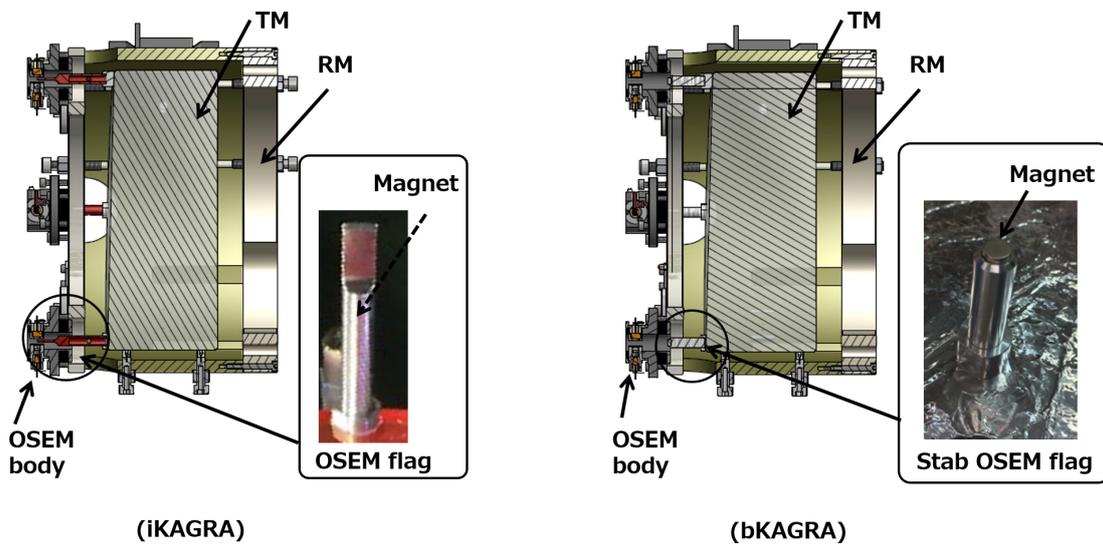

Figure 6.8: Difference of the OSEM system between the iKAGRA-PR3 SAS (*left*) and the type-Bp SAS (*right*)..
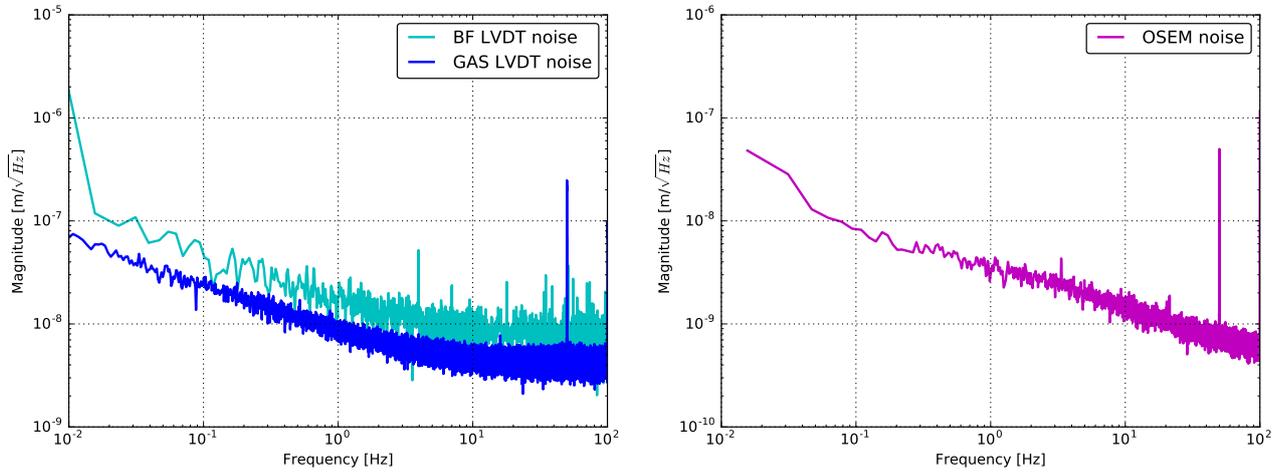
Figure 6.9: Assumed sensor noise models of the BF-LVDTs, GAS-LVDTs (*left*) and OSEMs (*right*).
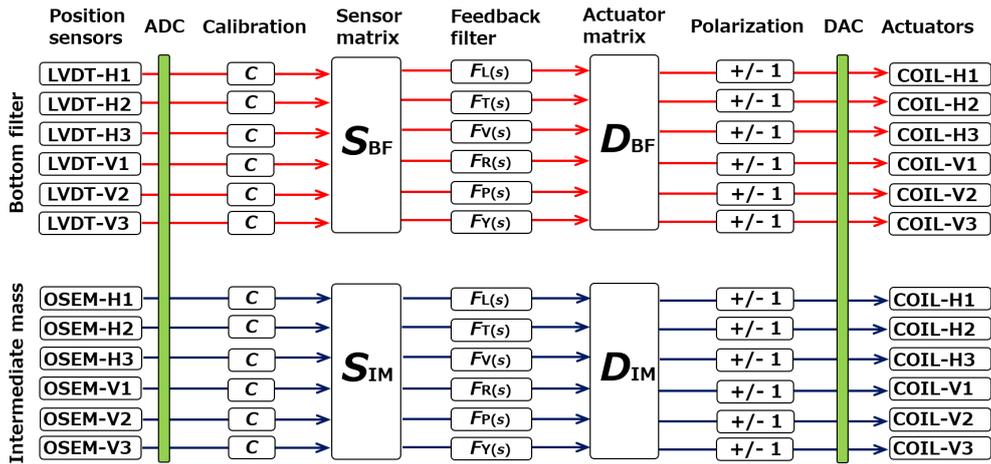
Figure 6.10: Conceptual control loops by the BF-LVDTs and IM-OSEMs.

6.4   Expected performance

The simulated performance of the newly designed type-Bp SAS is described in this subsection. This subsection includes the expected frequency responses of the suspension system, and its vibration isolation performances when the active controls are implemented. The modeled high noise seismic vibration at CLIO site is assumed in this simulation. According to the measured seismic vibration at KAGRA site, it seems to have shallow peak at around 2 Hz, while the vibration at the CLIO site does not have the structure. However, there is still no statistical measurement of the seismic vibration at KAGRA site and also the peak does not contribute a lot for current designing active control system. Thence the model obtained from measurement of CLIO site is used in this simulation, instead of the vibration of KAGRA site. In addition, optimally suspended system is also assumed. There is no horizontal discrepancy between the suspension point and the center of mass for each suspended mass.

Section 6.4.1 shows the expected transfer functions of the suspension system. The designed servo filters and the expected vibration isolation performances for the each control phase are described in section 6.4.2 to 6.4.4. In following figures, the variable names of L, T, V, R, P, Y are used for expressing the DoFs of the vibration in this section. They are the first letter of the direction of the vibration (longitudinal, transversal, vertical, roll, pitch, yaw). The following two letters describes the name of the rigid bodies in the suspension system.

6.4.1   Suspension mechanical response

The mechanical responses of the type-Bp SAS is explained in this section. Figures 6.11 to 6.28 show the expected diagonal transfer functions from the implemented actuators to the sensors. According to the previous investigation, these predicted transfer functions are expected to fit well with the measurement in the frequency band where the mechanical resonances to be suppressed are existing.

The transfer functions in this section are fed back to the servo filter designs. The resonant frequencies of the type-Bp SAS are summarized in table 6.3, and their eigenmode shapes are shown in appendix A.

Diagonal transfer functions
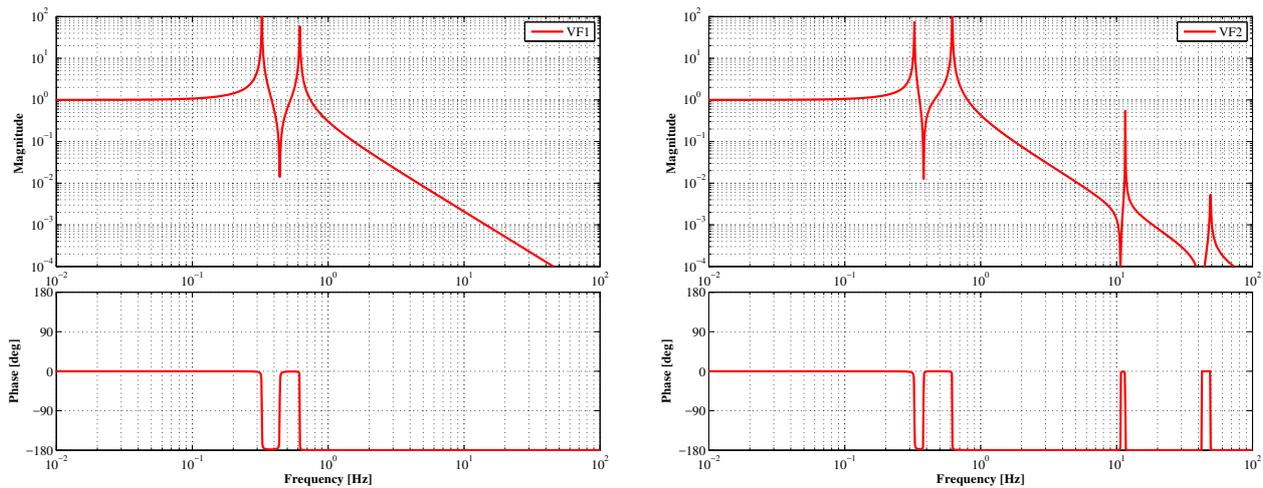
Figure 6.11: Diagonal transfer functions of GAS-LVDTs.
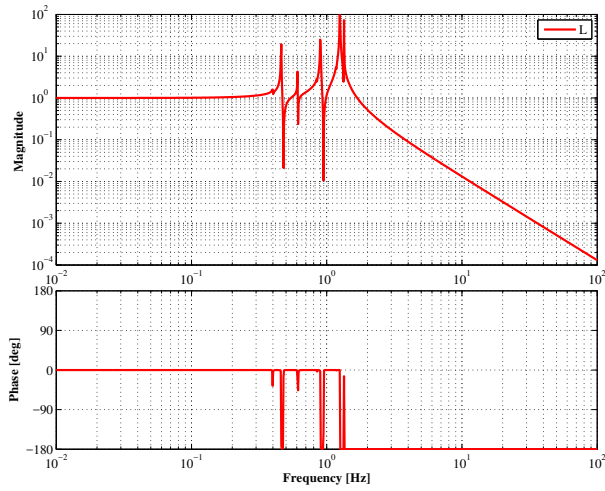
Figure 6.12: BF-LVDT (Longitudinal)
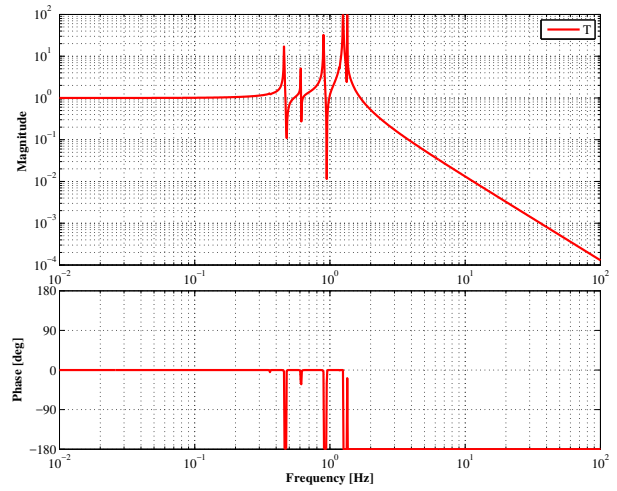
Figure 6.13: BF-LVDT (Transversal)
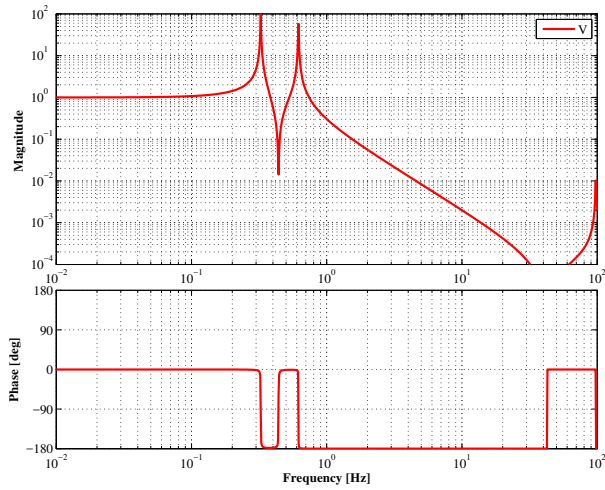
Figure 6.14: BF-LVDT (Vertical)
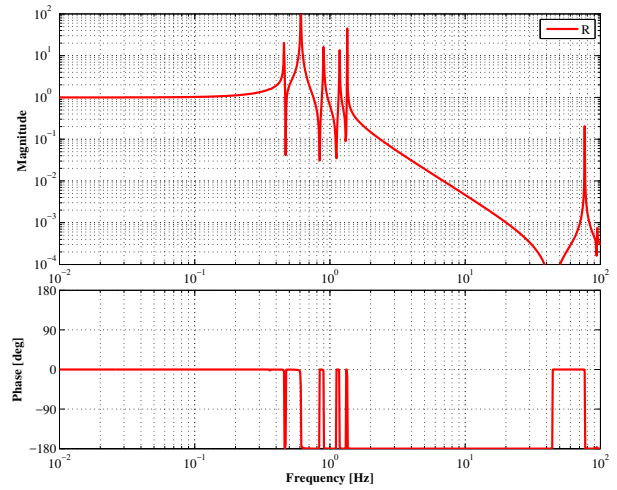
Figure 6.15: BF-LVDT (Roll)
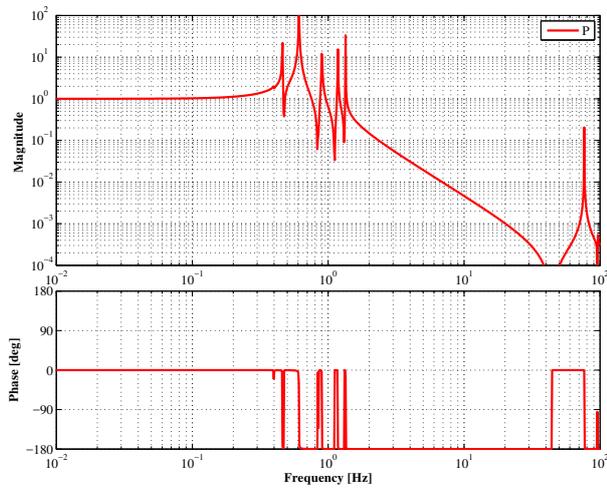
Figure 6.16: BF-LVDT (Pitch)
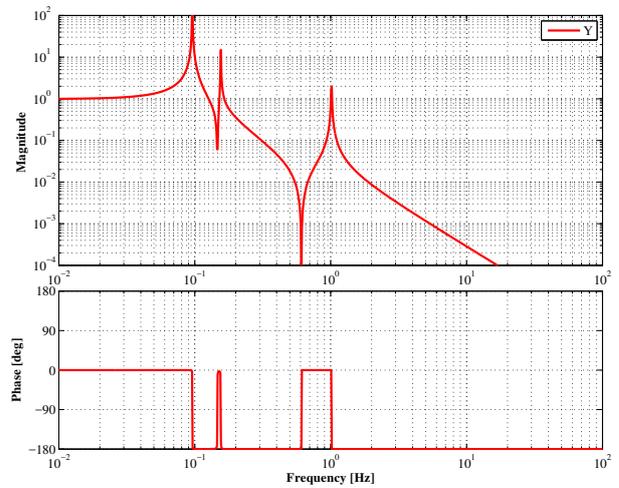
Figure 6.17: BF-LVDT (Yaw)
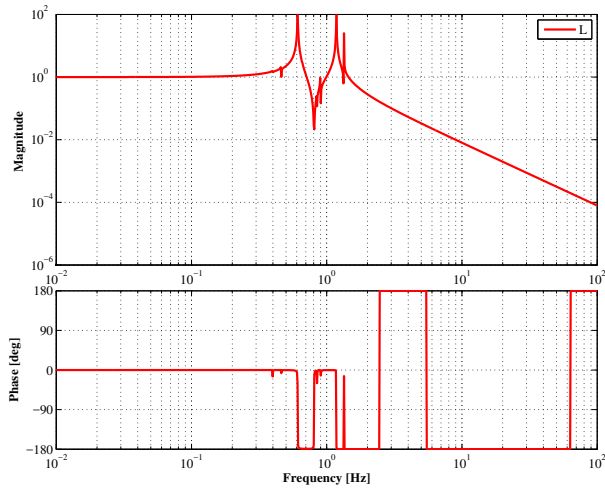
Figure 6.18: IM-OSEM (Longitudinal)
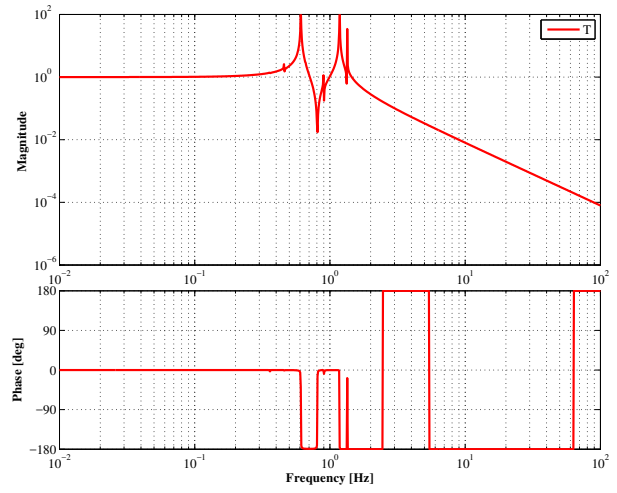
Figure 6.19: IM-OSEM (Transversal)
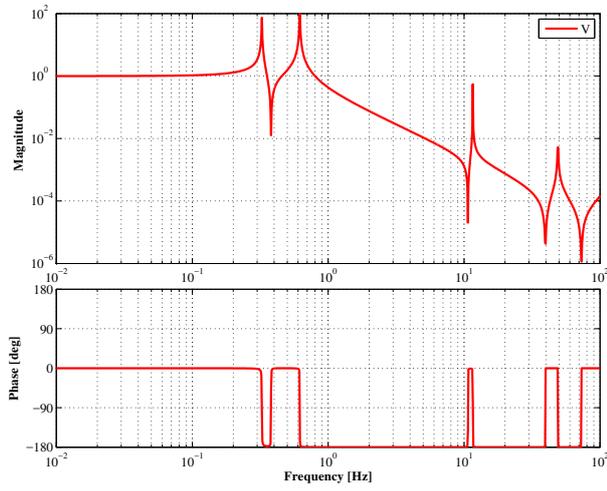

Figure 6.20: IM-OSEM (Vertical)
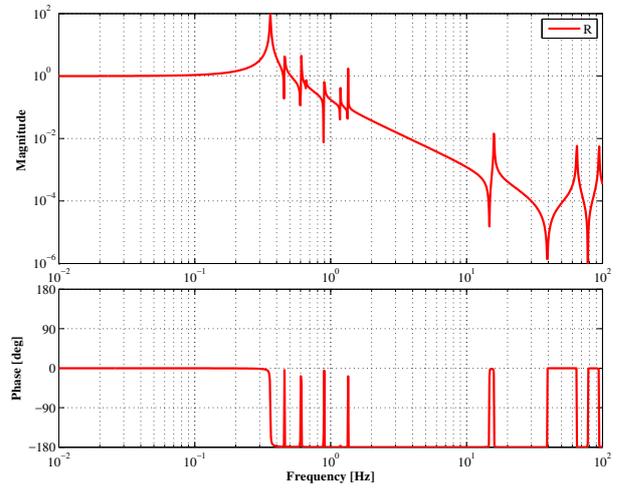
Figure 6.21: IM-OSEM (Roll)
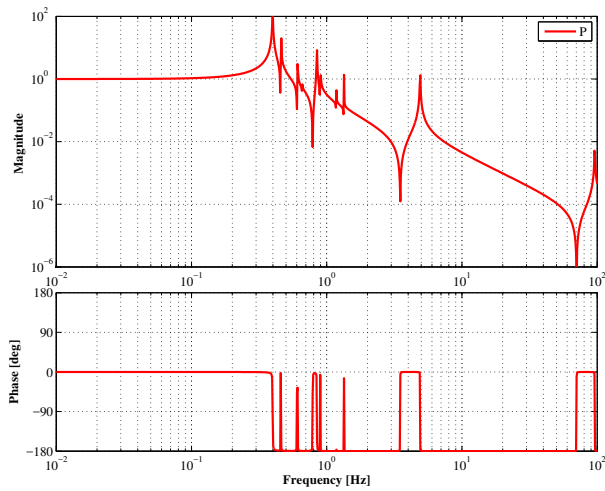
Figure 6.22: IM-OSEM (Pitch)
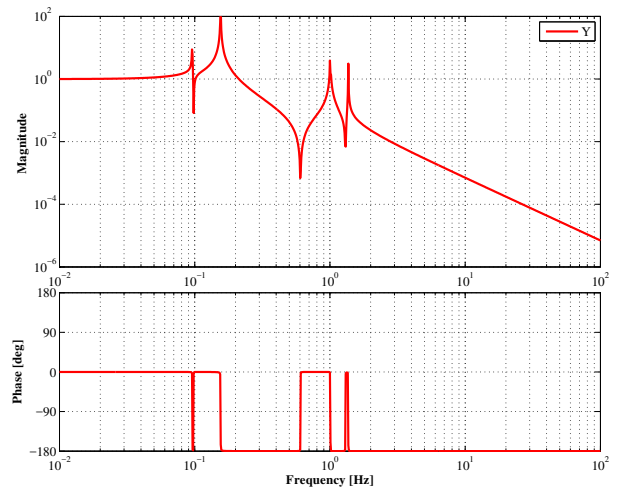
Figure 6.23: IM-OSEM (Yaw)
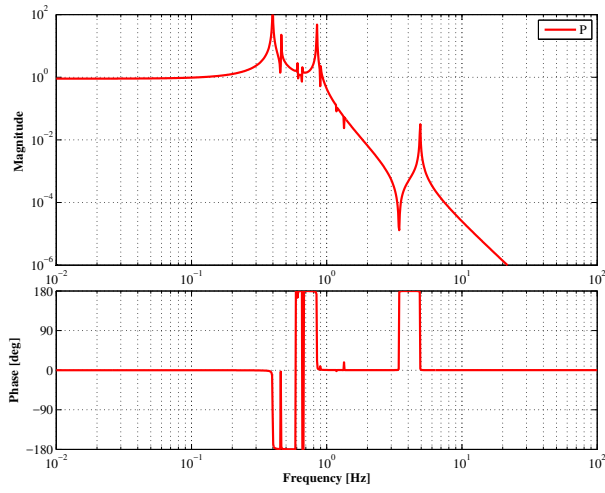
Figure 6.24: IM-OSEM to oplev (Pitch)
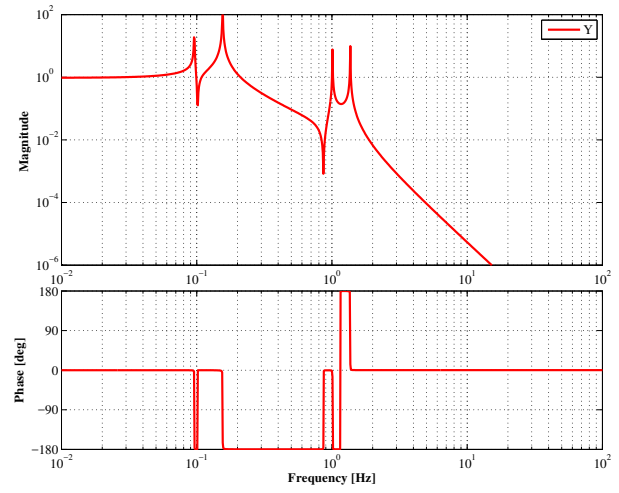
Figure 6.25: IM-OSEM to oplev (Yaw)
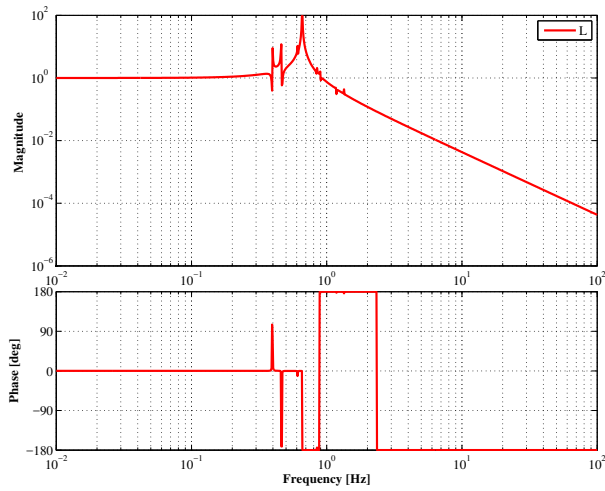
Figure 6.26: TM-OSEM to oplev (Longitudinal)
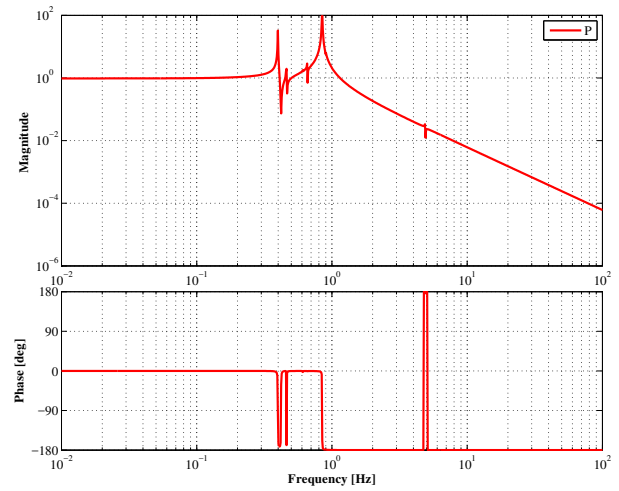
Figure 6.27: TM-OSEM to oplev (Pitch)
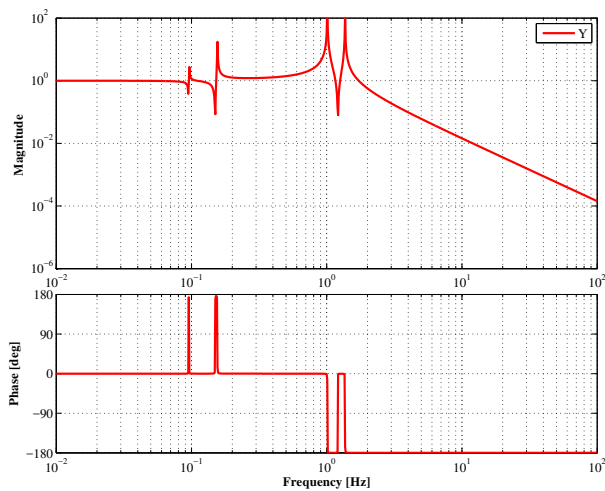
Figure 6.28: TM-OSEM to oplev (Yaw)

Eigenmodes from 3D rigid body model

#Mode No.	Frequwncy [Hz]	Mode shape	Note
#1	0.1	YBF, YIR, YRM, YTM	wire torsion
#2	0.161	YIM, YRM, YTM	wire torsion
#3	0.325	VBF, VIR, VIM, VRM, VTM	GAS filter
#4	0.376	RIM, RRM, RTM	IM roll
#5	0.414	PIM, PRM, PTM	IM pitch
#6	0.459	-RIM, TRM, -RRM, TTM, -RTM	main pendulum
#7	0.463	PIM, PRM, PTM	main pendulum
#8	0.612	RBF, TIR, RIR	BF roll
#9	0.613	-PBF, LIR, PIR, PTM	BF pitch
#10	0.618	VBF, VIR, -VIM, -VRM, -VTM	GAS filter
#11	0.659	-PIM, -LRM, -PRM, LTM, -PTM	TM-RM pendulum
#12	0.659	-RIM, TRM, -RRM, -TTM, -RTM	TM-RM pendulum
#13	0.849	PTM	TM pitch
#14	0.9	TBF, -RBF, -RRM, TIM, -TRM, -TTM	main pendulum
#15	0.901	-PBF, -PIR, PIM, PRM, -PTM	main pendulum
#16	1.011	YIM, -YRM, YTM	TM yaw
#17	1.017	YIR	IR yaw
#18	1.022	YBR	BR yaw
#19	1.186	RBF, -TIR, RIR, TIM	main pendulum
#20	1.186	PBF, LIR, PIR, -LIM	main pendulum
#21	1.261	LBR	BR pendulum
#22	1.261	TBR	BR pendulum
#23	1.351	-RBF, TIR, -RIR, TIM	IM pendulum
#24	1.352	PBF, LIR, PIR, LIM	IM pendulum
#25	1.369	YIM, -YTM	TM yaw
#26	4.906	-PIM, PRM	RM pitch
#27	11.611	-VIM, -VRM, VTM	TM vertical
#28	15.924	RTM	TM roll
#29	48.97	-YIM, YRM	VRM
#30	64.629	-RIM, RRM	RIM
#31	78.843	PBR	BR pitch
#32	78.843	RBR	BR roll
#33	97.094	RIR	IR roll
#34	98.66	PIR	IR pitch
#35	100.617	VBR	BR vertical
#36	126.38	VIR	IR vertical

Table 6.3: Simulated eigenmode list of Type-B SASp for bKAGRA

6.4.2 Controls in the calm-down phase

This section describes the active damping servos in the calm-down phase. The designing filters, its damping performances, and the sensor noise coupling to the interferometer signals are included. The servo filters are designed from the transfer functions from the implemented actuators and the sensors which are shown above.

Servo filter design

The schematic control diagram in the calm-down phase is shown in figure 6.29. The damping controls are set at the BF and IM levels by using the BF-LVDT units, and IM-OSEM units. Resonances of the vertical GAS filter vibration are damped by the GAS-LVDT and coil-magnet actuator unit, which is implemented into the SF. DC servos are also included in the GAS filter control loops to suppress the thermal drift of the GAS filters. At the test mass level, damping loops by the optical lever and optical length sensor are implemented to suppress the relative motion between test mass and its recoil mass, even though they have narrow linear range. This is because the sensors to measure the test mass motion in the type-Bp SAS are only them.

In this section, the performance in 2 cases are investigated. First option is the case when the optical lever and the optical length sensor are available. The other option is the case if they are not available. Figure 6.30 to 6.32 show the Bode-plots of the designed servo filters in the calm-down phase. The displacement signals obtained by OSEM sensors and LVDTs are converted into the velocities with differentiation filters to get the viscous damping forces. Then, the converted signals are sent to the actuators with appropriate gains. The feedback filters have gains which is proportional to frequency f, around the mechanical resonant frequencies to be suppressed. The SF control gain has larger gain at the low frequencies to compensate the thermal drift of the GAS filters. The gains at high frequencies are cut off by low pass Butterworth filters with certain frequencies. In this calm-down phase, the cut-off frequencies are set at the lowest ones where all the mechanical resonances are suppressed within the requirement.
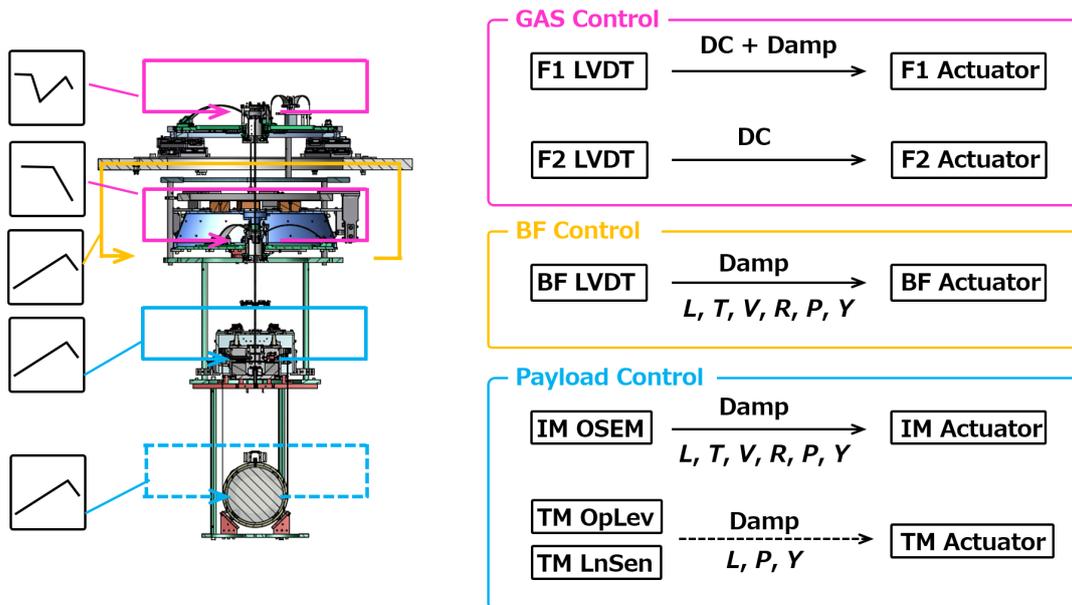

Figure 6.29: Control loops in the calm-down phase.
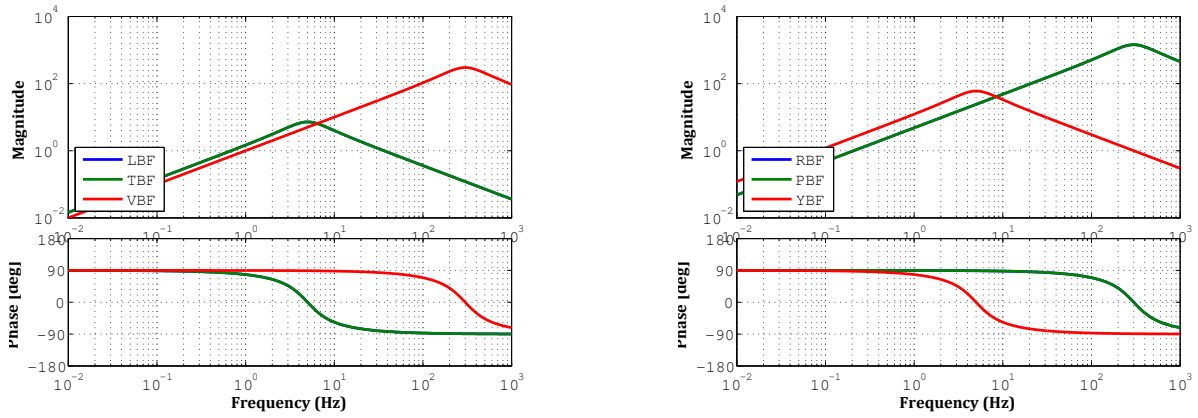
Figure 6.30: Servo filters for BF-level controls in the calm-down phase.
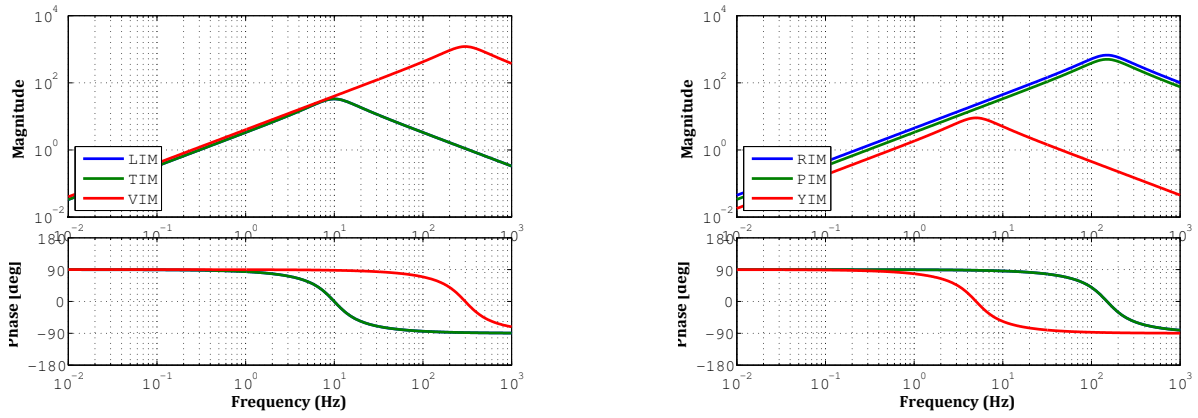

Figure 6.31: Servo filters for IM-level controls in the calm-down phase.
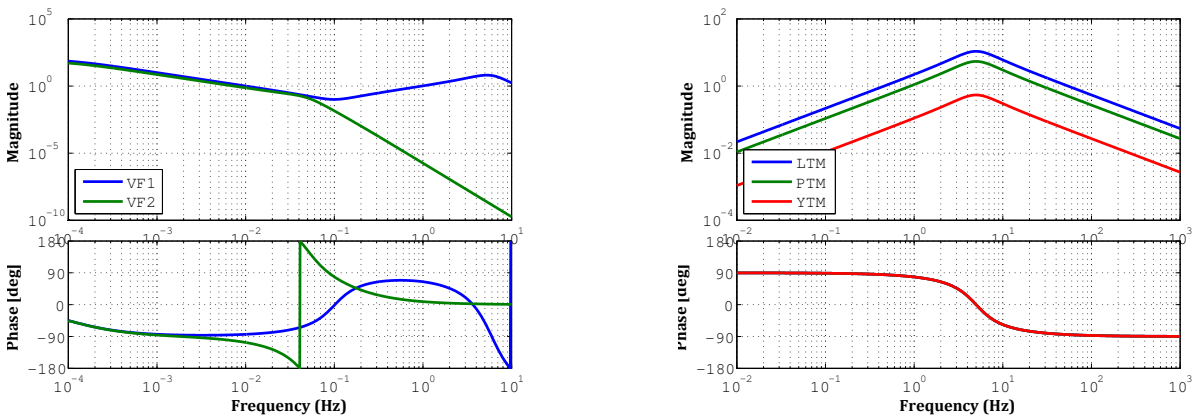
Figure 6.32: Servo filters for GAS controls (*Left*), for TM-level controls (*Right*) in the calm-down phase.

Expected damping performance

This subsection describes the performance of the damping control in terms of $1/e$ decay time of each mechanical resonance. $1/e$ decay time is a measure of the damping performance. The active control in this phase is required to damp the mechanical resonances with long decay time, especially at 0.1 Hz $\sim$ 1 Hz. The requirement is to reduce the $1/e$ decay time to less than 1 minute.

Figure 6.33 shows the expected $1/e$ decay time for each resonant frequency of the type-Bp SAS, with and without controls. The $left$ plot is the performance when the control loops with optical lever and optical length sensor at the test mass level are opened, while the $right$ plot describes that when the control with these optical sensors are turned on. The former considers the optical sensors at the test mass level are not available, while the latter supposes they are available. According to the plots in the former case, there are 3 resonant modes whose decay time exceed the requirement with active control, and according to the latter case, there is one such mode. Figure 6.34 shows those resonant mode shapes. All of these resonances are related with relative vibration between the test mass and its recoil mass in longitudinal, transversal and yaw DoFs, and thus to damp the resonances, sensing the test mass motion is needed. If the optical sensors are available in the calm-down phase, the test mass active control damps mode #11 and mode #16 (longitudinal and yaw DoF), which disturb the lock acquisition. On the other hand, the other mode #12 is not damped even if the test mass controls are switched on, since there is no sensors and actuators for the test mass motion in transversal DoF. However, the vibration which is related with the transversal DoF of the test mass is not disturb the interferometer operation, unless its amplitude becomes larger than 1 mm. Thus there is no problem for this mode even if its decay time is larger than the requirement.
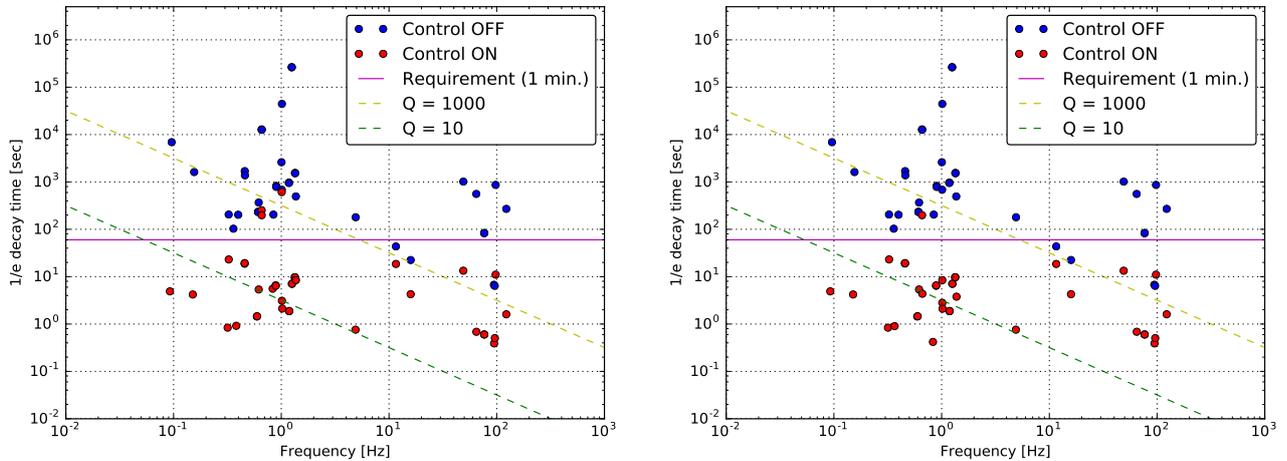

Figure 6.33: Expected $1/e$ decay time for each mechanical resonances in the type-Bp SAS with and without active control. $Left$ plot shows the performance when the active control with optical sensors are not available, while $right$ plot describes that when the controls with the optical sensors are included.

In conclusion, if the optical sensors at test mass level is available in the calm-down phase, the active controls damps all the mechanical resonances which disturb the interferometer operation, within 1 minute which is requirement for this controls. On the other hand, if the optical lever is not available in this phase, one has to wait typically $3 \sim 10$ minutes until the suspension system recovers its steady state.
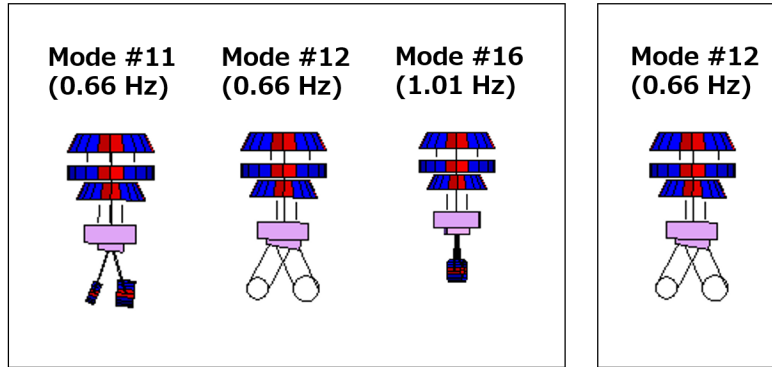
Figure 6.34: Mode shapes of the mechanical resonances whose $1/e$ decay time exceeds the requirement of 1 minute when the active control at test mass level are not available ($Left$), while when the control with the optical sensors are working ($Right$). The $1/e$ decay time under this controls is expected around 200 sec for the mode #11, 250 sec for the mode #12, and 610 sec for the mode #16.

Note that the angular fluctuation of the mirror is required to be suppressed lower than about 50 μrad to keep the optical lever within its linear regime. The relative motions between the test mass and its recoil mass tend to be excited by actuators, rather than the external disturbances such as earthquakes. For instance, the active controls in the lock-acquisition phase can excite such vibration by inputing pulse signal when the lock is failed. Here, consider a worst situation where a pulse signal with 10 V is input into the TM-OSEM actuators in longitudinal and yaw direction. Figure 6.35 shows the expected decay signals of the test mass with the active controls in the calm-down phase without test mass controls. According to the simulation, the excited amplitude are 2 mm, 7 mrad in longitudinal, yaw DoF respectively. In this calculation, it supposes that the high power coil drivers, which generate about 7×10^{-2} N per one coil, are used and this coil drivers are used for the coils on the test mass in the type-Bp SAS. It implies that it would take 12 minutes, 50 minutes to suppress the amplitude lower than 50 μm, 50 μrad where the optical levers work, following a formula:

$$\exp\left(-\frac{\Delta t}{\tau_e}\right) = \frac{A_{\text{final}}}{A_{\text{initial}}}. \tag{6.1}$$

Thence, if a pulse signal with 10 V is input into the actuators at the test mass, one might have to wait 50 minutes. On the other hand, if a pulse signal whose amplitude is lower than 70 mV, the optical lever is expected to be available. Thus decay time of those motion can be suppressed within 1 minute by the control loops with the optical lever.

In the actual system, however, when a large pulse signal is injected due to failure of the interferometer lock for instance, the circuits of the OSEM coils are to be shorted analogously by another system. In such situation, an eddy current damping system is constructed between the OSEM coils and magnets on the optic. Then, decay time for these resonances is expected to be shortened. The electrical short circuit is opened when the system gets steady state. Thus even if the 10 V pulse signal is injected into the optic actuator, the decay time should be smaller than 12 min or 50 min.

Consequently, it is expected that the optical lever would not be available, if a large pulse signal is introduced into the TM-OSEM actuators. However, it is also expected another passive damping system would be constructed for the optic and thus this issue might not be problematic. The efficiency if the passive damping performance is to be investigated by using actual type-Bp SAS.

Note that this issue would not be so effective for the type-B SAS. Since low power coil drivers are used for the test masses, they allows for the actuators to generate about 1/600 of force by the high

power coil drivers. Thence, even if the pulse signal with 10 V in input into the test mass, the excited impulse amplitudes are expected to be 3 μm, 11 μrad in longitudinal, yaw direction respectively. The optical lever is able to measure these vibration with in its linear regime.
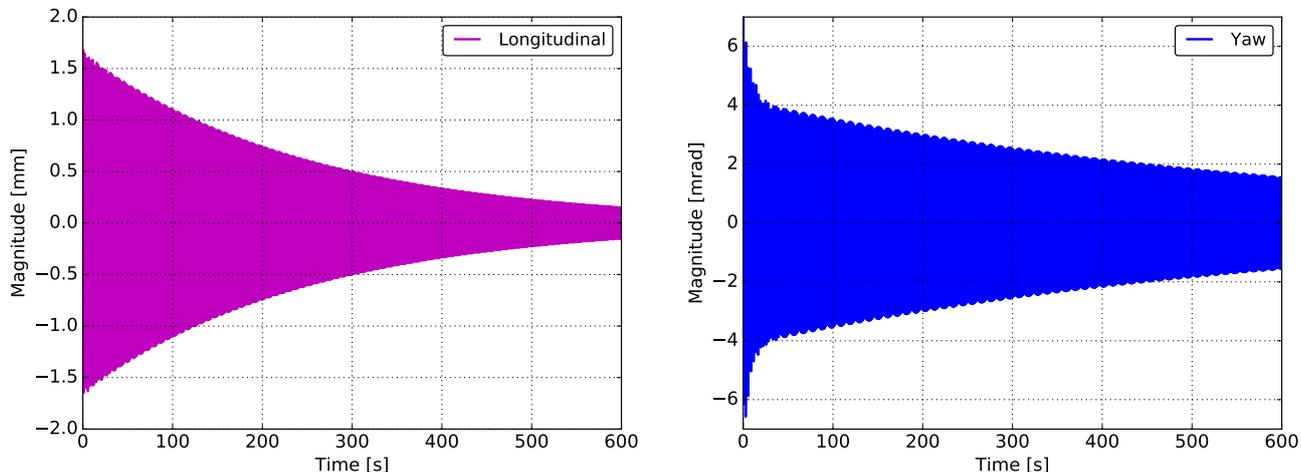

Figure 6.35: Expected $1/e$ decay time of longitudinal (*left*) and yaw (*right*) motion of the test mass with the active control in the calm-down phase (without the control loops for the test mass).

Sensor noise couplings in the calm-down phase

Figure 6.36 shows the expected noise couplings from each position sensor used in this control to longitudinal displacement of the test mass. The considered noise sources are GAS-LVDTs, BF-LVDTs, and the optical sensors at test mass level. The BF-LVDT, OSEM sensor, optical lever have 10^{-8} m/$\sqrt{\text{Hz}}$, 10^{-9} m/$\sqrt{\text{Hz}}$, and 10^{-7} rad/$\sqrt{\text{Hz}}$ for their noise level in the band of target gravitational waves, respectively. The displacement noise of the test mass caused by the IM-OSEMs and optical sensors are much larger than the required level as shown in the plot. Thence, the control with the OSEMs and the optical lever should be excluded or modified in the observation phase. The control noise from BF-LVDT also violates the requirement at 11 Hz. Since the peak at 11 Hz is comes from a resonant vibration of the test mass in vertical direction, the servos by BF-LVDTs and OSEMs are to be opened in vertical DoF, in the observation phase.

Table 6.4 shows the expected residual RMS values after the suspension system gets steady state. According to this table, all the simulated results meet the requirements for the calm down-phase controls. These predicted RMS values depend on mechanical Q factors of the resonant peaks, which have large uncertainty in this simulation. However, the actual mechanical Q factors of the KAGRA-SAS are either comparable with or lower than these predictions, comparing to the previous measurements. Thence the residual values of the actual suspension system is expected to be lower than the RMS. About yaw motion, this simulation does not include the prediction of its RMS, since predicting the precise yaw motion needs to consider asymmetry of the mechanical suspension system. There is also no detailed information about the asymmetry of the KAGRA-SAS. According to previous measurement which was done at TAMA site, where the magnitude of the seismic noise is much larger than that of the KAGRA site, its measured residual RMS of yaw motion was 40 μrad. Following these experiments, the amplitude of the residual yaw motion is expected to be lower than 40 μrad unless the suspension system has much asymmetries.

Item	displacement			velocity
	longitudinal [μm]	vertical [μm]	pitch [μrad]	longitudinal [μm/s]
Controlled RMS	1.1	0.01	1.3	2.5

Table 6.4: Expected RMS values in the calm-down phase. The longitudinal, vertical, pitch displacement, and longitudinal velocity of the mirror are described in each column.
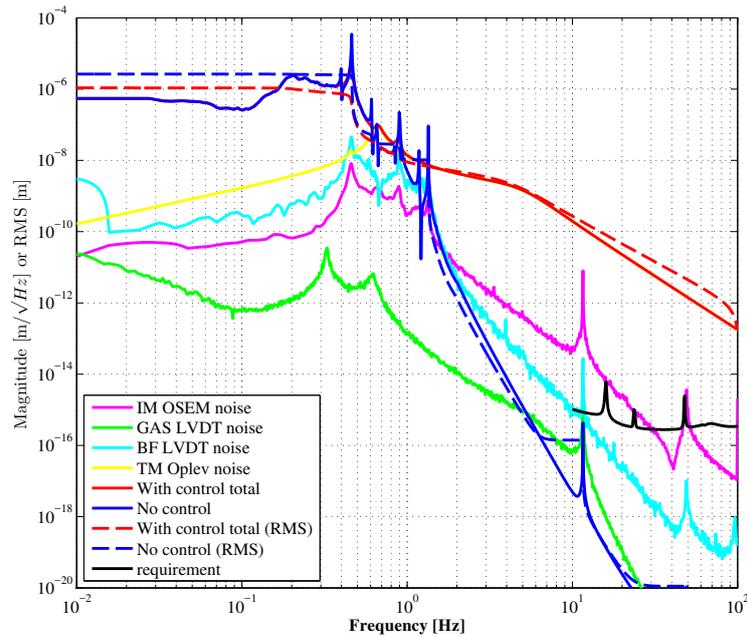

Figure 6.36: Expected control noise couplings to longitudinal displacement of the test mass in the active controls in the calm-down phase, due to sensor noise. Tn the plot, optical sensors are included into the control. This plot includes the noise coupling from IM-OSEMs (magenta), from GAS-LVDTs at SF and BF (green), from BF-LVDTs (cyan), optical sensors at test mass level (yellow). The total control noise (red), passive performance (blue) are also plotted. The dashed lines describe the RMS of total control noise and passive performance, down to 10^{-2} Hz. In this calculation, it is assumed that the suspension components are optimally suspended.

6.4.3   Controls in the lock-acquisition phase

The aim of the control in the lock-acquisition phase is to suppress the RMS longitudinal velocity and RMS angular motion of the test mass for the lock acquisition of the interferometer. Figure 6.37 shows the schematic diagram of this control phase. This active control is switched on, after the suspension system gets steady state.
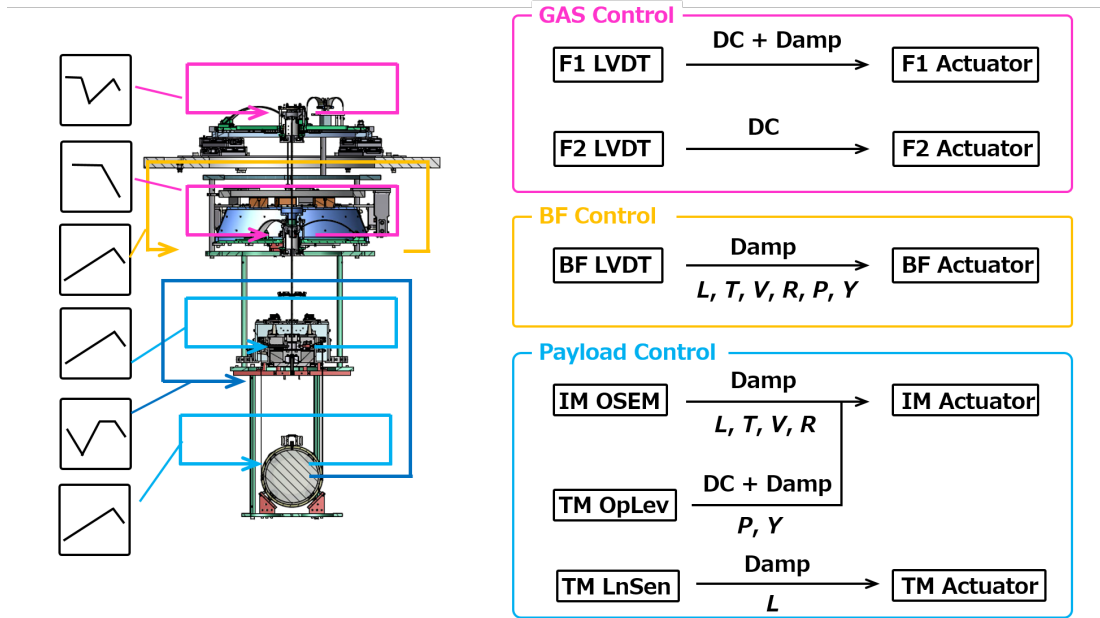

Figure 6.37: Control loops in the lock-acquisition phase.

In this phase, control loops for the payload are changed. Since important role of this phase is aligning the test mass for the interferometer lock, both of DC and damping servos are implemented in the mirror pitch and yaw motion. The control of the mirror angular motion is achieved by the alignment controls with the optical lever. The signals of mirror pitch and yaw vibration are measured by the optical lever, and are fed back to the actuators implemented at IM level. The damping filters for pitch and yaw vibration by IM-OSEMs are turned off when the controls with optical lever are switched on. This is aiming at avoiding competition between the optical lever control and OSEM one.

Figure 6.38 to 6.40 show the Bode-plots of the designed servo filters in the lock-acquisition phase. The cut-off frequencies for the damping filters by BF-LVDTs and IM-OSEMs are set at ones where the resonances, which contribute to the RMS displacement of the mirror vibration, are efficiently damped. Figure 6.40 *Right* shows the servo filters for aligning the test mass of suspended by the type-Bp SAS. The shapes of the servos are aimed at compensating the phase delay of the mechanical system. In these filters, DC servos are implemented at low frequencies for the mirror alignment. At the region between around 0.1 Hz to the unity gain frequencies ($\sim$ 2 Hz), the servo gains are raised by proportional to f^3 to compensate the phase delay due to the mechanical response. This is because the amplitude of the mechanical response gets smaller by proportional to f^{-4} and its phase delays 360 deg at high frequencies. The notch filter at 4.9 Hz in the pitch servo is included to avoid the instability of due to the mechanical response related with the pitch vibration of the recoil mass.

The expected RMS of longitudinal displacement, velocity and pitch angular displacement in this controls are described in table 6.5. It is confirmed that the active controls for this phase are met with the requirements. The RMS of test mass yaw motion is not calculated, however, according to the

previous measurement, it is expected to meet the requirement.

Servo filter design
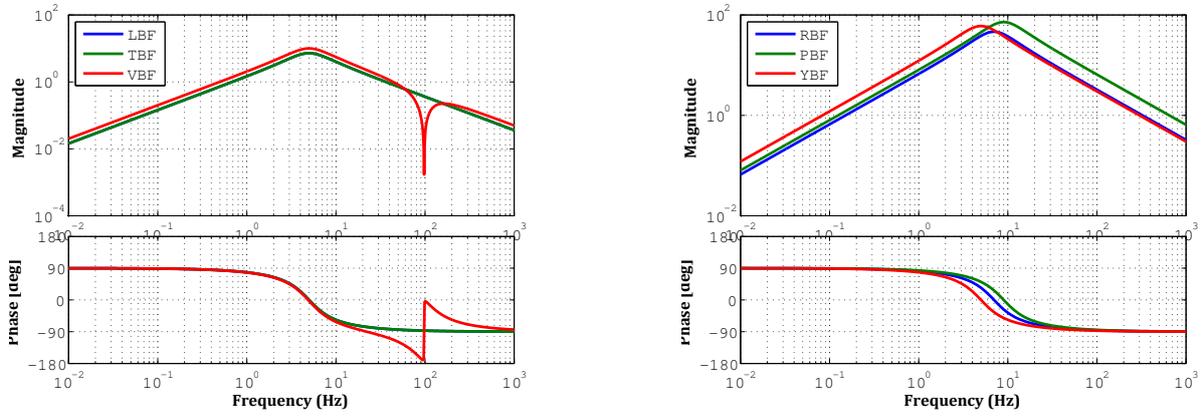
Figure 6.38: Servo filters for BF level controls in lock-acquisition phase.
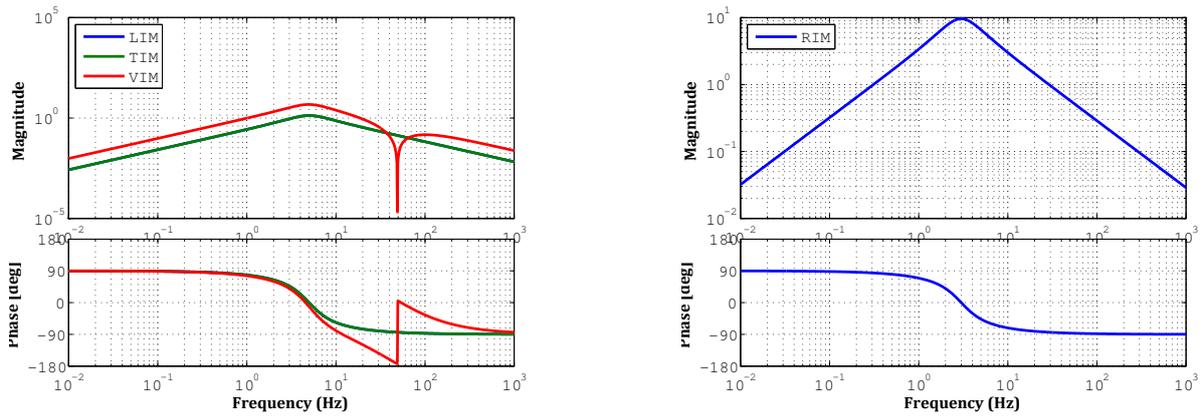
Figure 6.39: Servo filters IM level controls in lock-acquisition phase.
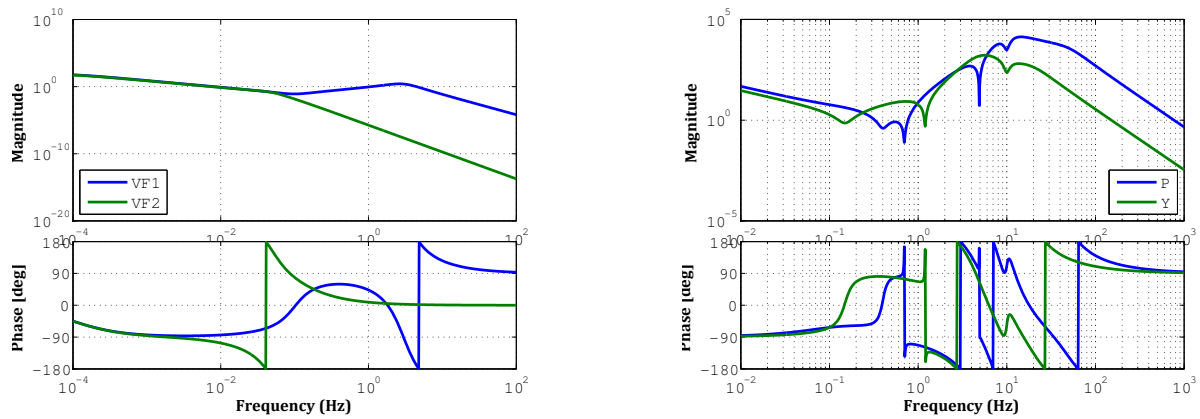
Figure 6.40: Servo filters for GAS controls (*Left*), for TM-level controls (*Right*) in lock-acquisition phase.

Item	displacement [μm]	velocity [μm/s]	pitch [μrad]
Without controls	2.6	7.4	16.9
With controls	1.0	2.3	1.9

Table 6.5: Expected RMS values of residual vibration in the lock-acquisition phase. The longitudinal displacement, longitudinal velocity, and pitch vibration of the mirror are described.

6.4.4   Controls in observation phase

The most important role of the control in the observation phase is to suppress the displacement noise lower than the requirement at 10 Hz, keeping the requirements on the RMS. The servo filters shown in the previous subsection are also used in the observation phase. After the lock-acquisition phase, only the optical lever is to be changed into the wave front sensor (WFS) to reduce the noise level at the target gravitational wave band. Here it supposes that the WFS noise has flat noise of 10^{-12} rad/$\sqrt{\text{Hz}}$ rad in frequency domain.

Since the BF-LVDTs and IM-OSEMs have large sensor noises, the control by these sensors have to be opened in the observation phase if lower noise coupling at above 10 Hz is needed. However, the loops for horizontal and angular DoFs by BF-LVDTs are not possible to open them in the type-Bp SAS control system. This is because the resonant modes which have large contribution to the RMS are the main pendulum motion at 0.45 Hz, which are the mode #6, #7 shown in appendix A, and they have to be damped with the controls by using BF-LVDTs. In addition, the active controls for vertical DoF by BF-LVDTs and OSEMs induce the vertical resonance of the test mass at 11 Hz, and this vibration causes the violation of the displacement requirement, as shown in figure 6.36. Thus the vertical controls by them are to be opened in this phase.

Consequently, the available sensors and DoFs are BF-LVDTs except for vertical DoF, and IM-OSEMs for longitudinal, transversal, roll DoFs. This section describes 2 options for the controls in the observation phase based on the issues.

Control without IM-OSEMs

In this controls, the loops by IM-OSEMs are opened to avoid inducing test mass longitudinal vibration due to their sensor noise. In addition, the vertical control by BF-LVDT is also excluded not to excite the peak at 11 Hz by its sensor noise. Consequently, this control includes DC and damping servos by GAS-LVDTs, damping filters by BF-LVDTs except for the vertical DoF, and DC and damping filters by WFS. Figure 6.41 describes the control diagram of this controls.
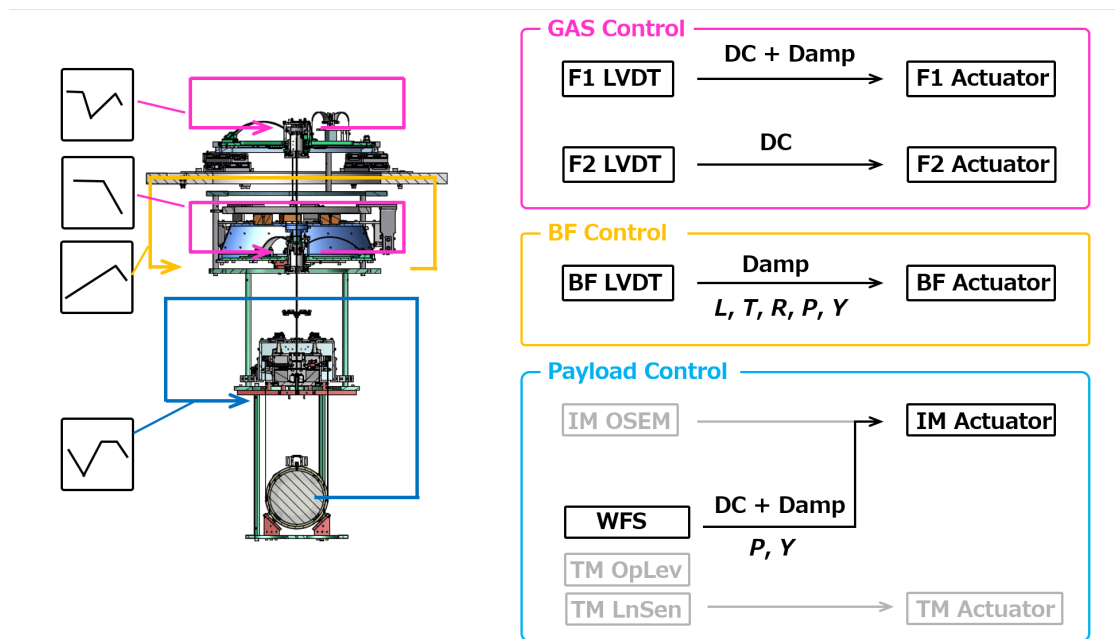

Figure 6.41: Control diagrams in observation phase without controls by IM-OSEMs.
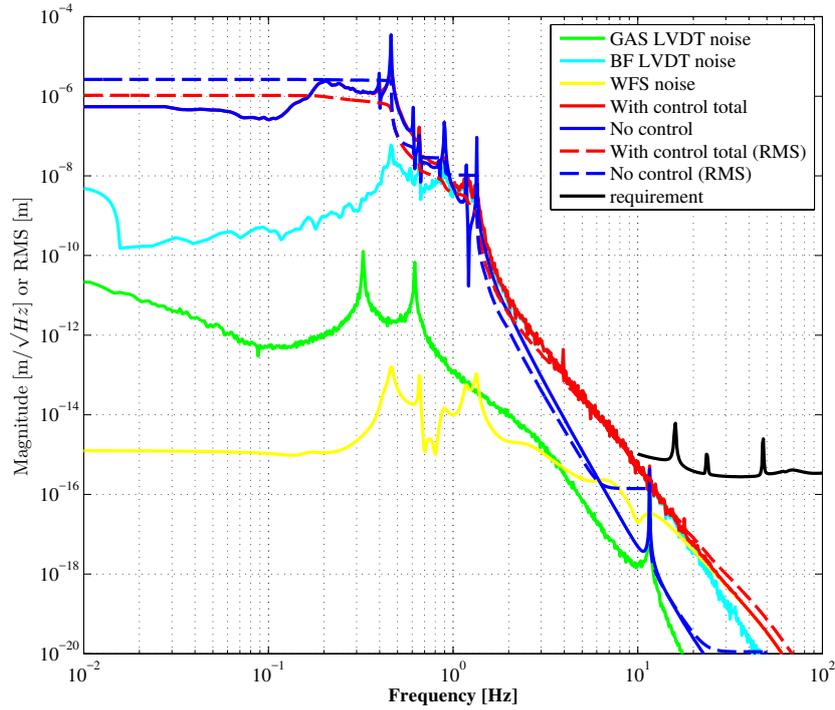
Figure 6.42: Control noise coupling to longitudinal displacement of the TM in the observation phase. This performance is obtained without IM-OSEM loops.

The expected control noise coupling into the test mass longitudinal direction in this control is shown in figure 6.42. The dominant coupling in $1 \sim 10$ Hz region comes from the BF-LVDT controls, and is close to the requirement at 10 Hz. However, it is unavoidable unless the BF-LVDTs are used. If the amplitudes of the servos by the BF-LVDTs, even though one can have larger margin at 10 Hz, the loops fail to suppress the RMS pitch motion lower than the requirement. Table 6.6 explains the active control performance in this phase. All the described parameters meet the requirements.

Item	RMS displacement	displacement at 10 Hz	RMS pitch
With controls	1.1 μm	5×10^{-16} m/$\sqrt{\text{Hz}}$	1.8 μrad

Table 6.6: Expected performance in the observation phase. The longitudinal displacement, longitudinal velocity, and pitch vibration of the mirror are described.
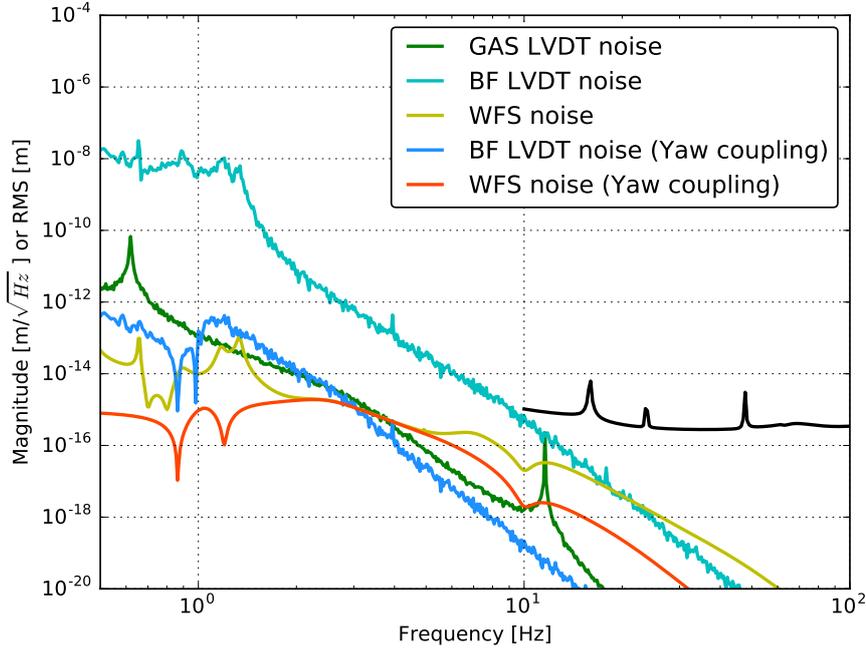
Figure 6.43: Control noise coupling due to 1 mm mis-centering of the beam spot. 2 curves (orange and blue) are added to the noise curves shown in figure 6.42. It assumes the system is optimally suspended, and also the beam spot at the mirror is shifted horizontally by 1 mm.

Figure 6.42 describes the performance when the interferometer beam is centered. However, the beam spot can be mis-centered in actual situation. If the beam is shifted horizontally, yaw DoF motion couples to longitudinal vibration. Figure 6.43 shows the the noise couplings from yaw motion of the mirror at around 10 Hz. It assumes that the interferometer beam is shifted by 1 mm from the center. According to the result, the yaw couplings due to the mis-centered of the beam by 1 mm is lower than the requirement and also the couplings from BF-LVDTs. Since its beam shift is aligned within 1 mm for the interferometer operation, the effect of yaw coupling due to mis-centering of the beam is not affect to the requirement.

Controls with IM-OSEMs

This section describes the controls including the IM-OSEM feed back loops for the observation phase. In above section, it is presented that the active controls without IM-OSEM controls meet the requirements. However, the actuation forces can excite resonance which disturbs the interferometer operation if there are couplings from other DoFs due to the imperfection of actuator diagonalization. If it happens, the vibration excited by the IM actuators can transmit to the test mass directly. In this situation, including damping controls by IM-OSEMs would be useful to avoid exciting such resonances. Figure 6.44 shows the diagram of this control. To avoid inducing the resonant peak at 11 Hz related with test mass vertical vibration, the damping filters for vertical DoF at BF and IM are excluded. The loops for pitch and yaw DoF at IM are also opened to prevent from competition between the control by WFS and that by IM-OSEMs.

The expected noise coupling in this controls is shown in figure 6.45, and it includes the couplings

from the test mass yaw motion due to mis-centering of the interferometer beam by 1 mm. According to the simulation, the expected IM-OSEM control noise is lower than the requirement, even though it becomes dominant at above 10 Hz. The obtained RMS longitudinal displacement, RMS pitch vibration, and longitudinal displacement at 10 Hz are 1.0 μm, 1.8 μrad, and 8.5×10^{-16} m$/\sqrt{\text{Hz}}$, respectively. Since, the IM control cannot damp the main pendulum modes at 0.45 Hz, the RMS of them are not changed comparing to the other control system in the observation phase.

Consequently, it is possible for the type-Bp SAS to include the control loops by IM-OSEMs even in the observation phase. It is not needed to include the controls by the IM-OSEMs in the observation phase, however, it would be safer to use the IM-OSEM damping servos in this phase, from viewpoint of actual situation.
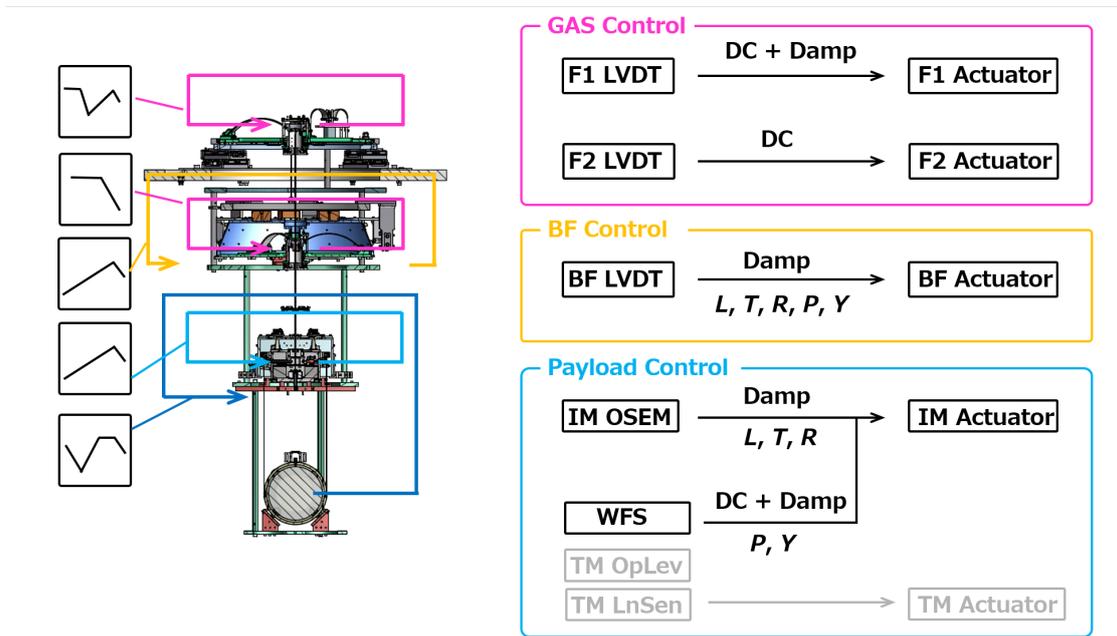

Figure 6.44: Control diagrams in observation phase with controls by IM-OSEMs.
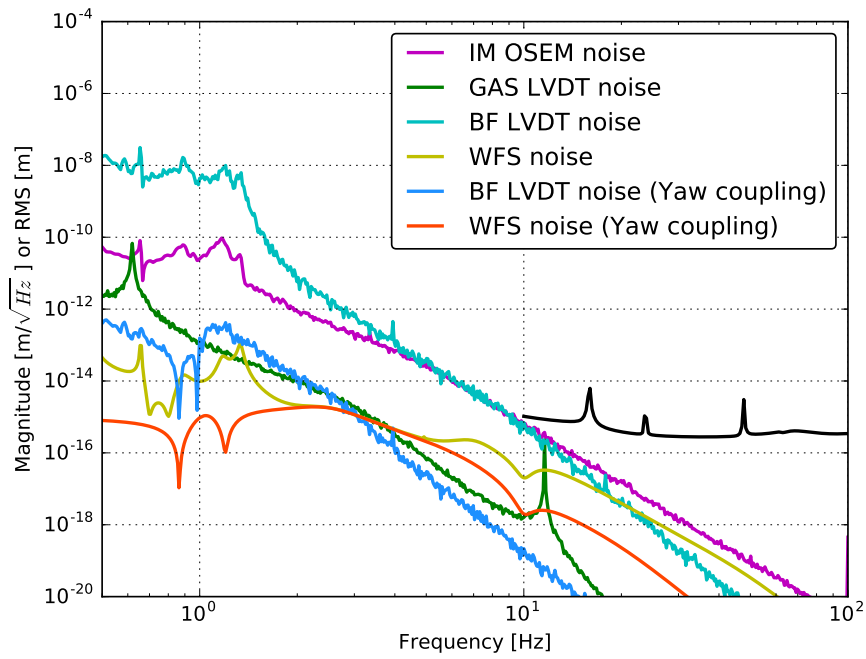
Figure 6.45: Control noise coupling to longitudinal displacement of the TM in the observation phase. This performance is obtained with IM-OSEM loops.

6.5   Conclusion

From the simulation in this chapter, it is confirmed that the designed active control system for the newly designed type-Bp SAS meets fundamental requirements which are set in chapter 4. Table 6.7 summarizes the requirements which are set for the type-Bp SAS active control system and simulated performance. Note that this table assumes that the optical sensors are available in the calm-down phase and thus the table is valid for a situation where the amplitudes of the test mass vibration are smaller than 50 μm, 50μrad. The prediction in yaw DoF is not included in this calculation, since there is no information about the mechanical asymmetry which the KAGRA-SAS typically have. However, it is expected that the active controls is able to clear the requirement for yaw motion, according to the previous experiments.

The problematic issue in the active control system for the type-Bp SAS is that it might be wanted for more rapid damping to use the optical sensors in the calm-down phase, which have narrow linear range. In the worst case, if a huge disturbance is introduced into the test mass and the optical sensors are not available, one has to wait order of 10 minutes. Such situation would not be happened according to the eddy-current damping system. The performance of the damping system is to be investigated.

The calm-down phase		
Items	Requirements	Expected performance
$1/e$ decay time	< 1 min.	< 23 sec.
RMS displacement (longitudinal)	< 50 μm	1.1 μm
RMS displacement (vertical)	< 1 mm	0.01 μm
RMS angle (pitch)	< 50 μrad	1.3 μrad
The lock acquisition phase		
RMS velocity (longitudinal)	< 6.5 μm/sec.	2.3 μm/sec
RMS angle (pitch)	< 2 μrad	1.9 μm/sec
The observation phase		
Control noise at 10 Hz (longitudinal)	< 1×10^{-15} m/$\sqrt{\text{Hz}}$	$5 \sim 8 \times 10^{-16}$ m/$\sqrt{\text{Hz}}$
RMS displacement (longitudinal)	< 70 μm	1 μm
RMS angle (pitch)	< 2 μrad	1.8 μrad

Table 6.7: Fundamental requirements of the active controls for the type-Bp SAS and the expected performance.

Study of the localization of coalescing binaries with a hierarchical network of gravitational wave detectors

PartIII

Overview

This part describes the expected fast sky localization of coalescing binaries with a hierarchical network of three gravitational wave (GW) detectors, HLV (Hanford/Livingston/Virgo), and four detectors, HLVK (Hanford/Livingston/Virgo/KAGRA). A hierarchical network is used for detection of objects with different sensitivity GW detectors, and aims to make effective use of the least sensitive detector's information. In this method, the less sensitive detectors participate only when a trigger is found with the more sensitive detectors' coincidences. However, the signal to noise ratio (SNR) thresholds of the less sensitive detectors are set lower than that of the higher sensitivity ones. The main target of this work is to estimate the benefit of this detection network with 3 or 4 different sensitivity detectors.

In this part, the localization with two higher sensitivity LIGO detectors and the less sensitive Virgo detector and KAGRA detector, is demonstrated by using the previous Mock Data Challenge (MDC) result. In the demonstration, it supposes that this method is implemented into a pipeline for GW and Electromagnetic-wave (EM) follow-up observation. The target GW sources of the pipeline is coalescing compact binary systems. The performances of the localization is investigated in terms of sky maps generated from a pipeline for detection of GWs from compact binary coalescences (CBCs), called Multi-Band Template Analysis (MBTA), and a sky localization pipeline, called BAYESian Tri-Angulation and Rapid localization (BAYESTAR). This part presents the expected localization with HLV and HLVK hierarchical search, and the optimization of threshold SNR for the Virgo and KAGRA detectors.

Source localization and a hierarchical network
Chapter 7

This chapter describes the background on low-latency analysis in GW detection, and motivation of the hierarchical search.

7.1 Background on GW data analysis

Some of the back ground quantities, which are used in the field of the GW data analysis, will be explained in this chapter.

7.1.1 Antenna function

The amplitude of a GW $h(t)$ incidents into a detector is given by

$$h(t) = F_+(\theta, \phi, \psi)h_+(t) + F_\times(\theta, \phi, \psi)h_\times(t), \tag{7.1}$$

where F_+, $F_\times$ are the detector response functions, called antenna function, and $h_+(t)$, $h_\times(t)$ are the two polarization of the GW. The antenna functions depend on the sky location (θ, ϕ), and also the polarization of the source ψ, relative to the detector. The antenna functions are parameters which depend on the geometric of the detector and the source. In a coordinate system with the x, y axes aligned with the detector-arm, its antenna functions are given by

$$F_+(\theta, \phi, \psi) = \frac{1}{2}(1 + \cos^2\theta)\cos 2\phi \cos 2\psi - \cos\theta \sin 2\phi \sin 2\psi, \tag{7.2}$$

$$F_\times(\theta, \phi, \psi) = \frac{1}{2}(1 + \cos^2\theta)\cos 2\phi \sin 2\psi + \cos\theta \sin 2\phi \cos 2\psi. \tag{7.3}$$

The antenna functions F_+, $F_\times$ describe how the two GW polarizations are combined at the detector sensing. The more details is explained in [58].

7.1.2 Effective distance, horizontal distance and detection range

Effective distance

The effective distance of a source inducing a given signal at the detection output, is the distance of an optimally located and oriented source that would produce the same signal strength. Thence, the effective distance denotes the distance to the source when the source is located at just above the detector. Here, substitute a binary inspiral waveform obtained from the post-Newtonian approximation into the equation(7.1). If one focus on either $h_+(t)$ or $h_\times(t)$ term, the strain amplitude $h(t)$ can be described as In this form, the waveform is described as

$$\begin{aligned} h(t) &= \frac{D(t)}{D_{\text{eff}}} \cos\left(\Phi(t) + \Phi_0\right) \\ &= \frac{1}{D_{\text{eff}}} \left(D_c(t)\cos\Phi_0 + D_s(t)\sin\Phi_0\right), \end{aligned} \tag{7.4}$$

where $D(t)$ is a certain distance, D_c, D_s are the cosine and sine part of the waveform at some reference distance, D_{eff} is known as the effective distance to the source, and Φ_0 is the coalescence phase as observed at the detector. D_c, D_s have information of the intrinsic parameters, such as the

chirp mass and spin of the binary. Both of the effective distance and the coalescence phase, depends on the location and orientation of the binary respect to the detector. Especially, the effective distance D_{eff} is defined as

$$D_{\text{eff}} = \frac{R}{\sqrt{\frac{1}{4}F_+{}^2(1 + \cos^2 \iota)^2 + F_\times{}^2 \cos^2 \iota}}, \tag{7.5}$$

where R is the actual physical distance to the source, ι is the inclination angle of the source.

Horizontal distance

The horizontal distance R_{H} is the distance at which an optimally located and oriented source would produce a certain SNR ρ_0 in a detector. Usually, the ρ_0 is set at 8 [59]. The horizontal distance is defined by using sensitivity of a detector, as follows. First, the output from a detector $s(t)$ is described as

$$s(t) = n(t) + h(t), \tag{7.6}$$

where $n(t)$ is the instrumental and environmental noise, $h(t)$ is the GW signal which can be present or absent. Here, the ensemble average of the Fourier components of the noise satisfies

$$\langle \tilde{n}(f)\tilde{n}^*(f') \rangle = \frac{1}{2}\delta(f - f')S(f), \tag{7.7}$$

where angle $\langle ... \rangle$ denotes an ensemble average. The one-sided power spectra density of the detector noise $S(f)$ is defined by eq (7.7). $S(f)$ has dimension of Hz^{-1}, and satisfies $S(-f) = S(f)$. The factor of $1/2$ is inserted in the definition so that the total noise power is calculated by integrating over the range $0 \leq f < \infty$:

$$\langle n^2(t) \rangle = \int_0^\infty df S(f). \tag{7.8}$$

Then, if an inner product is defined as

$$(a|b) = 4Re\left[\int_0^\infty df \, \frac{\tilde{a}(f)\tilde{b}^*(f)}{S(|f|)}\right], \tag{7.9}$$

the SNR of the detector ρ for a given signal h is calculated by

$$\rho^2(t) = (h|h). \tag{7.10}$$

The corresponding detector sensitivity σ in dimension of length is expressed by

$$\sigma^2 = \rho^2 \times D_{\text{eff}}{}^2. \tag{7.11}$$

Thence, the of signal amplitude ρ is proportional to the $D_{\text{eff}}{}^{-1}$. Note that σ can be also expressed by $\sigma^2 = (D_c|D_c)$ according to eq (7.4). Then, the horizontal distance, which is described as the effective distance at the SNR $\rho_0 = 8$, is described by

$$R_{\text{H}} = D_{\text{eff}}(\rho = \rho_0) = \frac{\sigma}{\rho_0} = \frac{\sigma}{8}. \tag{7.12}$$

Detection range

The detection range R_{det} is the spherical radius, whose volume is equal to the volume surrounded by detection radius r_{det}. The detection radius r_{det} is the distance that the detector can sense the signals in each direction for an orientation of the source. The detection radius r_{det} is defined as

$$r_{\text{det}} = R_{\text{H}} \sqrt{\frac{1}{4} F_+{}^2 (1 + \cos^2 \iota)^2 + F_\times{}^2 \cos^2 \iota}, \tag{7.13}$$

where R_{H} is the horizontal distance. By using the detection radius, the detection range is obtained as follows.

$$
\begin{aligned}
R_{\text{det}}(\iota, \psi) &= \left(\frac{3}{4\pi} V(\iota, \psi) \right)^{1/3} \\
&= \left(\frac{3}{4\pi} \int_0^{r_{\text{det}}(\theta, \phi, \iota, \psi)} dr \int_0^\pi d\theta \int_0^{2\pi} d\phi \ r^2 \sin\theta \right)^{1/3} \\
&= \left(\frac{1}{4\pi} \int_0^\pi d\theta \int_0^{2\pi} d\phi \ \left(r_{\text{det}}(\theta, \phi, \iota, \psi) \right)^3 \sin\theta \right)^{1/3}.
\end{aligned}
\tag{7.14}
$$

Due to the directional sensitivity or antenna pattern of the detectors, the detection range R_{det} is smaller than the horizontal distance R_{H} by a factor of 2.26, for the same SNR threshold[52],[53]. Then, the relation is given by

$$\frac{R_{\text{H}}}{R_{\text{det}}} = 2.26. \tag{7.15}$$

Expected SNR

The SNR of a detector is deduced from the detection range and the effective distance. By combining (2.10), (2.11), (2.14), the SNR ρ is given by

$$\rho = \frac{\sigma}{D_{\text{eff}}} = \frac{\rho_0 \, R_{\text{H}}}{D_{\text{eff}}} = \frac{\rho_0 \ \times \ 2.26 \ \times R_{\text{det}}}{D_{\text{eff}}} = \frac{8 \ \times \ 2.26 \ \times R_{\text{det}}}{D_{\text{eff}}}. \tag{7.16}$$

7.1.3   Matched filtering

Matched filtering is the analysis method used in searching GW signals from compact binary coalescences. The matched filter compares the measured signal and the theoretical signal by taking into account of the detector noise, and outputs the SNR $\rho(t)$. Even though the theoretical GW signals from CBC are well known, the wave forms depend on the masses and the spins of the binaries. Thus, the matched filtering needs theoretical wave forms corresponding to all the possible masses and the spins. These waveforms are called templates. The output SNR $\rho(t)$ is given by [52]:

$$
\begin{aligned}
\rho(t) &= \int_{f_{\text{low}}}^{f_{\text{high}}} \frac{Measure(f) \times Template^*(f)}{Noise(f)} \ df \\
&= 4Re \left[\int_{f_{\text{low}}}^{f_{\text{high}}} \frac{\tilde{s}(f) \ \tilde{h}^*_{\text{template}}(f)}{S(f)} \ \exp(2\pi i f t) \ df \right],
\end{aligned}
\tag{7.17}
\tag{7.18}
$$

where f_{low} and f_{high} are the low and high frequency cut offs. The use of a Fast Fourier Transformation (FFT) allows extraction of the signals for all possible arrival times. Then, the sets which give higher SNR than a threshold SNR, are to be searched. The maximum SNR above the threshold is called a trigger, and the corresponding event is considered as a candidate event. The generated triggers are also used to make the detection network by several detectors.

7.1.4   Source localization

When a GW event is detected by several GW detectors, the source position can be obtained from the detection time lags of each detector, by the triangulation. The principle is describes as

$$\theta \;=\; \arccos\left(\frac{c}{d}\,\Delta t\right), \tag{7.19}$$

where θ is an incident angle of the GW, c is speed of light, d is distance of detectors, and Δt is detection time lag between the detectors. Figure 7.1 describes the principle of the triangulation.
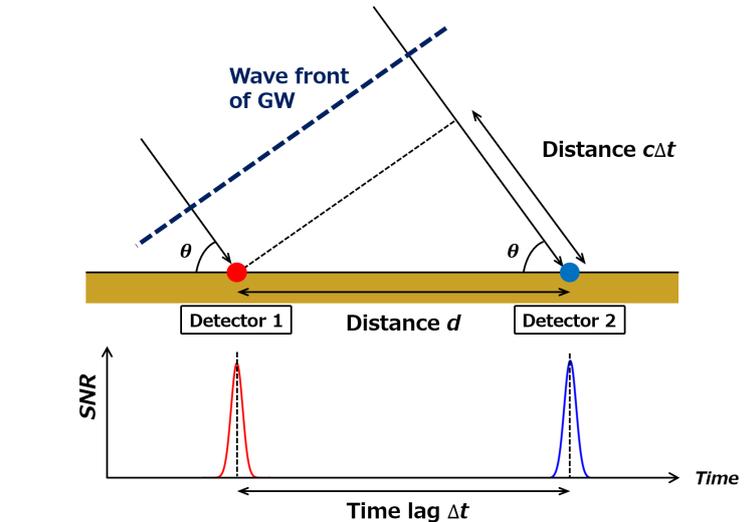

Figure 7.1: Principle of triangulation.

7.2   Hierarchical network search

In order to enhance preciseness of rapid source localization by GW detectors, several GW detectors should be operated together, and thus observation with several GW detectors is important for opening GW astronomy. However, the sensitivities of those detectors, which are operated together, can be different from each other, even if they are operated at the same time. For instance, just after completion of construction of a detector, its sensitivities is expected to be lower than its target sensitivity, and also lower than the already operating detectors' sensitivities. Actually after the LIGO observation O2, operation of the newly made Virgo detector should be started, and it is expected that the sensitivity of the Virgo will be lower than the sensitivities of the LIGO Hanford (H1) and LIGO Livingstone (L1) detector[1]. In such situation, the less sensitive detectors can still contribute to the improvement of the GW source localization.

Here, for example, consider an observation by three GW detectors and the two of them have higher sensitivity. In this situation, if one set a same detection SNR threshold for all the detectors, it is expected that the chances to detect an GW event in all the three detectors are rare. This is because the GW signals can be easily buried into the noise in the lower sensitive detectors, compared to that in the higher sensitivity ones, and thus the lower sensitivity detector generates fewer triggers which are based on GW signals than the higher sensitivity ones. Consequently, even if the two higher sensitivity detectors are able to detect the event, the lower sensitivity one might miss to detect it. Thence, in

---

[1]The sensitivity of the V1 is expected at around 20 Mpc, while for the two LIGOs are expected at around 70 Mpc for 1.4 $M_\odot$ binary neutron star.

order to use the information of the less sensitive detector more, one wants to set lower SNR threshold for the less sensitive one. However, if one lowers the threshold, one has to handle a lot of triggers based on back ground noise, and the large numbers of those triggers can easily increase the computational and time cost. This situation is not suitable for low-latency search. Thence, one has to lower the SNR threshold for the less sensitive detector so that too may background triggers are not generated. The hierarchical search is one method which realizes this aim.

In the hierarchical search, the less sensitive detectors are included into the network with lower threshold SNR than the SNR of the higher sensitive detectors, only when a triggers, which is generated from higher sensitive detector's coincidences, is searched. By using this method, one can set the threshold at lower threshold for the less sensitive detectors without having to handle a lot of the triggers. This searching method would increase chances which the less sensitive detectors are used as the network detectors, and also increase chances to have more precise localization. It is thus expected that opportunities of GW and electromagnetic (EM) wave follow-up observation would be increased by using this hierarchical searching method. This is why the hierarchical search would be useful for including detectors which are newly constructed and have not achieved their target sensitivities yet. The hierarchical analysis is expected to be one approach to include low sensitive detectors into the network.

7.3   Research target and outline

The goal of this work is to study GW source localization with a hierarchical network of 3 or 4 detectors, when the search is implemented into a low latency searching pipeline for GWs from CBC. In particular, there are two targets. First is to optimize the SNR threshold for the less sensitive detectors, and the second is to get the expected localization at the threshold. In this work, hierarchical network with 3 or 4 detectors is assumed to be implemented into a GW-EM follow up pipeline. In order to study the localization of the hierarchical search, previous MDC results are used.

The outlines of this report is as follows. Chapter 8 explains the elements of the GW-EM follow up pipeline, in which the hierarchical network is assumed to be implemented. Chapter 9 explains the localization quantities and the set up for this work. Then, in chapters 10 and 11, the optimization of the SNR threshold for the low sensitivity detectors in the hierarchical search with three or four detectors is described. Chapter 12 summarizes the expected fast localization performance with the hierarchical network search.

GW-EM follow up pipeline
Chapter 8

This chapter highlights the main elements of the GW-EM follow up pipeline. This pipeline is used for the detection of GWs from CBCs. The signals output from GW detectors will pass the pipeline as follows. First, the signals enter a low latency coincident analysis pipeline called Multi-Band Template Analysis (MBTA)[54]. Then, GW candidate events detected by the MBTA are uploaded onto the gravitational wave candidate event database (GraceDb). Finally, the uploaded events are analyzed by a Bayesian triAngulation and rapid localization, called BAYESTAR[55], whereby the probability sky maps for the sky localization of GW candidate events is generated. Events which pass validation process by human monitors are distributed to astronomical partners for EM follow up. Figure 8.1 shows the conceptual diagram of the GW-EM follow up pipeline. Chapter 8.1, 8.2 describes the key elements of the MBTA and BAYESTAR pipeline, respectively.

GW detectors	→	MBTA	→	GraCEDb	→	BAYESTAR	→	EM telescopes
GW data production		Identification of candidate GW events		Uploading information and event validation		Sky localization		EM follow up observations
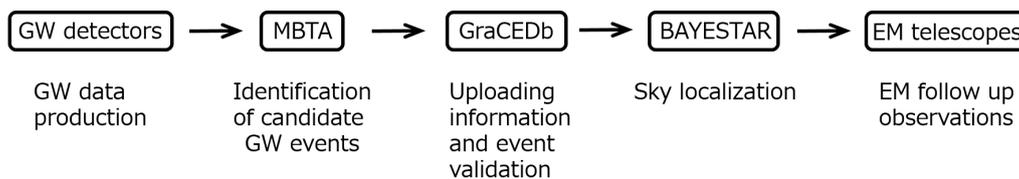
Figure 8.1: GW-EM pipeline.

8.1   Multi-Band Template Analysis : MBTA

The MBTA is a low latency, low computational coincidence analysis pipeline used for detecting GWs from CBCs. In the MBTA, the standard matched filter is implemented to extract CBC signals from GW channel data of each detector in the network independently, before the outputs are combined to find GW candidate events. MBTA is mainly used for the on-line detection of GW candidate events with sub-minute latency, and also for the data quality studies due to the low computational cost. MBTA determines significance of GW candidate events by calculating the false alarm rate (FAR) using data just before the event, to evaluate the detector background noise at the time of the event.

This chapter describes the main elements of MBTA as follows. Chapter 8.1.1 describes what is performed in single detector analysis, before information from each detector is combined. Chapter 8.1.2 highlights the functionality to identify coincidences event.

8.1.1   Single detector analysis

The main functionalities in the part of single detector analysis of MBTA is Multi band matched filtering, χ^2 cut, Matched filter output shape cut, as follows.

Multi-band matched filter

In the MBTA, the matched filter is split into two or more frequency bands. The boundary frequency f_c between the low and high frequency bands is selected so that the SNR is roughly equal between

both of the frequency bands. The typical f_c is set at around 100 Hz. This multi-band method allows a computational reduction, without losing SNR on average compared to a matched filter performed with a single band analysis. This computational reduction is obtained by using shorter templates in each frequency band. Since the phase of the GW signal is tracked over fewer cycles, the multi-band method reduces the number of templates which are required to cover the equivalent parameter space of a single band analysis. Another merit of the multi-band method is that a reduced sampling rate can be set for the low frequency band. Due to the sampling rate reduction, the cost of the Fast Fourier Transforms (FFTs) related with the filtering is reduced.

χ^2 cut

The MBTA has a functionality of χ^2 cut, which checks that the repartition of the SNR of a trigger between the low and high frequency band is consistent with what is expected for a true signal. The χ^2 cut is set at $\chi^2 < (A + B \times \text{SNR}^2)$, for the two band analysis. These typical values are $A = 6$, $B = 0.075$.

Matched filter output shape cut

To reject noise events more efficiently, another signal based consistency test is included. This function is called matched filter output shape cut (MFO shape cut). The MFO shape cut is based on the fact that the SNR time series of the MFO for a GW signal will have one steep peak, while for noise the MFO will have a broader peak with multiple maximums around the central structure. First, the MFO shape cut calculates a ratio R between integrated SNR in the 100 ms surrounding a trigger excluding a small central window of 7.5 ms, and the integrated SNR inside the central window. Then, triggers which do not behave as GW signals, are rejected according to the following formula,

$$R = \frac{\text{surrounding around central window}}{\text{central window}} > \frac{A}{\text{SNR}^2} + B, \tag{8.1}$$

where typically $A = 65$, $B = 0.4$. They are the empirical values.

8.1.2   Identification of coincidences event

The list of the single detector triggers are combined to find coincidence events among GW detectors. The FAR and the combined SNR are computed. MBTA identifies the coincident events by using following time coincidence test and the exact match coincidence test.

Time coincidence test

This test checks the time coincidence of the events between the detectors, considering not only GW time flight between the detectors but also the experimental uncertainty in arrival timing measurement.

Exact match coincidence test

This test requires for the events to be found in all detectors with the same template parameters. The tested template parameters are the component masses and the spins.

8.1.3   Upload to GraceDb

Low FAR events generated by MBTA, which pass a given threshold FAR are uploaded onto the GraceDb. The typical threshold is 1.0×10^{-4} Hz. The submitted information includes the GW arrival times, the arrival timing, SNR amplitudes, the GW phase at coalescence, and the noise curve for each detector at the time of detection of the event.

8.1.4   Template region

Templates of MBTA are divided into three parts on the parameter space depending on masses of binary components: the region 1, the region 2, and the region 3. The region 1 has templates calculated by using low mass binaries such as neutron star binaries. Templates of the region 3 are generated by using high mass binaries composed by such as black holes. The region 2 includes templates obtained from middle mass binaries. The number of templates for the region 1, th region 2, and the region 3 are set at 2×10^5, 4414, and 25604 in this research. Basically, trigger collecting time window is set shorter down to the region 1, whereas, the time window is longer up to the region 3. The region 2 is analyzed by the middle time length.

8.2   BAYESian TriAngulation and Rapid localization : BAYESTAR

The BAYESTAR is a rapid Bayesian sky localization method that takes a few minutes however achieves nearly the same accuracy as a full parameter estimation such as the LALINFERENCE stochastic samplers [56],[57]. Using the information of the GW candidate event, BAYESTAR generates a probability sky map. The main feature of BAYESTAR are highlighted in section 8.2.1, while the section 8.2.2 describes the effect of the arrival time of each detector.

8.2.1   Probability sky localization

BAYESTAR uses the Bayesian approach to make use of the GW observations and prior distributions across the source parameters. It also considers the phase consistency across all detectors in the network. The important characteristic of BAYESTAR is to treat the matched filter detection pipeline, such as MBTA, as a measurement system, treating the parameter estimates that it provides as the experimental input data. It does not use the full GW time series data as in the case of the rigorous full parameter estimated analysis. This approach not only reduces the dimensionality of the data and the signal model, but also allows to avoid directly computing the post-Newtonian model waveforms, making the likelihood much faster to evaluate.

The BAYESTAR likelihood function depends only on trigger information, namely, the time, the phase and the SNR amplitude of the GW event at each detector. BAYESTAR uses the leading order independences of errors in the extrinsic and intrinsic parameters by keeping the masses fixed at the values estimated by the detection pipeline. The simplified probability distribution for the sky positions of sources are generated by numerically integrating the probability in each pixel of the sky map.

All detected GW candidate events are followed up with sky localization probability by BAYESTAR. An example of the sky map generated by BAYESTAR is shown in figure 8.2.
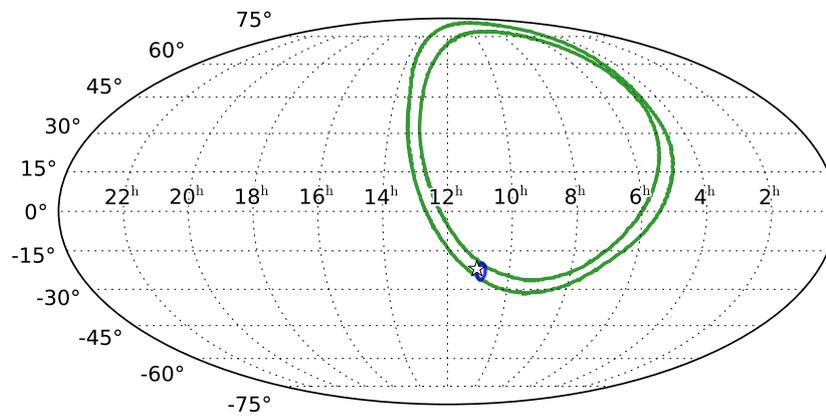
Figure 8.2: Sky map probability generated by BAYESTAR for a simulated GW event detected by MBTA with H1-L1 network (green), H1-L1-V1 network (blue). Astro-hours-Mollweide projection is used as geographic coordinates in this plot. The star shows the position of the injected GW signal and the projected area describes the 90 % confidence area.

8.2.2   Effect of arrival timing to sky map

The BAYESTAR handles two kinds of timing errors. First one is the timing error due to the noise curves, and the second is the timing error depending on the arrival timing among the detectors. The first timing error is used to calculate the resolution of the sky map. The second is for pointing the location of the predicted position. Figure 8.3 shows how the BAYESTAR uses the two kinds of timing errors. The blue and red circled sky maps are obtained from triple coincidence search with H1, L1, V1. The blue map is calculated with using only the timing error from the noise curve. According to the map, the error from noise curve gives only the resolution of the predicted map. On the other hand, the red map is from both of the timing errors, so that, the error from the noise curve and the arrival timing error are considered. In this case, the prediction position is shifted while keeping its resolution for the most part.

According to the maps, the timing error calculated from the noise curve is used to obtain only the uncertainty of the maximum probability.
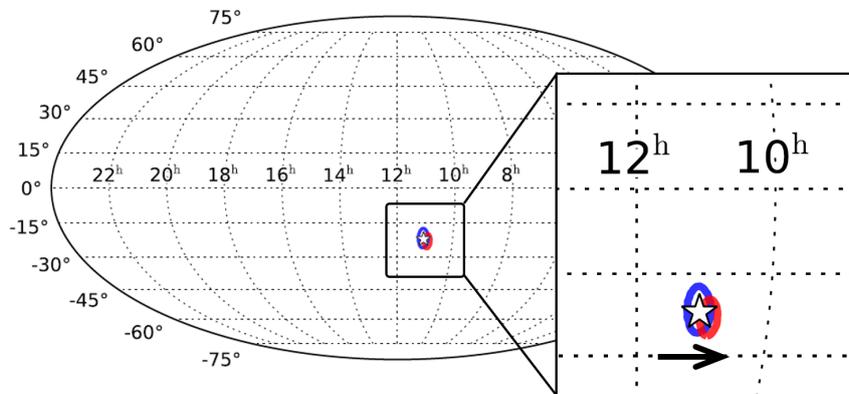

Figure 8.3: Effect of noise curve on its prediction. Blue circled map is generated with using only timing error based on noise curve. Red map is from both of the timing error based on the noise curve and arrival timing.

Calculation setup
Chapter 9

This chapter explains the quantities which measure the localization performance, and how the simulation is conducted. The main flow of this work is shown in figure 9.1. The target is to get the expected sky localization performance with the hierarchical network of three or four detectors, when this method is implemented into GW-EM follow up pipeline. This work focuses on a condition that the two LIGO detectors have higher sensitivity than the Virgo and the KAGRA detector, and investigates the measures of the localization, which are generated from detector coincidence analysis through the MBTA and the BAYESTAR.

Necessary information for this investigation is SNR, arrival time, phase of gravitational waves, and noise power spectral density (PSD) of each detector as the inputs for the BAYESTAR. Those information for the two LIGO detectors are obtained from previous MDC result, while those information for the less sensitive detectors are produced artificially.
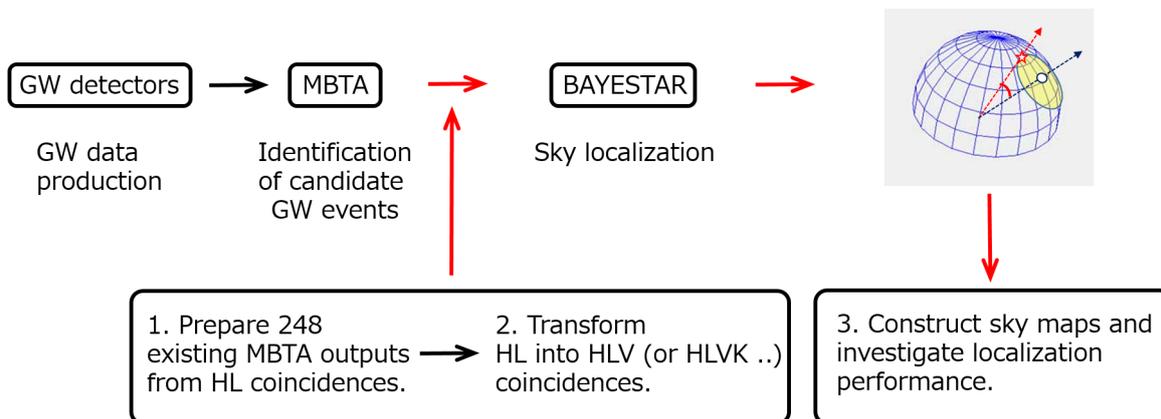

Figure 9.1: Main flow of this work.

This chapter describes the sky localization quantities and how these quantities are generated in this work, including how the information of the low sensitivity detectors are produced. Chapter 9.1 explains sky localization quantities to be investigated. chapter 9.2, 9.3, 9.4 describe the used injection data set, how the information of SNR are generated, and which noise curve is used in this work, respectively. Then, chapter 9.5 summarize the expected localization performance of the two LIGO detectors search. Finally, chapter 9.6 describes how the lower sensitivity detector's information is produced.

9.1 Sky localization quantities

The quantities which describe the Sky localization performances are summarized in this chapter. Two quantities, called the offset angle and the searched area, are especially used to decide the optimal thresholds. This is because both the offset angle and the searched area describe how far the localization is from the true injected position.

9.1.1 Offset angle

The offset angle is the angle between the sky location of the injected GW signal and the reconstructed pixel which has the maximum probability. This is also shown in the schematic diagram in figure 9.2.

9.1.2 Searched area

The searched area is the smallest area of the highest confidence region around the pixel of maximum probability, that includes the sky location of the injected GW signal. For instance, if the injected position is at a pixel of probability p, the searched area is calculated from the sum of all the pixels, which have larger probabilities than p. According to this definition, the searched area should have a similar behavior as the offset angles. The schematic diagram is also in figure 9.2.

9.1.3 Confidence area

The confidence area describes how a sky map is spread or concentrated. This area is calculated as follows. First, pixels are ranked by descending posterior probability. Then, the cumulative sum of the probabilities of the pixels is computed in order. Finally, one obtains the confidence area by finding the index of the pixels of which the cumulative sum is equal to a given value. For example, in order to find the 90 % confidence area, this value is set 0.9.

9.1.4 Probability-Probability plot (P-P plot)

The Probability-Probability plot is used to check the self-consistency of the Sky localization performances. As described above, the searched area explains the accuracy of the sky map, whereas a certain confidence area shows the precision. However, these two quantities should be correlated. For instance, 90 % of events should have their true locations contained within their respective 90 % confidence area, on average. More generally, if we make a cumulative histogram of the confidence levels corresponding to the searched areas of all the events, it should be find close to a diagonal line in the plot, with small deviations due to finite sample size. The plot is called Probability-Probability plot (P-P plot). Particularly, the horizontal axis corresponds to certain confidence area, while the vertical axis is the function of the injections whose true location are within the corresponding confidence areas. This self-consistency test is necessary but not sufficient condition for the validity of any Bayesian parameter estimation scheme.

Basically, if the curve is far below the diagonal line, the obtained statistics are interpreted as optimistic result, according to the sky localization. This is because, for example, even if we search for 90 % confidence area, we cannot find 90 % of the injections. On the other hand, if the curve is far above the diagonal line, the result is regarded as pessimistic.
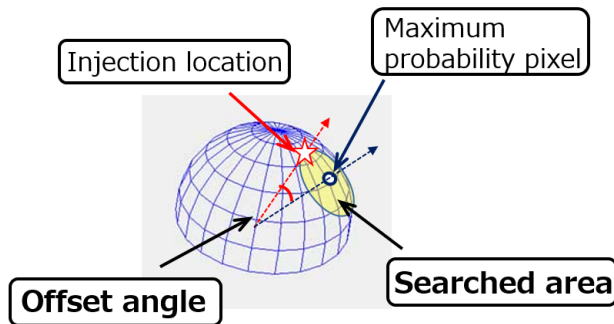
Figure 9.2: Overview of offset angle and searched area. Offset angle and searched area describes the accuracy of the sky map.

9.2   Injection meta data set

248 injection sets, which are selected for a previous MDC, are used in this work[1]. All the waveforms of the injections are Binary Neutron Star (BNS). The waveforms are 'SpinTaylorT4', which are accurate to 3.5 PN order in phase and 1.5 PN order in amplitude. The component masses are distributed between 1.2 $M_\odot$ and 1.6 $M_\odot$ uniformly, and each component has random spin with maximum magnitude 0.05. The 248 sources are located uniformly over the sky as shown in figure 9.3.

---

[1]The investigation and the injection file are available from here :
https://www.lsc-group.phys.uwm.edu/ligovirgo/cbcnote/MBTAlocalisationMDC/2015MDC
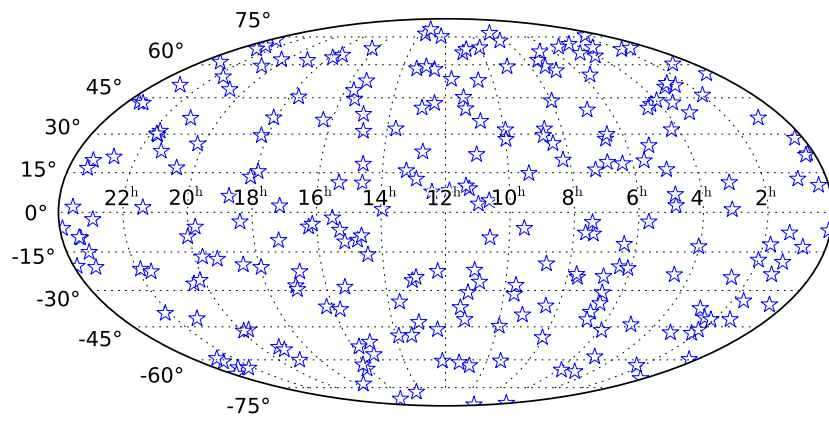
Figure 9.3: Injected source positions. The blue stars describe the location of each injection.

9.3   SNR distribution and False Alarm Probability

This investigation uses the SNR distribution, and the False Alarm Probability (FAP) which is generated from the SNR distribution. They are based on the measurements in the O1 run. The measured SNR distribution is used to produce V1 and K1 SNR, while the FAP is used to decide if a trigger is generated from either a noise, such as a glitch, or a real GW signal. This chapter describes how the SNR distribution and the FAP are constructed.

9.3.1   Measured SNR distribution in O1 run

The SNR for the low sensitivity detectors are generated by using random generator following a SNR distribution. In this work, one SNR distribution based on the O1 measurements, is constructed as follows.

First, some of the measured SNR distributions from about 30 hours data with H1 or L1 detectors are fitted. An example of the measured SNR distribution and the fitted distributions are shown in figure 9.4 and figure 9.5 respectively. These triggers are collected in the period when the H1 and the L1 detector are stationary, namely, when they were not generating many glitches. The curves are extrapolated below SNR 6, because only the data above SNR 6 was recorded. Then, one typical curve is selected from those fitted distributions. In this work, the worst distribution is selected for one below the SNR of 6, while arbitrary one for above the SNR of 6. This is because the random generator should be affected from lower SNR distribution, rather than the higher SNR distribution.
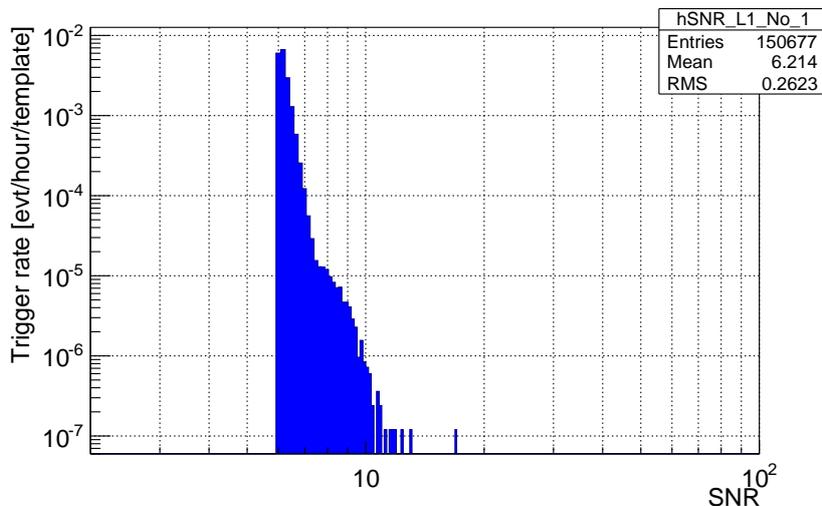

Figure 9.4: An example of the background SNR distribution measured at L1 detector in O1 run.

The selected SNR distribution and its cumulative distribution are plotted in figure 9.6. The cumulative SNR distribution is obtained by counting the cumulative number of the trigger rate in all the bins down to the specific bin. The SNR which holds the lowermost counted bin is called SNR threshold in this theses. The vertical axis is normalized into trigger rate, which is the number of the triggers divided by the analyzed time and by the number of the templates. In the O1 running, only the information of the region 1 of the MBTA was used, and it had about 2×10^5 templates. Thus, all the trigger rates in figure 9.5, figure 9.6 are divided by 2×10^5 templates.
EITHER ADD INFORMATION ABOUT THE REGION, OR REMOVE 'REGION'.
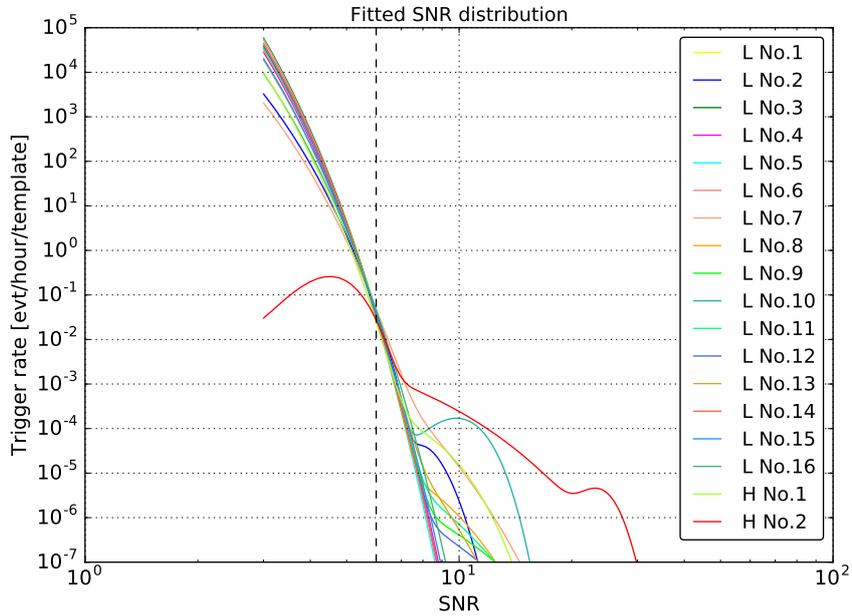
Figure 9.5: Examples of fitted background SNR distribution at H1 and L1 detector in O1 run.
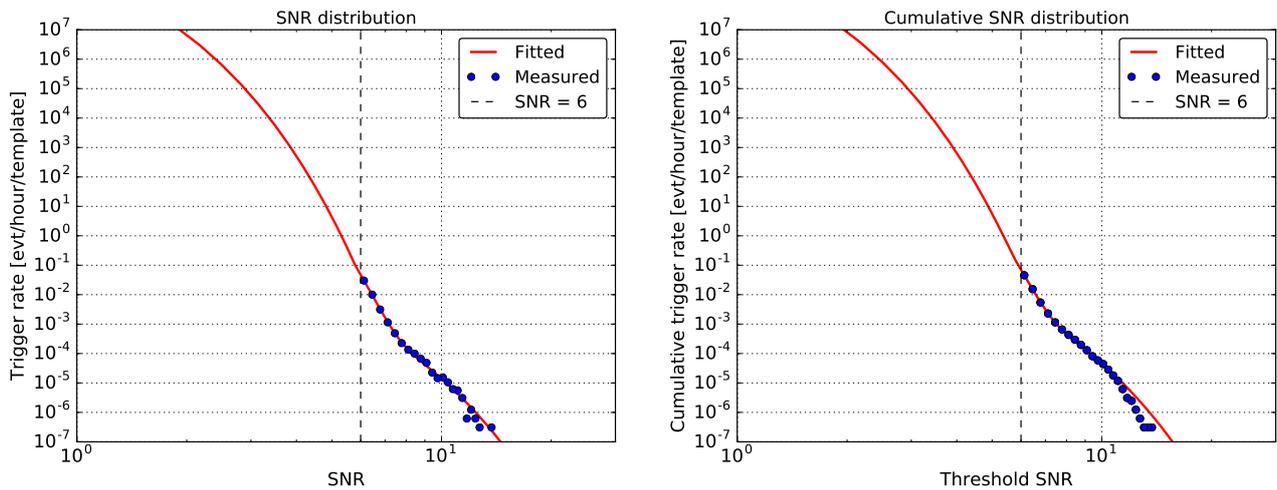

Figure 9.6: Fitted background SNR distribution (*Left*). Fitted cumulative background SNR distribution per template (*Right*). The blue dots are the measured points, while the red curves are obtained by fitting. The vertical axis is normalized into trigger rate, which is the number of the triggers divided by the analyzed time.

9.3.2   Validation of extrapolation

The behavior of other SNR distributions, which have information of lower SNR distribution, are investigated in this section. The purpose is to confirm if the extrapolation at low SNR, which is exerted in above section, is reasonable or not. Then, some SNR distributions from different MBTA searching method[2] are investigated. The obtained distributions and their cumulative distributions are shown in figure 9.7. The curves, except for the red one in figure 9.7, are outputs from off-line analysis. The difference among the curves is the collecting time period to record the triggers. In figure 9.7, the trigger collecting time period becomes shorter and shorter, in the order of the color of green, magenta, yellow, blue and cyan. All triggers except for the red curves are collected in quiet period of H1 detector, in this plot.
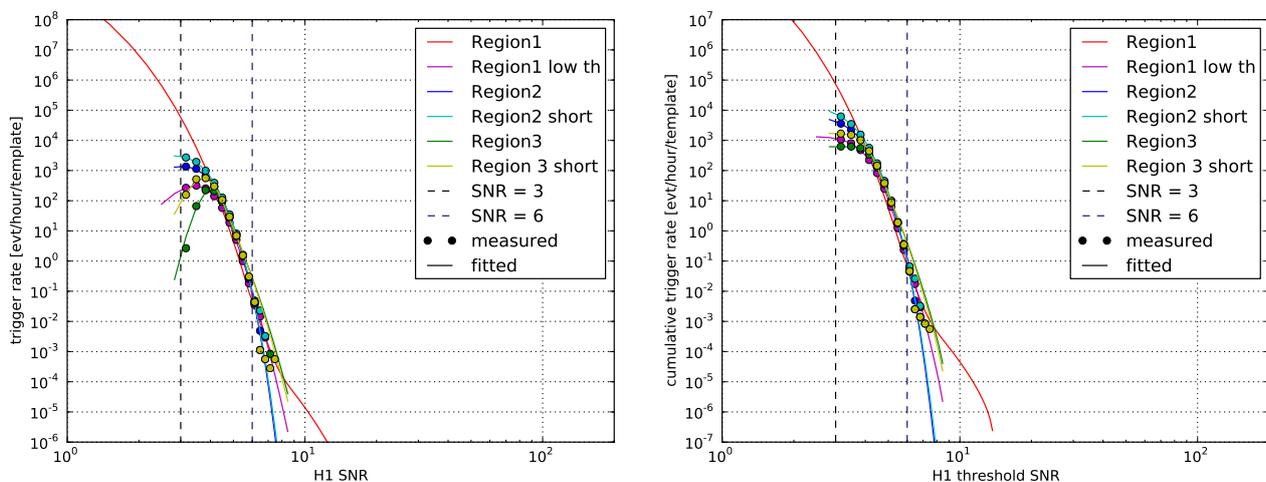

Figure 9.7: SNR distribution (*Left*), cumulative SNR distribution (*Right*). The red curve are extrapolated below SNR 6. Regions denote the template region of MBTA. The 'low th' shows the SNR distribution obtained by using data with lower SNR threshold. Note that this 'Region 1 low th' is analyzed by using 4933 templates. The 'short' represents the SNR distribution calculated by shorter collecting time data. The collecting time becomes longer in the order of the region 1, region 2 and the region 3. The cumulative distribution of the 'region 1 low th' saturates relatively at lower trigger rate. This is because there might a lot of triggers in its collecting time and miss to count large number of the triggers, compared to the other analysis except for the 'region 3' in the plot.

According to the plots, above the SNR of around 4, all the off-line analyzed distributions follow in accordance with with the red line, and behave in mostly the same manner. The differences between the red curve and the others at SNR of 5 is around a factor of 3. It means that the extrapolation in the red line between SNR of 4 and 6, is close to the realistic distribution. In addition, the behavior of the distributions does not depend on the template regions. This fact tells us the SNR distribution does not depend on how the analysis is done, at high SNR.

On the other hand, below around SNR of 4, all the behavior seem to be different, and number of triggers are decreased at low SNR, as shown in figure 9.7 *Left*. The cumulative distribution have a saturation below SNR 4, because of the behavior, as seen in figure 9.7 *Right*. However, this behavior seems to be from artificial problem, due to the following reason. This is because when the time period

---

[2]In O1 running, the MBTA has only one region template (region 1), thus, to produce the SNR distributions from another regions, off-line analysis is necessary.

to collect the triggers is changed, the behavior of the distribution is also changed. For instance, if the time period to collect the triggers is set shorter, the decrease in the distribution or the saturation in the cumulative distribution at low SNR becomes less effective, and becomes closer to the extrapolated red curve. Due to this behavior, the decrease or saturation of the distributions seems to be caused by a method to collect the triggers in the MBTA. The MBTA records only one trigger in a certain time length, above a threshold SNR. The conceptual diagram is in figure 9.8. According to the functionality, if the threshold is not high enough, or if the collecting time is not short enough, some triggers can be missed, without being recorded. This collecting time effect seems to lead the behavior shown in figure 9.7.

Consequently, based on the above result, it is confirmed that the selected red color SNR distribution is available. This is because the extrapolation is valid at high SNR, especially above SNR of 4, and also even below the SNR of 4, the proper distribution seems to be closer to the red colored curve, rather that the others.

Note that apart from the issue about validation of the SNR distribution, it is found that MBTA can not output correct SNR distribution at low SNR, if the collecting time is set too long.
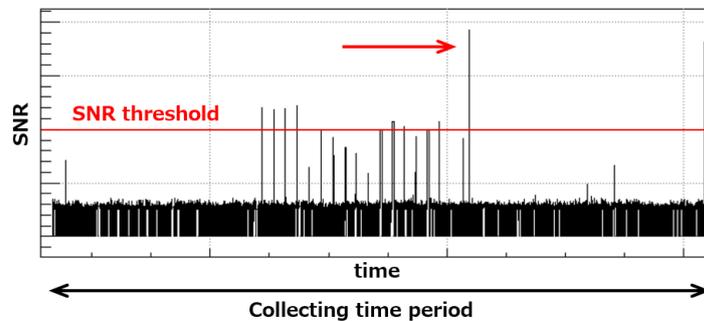

Figure 9.8: Conceptual diagram of collecting triggers in the MBTA. Only one trigger above a given threshold (marked in red), is recorded within a certain time period. If the collecting time period is shortened, the chance to get correct number of triggers is increased.

9.3.3   FAP based on measured SNR distribution

The FAP is calculated from the measured SNR distribution constructed above, via the cumulative distribution, by using the following formula:

$$\text{FAP} \equiv 1 - \exp(-R \times T), \tag{9.1}$$

where R is a cumulative rate of background triggers above a given threshold SNR per one template, which is obtained from the measured O1 data, and T is the time used in the analysis of low sensitivity detectors. The number of the template is set at 2×10^5 for both the Virgo and KAGRA detectors. On the other hand, T is at 70 ms for Virgo, while 80 ms for KAGRA. These numbers come from the differences of typical arrival timing of each detector. In this process, the cumulative distribution is normalized into trigger rate per template. This is because the low sensitivity detectors are analyzed for only one template in this work and there is no need to look for all of the templates in the hierarchical search. The acquired FAP is shown in figure 9.9. In the plot, the horizontal axis is the SNR threshold of one detector, while the vertical axis denotes the probability. According to the plot, the FAP reaches to 1 at around SNR threshold of 3. The shown curves are the FAPs for Virgo and KAGRA detector, which are used in following calculation.
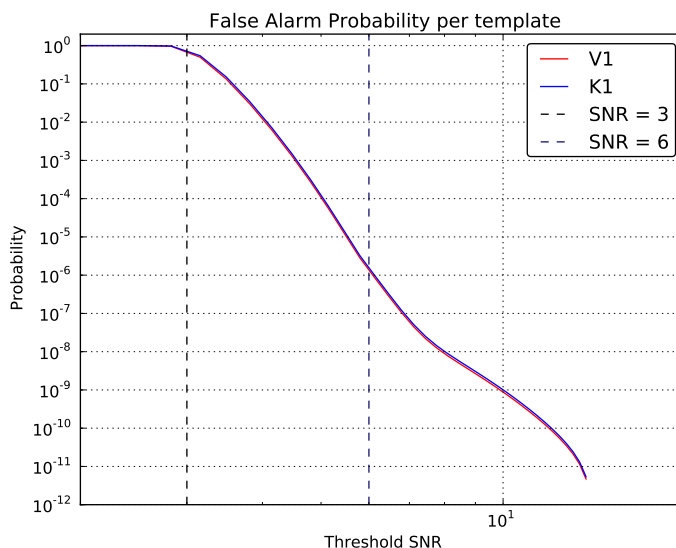

Figure 9.9: False alarm probability (FAP) for V1 (red) and K1 (blue) detector, which are used in this investigation. They are obtained from measured SNR distribution on O1 running, described in chapter 9.3.1.

9.4   Noise curves

The BAYESTAR uses shapes of noise curves[3] to calculate an uncertainty of the maximum probability, via timing uncertainties obtained from the noise curves. This section describes information of used noise curves in this work. Figure 9.10 shows some previously generated noise curves. The curves are based on the expected configuration for the first advanced era observation run in 2015 and 2016 [60]. In the *psd* 2015, the LIGO Hanford (H1) and LIGO Livingston (L1) are assumed to be operating with range of a 54 Mpc for averaged 1.4 $M_\odot$ - 1.4 $M_\odot$ BNS. On the other hand, In the *psd* 2016, the H and L are assumed to be operating with an averaged 1.4 $M_\odot$ - 1.4 $M_\odot$ BNS range 108 Mpc, and the addition of Virgo (V1) with a range of 36 Mpc. The plotted noise curves are Gaussian noise colored to match the expected noise amplitude spectral density curves of these H1, L1, and V1 detectors obtained by mimicking the expected configuration for the first advanced era observation run in 2015 and 2016[4]. The noise curves, labeled as *psd* 2016 in figure 9.10, are used for this calculation.
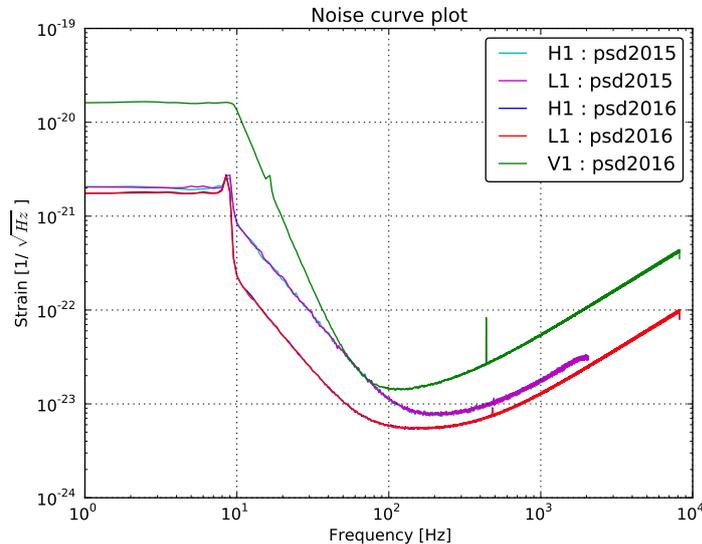

Figure 9.10: Modeled detector noise curves.

---

[3]The sensitivities and noise curves can be input separately in the BAYESTAR.

[4]The noise curves of the *psd* 2016, which are used in this study, are different from what is used in previous investigation. In the previous test, *psd* 2015 was used.

9.5   Sky localization with 2 detectors

This section describes the localization performance of the double coincidences with the H1 and the L1 detector. As seen above, the necessary information to generate a sky map are detected SNR, arrival timing, phase of GW, and a noise curve of each detector. In this investigation of double detectors search, the input information for the BAYESTAR, namely the output of MBTA, was previously generated in a software injection test using injection meta data set introduced in chapter 9.2. The localization performances with the two detector search using such information, are summarized in figure 9.11. In this calculation, 248 sky maps are generated and their statistics of the offset angle, the searched area, 90 % confidence area, and the P-P plot are in the plots. According to the results, the median values of the offset angle, searched area, and 90 % confidence area are 21 deg, 137 deg^2, and 840 deg^2 respectively.

Uncertainties of arrival timing and SNR are shown in figure 9.12. These uncertainties are the ones which are expected to be included during the passing through the MBTA. Figure 9.13 shows the relation between the uncertainties of timing and the expected detection SNR for each H1 and L1 detector. According to them, the absolute value of the timing uncertainties becomes smaller if the detected SNR becomes larger. The SNR dependences of the arrival timing are fitted as follows,

$$\delta t_{\mathrm{H1}} = 0.65 \text{ ms} \times \frac{6}{\mathrm{SNR}_{\mathrm{H1}}^{\mathrm{expected}}},$$

$$\delta t_{\mathrm{L1}} = 0.67 \text{ ms} \times \frac{6}{\mathrm{SNR}_{\mathrm{L1}}^{\mathrm{expected}}}$$

,where the δt_{H1}, δt_{L1} are the absolute values of arrival timing error of each H1, L1 detector.
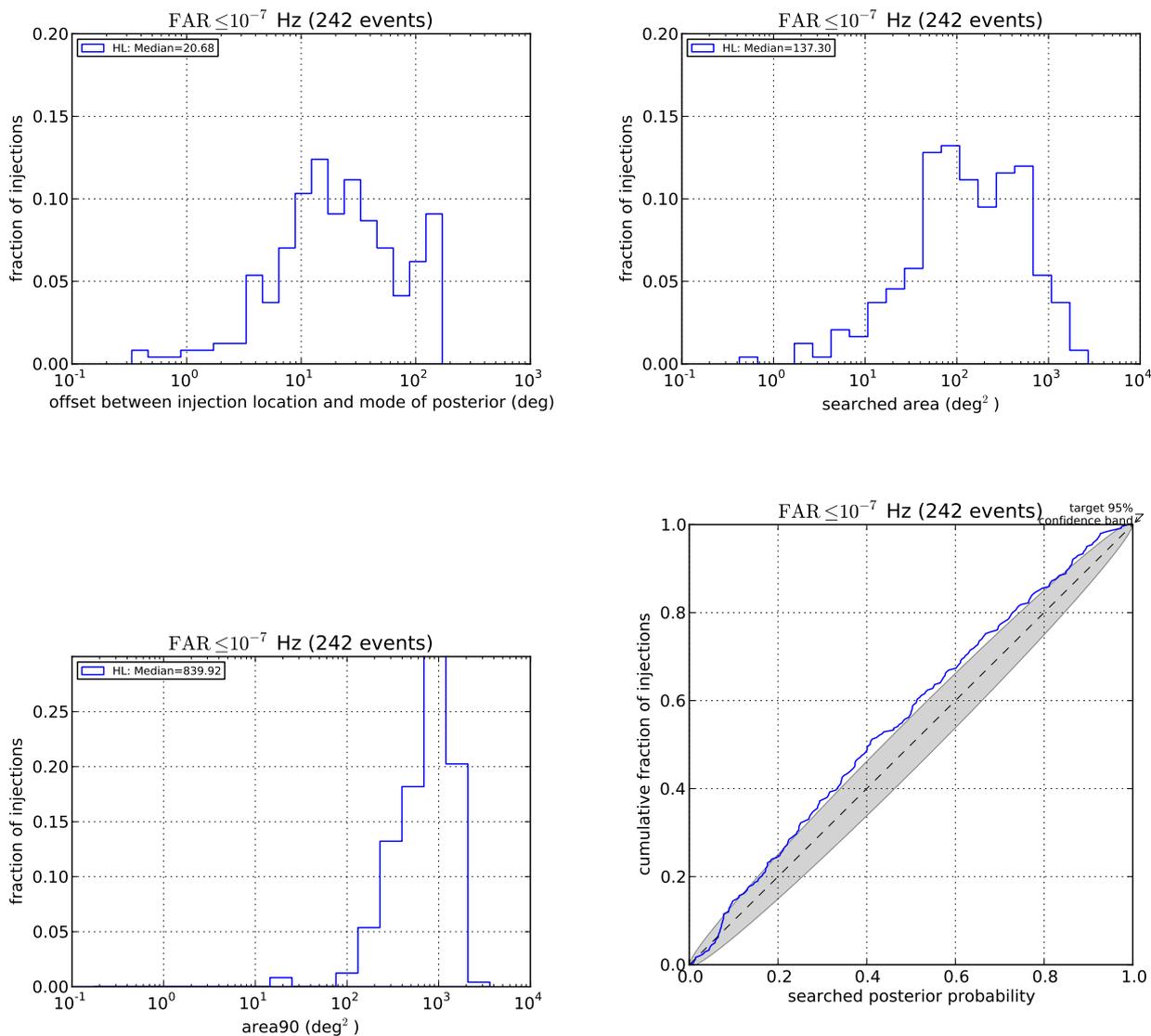
Figure 9.11: Statistics of sky localization performances. Offset angle (*Upper left*), searched area (*Upper right*), 90 % confidence area (*Lower left*), searched probability (*Lower right*) are illustrated. The gray colored area, in the 90 % confidence area plot, denotes the 95 % confidence band. In this thesis, it is regarded as self-consistent if the curve is plotted within or close to the gray area.

	Offset angle	searched area	90 % confidence area
HL (psdHLV_2016MDC)	21 deg	137 deg^2	840 deg^2

Table 9.1: Sky localization performance with HL double coincidence search. The median values of the offset angle, searched area, 90 % confidence area are described.
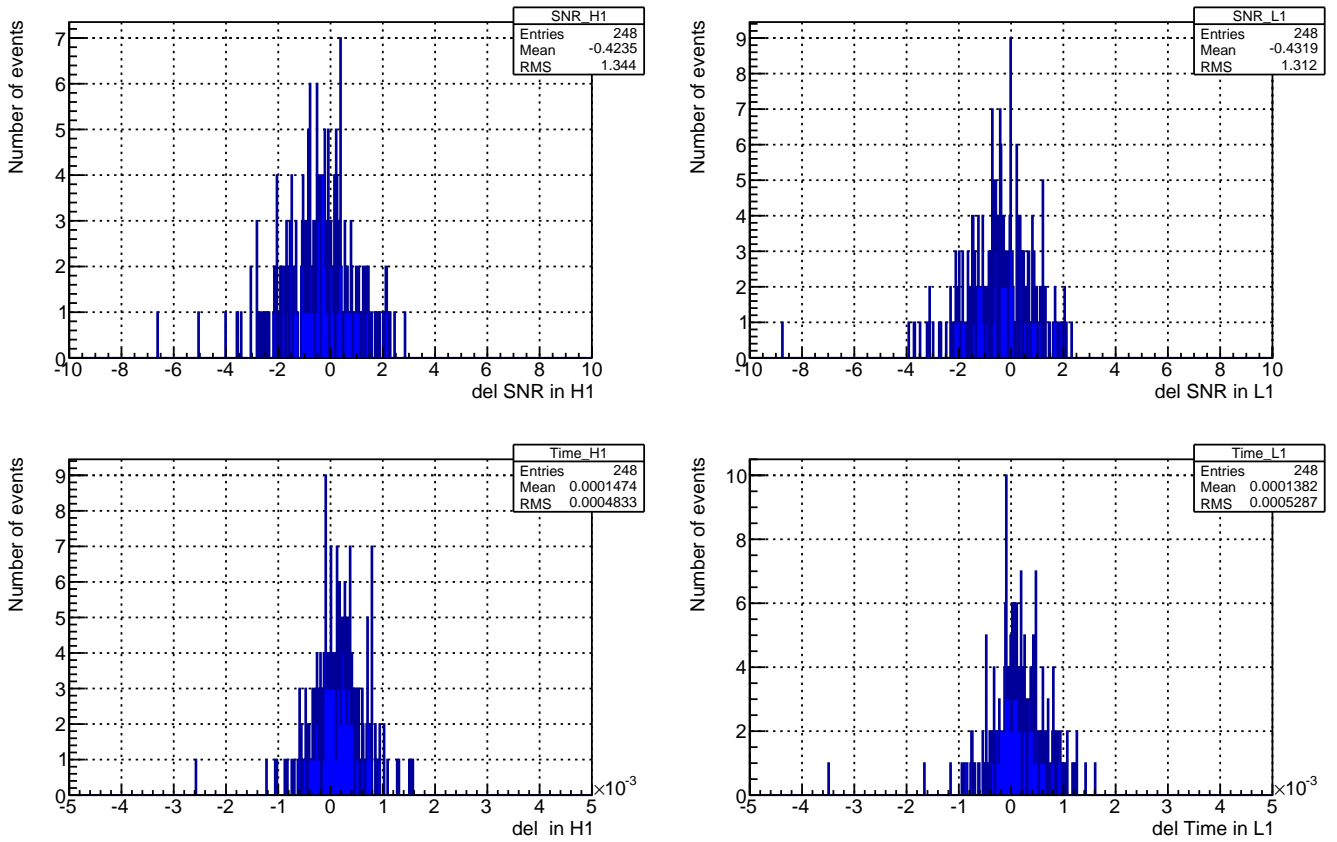
Figure 9.12: Added uncertainties of SNR and timing for H1, L1 detectors.
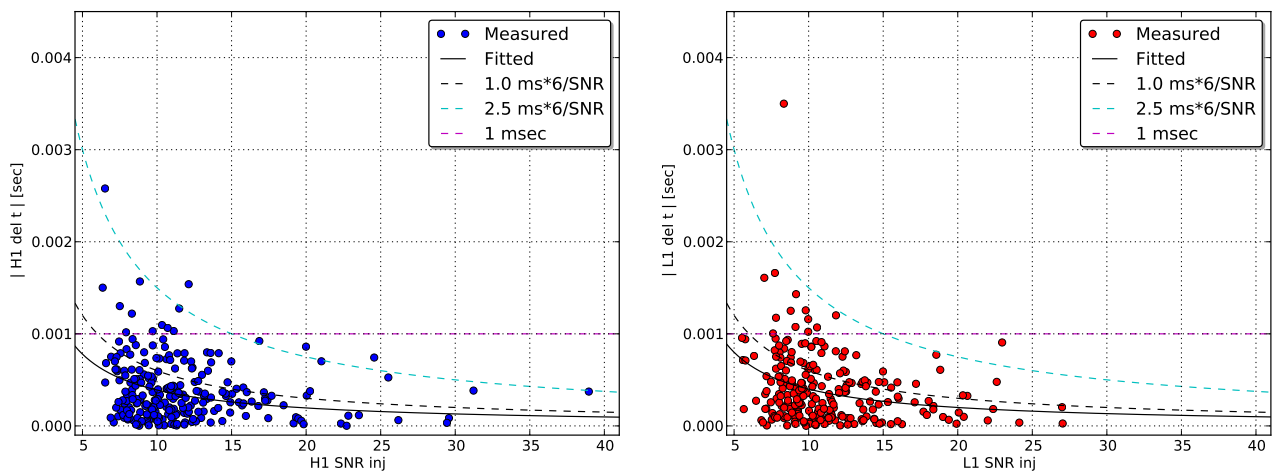
Figure 9.13: SNR dependence of arrival timing error for H1 (*Left*), L1 (*Right*).

9.6   Generating triggers for low sensitivity detectors

The trigger information of the low sensitivity detectors, such as Virgo or KAGRA, is generated as described in this chapter. This is because those detectors are still under construction, and real information is yet to be known. Necessary information for this work is SNR, arrival timing, phase of gravitational waves, and noise curve of each detectors. In this work, the effective distance D_{eff} and the expected SNR is related as described in the 7.1.2. In this simulation, detection ranges for two LIGO detectors (H1, L1) are assumed at 70 Mpc, while 20 Mpc for the Virgo, KAGRA detectors, to consider realistic condition when newly constructed detectors entered the detection network.

The trigger information for Virgo or KAGRA is added to the previous triggers from the double coincidences with H1, L1. Then, information is converted into sky maps via the BAYESTAR.

There are two ways of generating a trigger, and three procedures, as follows.

9.6.1   Triple detector search with HLV

This section describes transforming a set of HL double coincidences, detected in the sky localization MDC into HLV coincidences.

Generating random triggers : V_{random}

This is for a case if we want to make a trigger, which is generated from noise such as glitches:

- SNR = Random above a threshold SNR, following measured O1 SNR distribution.

- Time = $t_0 + \Delta t$
  - $t_0 = t_{\text{H1}}$ if $\text{SNR}_{\text{H1}} > \text{SNR}_{\text{L1}}$, otherwise $t_0 = t_{\text{L1}}$
  - Δt = random uniform number:
    from -35 ms to 35 ms, for V1.

- Phase = random uniform number from 0 rad to 2π rad.

- Effective distance $D_{\text{eff}} = 2.26 \times$ detection range $\times$ 8 / SNR

Generating triggers based on injection parameters : V_{inj}

This is for a case if we want to make a trigger, which is generated from a GW signal :

- SNR = $\text{SNR}^{\text{expected}} + \Delta\text{SNR}$,
  - $\text{SNR}^{\text{expected}} = 2.26 \times$ detection range $\times$ 8 / D_{eff},
  - $\Delta\text{SNR} = $ random Gaussian(0, 1),
  - $D_{\text{eff}} = $ injection meta data,
  - detection range for V1 = 20 Mpc.

- Time = $t^{\text{expected}} + \Delta t$,
  - $t^{\text{expected}} = $ injection meta data,
  - $\Delta t = $ random Gaussian(0, 0.66 ms $\times$ 6 / $\text{SNR}^{\text{expected}}$).

- Phase = $\phi_0 + \Delta\phi$,
  - $\phi_0 = \phi_{\text{H1}} - \Delta\phi_{\text{HV}}^{\text{expected}}$ if $\text{SNR}_{\text{H1}} > \text{SNR}_{\text{L1}}$, otherwise $\phi_0 = \phi_{\text{L1}} - \Delta\phi_{\text{LV}}^{\text{expected}}$, for V1,
    $\phi_{\text{H1}}, \phi_{\text{L1}} = $ measured data by MBTA in the previous injection test,
    $\Delta\phi_{\text{HV}}^{\text{expected}}, \Delta\phi_{\text{LV}}^{\text{expected}}$ are generated from injection meta data,
  - $\Delta\phi = $ random Gaussian(0, 0.25 rad).

Note that the Gaussian(μ, σ) corresponds to this function:

$$\text{Gaussian}(\mu, \sigma) \equiv \frac{1}{\sqrt{2\pi\sigma^2}} \exp\left(-\frac{(x - \mu)^2}{2\sigma^2}\right). \tag{9.2}$$

Here, the $\sigma = 1$ in ΔSNR and $\sigma = 0.25$ rad in $\Delta\phi$ come from measured data by MBTA in the previous injection test.

Mixing procedure

By using V$_{\text{random}}$ and V$_{\text{inj}}$ triggers which are generated as described above, the coincidences of the detectors are constructed as follows. In this procedure, the curve in figure 9.9 is used for the FAP for V1. In the following, p_{V1} is a random uniform number from 0 to 1.

Case 1: V1 triggers are random

This is for the worst case with three detector search.

$$p_{V1} < FAP_{V1} \quad \Rightarrow \quad \text{HL} + \text{V}_{\text{random}} \tag{9.3}$$
$$p_{V1} > FAP_{V1} \quad \Rightarrow \quad \text{HL} + \tag{9.4}$$

Case 2: V1 triggers are based on injection parameters

This is for the best case with three detector search.

$$\text{SNR}_{V1} > \text{Threshold}_{V1} \quad \Rightarrow \quad \text{HL} + \text{V}_{\text{inj}} \tag{9.5}$$
$$\text{SNR}_{V1} < \text{Threshold}_{V1} \quad \Rightarrow \quad \text{HL} + \tag{9.6}$$

Case 3: V1 triggers are either random or based on injection parameters

This is for a more realistic case with three detector search. The coincidences are generated according to the FAP and a given threshold.

$$FAP_{V1} = FAP_{V1}(\text{SNR}) \text{ if SNR}_{V1} > \text{Threshold}_{V1}, \text{ otherwise } FAP_{V1} = FAP_{V1}(\text{Threshold}_{V1})$$

- $p_{V1} < FAP_{V1}$ $\quad\Rightarrow\quad$ HL + V$_{\text{random}}$ (9.7)
- $p_{V1} > FAP_{V1}$ and SNR$_{V1} >$ Threshold$_{V1}$ and $\Rightarrow$ HL + V$_{\text{inj}}$ (9.8)
- $p_{V1} > FAP_{V1}$ and SNR$_{V1} <$ Threshold$_{V1}$ and $\Rightarrow$ HL + (9.9)

$$\tag{9.10}$$

9.6.2 Quadruple detector search with HLVK

This section describes transforming the set of HL double coincidences detected in the sky localization MDC into HLV, HLK, or HLVK coincidences. The concept is same as the case with three detectors search.

Generating random triggers : V_{random}, K_{random}

- SNR = Random above a threshold SNR, following measured O1 SNR distribution.

- Time = $t_0 + \Delta t$
  - $t_0 = t_{H1}$ if $SNR_{H1} > SNR_{L1}$, otherwise $t_0 = t_{L1}$
  - Δt = random uniform number:
    from -35 ms to 35 ms, for V1.
    from -30 ms to 30 ms, for K1 to H1.
    from -40 ms to 40 ms, for K1 to L1.

- Phase = random uniform number from 0 rad to 2π rad.

- Effective distance $D_{eff} = 2.26 \times$ detection range $\times 8$ / SNR

Generating triggers based on injection parameters : V_{inj}, K_{inj}

- SNR = $SNR^{expected} + \Delta SNR$
  - $SNR^{expected} = 2.26 \times$ detection range $\times 8$ / D_{eff}
  - $\Delta SNR =$ random Gaussian(0, 1).
  - $D_{eff} =$ injection meta data
  - detection range for V1 = 20 Mpc
  - detection range for K1 = 20 Mpc

- Time = $t^{expected} + \Delta t$
  - $t^{expected} =$ injection meta data
  - $\Delta t =$ random Gaussian(0, 0.66 ms $\times$ 6 / $SNR^{expected}$).

- Phase = $\phi_0 + \Delta\phi$
  - $\phi_0 = \phi_{H1} - \Delta\phi_{HV}^{expected}$ if $SNR_{H1} > SNR_{L1}$, otherwise $\phi_0 = \phi_{L1} - \Delta\phi_{LV}^{expected}$, for V1
  - $\phi_0 = \phi_{H1} - \Delta\phi_{HK}^{expected}$ if $SNR_{H1} > SNR_{L1}$, otherwise $\phi_0 = \phi_{L1} - \Delta\phi_{LK}^{expected}$, for K1
    $\phi_{H1}, \phi_{L1} =$ measured data by MBTA in the previous injection test
    $\Delta\phi_{HV}^{expected}, \Delta\phi_{LV}^{expected}, \Delta\phi_{HK}^{expected}, \Delta\phi_{LK}^{expected}$ are generated from injection meta data.
  - $\Delta\phi =$ random Gaussian(0, 0.25 rad).

Note that the Gaussian(μ, σ) corresponds to this function:

$$\text{Gaussian}(\mu, \sigma) \equiv \frac{1}{\sqrt{2\pi\sigma^2}} \exp\left(-\frac{(x-\mu)^2}{2\sigma^2}\right) \tag{9.11}$$

Mixing procedure

p_{V1}, p_{K1} = random uniform number from 0 to 1.

Case 1: V1, K1 triggers are random

$$p_{V1} < FAP_{V1} \text{ and } p_{K1} < FAP_{K1} \Rightarrow \text{HL} + \text{V}_{\text{random}} + \text{K}_{\text{random}} \tag{9.12}$$
$$p_{V1} > FAP_{V1} \text{ and } p_{K1} < FAP_{K1} \Rightarrow \text{HL} + \qquad\qquad + \text{K}_{\text{random}} \tag{9.13}$$
$$p_{V1} < FAP_{V1} \text{ and } p_{K1} > FAP_{K1} \Rightarrow \text{HL} + \text{V}_{\text{random}} + \tag{9.14}$$
$$p_{V1} > FAP_{V1} \text{ and } p_{K1} > FAP_{K1} \Rightarrow \text{HL} + \qquad\qquad + \tag{9.15}$$

Case 2: V1, K1 triggers are based on injection parameters

$$\text{SNR}_{V1} > \text{Threshold}_{V1} \text{ and } \text{SNR}_{K1} > \text{Threshold}_{K1} \Rightarrow \text{HL} + \text{V}_{\text{inj}} + \text{K}_{\text{inj}} \tag{9.16}$$
$$\text{SNR}_{V1} < \text{Threshold}_{V1} \text{ and } \text{SNR}_{K1} > \text{Threshold}_{K1} \Rightarrow \text{HL} + \qquad + \text{K}_{\text{inj}} \tag{9.17}$$
$$\text{SNR}_{V1} > \text{Threshold}_{V1} \text{ and } \text{SNR}_{K1} < \text{Threshold}_{K1} \Rightarrow \text{HL} + \text{V}_{\text{inj}} + \tag{9.18}$$
$$\text{SNR}_{V1} < \text{Threshold}_{V1} \text{ and } \text{SNR}_{K1} < \text{Threshold}_{K1} \Rightarrow \text{HL} + \qquad + \tag{9.19}$$

Case 3: V1, K1 triggers are either random or based on injection parameters

$FAP = FAP(\text{SNR})$ if SNR > Threshold, otherwise $FAP = FAP(\text{Threshold})$

- $p_{V1} < FAP_{V1}$ and $p_{K1} < FAP_{K1}$ $\Rightarrow$ HL + V_{random} + K_{random} (9.20)

- $p_{V1} < FAP_{V1}$ and,
  $p_{K1} > FAP_{K1}$ and $\text{SNR}_{K1} > \text{Threshold}_{K1}$ $\Rightarrow$ HL + V_{random} + K_{inj} (9.21)

- $p_{V1} > FAP_{V1}$ and $\text{SNR}_{V1} > \text{Threshold}_{V1}$ and
  $p_{K1} < FAP_{K1}$ $\Rightarrow$ HL + V_{inj} + K_{random} (9.22)

- $p_{V1} > FAP_{V1}$ and $\text{SNR}_{V1} > \text{Threshold}_{V1}$ and
  $p_{K1} > FAP_{K1}$ and $\text{SNR}_{K1} > \text{Threshold}_{K1}$ $\Rightarrow$ HL + V_{inj} + K_{inj} (9.23)

- $p_{V1} < FAP_{V1}$ and
  $p_{K1} > FAP_{K1}$ and $\text{SNR}_{K1} < \text{Threshold}_{K1}$ $\Rightarrow$ HL + V_{random} + (9.24)

- $p_{V1} > FAP_{V1}$ and $\text{SNR}_{V1} < \text{Threshold}_{V1}$ and
  $p_{K1} < FAP_{K1}$ $\Rightarrow$ HL + $\qquad$ + K_{random} (9.25)

- $p_{V1} > FAP_{V1}$ and $\text{SNR}_{V1} > \text{Threshold}_{V1}$ and
  $p_{K1} > FAP_{K1}$ and $\text{SNR}_{K1} < \text{Threshold}_{K1}$ $\Rightarrow$ HL + V_{inj} + (9.26)

- $p_{V1} > FAP_{V1}$ and $\text{SNR}_{V1} < \text{Threshold}_{V1}$ and
  $p_{K1} > FAP_{K1}$ and $\text{SNR}_{K1} > \text{Threshold}_{K1}$ $\Rightarrow$ HL + $\qquad$ + K_{inj} (9.27)

- $p_{V1} > FAP_{V1}$ and $\text{SNR}_{V1} < \text{Threshold}_{V1}$ and
  $p_{K1} > FAP_{K1}$ and $\text{SNR}_{K1} < \text{Threshold}_{K1}$ $\Rightarrow$ HL + $\qquad$ + (9.28)

Sky localization with hierarchical search of 3 detectors

Chapter 10

This chapter describes the expected fast localization with the hierarchical search of three GW detectors of H1, L1, and V1 network. Results shown in this chapter are obtained by following the procedure described in chapter 9.6.1. Chapter 10.1 describes the typical sky maps, and the typical localization performances with HLV hierarchical search. Chapter 10.2 shows the optimization of the SNR threshold for the V1 detector, according to the localization performances. Chapter 10.3 tests if the artificial trigger information is reasonable. The localization for cases where there are a lot of background triggers, is investigated in chapter 10.4. Chapter 10.5 describes the localization performance of HLV hierarchical search compared to HL double coincidence search.

10.1   Sky localization performance

Typical sky maps generated from MBTA outputs through BAYESTAR are shown in figure 10.1 and figure 10.2. They are from HL double coincidences, and HLV triple coincidences. Figure 10.1 shows the sky map generated from triple coincidences with V1 trigger based on noise, while figure 10.2 shows the sky map from triple coincidences with V1 trigger based on GW signal. Table 10.1 describes the localization performance of the two events shown in figure 10.1 and figure 10.2. These events are found when the threshold SNRs are set at 5 for H1 and L1, while 3.5 for V1 detector.

Item	Offset [deg]	Searched area [deg^2]	90 % area [deg^2]
Contribution of V$_{\mathrm{ran}}$			
HLV$_{\mathrm{ran}}$	45	429	247
HL	28	315	916
Contribution of V$_{\mathrm{inj}}$			
HLV$_{\mathrm{inj}}$	2	8	61
HL	132	1134	1357

Table 10.1: An example fast sky localization with HLV hierarchical network. The upper row event is found with SNRs of 9.5, 10.7, 4.1 for H1, L1, V1. This event is generated from HLV hierarchical network with V1 trigger based on noise. While the lower event is found with SNR of 8.2, 7.2, 5.5 for H1, L1, V1. This event is from HLV hierarchical network with V1 trigger based on GW signal. The corresponding performance of HL search is described.

According to the two events, the V$_{\mathrm{ran}}$ does not contribute to the improvement of the sky map accuracy, even though the resolution of the prediction is improved. On the other hand, V$_{\mathrm{inj}}$ improves both the precision and the accuracy of the map.
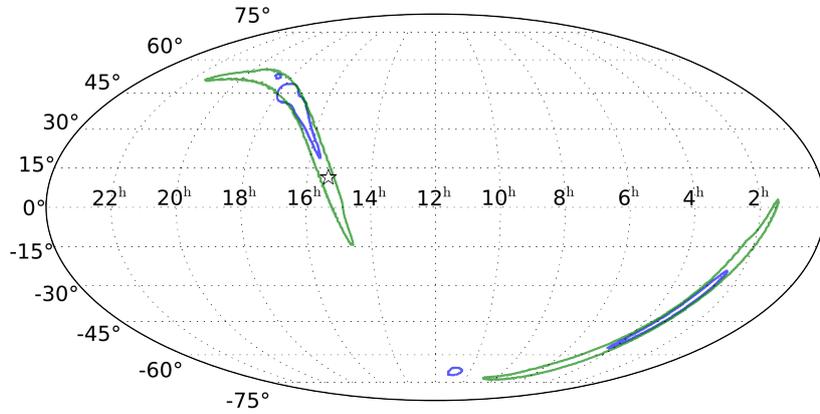
Figure 10.1: Examples of sky maps from the trigger HL double coincidences (green) and from HLV_{ran} triple coincidences (blue). The star indicates the location of the injected source. Even though the precision of the prediction is improved, the injected location is found out of the 90 % confidence area.
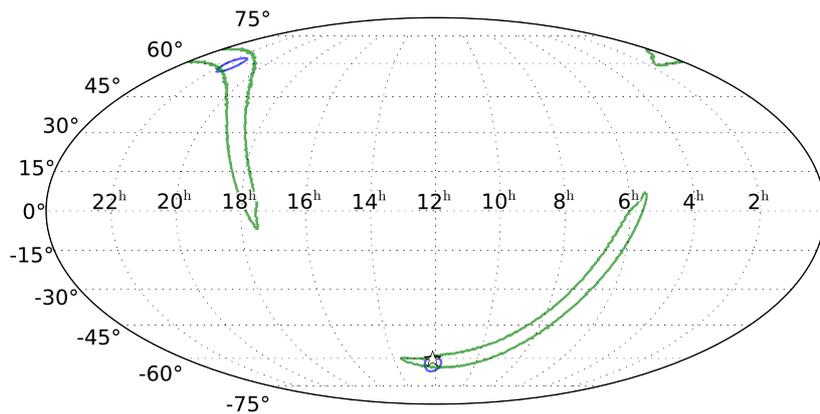

Figure 10.2: Examples of sky maps from the trigger HL double coincidences (green) and from HLV_{inj} triple coincidences (blue). The star indicates the location of the injected source. Both precision of the prediction and accuracy of the sky map are improved.

To confirm localization performance more statistically, offset angle, searched area, 90 % confidence area are collected into the histograms shown in figure 10.3 for all 248 events, and for each case. The color indicates the information of the cases which are defined in the chapter 9.6.1. All performances shown in figure 10.3 are obtained when the SNR threshold is set at 3.5 for V1, while 5 for the H1 and L1.
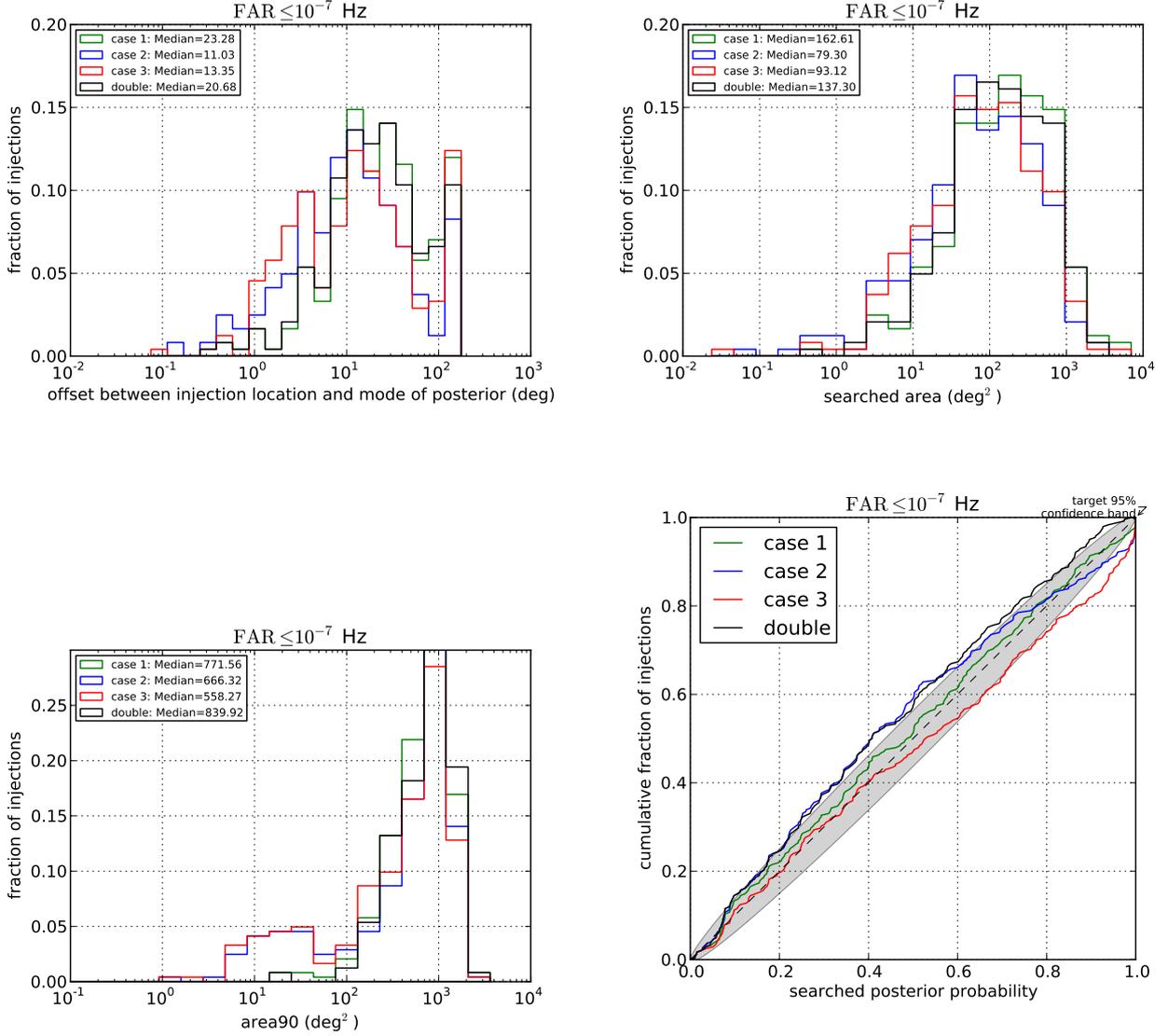
Figure 10.3: Offset angle (*upper left*), serched area (*upper right*), cumulative 90 % confidence area (*lower left*), P-P plot (*lower right*). The green, blue, red, black curves correspond to case 1, case 2, case 3 with 3-detector search with HLV, and 2-detector search with HL, respectively.

According to the offset angle and the searched area, in case 1 (green), the V1 triggers from noise do not contribute to the improvement of the localization. This is because, for instance, in the offset angle plot (Fig 10.3 *upper left*), the population at the lower angle becomes smaller, while the the

population at the higher angle becomes larger, compared to the result of the HL double coincidences search. Then, the V1 triggers generated from noises give only worse localize performances, and thus the behavior of case 1 tells the worst performances of the analysis method at the threshold SNR. This effect can also be seen in the median values of the offset angle and the searched area. In the investigation of the threshold 3.5, case 1 has 13 % of the V1 triggers from the noise, while about 87 % are HL double triggers. On the other hand, in case 2 (blue) and case 3 (red), the population of lower angle becomes larger while that of higher angle becomes smaller, compared to the HL double coincidence search. According to this, the V1 triggers based on real GW signals, improve the localize performances. In case 2, all V1 triggers are based on the GW signals, even if one sets a low threshold SNR for the V1, such as 2. While in case 3, the V1 triggers are a mixture of both triggers from noises and the GW based triggers. This is why case 2 investigation gives better results than the case 3 search at the threshold. Thus, the results of case 2 give the best performances of the localization. However, in a more realistic situation, some triggers generated from noises should be included, if one sets low threshold SNR around 2. Thus, the results of case 3 provide more realistic localize performances.

The 90 % confidence area (Fig 10.3 *lower left*) describes that the size of the predicted confidence area tends to shrink by adding V1 information. This happens if one uses a V1 trigger from noise.

The P-P plot describes if the obtained histograms are realistic or not, as described previously. If the calculation is done with proper settings, the curve should follow the diagonal line. This is because in such situation, 90 % of the injections should be found in the 90 % confidence area, for instance. Thus, if the curve is below the diagonal line, then too much timing uncertainties are added into the V1 triggers. Then according to the blue line (case 2) in figure 10.3 *lower right*, the added timing error into the V1 triggers is adequate, because the most of the curve follows the diagonal line. Other curves except for case 2, which are generated by using some of V1 triggers from noises, and thus the P-P plots tends to stay below the diagonal line or the curve of the HL double search. This is because the V1 triggers from noise should have large timing errors, compared to the timing error expected from the noise curve.

Note that in case 2, there are 28 % V1 triggers based on the GW signals and 72 % of HL double coincidences. While case 3 has 11 % of triggers from noises, 29 % of GW based triggers, and 60 % of HL double coincidences.

Consequently, in the worst case at this threshold, even if V1 enters the detection network, the localize performance does not improve and can get worse. On the other hand, according to the case 2 investigation, the V1 triggers based on the GW signals improve localization. If the V1 threshold is set at 3.5, the median value of the offset angle can be about 60 %times smaller than that of the HL double detector search.

10.2   Optimization of V1 threshold SNR

This chapter describes the optimization of the SNR threshold for the V1 detector using localization performances. The median values of the sky localization statistics shown in figure 10.3, are collected for each case by changing the V1 SNR threshold. The purpose of this investigation is to obtain the optimal SNR threshold for the V1 detector. Table 10.2 describes the population of the triggers, offset angle, and the searched area, 90% confidence area of each case at each V1 threshold. Note that in this calculation, threshold SNR of H1, L1 are set at 5, and the mean values of the SNR for H1, L1 are 11. In addition, the median values of the offset angle and the searched area by double coincidences HL are 21 deg, 137 deg^2, respectively.

V1 threshold	HLV_{ran}	HLV_{inj}	HL	Offset [deg]	Searched area [deg^2]	90 % area [deg^2]
Case 1						
3.0	78 %	0 %	22 %	28	249	489
3.5	13 %	0 %	87 %	23	163	772
4.0	1 %	0 %	99 %	21	137	834
5.5	0 %	0 %	100 %	21	137	840
Case 2						
2.0	0 %	59 %	41 %	7	61	511
3.0	0 %	37 %	63 %	10	94	645
3.5	0 %	28 %	72 %	12	95	666
4.0	0 %	22 %	78 %	13	102	723
5.5	0 %	10 %	90 %	17	107	791
7.0	0 %	5 %	95 %	19	120	812
8.0	0 %	4 %	96 %	19	124	820
10.0	0 %	1 %	99 %	21	133	835
Case 3						
2.0	66 %	34 %	0 %	14	112	353
2.5	67 %	33 %	0 %	15	124	358
3.0	52 %	33 %	16 %	14	117	382
3.1	41 %	33 %	26 %	13	103	391
3.2	32 %	32 %	36 %	13	134	434
3.3	25 %	30 %	45 %	13	97	494
3.4	19 %	30 %	51 %	14	103	544
3.5	11 %	29 %	61 %	13	95	599
3.6	8 %	28 %	64 %	13	94	628
3.7	5 %	27 %	68 %	13	94	650
3.8	3 %	25 %	72 %	14	97	673
3.9	2 %	24 %	74 %	14	96	681
4.0	1 %	23 %	76 %	14	103	714
4.5	0 %	18 %	82 %	15	103	729
5.0	0 %	15 %	85 %	15	107	766
5.5	0.4 %	10.5 %	89.1 %	16	107	746
7.0	0 %	5 %	95 %	19	126	830
8.0	0 %	3 %	97 %	20	129	832
10.0	0 %	1 %	99 %	21	136	835

Table 10.2: Trigger population, offset angle, searched area, 90% confidence area of HLV hierarchical search.

Figure 10.4 shows the median values of the offset angle and the searched area at each threshold, compared to the results of HL search. In case 3 investigation, calculation is repeated for three times, using different set of random numbers, to estimate the uncertainties of these median values. Thence, the averaged values of case 3 results are shown in table 10.2. Figure 10.4 gives the following information.
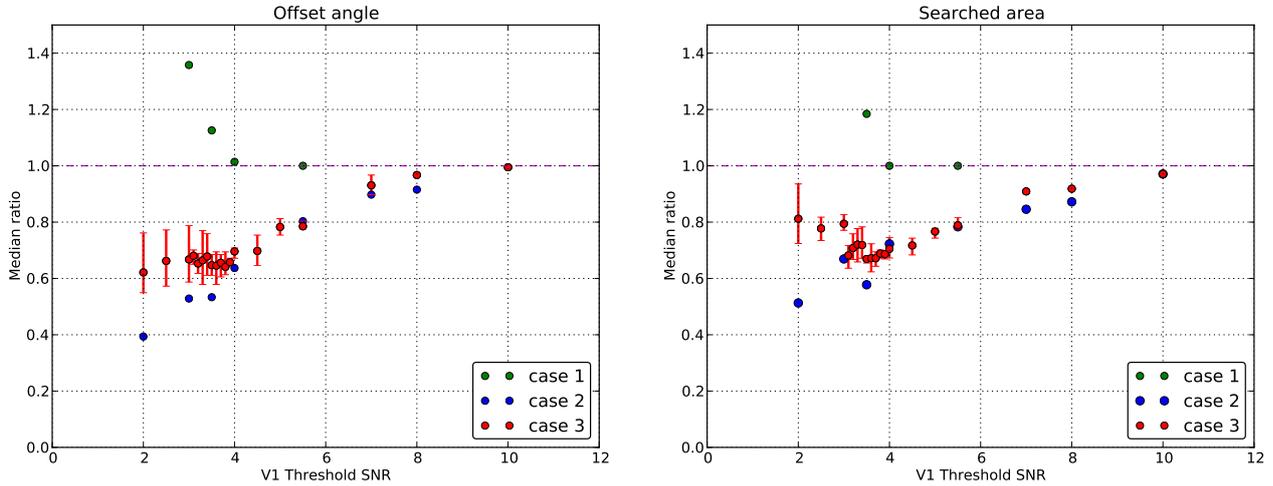

Figure 10.4: Median ratio of Offset angle ($Left$), searched area ($Right$). Both of the vertical axes are normalized with the values of the double coincidence search. In case 3 investigation, calculation is repeated for three times, using different set of random numbers.

First, in all the cases, if the V1 threshold is set at high SNR, such as 10, the performance becomes closer to that of double coincidences, because the number of the HL double coincidence triggers are increased when the threshold is set higher.

Second, according to case 1, the V1 triggers generated from noise do not contribute to the improvement of the Sky localization performances. If the V1 threshold is lowered in this case, the localization performance worsens, because of an increase in the number of the V1 triggers from noise. This is the worst performance with the hierarchical search using H1,L1,V1.

Third, in case 2, the lower the V1 SNR threshold is set, the better the localization becomes. Case 2 investigation gives the best performance at each threshold, because all V1 triggers are GW signals. If the MBTA could find the triggers generated only from GW signals from V1 detector signal, the offset angle and the searched area are reduced from 21 deg, 137 deg^2 to 7 deg, 61 deg^2 at threshold 2.

Fourth, in case 3, a more realistic behavior of the localization is shown, because the triggers in this case include all the triggers. The triggers consist of HL and V1 triggers from noise, HL and V1 triggers based on GW signals, and HL double coincidence triggers. They are mixed depending on the FAP and the threshold SNR. The uncertainties of the median values become larger below threshold SNR of 4, because the population of the triggers can be changed easier, compared to the higher threshold case. Since the FAP becomes larger than 0.01 at those thresholds, the FAP become to comparable value to the generated random numbers. According to the figure 10.4, the searched area has a local minimum value. This is because, if the threshold is set too low, the number of the V1 triggers from noise increases and effect of the noises become more dominant than the effect of the V1 triggers from the signals.

Finally, according to the two statistics, the optimal threshold for the V1 detector in the hierarchical search is between 3.5 and 4. At the threshold, the offset angle, the searched area are around 0.7 times

smaller than the values with double coincidence search.

On the other hand, figure 10.5 gives 90 % confidence area as a function of the V1 SNR threshold of the HLV hierarchical search. As described in the previous section, a confidence area gives information of precision of the predicted region, while offset angle and searched area give information of accuracy of the predicted sky map. According to the plot, the areas for all cases are reduced when the SNR threshold is lowered, due to the increase in number of the participating detectors in the network. The saturation seen in the case 3 curve happenes because all the triggers are generated from triple coincidences. The expected minimum value of the 90 % confidence area with HLV hierarchical search is 380 deg^2 below the threshold SNR 3 in this investigation.
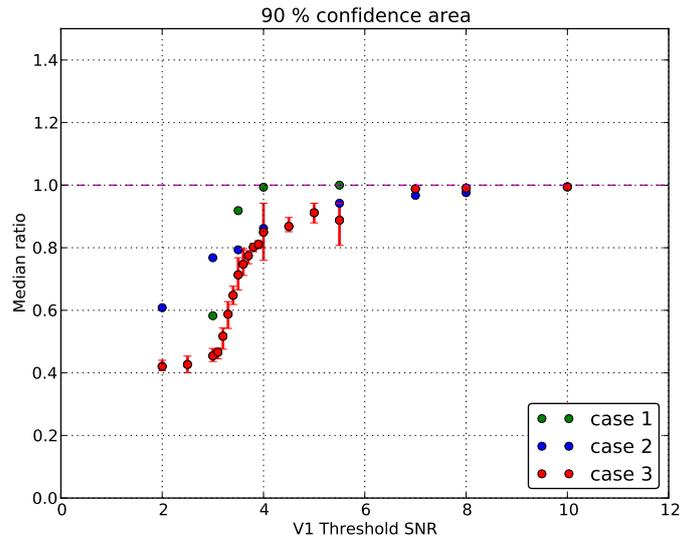
Figure 10.5: 90 % confidence area with HLV hierarchical search. The vertical axis is normalized with the value obtained in HL double search.

Thus, from the point of view of 90 % confidence area, setting low SNR threshold as long as possible, would give better localization. In the end, based on all of the offset angle, searched area, and the confidence area, the optimal threshold for the V1 detector in this search is around 3.5. At the threshold, expected offset angle, searched area, and 90 % confidence area are about 13 deg, 93 deg^2, 600 deg^2, respectively. At the threshold, about 40 % of all the triggers are from HLV triple coincidences, while others are from HL double coincidences. Also the HLV$_{\mathrm{ran}}$ triggers comprise 11 % of all the triggers at the threshold of 3.5.

In conclusion, it is confirmed that the hierarchical search allows making effective use of the low sensitivity detector. The expected fast localization of the HLV hierarchical network at the optimal SNR threshold is summarized in table 10.3.

SNR threshold	Offset [deg]	Searched area [deg^2]	90 % area [deg^2]
5 for H1, L1, 3.5 for V1	13 deg	93 deg^2	600 deg^2

Table 10.3: Expected fast sky localization performance with HLV hierarchical network.

This V1 optimal threshold, however, largely depends on a lot of assumptions, especially the sensitivities of each detector, the SNR distribution, and FAP. Thus, if more exact optimal threshold is necessary, this investigation should be repeated by using more realistic SNR distribution, FAP based on a measurement.

10.3   Self-consistency test

As described above, the optimal threshold is obtained at around 3.5, based on the statistics of offset angle, searched area, and 90 % confidence area in the calculation of case 3. This section tests the feasibility of the results according to the P-P plot. This plot describes whether or not the added timing error for V1 detector is reasonable. As described in chapter 9.1.4, the curve should follow the diagonal line if the performance is feasible. In other words, curves in P-P plot becomes closer to the diagonal line if the added timing uncertainties are adequate. For example, if an added timing error is too large, the number of the injections detected within a certain confidence area tends to become smaller, and thus the curve tends to shift towards a lower direction, compared to the diagonal line.

Figure 10.6 shows the P-P plots, obtained in the optimization work. All those curves are from case 2 investigation. This is because if case 3 is investigated, one has to treat V1 triggers based on noise. Since the purpose of this self-consistency test is to verify if the added timing error is reasonable or not, one has to remove V1 triggers based on noise in this test. The *Left* plot shows the P-P plot when the timing uncertainty Δt is generated from following Gaussian function, $\Delta t \equiv \text{Gaussian}(\mu, \sigma) = \text{Gaussian}(0, 0.66 \text{ ms} \times 6/\text{SNR}^{\text{expected}})$. While, the *Right* plot shows the dependence of the RMS value of the timing uncertainty σ when the V1 SNR threshold is set at 2.0. The left plot implies that the added uncertainties into the V1 timing in this work is appropriate, because all the curves are not so far from the target 95 % confidence band.
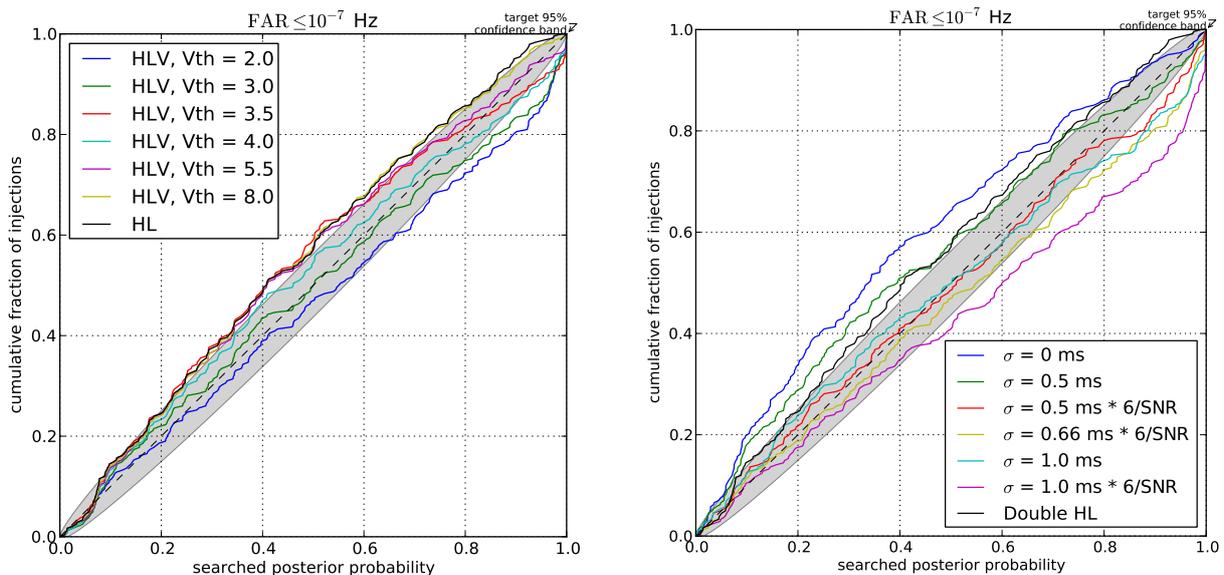
Figure 10.6: P-P plot in the case 2 with various V1 SNR thresholds (*Left*), P-P plot in the case 2 at the SNR threshold 2 with various timing error σ (*Right*)

However, when the threshold is set at a lower value than around 3, the added timing error seems to slightly largen. While the right plot implies that if σ is set at small value, the curve shifts upwards. It seems to be better to set σ as $\sim 0.5 \text{ ms} \times 6/\text{SNR}^{\text{expected}}$, at the SNR threshold 2. Thence, the model of the timing error which was used in this investigation works around the optimal SNR threshold. However it is not the best model for investigation of low threshold behavior such as below around 2.

Consequently, it is confirmed that the added timing error for V1 is reasonable at around the optimal

threshold. If one wants to study the behavior at the SNR threshold of around 2 more in detail, it is better to use more realistic SNR dependence of σ.

10.4   Effect of noisy background triggers

Above investigations focuse on the case where the less sensitive V1 detector is stable. However, GW detectors sometimes generate a lot of background triggers called glitches. The condition which a detector generates glitches is called 'noisy' condition in this section. In this situation, the background SNR distribution differs from the one seen in previous section. In the actual low latency search, the data from noisy background can be included into the analysis because veto system in the latency search is not set so strictly. This chapter describes the localization performance when the low sensitivity detector generates a lot of background triggers. The purpose of this investigation is to know how the noisy condition contributes to the sky localization.

10.4.1   SNR distribution and FAP in noisy case

In this noisy case investigation, the SNR distribution and the FAP of the V1 detector is changed. Figure 10.7 describes the SNR distribution and the FAP in this investigation. The red colored curves are for the case when the detector is stable, while the blue curves correspond to the noisy condition. Thus, the main effect of the noisy SNR distribution would occur above the SNR 4, and the optimal threshold would be the same as the previous result.
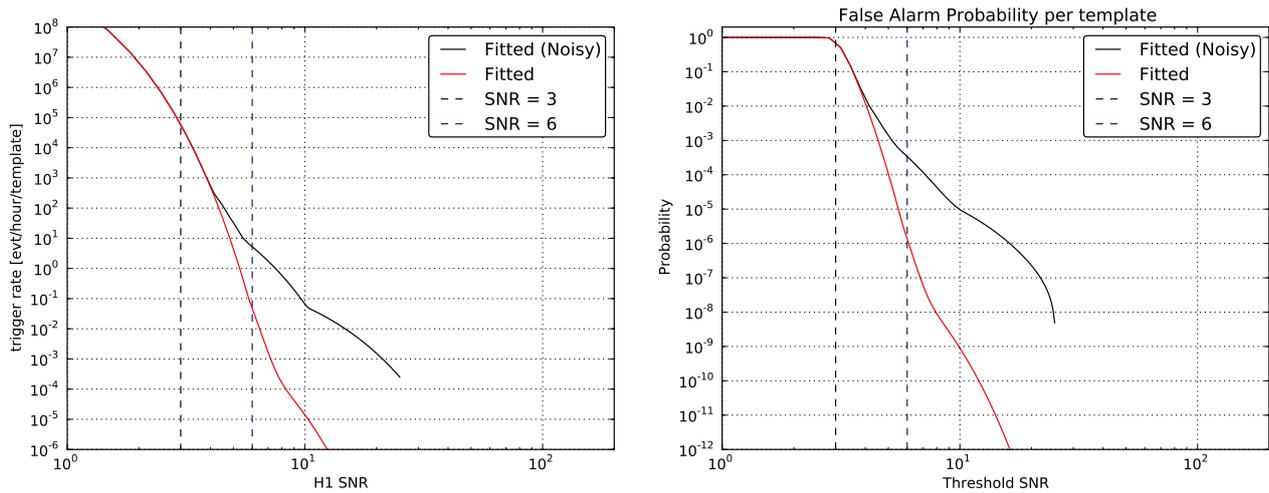
Figure 10.7: SNR distribution in a noisy case ($Left$), FAP in a noisy case ($Right$)

10.4.2   Localization in noisy case

Table 10.4 summarizes the performance in a noisy case, and figure 10.8 shows the obtained sky localization performance using noisy SNR distribution and FAP. The V1 triggers are generated in accordance with the procedure described in the chapter 9.6.1. This investigation is done only for case 1 and case 3, which depend on the SNR distribution and the FAP. The yellow and black dots mean the results from case 1 and case 3, respectively. The behavior of case 1, above the threshold SNR 4, becomes closer to that of the HL double detector search.

V1 threshold	HLV$_{ran}$	HLV$_{inj}$	HL	Offset [deg]	Searched area [deg^2]	90 % area [deg^2]
case 1						
3.0	78 %	0 %	22 %	29	245	440
3.5	14 %	0 %	86 %	21	151	764
4.0	2 %	0 %	98 %	21	145	834
5.5	0.4 %	0 %	99.6 %	21	138	841
case 3						
2.0	66 %	34 %	0 %	13	103	365
3.0	51 %	33 %	16 %	14	109	375
3.3	24 %	32 %	44 %	13	99	495
3.5	11 %	29 %	60 %	13	95	597
3.8	3 %	25 %	72 %	13	92	673
4.0	2 %	23 %	76 %	14	95	694
4.5	1 %	18 %	81 %	15	99	726
5.0	0.1 %	13 %	87 %	16	105	758
5.5	0.1 %	10 %	89.9 %	17	107	789
7.0	0 %	5 %	95 %	19	126	829
8.0	0 %	3 %	97 %	20	129	835
10.0	0 %	1 %	99 %	21	133	835

Table 10.4: Simulation summary in a noisy case
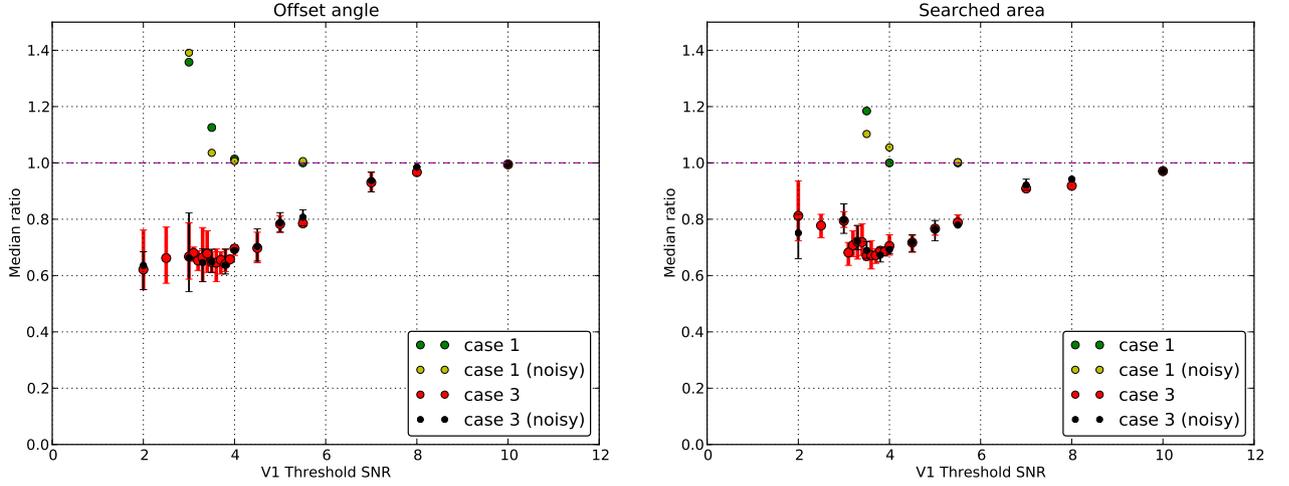
Figure 10.8: Offset angle (*Left*) and searched area (*Right*), when the V1 detector generates a lot of background triggers. In case 3 investigation, calculation is repeated for three times, using different set of random numbers.

According to the offset angle, searched area, and 90 % confidence area, the localize performance does not become worse even if the low sensitivity detector generates a lot of background triggers. The saturation shown in offset angle and the minimum in the searched area depend on the accuracy of the arrival timing and also the number of the HLV$_{ran}$ triggers. The number of the HLV$_{ran}$ triggers depends on the FAP, and thence it is found that the more critical part for the localization performance

is the behavior at the region where the FAP per template is larger than around 10^{-2}.

In conclusion, the HLV hierarchical search works even in consideration of the noisy background triggers from the low sensitivity detector.
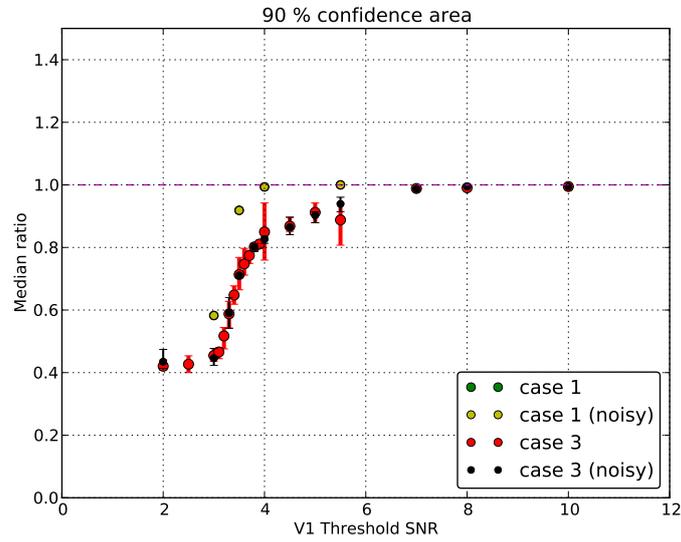
Figure 10.9: 90 % confidence area with HLV hierarchical search, when the V1 detector generates a lot of background triggers. The vertical axis is normalized with the value obtained in HL double search.

10.5   Typical error of sky maps

Above sections explain the statistical merit of the HLV hierarchical network by investigating the discrepancies between the predicted position and the source location. According to the above results, the prediction has a systematic error, such as 13 deg in the offset angle at the optimal SNR threshold. However, it is also important to investigate how the 90 % confidence area and the source position appear in the celestial sphere. This section describes the relation between the predicted 90 % confidence area and the injected source location.

In the hierarchical search, it is found that BAYESTAR can fail to point the injection position within the 90 % confidence area, when it constructs the sky maps from HLV triple coincidence triggers. This situation sometimes happens, especially if the V1 triggers are generated from noise, as shown in figure 10.10. However, this error also happens even if the sky map is generated from triple coincidence trigger with the V1 triggers based on GW signal, as seen in figure 10.11. Table 10.5 summarizes the number of events which the injected location is inside or outside the 90 % confidence area. These numbers are collected when the V1 SNR threshold is set at optimal one.

Trigger type	Inside HL Inside HLV	Inside HL Outside HLV	Outside HL Intside HLV	Outside HL Outside HLV	SUM
HLV_{ran}	22 event	6 events	0 events	1 events	29 events
HLV_{inj}	59 event	10 events	3 events	1 events	73 events

Table 10.5: Number of the events in which the injected location is inside/outside the 90 % confidence area.

According to this table, when the EM counterpart is searched based on the sky map generated from the HLV triple coincidence triggers of hierarchical network, around 20 % of events are found outside its 90 % confidence area. However, even if the EM counterpart does not appear in the 90 % confidence area predicted by HLV triple coincidence trigger, the source is expected to appear within the confidence area from HL double coincidences. Also the source location appears next to the HLV 90 % confidence area in most cases.

Thence following method would help faster identification of the counterpart using EM telescopes. First, one looks for the source based on the sky map predicted by HLV hierarchical network. Then if the source does not appear within the HLV map, one searches the counterpart based on the HL map by expanding the HLV map along the HL prediction.
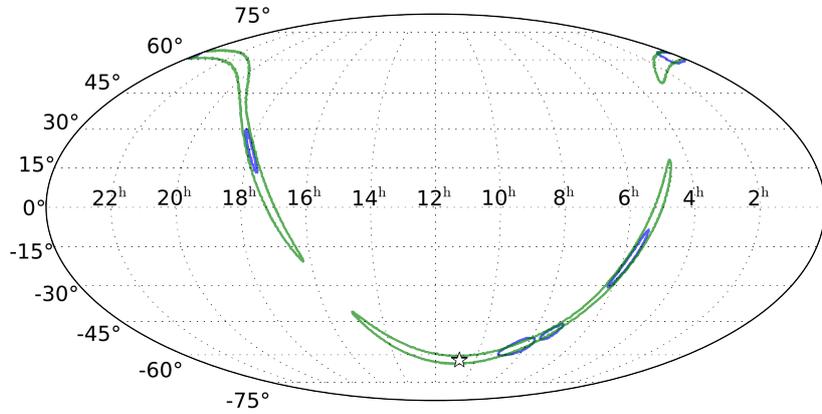
Figure 10.10: Example of sky map error generated from the trigger of H,L and V_{ran} coincidences. The green and blue map are constructed from the trigger HL double coincidences, and the HLV_{ran} triple coincidences.The star indicates the location of the injected source.
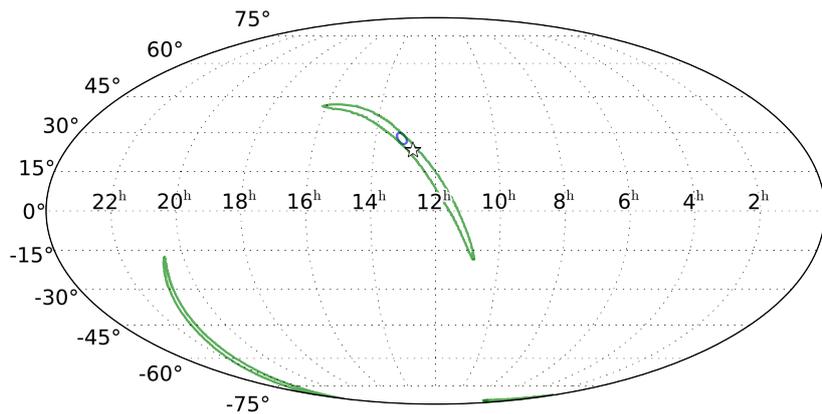

Figure 10.11: Example of sky map error generated from the trigger of H,L and V_{inj} coincidences.The green and blue map are constructed from the trigger HL double coincidences, and the HLV_{inj} triple coincidences.The star indicates the location of the injected source.

Sky localization with hierarchical search of 4 detectors

Chapter 11

Rapid sky localization with the hierarchical search of 4 detector network of H1, L1, V1, K1 are investigated in this chapter. In this calculation, the sensitivities of each detector are set at 70 Mpc for H1 and L1, while 20 Mpc for V1 and K1 detector. The noise curve for K1 detector is the same as the V1 curve described in chapter 9.3.3. In all cases, the K1 threshold is set at the same value of the V1 threshold for simple investigation.

Chapter 11.1 describes the expected localization with 4 detector hierarchical search, and the optimization of V1 and K1 SNR threshold. In chapter 11.2, contribution of the fourth detector for the localization is explained.

11.1   Optimization of V1, K1 threshold SNR

The investigation of 4 detector hierarchical search is described in this section. This calculation is done in accordance with the procedure explained in chapter 9.6.2. The results of trigger population and expected localization are summarized in table 11.1, 11.2. Figure 11.1 shows the median values of the offset angle and the searched area as a function of the SNR threshold, which are obtained from investigation of 4 detector hierarchical search. The corresponding 90 % confidence area is shown in figure 11.2.

According to figure 11.1 and figure 11.2, the behavior of the offset angle, searched area, and 90 % confidence area are same as those of 3 detector hierarchical search. The optimal SNR threshold is around 3.5 according to the searched area. The expected typical offset angle, the searched area, 90 % confidence area at the threshold are 12 deg, 87 deg^2, 500 deg^2, respectively.
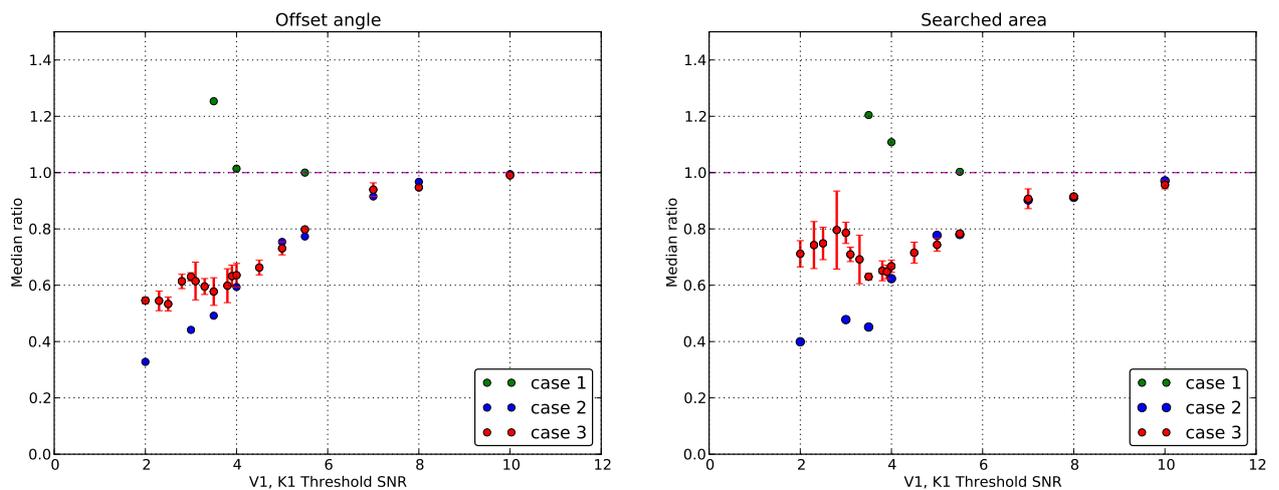
Figure 11.1: Offset angle ($Left$), searched area ($Right$) with 4 detector hierarchical search. In case 3 investigation, calculation is repeated for two times, using different set of random numbers.

175
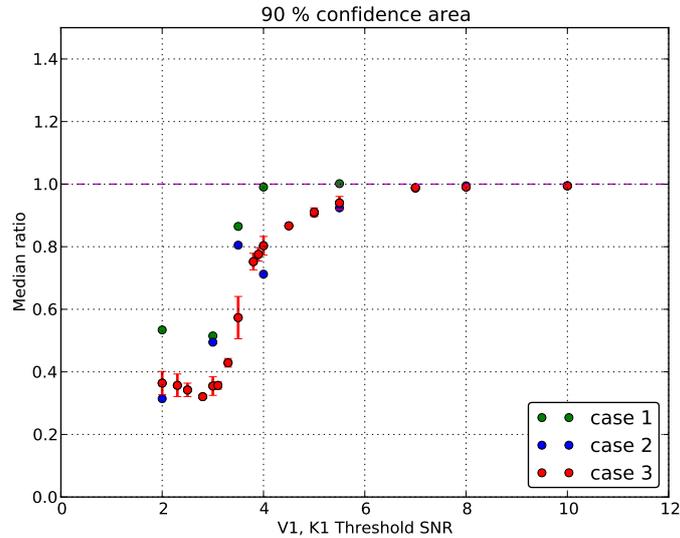
Figure 11.2: 90 % confidence area with 4 detector hierarchical search.

Typical sky maps generated by the triggers from HLVK quadruple coincidences in its hierarchical network are shown in figures 11.3 to 11.6. In these figures, 'ran' and 'inj' denote triggers based noise and injection parameters respectively. If all triggers from each detector in the network are based on GW signals, the maps from the HLVK coincidences are expected to point the location of the source as shown in figure 11.3. Meanwhile, if the trigger from the low sensitivity detector is based on noise, the generated map starts to spread within the 90 % confidence area of HL, in most cases. Also accuracy of the prediction starts to worsen. However, the source is expected to appear next to the confidence area from HLVK trigger. If both of the triggers from the low sensitivity detectors are generated from noise, the HLVK triggered map cannot predict the source position anymore, and this worst situation can be seen in around 5 % of HLVK triggered maps.

This point like prediction is much more useful for the EM counterparts search, compared to the HL search or HLV hierarchical search. This implies adding another low sensitivity detector into the hierarchical network of two more sensitive detectors and one less sensitive detector brings more benefits for fast localization and for looking for EM counterparts.

Table 11.3 describes the number of events in which the injected location is inside or outside the 90 % confidence area from HL or HLVK hierarchical network search.

V1, K1 threshold	Offset [deg]	Searched area [deg^2]	90 % area [deg^2]
case 1			
2.0	35	311	449
3.0	33	271	432
3.5	26	165	726
4.0	21	152	832
5.5	21	138	841
case 2			
2.0	7	55	264
3.0	9	66	416
3.5	10	62	676
4.0	12	86	589
5.0	16	107	761
5.5	16	107	776
7.0	19	124	829
8.0	20	125	835
10.0	21	133	835
case 3			
2.0	11	98	306
2.3	11	102	300
2.5	11	103	287
2.8	13	109	269
3.0	13	108	298
3.1	13	97	300
3.3	12	95	360
3.5	12	87	482
3.8	12	89	632
3.9	13	89	652
4.0	13	92	674
4.5	14	98	728
5.0	15	102	765
5.5	17	108	790
7.0	19	125	831
8.0	20	126	832
10.0	20	131	835

Table 11.1: Simulation summary of HLVK quadruple network

V1, K1 threshold	HLV$_{ran}$K$_{ran}$	HLV$_{ran}$	HLK$_{ran}$	HLV$_{inj}$K$_{inj}$	HLV$_{inj}$	HLK$_{inj}$	HLV$_{ran}$K$_{inj}$	HLV$_{inj}$K$_{ran}$	HL
Case 1									
2.0	100	0	0	0	0	0	0	0	0
3.0	59	15	19	0	0	0	0	0	7
3.5	2	11	13	0	0	0	0	0	74
4.0	0	1	2	0	0	0	0	0	97
5.5	0	0	0	0	0	0	0	0	100
Case 2									
2.0	0	0	0	43	16	13	0	0	28
3.0	0	0	0	22	14	15	0	0	48
3.5	0	0	0	15	15	15	0	0	55
4.0	0	0	0	10	12	10	0	0	67
5.5	0	0	0	2	8	7	0	0	83
7.0	0	0	0	2	3	3	0	0	92
8.0	0	0	0	1	1	2	0	0	95
10.0	0	0	0	0	0.5	0.5	0	0	99
Case 3									
2.0	53	0	0	17	0	0	12	18	0
2.3	53	0	0	17	0	0	12	18	0
2.5	53	0	< 0.5	17	0	0	12	18	0
2.8	49	2	2	17	1	1	11	17	0
3.0	31	7	11	16	4	3	10	14	4
3.1	20	11	14	16	6	5	7	11	10
3.3	7	12	15	14	10	8	5	7	22
3.5	1	7	9	12	13	10	2	2	44
3.8	0	3	2	10	12	11	< 0.5	1	61
3.9	0	3	1	9	12	10	< 0.5	< 0.5	64
4.0	0	1	1	9	12	9	< 0.5	< 0.5	66
4.5	0	< 0.5	< 0.5	6	11	9	0	0	74
5.0	0	0	< 0.5	4	9	7	0	0	80
5.5	0	0	< 0.5	4	6	5	0	0	85
7.0	0	0	0	2	2	3	0	0	93
8.0	0	0	0	1	2	2	0	0	95
10.0	0	0	0	1	1	1	0	0	97

Table 11.2: Trigger population of HLVK hierarchical search (in %).
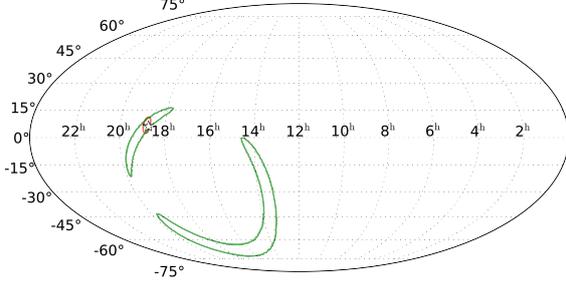
Figure 11.3: $HLV_{inj}K_{inj}$ sky map(a)
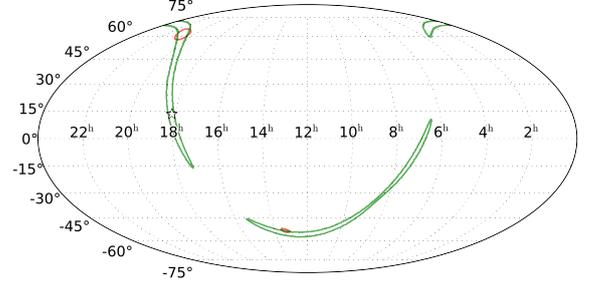
Figure 11.4: $HLV_{ran}K_{ran}$ sky map(b)
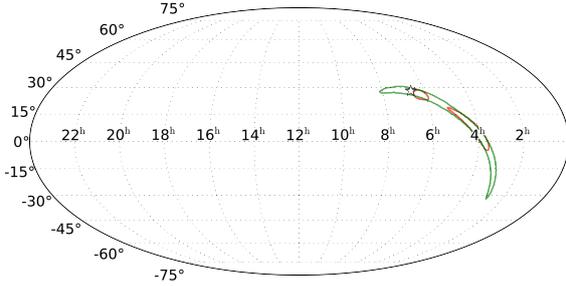
Figure   11.5: $HLV_{ran}K_{inj}$ sky map(c)
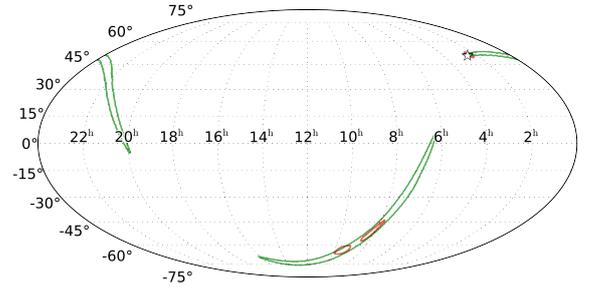
Figure 11.6: $HLV_{inj}K_{ran}$ sky map(d)

11.2   Contribution of fourth detector

This section describes how the fourth detector contributes to the fast localization with the hierarchical search of 3 detectors. Figure 11.7, 11.8 show the comparison of the offset angle, searched area, and 90 % confidence area. All of them are obtained from case 3 investigation.

It is found that the optimal thresholds for V1, K1 detectors in the 4 detector search, and the accuracy of the sky maps at the threshold are mostly the same as the 3 detector search. This is because the same parameters as V1 detector are used for KAGRA detector. The accuracy of the sky maps seen in the offset angle and the searched area depend on the number of V1, K1 triggers based on GW signals, and also depend on the added timing uncertainties and sensitivities of each detector. Since same FAP, timing uncertainties, and sensitivity as V1 detector are used for the K1 detector in

Trigger type	Inside HL Inside HLVK	Inside HL Outside HLVK	Outside HL Inside HLVK	Outside HL Outside HLVK	SUM
$HLV_{ran}K_{ran}$	0 event	2 events	0 events	0 events	2 events
$HLV_{rad}K_{inj}$	3 event	2 events	0 events	0 events	5 events
$HLV_{inj}K_{ran}$	5 event	0 events	0 events	0 events	5 events
$HLV_{inj}V_{inj}$	25 event	3 events	1 events	0 events	29 events
HLV_{ran}	15 event	3 events	0 events	0 events	18 events
HLV_{inj}	24 event	3 events	2 events	1 events	30 events
HLK_{ran}	16 event	4 events	0 events	0 events	20 events
HLK_{inj}	17 event	5 events	0 events	0 events	22 events

Table 11.3: Number of events in which the injected location is inside/outside the 90 % confidence area of HLVK, HL search.

this investigation, it is expected that the accuracy of the sky maps do not improve so much, compared to the 3 detector hierarchical search. The obtained result of 4 detector hierarchical search is consistent with this issue.

If different sensitivity is selected for each low sensitivity detector, the optimal threshold for each detector, and the expected localization performance would produce different results.
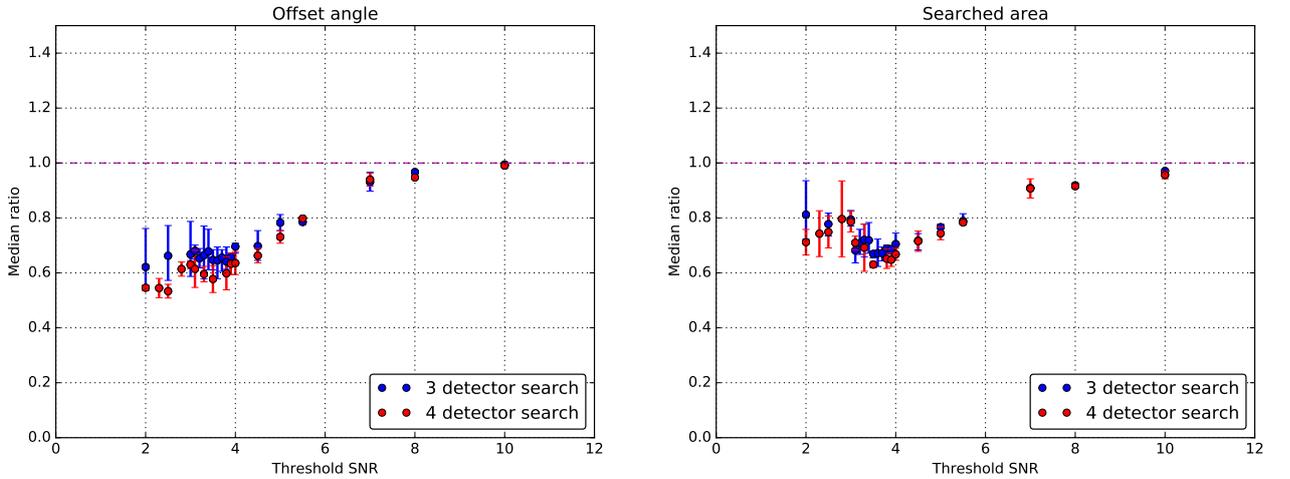
Figure 11.7: Comparison of offset angle (*Left*), searched area (*Right*) between 3 detector hierarchical search and 4 detector search. Offset angle and searched area are reduced from 13 deg, 93 deg^2 to 12 deg, 87 deg^2 at the SNR threshold of 3.5.

On the other hand, 4 detector search improves the 90 % confidence area as shown in figure 11.8. The median value of the confidence area is reduced to around 500 deg^2 at the optimal threshold, which is smaller than HLV hierarchical search by around 100 deg^2.

Even though the systematic prediction errors seen in offset angle and searched area are not improved, the 4 detector search gives more precise sky maps. This would increase opportunities whereby the source objects are found in EM follow up observation.
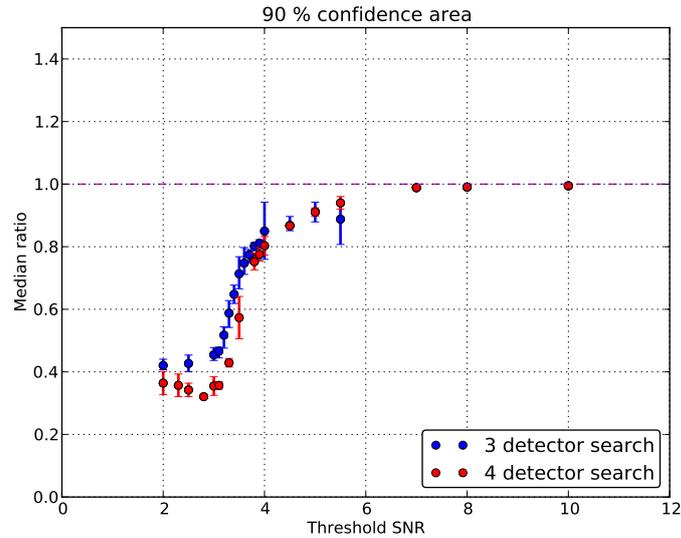
Figure 11.8: Comparison of 90 % confidence area between 3 detector hierarchical search and 4 detector search. At below SNR 4, the area is further reduced due to the contribution of quadruple triggers than 3 detector hierarchical network.

In conclusion, if the hierarchical network is constructed with two high sensitivity detectors, and two low sensitivity ones are implemented into the pipeline, it is expected that same accuracy of the sky maps are obtained as that of three detector hierarchical search with two high sensitivity detectors and one low sensitivity detector. However, the confidence area in the four detector search is reduced compared to the three detector search, and thus the four detector search is more useful for looking for the EM counterpart.

If more accurate sky maps are necessary, the arrival timing uncertainties of the low sensitivity detectors should be improved, so that higher SNR triggers are analyzed. In addition, more stable operation is necessary so that they do not to generate a lot of back ground triggers.

Conclusion and future work
Chapter 12

12.1   Conclusion

The fast localization with hierarchical network is demonstrated in this work. This is the first time to demonstrate this localization method with 3 and 4 detectors, quantitatively. The expected performance of 3 and 4 detector network search at the optimal thresholds are summarized in table 12.1. In the actual situation, the sensitivities of all the four detectors which are considered in this investigation are expected to be improved. Especially, as for the fast localization with 4 detector hierarchical search, more improvement in performance is expected, when the search is implemented into the pipeline.

	Offset [deg]	Searched area [deg^2]	90 % area [deg^2]
HL search	21	137	840
HLV search	13	93	600
HLVK search	12	87	500

Table 12.1: Expected localization performance with the hierarchical network. This table describes median values a the optimal SNR threshold, when the sensitivity of H1, L1 is 70 Mpc, while that of V1, K1 is set at 20 Mpc.

The optimal SNR threshold for the low sensitivity detectors are obtained at around 3.5, according to the accuracy of the sky maps. Based on these results, it is confirmed that the hierarchical network is one effective method to construct the detection network with different sensitivity detectors. This searching method is useful for newly constructed detectors.

12.2   Future work

In this work, the two LIGO detectors are assumed to maintain its work. However, H1 and L1 detector can discontinue their operation for some reason. If GW signals come in this condition, information from double (or more) coincidences is to be generated from different sensitivity detectors. In this case, for making effective use of the low sensitivity detectors, it is expected to set high SNR threshold for higher sensitivity detectors, while lower threshold for the less sensitive ones. This method is to be investigated from the point of view of the sky maps.

The searched area as a function of the SNR threshold for the low sensitivity detector, has a minimum value as shown in figure 10.4. It is expected that it depends on the number of the V1 triggers from noise, and the accuracy of the added timing uncertainties. However, it is still not described theoretically. The theoretical prediction of the localization performance can simplify the finding procedure of the optimal thresholds of less sensitive detectors in the hierarchical search. It can also help making detailed plan for adding newly constructed detectors into the network, and thence this is also to be investigated.

Summary
PartIV

Conclusion and future work

This research focused on the development of the seismic attenuation system for the power recycling mirrors of the KAGRA detector. It also studied a localization method by using a network of gravitational wave detectors with different sensitivities.

Development of a low frequency vibration isolation system for KAGRA

This work verified a performance of an existing simulation tool for mechanical suspension systems and active control systems of them. This verification was done by using the iKAGRA-PR3 SAS at the KAGRA site in the Kamioka underground. In the experiment, it is found that the simulation predicts consistent performances with the actual ones, though it tends to larger RMS values than the actual values. Based on this, it is confirmed that this simulation works for designing the active control system for the suspension system.

For further precise prediction, one might has to investigate the uncertainties due to mechanical assembly. The predictions at higher frequencies than ~ 1 Hz are to be tested by using more sensitive sensors.

This work also designed the active control systems for the type-Bp SAS by using the simulation tool and confirmed that the designed control systems met the fundamental requirements on the active control systems for the suspension system.

A fact predicted from this simulation is that in the calm-down phase, it might be wanted to use optical sensors, which have narrow linear range, for a rapid damping. It is expected that, even in absence of these optical sensors, one can rapidly damp the resonant motions, which may disturb the lock-acquisition of the interferometer, by using an eddy-current damping system. Though, the performance of the damping system is to be investigated in order to realize a stable control system for the type-Bp suspension system.

Study of the localization of coalescing binaries with a hierarchical network of gravitational wave detectors

This work demonstrated the rapid localization of coalescing binaries with a hierarchical network by using a network of gravitational wave detectors with different sensitivities. This demonstration focused on this method by 3 or 4 gravitational wave detectors. A hierarchical network search aims to make effective use of the least sensitive detectors' information.

According to the investigation, the offset angle and the searched area will be reduced by a factor of ~ 0.7, compared to those obtained by the 2 higher sensitivity detectors' coincidences search. Here it assumes that the higher sensitivity detectors have 70 Mpc and the lower ones have 20 Mpc for their detection range. Also the SNR thresholds are set at 5 for the higher ones, while 3.5 for the lower ones. This study confirmed that the hierarchical network search is useful for newly constructed detectors. Since the sensitivities of these detectors will be more improved than those assumed in this simulation,

the actual localization by this method performance will be also improved.

For future work, a theoretical prediction of the localization performance is also to be investigated for establishing simpler optimization method of the SNR thresholds for the less sensitivity detectors.

In addition, a network search by two different sensitivity gravitational wave detectors is to be investigated. This is because one of higher sensitivity detectors can be out of the operation, in an actual observation.

Eigenmodes of type-Bp SAS
Chapter A

#11   0.659Hz   More

#12   0.659Hz   More

#13   0.849Hz   More

#14   0.9Hz   More

#15   0.901Hz   More

#16   1.011Hz   More

#17   1.017Hz   More

#18   1.022Hz   More

#19   1.186Hz   More

#20   1.186Hz   More

#21   1.261Hz   More

#22   1.261Hz   More

#23   1.351Hz   More

#24   1.352Hz   More

#25   1.369Hz   More

#26   4.906Hz   More

#27   11.611Hz   More

#28   15.924Hz   More

#29   48.97Hz   More

#30   64.629Hz   More

#31   78.843Hz   More

#32   78.843Hz   More

#33   97.094Hz   More

#34   98.66Hz   More

#35   100.617Hz   More

#36   126.38Hz   More

Active control system for type-Bp SAS

Chapter B

B.1   Controls in calm-down phase
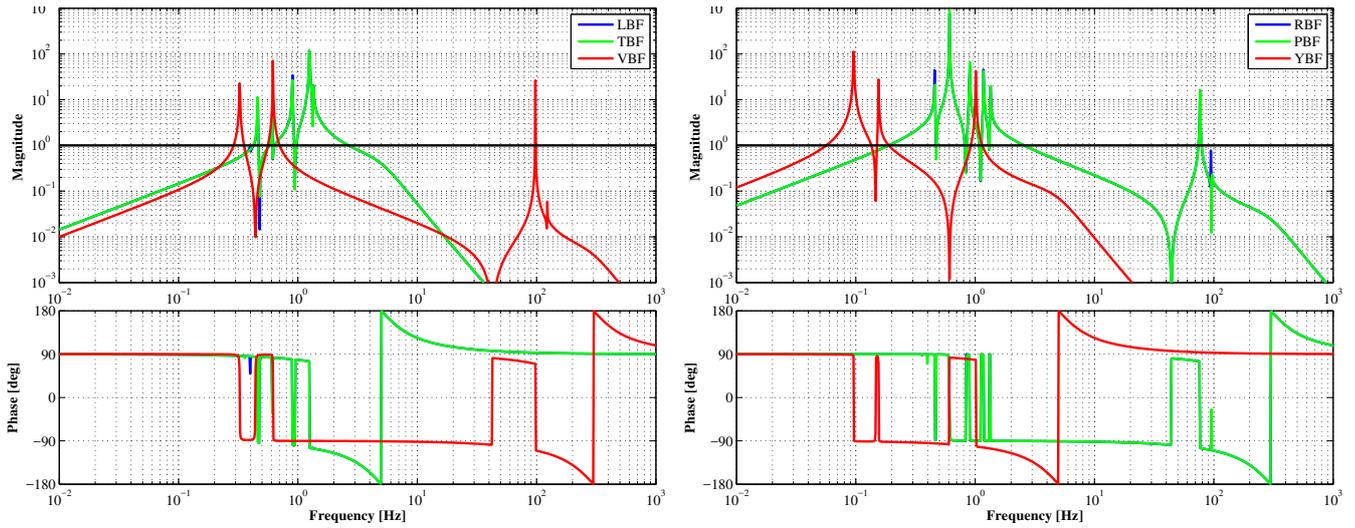
Figure B.1: Open loop transfer functions of active damping controls at BF level.
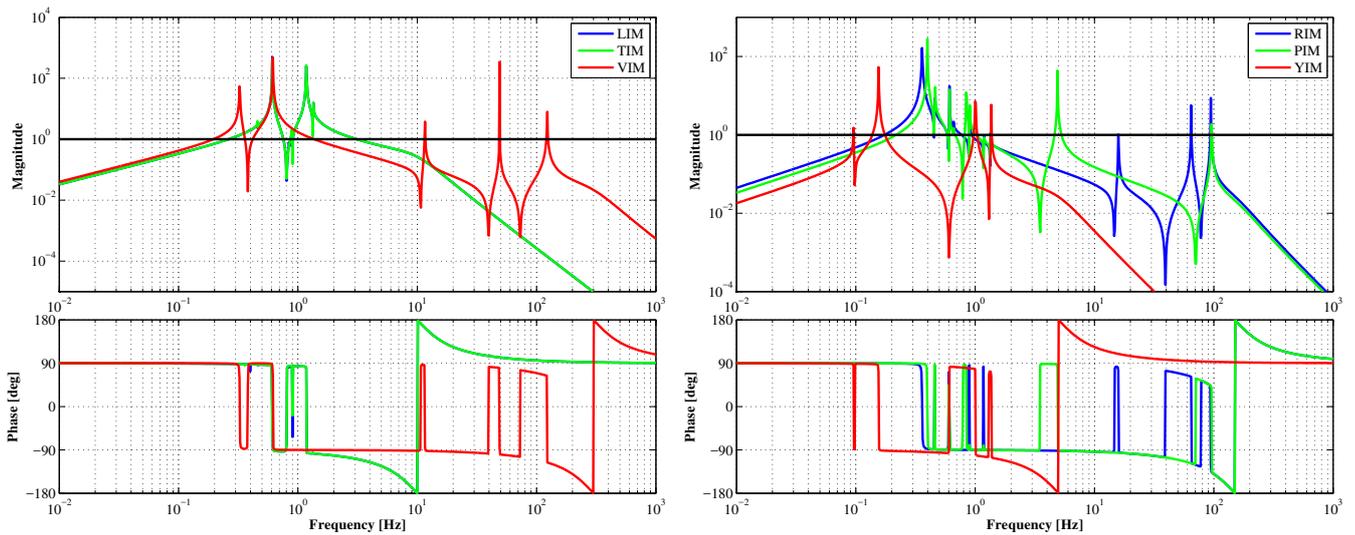
Figure B.2: Open loop transfer functions of active damping controls at IM level (*Right*).
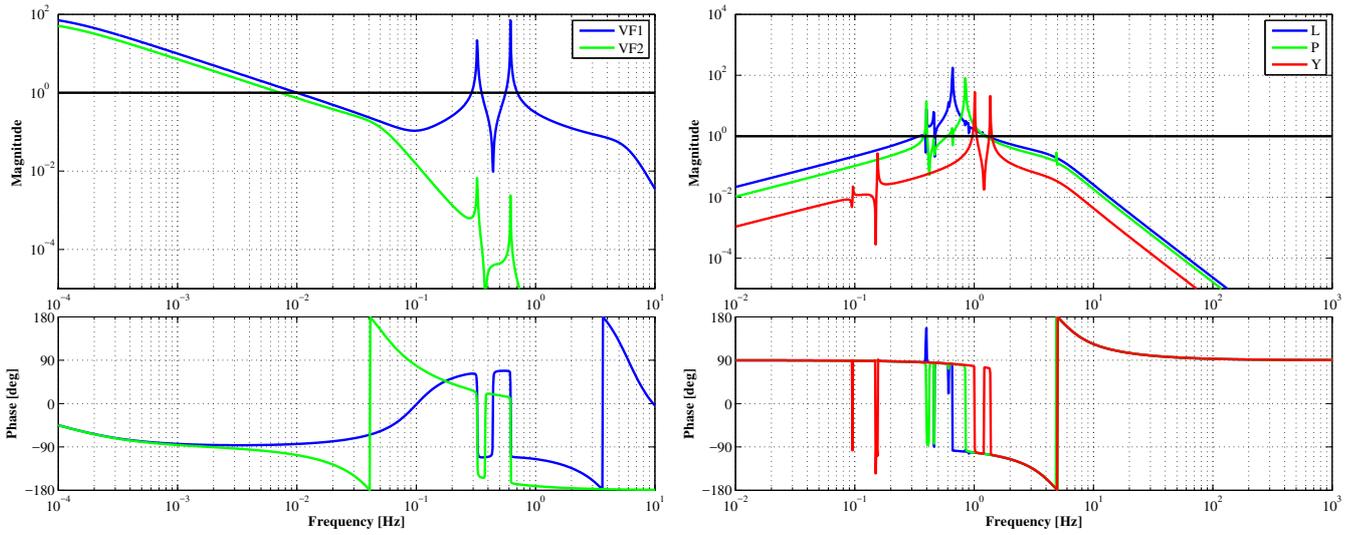
Figure B.3: Open loop transfer functions of active damping controls for GAS filters (*Left*) and at TM level.
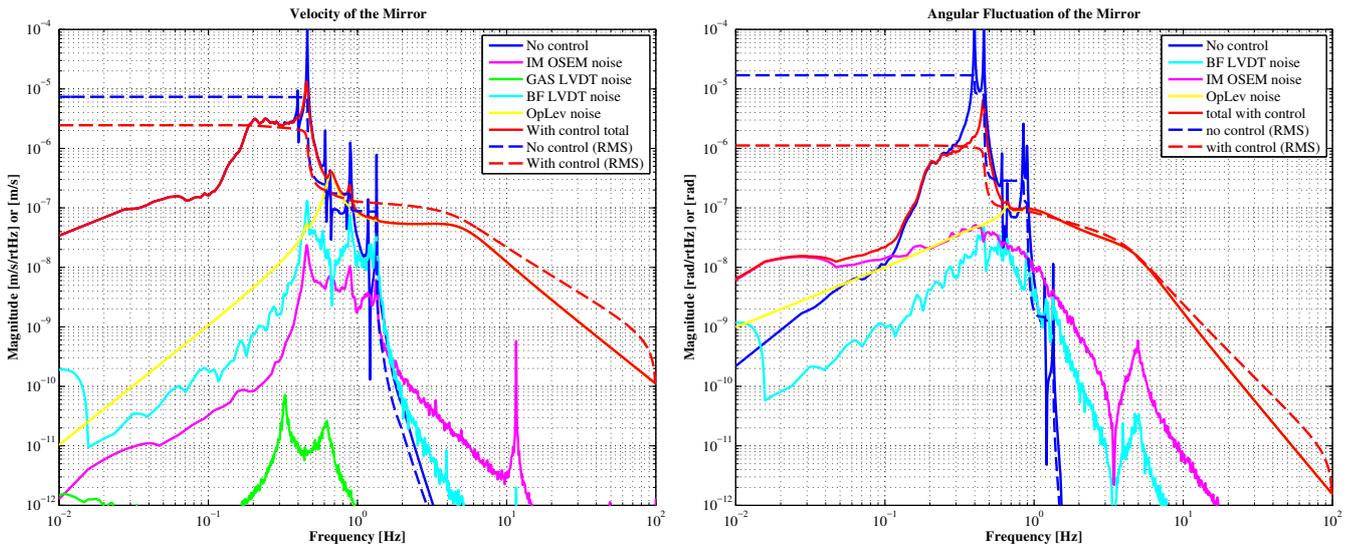
Figure B.4: Expected control noise coupling into longitudinal velocity fluctuation (*Left*) and into the pitch vibration (*Right*) of the mirror in the calm-down phase.

B.2   Controls in lock acquisition and observation phase
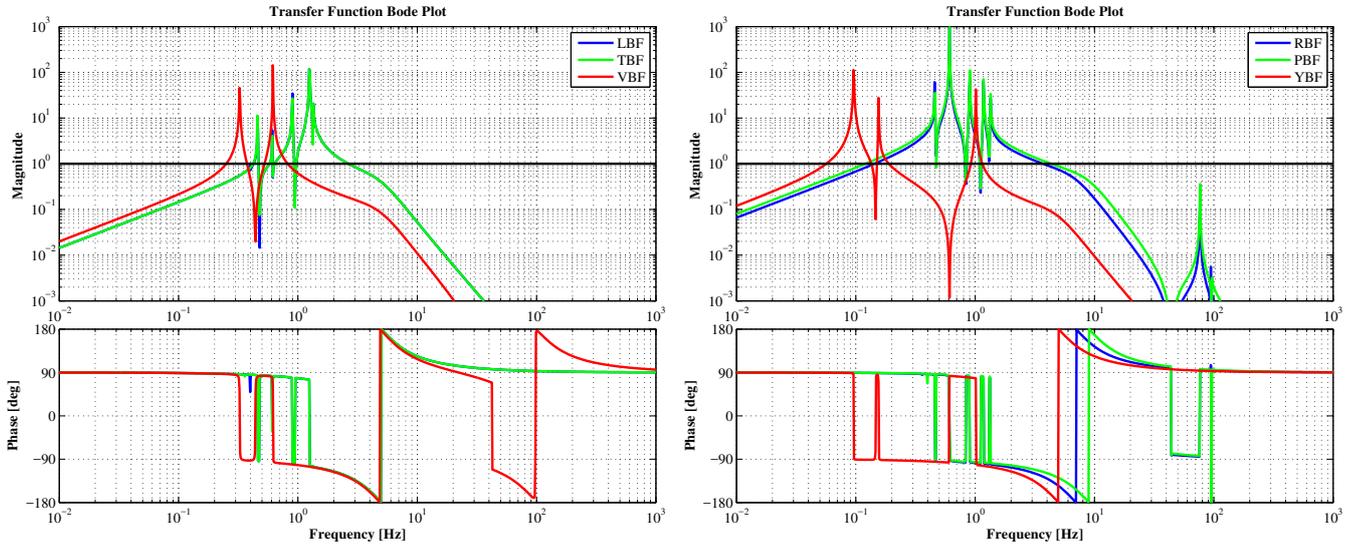
Figure B.5: Open loop transfer functions of active controls at BF level in the lock acquisition and the observation phase.
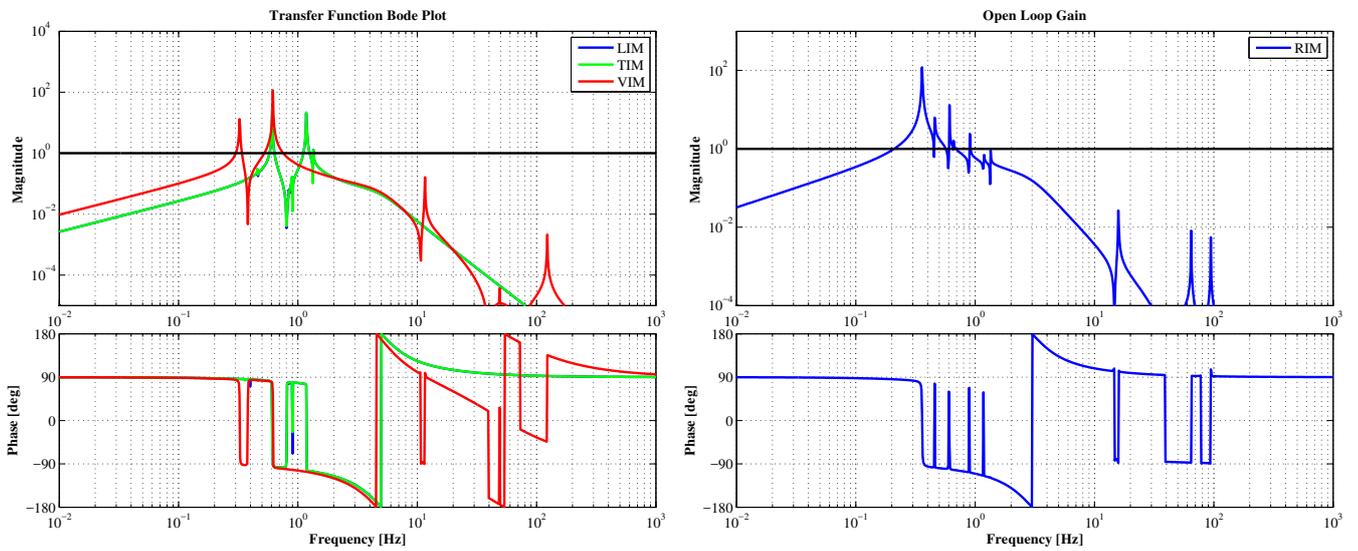
Figure B.6: Open loop transfer functions of active controls at IM level in the lock acquisition and the observation phase.
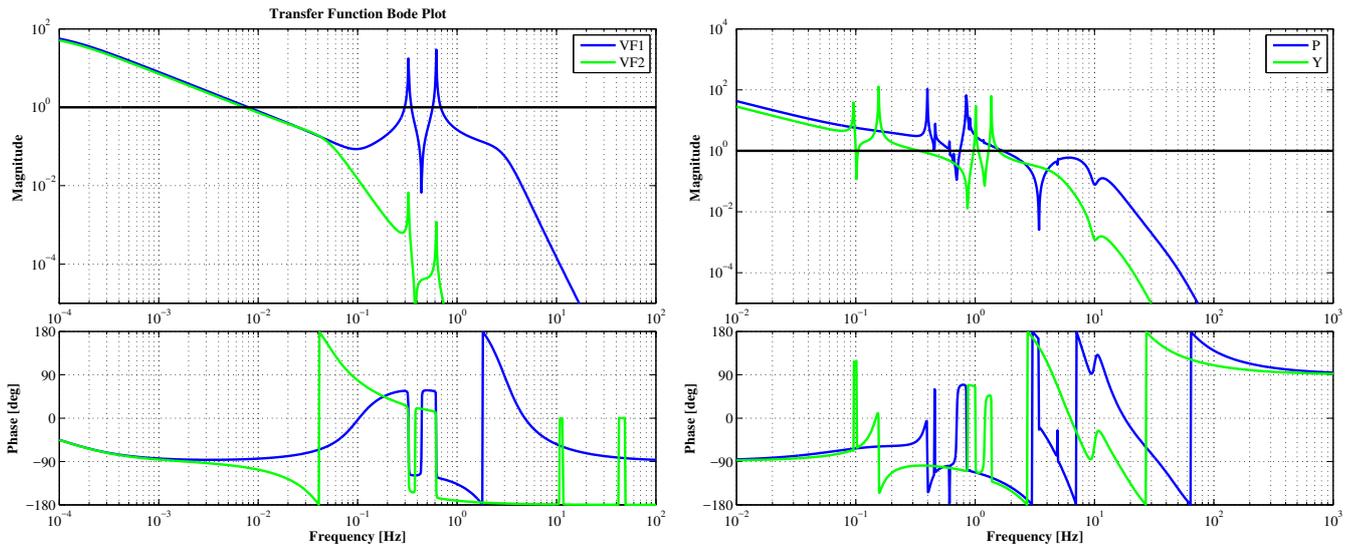
Figure B.7: Open loop transfer functions of active controls for GAS filters ($Left$) and at TM level in the lock acquisition and the observation phase.
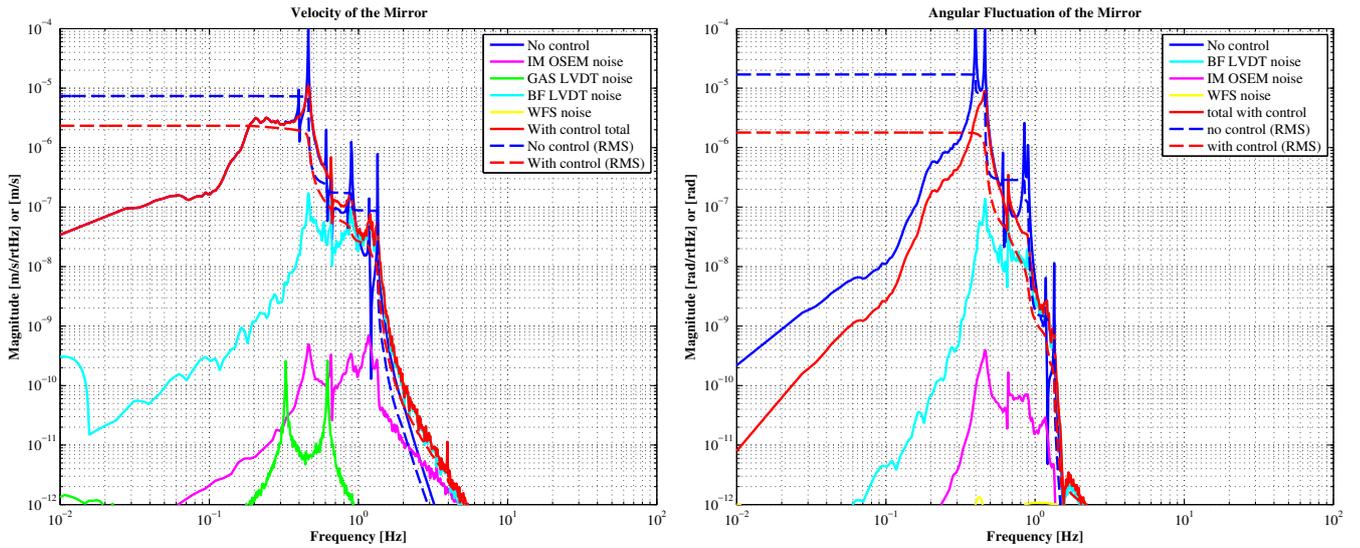
Figure B.8: Expected control noise coupling into longitudinal mirror vibration in velocity ($Left$) and into the pitch vibration ($Right$) of the mirror in observation phase.

Acknowledgements

Bibliography

[1] A. Einstein, Ann. der Phys., 354 (7), 769822, (1916).

[2] B. Abbott et al., Phys. Rev. lett, 116, 061102 (2016).

[3] Y. Suto, 'Introduction of general relativity', Nihon-hyoron-sha (2010), (in Japanese).

[4] T. Nakamura, N. Mio, and M. Ohashi, 'Detecting gravitational waves', Kyoto University Press, (1998), (in Japanese).

[5] C. Cutler and K. Thorne, arXiv, 0204090 [gr-qc], (2002).

[6] M. Maggiore. 'Gravitational Waves: Theory and Experiments', Oxford University Press, (2008).

[7] C. D. Ott, Class. Quant. Grav., 26, 063001, (2009).

[8] T. Damour, A. Vilenkin, Phys. Rev. D, 71, 063510, (2005).

[9] B. Allen, et al., Phys. Rev. D, 85, 122006 (2012).

[10] The LIGO Scientific Collaboration and The Virgo Collaboration, Nature, 460, 990994, (2009).

[11] M. G. Beker, PhD thesis, Vrije Universiteit, (2013).

[12] K. Riles, arXiv, 1209.0667v3 [hep-ex] (1916).

[13] K. Kawabe, PhD thesis, University of Tokyo, (1998).

[14] B. Bochner, Gen. Relativ. Gravit., 35 (6), 10291055, (2003).

[15] A. Buonanno and Y. Chen, Phys. Rev. D, 64, 042006, (2001).

[16] W. J. Startin et al., Rev. Sci. Instrum., 69 (10), 36813689, (1998).

[17] S. Rowan et al., Phys. Lett. A, 265, 40309, (2000).

[18] T. Tomaru et al., Phys. Lett. A, 301, 215219, (2002).

[19] J. Peterson, Open File Report, pages 93322, (1993)

[20] P. Shearer. 'Introduction to Seismology Second Edition', Cambridge Univirsity Press, (2009).

[21] M. G. Beker et al., Gen. Relativ. Gravit., 43, 623656, (2011).

[22] H. A. Sodano et al., J. Vib. Acoust., 128, 294302, (2006).

[23] A. Takamori, PhD thesis, University of Tokyo, (2002).

[24] G. Losurdo et al., Rev. Sci. Instrum., 70 (5), 25072515, (1999).

[25] G. Cella et al., Nucl. Instrum. Methods A, 540, 502519, (2005).

[26] M. Blom, PhD thesis, Vrije Universiteit (2015).

[27] A. Stochino et al., Nucl. Instrum. Methods A, 580, 15591564, (2007).

[28] F. Cordero et al., Journal of Alloys and Compounds, 310, 400404, (2000).

[29] H. M. Ledbetter et al., Materials Science and Engineering, 72, 65-69 (1985).

[30] Y. Aso et al., Class. Quant. Grav., 29, 124008, (2012).

[31] KAGRA Main Interferometer Working Group, KAGRA Internal Document, JGW-T1200913-v6, (2014).

[32] K. Somiya, Class. Quant. Grav., 29, 124007, (2012).

[33] T. Sekiguchi, Master's thesis, University of Tokyo, (2012).

[34] G. Hammond, LIGO Internal Document, T010171-00-D, (2001).

[35] S. Aston, LIGO Internal Document, T050111-04-K, (2009).

[36] 'Advanced Virgo Technical Design Report', Virgo Internal Document, VIR-0128A-12, (2012)

[37] E. D. Black, Am.J.Phys., 69, 79 (2001).

[38] A. J. Mullavey et al., Optics Express, 20 (1), 8189 (2011).

[39] K. Izumi, Master's thesis, University of Tokyo (2009). (in Japanese).

[40] Y. Aso et al., Phys. Rev. D, 88, 043007 (2013).

[41] Y. Michimura, KAGRA Internal Document, JGW-T1202403-v1 (2014).

[42] T. Sekiguchi, PhD thesis, University of Tokyo (2016).

[43] M. Beccaria et al., Nucl. Instrum. Methods A, 404, 455469, (1998).

[44] K. Agatsuma et al., Class. Quant. Grav., 27, 084022, (2010).

[45] T. Sekiguchi, KAGRA internal document JGW-T1402971-v1 (2014).

[46] H. Tariq et al., Nucl. Instrum. Methods Phys Res A, 489, 570576, (2002).

[47] KAGRA Internal Document, JGW-T1201255-v1, (2012).

[48] Y. Fujii, KAGRA internal document JGW-T1706050-v2 (2017).

[49] Y. Fujii, KAGRA internal document JGW-G1605149-v4 (2016), (in Japanese).

[50] S. Zeidler, KAGRA internal document JGW-T1605788-v5 (2016).

[51] K. Okutomi, KAGRA internal document JGW-T1605707-v4 (2016).

[52] B. Allen, et al., Phys. Rev. D, 85, 122006 (2012).

[53] J. Abadie, et al., arXiv:1203.2674 (2012).

[54] T. Adams, et al., arXiv:1512.02864 (2012).

[55] L. Singer, et al., arXiv:1508.03634 (2016).

[56] J. Abadie et al., A&A, 541, A155 (2012).

[57] J. Aasi et al., Phys. Rev. D, 88, 062001 (2013).

[58] M. Maggiore, Physics Reports 331, 283, (2000).

[59] L. Singer, PhD Thesis, California Institute of Technology, (2015).

[60] L. Singer, et al., The Astrophysical Journal 795, 105, (2014).